Defect-Related Luminescence in Nanocrystals: Spectroscopy and Computation

Heidi Danielle Nelson

A dissertation

submitted in partial fulfillment of the

requirements for the degree of

Doctor of Philosophy

University of Washington

2018

Reading Committee:

Daniel R. Gamelin, Chair

Xiaosong Li

Brandi M. Cossairt

Program Authorized to Offer Degree:

Chemistry

University of Washington

Abstract

Defect-Related Luminescence in Nanocrystals: Spectroscopy and Computation

Heidi Danielle Nelson

Chair of the Supervisory Committee:

Daniel R. Gamelin

Department of Chemistry

Dopants and defects play an important role in the luminescence of semiconductors, from classic bulk phosphors to more recently developed colloidal nanocrystals. This thesis describes several studies on the photophysics of defect-related luminescence in semiconductor nanocrystals, with a particular focus on copper and silver charge-transfer luminescence. The combination of density functional theory (DFT) and spectroscopy can provide deeper insight into the photophysics of these materials and help resolve unanswered questions about their luminescence. In chapter 2, DFT is used to investigate various aspects of the electronic structure and photoluminescence mechanism of copper-doped CdSe nanocrystals, including the copper oxidation state, the origin of the broad luminescence line width, and the excited-state singlet−triplet splitting. These calculations support and expand upon previous experimental results. Chapter 3 extends these experimental and computational studies to silver-doped CdSe nanocrystals. These materials have very similar photoluminescence properties to their copper-doped analogues, but they have

significant electronic-structure differences due to inverted bonding between the silver dopant and its neighboring anions. Chapter 4 addresses the similarities between the photoluminescence of copper-doped and copper indium sulfide nanocrystals. DFT calculations demonstrate a significant tendency for the hole to localize in the valence band of copper indium sulfide, which has significant copper character and resembles the copper impurity level in doped nanocrystals. Other dopants and defects can also influence nanocrystal luminescence in different ways. Chapter 5 addresses the effects of slow electron trapping and detrapping on the intensity and dynamics of delayed luminescence in nanocrystals by varying the excitation pulse width. Chapter 6 is an investigation of photoinduced magnetization in manganese-doped CdSe nanocrystals; the formation of excitonic magnetic polarons is studied by continuous-wave and time-resolved magneto-optical spectroscopies. Together, these studies demonstrate a variety of ways that dopants and defects can affect the photoluminescence of semiconductor nanocrystals.

TABLE OF CONTENTS

List of Figures v

Chapter 1. Introduction: Electronic Structure and Luminescence of Copper-Doped and Silver-Doped Semiconductor Nanocrystals 1

1.1 Copper and Silver Luminescence 1

1.2 Copper-Doped Nanocrystals 3

1.3 Silver-Doped Nanocrystals 6

1.4 Photophysics of Cu^+-Doped and Ag^+-Doped Nanocrystals 9

1.5 $CuInS_2$ and Related Nanocrystals 20

1.6 Summary 22

1.7 References 23

Chapter 2. Computational Studies of the Electronic Structures of Copper-Doped CdSe Nanocrystals: Oxidation States, Jahn–Teller Distortions, Vibronic Bandshapes, and Singlet–Triplet Splittings 33

2.1 Overview. 33

2.2 Introduction 34

2.3 Computational Methods 37

2.4 Results and Analysis 38

2.5 Conclusion 56

2.6 Acknowledgments 57

2.7 Supporting Information 57

2.8 References 57

Chapter 3. Mid-Gap States and Normal *vs* Inverted Bonding in Luminescent Cu^{+}- and Ag^{+}-Doped CdSe Nanocrystals 62

3.1 Overview 62

3.2 Introduction 63

3.3 Methods 66

3.4 Results and Analysis 69

3.5 Discussion 85

3.6 Conclusion 89

3.7 Acknowledgments 91

3.8 Supporting Information 91

3.9 References 92

Chapter 4. Valence-Band Electronic Structures of Cu^{+}-Doped ZnS, Alloyed Cu–In–Zn–S, and Ternary $CuInS_2$ Nanocrystals: A Unified Description of Photoluminescence Across Compositions 97

4.1 Overview 97

4.2 Introduction 98

4.3 Methods 100

4.4 Results and Analysis 101

4.5 Discussion 113

4.6 Conclusion 115

4.7 Acknowledgments 117

4.8 Supporting Information 117

4.9 References 117

Chapter 5. Strong Dependence of Quantum-Dot Delayed Luminescence on Excitation Pulse Width 123

5.1 Overview 123

5.2 Introduction 124

5.3 Results 125

5.4 Model 132

5.5 Discussion 137

5.6 Supporting Information 140

5.7 Acknowledgments 140

5.8 References 141

Chapter 6. Picosecond Dynamics of Excitonic Magnetic Polarons in Colloidal Diffusion-Doped $Cd_{1-x}Mn_xSe$ Quantum Dots 143

6.1 Overview 143

6.2 Introduction 144

6.3 Results and Analysis 149

6.4 Discussion 168

6.5 Summary 171

6.6 Methods 172

6.7 Acknowledgments 175

6.8 Supporting Information 175

6.9 References 175

Appendix A. Supporting Information for Chapter 2 182

Appendix B. Supporting Information for Chapter 3 190

Appendix C. Supporting Information for Chapter 4 197

Appendix D. Supporting Information for Chapter 5 208

Appendix E. Supporting Information for Chapter 6 219

LIST OF FIGURES

Figure 1.1. Copper PL mechanism and effect of quantum confinement on PL energy. 4
Figure 1.2. Comparison of undoped and Cu^+-doped CdSe NCs. 5
Figure 1.3. Comparison of Cu^+:CdSe and Ag^+:CdSe NCs. 6
Figure 1.4. Electronic excitations in Cu+-doped and Cu2+-doped NCs. 9
Figure 1.5. Singlet−triplet splitting in Cu^+-doped NCs. 13
Figure 1.6. Origin of the broad PL line width and large Stokes shift in Cu^+-doped NCs. 16
Figure 1.7. Absorption and PL of $CuInS_2$ NCs. 20
Figure 2.1. Calculated HOMO and LUMO surfaces and molecular-orbital energies for undoped, Cu^{2+}-doped, and Cu^+-doped NCs. 41
Figure 2.2. Calculated absorption spectra of undoped, Cu^{2+}-doped, and Cu^+-doped NCs. 43
Figure 2.3. Energy levels of singlet and triplet excited states. 45
Figure 2.4. Natural transition orbitals. 48
Figure 2.5. Excited-state bond length changes. 49
Figure 2.6. Excited-state distortions, single-configurational-coordinate diagrams, and simulated PL spectrum. 51
Figure 2.7. Dependence of singlet−triplet splitting on dopant location. 53
Figure 3.1. Absorption and PL of Ag^+- and Cu^+-doped CdSe NCs. 71
Figure 3.2. MCPL and TRPL of Ag^+:CdSe NCs. 72
Figure 3.3. MO energies and compositions for undoped, Cu^+-doped, and Ag^+-doped CdSe NCs. 75
Figure 3.4. Mid-gap MOs of Cu^+-doped and Ag^+-doped CdSe NCs. 77
Figure 3.5. Calculated absorption and PL spectra for Cu^+-doped and Ag^+-doped CdSe NCs. 79
Figure 3.6. Natural transition orbitals for Cu^+:CdSe and Ag^+:CdSe NCs. 81
Figure 3.7. Excited-state bond lengths for Cu^+:CdSe and Ag^+:CdSe NCs. 84
Figure 3.8. Molecular-orbital diagrams illustrating normal and inverted bonding. 87
Figure 4.1. Calculated electronic structures of randomly alloyed Cu−In−Zn−S NCs. 103
Figure 4.2. HOMOs and LUMOs of randomly alloyed Cu−In−Zn−S NCs. 105
Figure 4.3. HOMOs of Cu^+,In^{3+}:ZnS NCs with increasing Cu^+ and In^{3+} concentrations. 107
Figure 4.4. HOMOs of 77-cation ZnS NCs containing Cu^+ trimers. 109

Figure 4.5. HOMO surfaces and atomic-orbital contributions for 77-cation ZnS NCs containing Cu^+ dimers with different In^{3+} positions. 110
Figure 4.6. Comparison of the HOMOs of modified $CuInS_2$ NCs. 112
Figure 4.7. Schematic illustration of the electronic structure and radiative recombination mechanism in Cu^+-doped and $CuInS_2$ NCs. 114
Figure 5.1. PL decay of $CuInS_2$ NCs under pulsed and square-wave excitation. 126
Figure 5.2. Dependence of delayed luminescence on pulse width and power for $CuInS_2$ NCs. ..127
Figure 5.3. Dependence of delayed luminescence on pulse width and power for CdSe NCs. 131
Figure 5.4. Delayed luminescence model and simulated results. 133
Figure 6.1. Single-magnetic-coordinate diagram describing EMP formation in a DMS QD. 146
Figure 6.2. Temperature-dependent CW absorption and PL. 150
Figure 6.3. Temperature- and field-dependent absorption, MCD and MCPL. 153
Figure 6.4. Time-resolved MCPL. 155
Figure 6.5. Comparison of CW and time-dependent magnetization. 157
Figure 6.6. Saturation of the MCPL polarization ratio at low temperatures. 158
Figure 6.7. Comparison of experimental and simulated MCPL temperature and field dependence. 159
Figure 6.8. TRFR for varying Mn^{2+} concentrations and pump/probe energies. 163
Figure 6.9. Simulated pump/probe energy dependence of the TRFR phase. 166
Figure 6.10. Multidimensional magnetic coordinate diagram. 169
Figure A.1. Binned density-of-states plots. 183
Figure A.2. Comparison of ground- and excited-state bond lengths. 185
Figure A.3. Comparison of bond lengths for a ground-state Cu^{2+}-doped NC and an excited-state Cu^+-doped NC. 186
Figure A.4. Excited-state distortions for a 34-cation NC. 187
Figure A.5. Excited-state bond length changes at Cu. 187
Figure B.1. Variable-temperature PL spectra of Ag^+:CdSe NCs. 190
Figure B.2. Binned density-of-states plots for Cu^+:CdSe and Ag^+:CdSe NCs. 191
Figure B.3. Molecular-orbital energies for different sizes of Cu^+:CdSe and Ag^+:CdSe NCs. 192
Figure B.4. Natural transition orbitals for 34-cation NCs. 193
Figure B.5. Ground- and excited-state bond lengths for 34-cation NCs. 194

Figure B.6. Molecular orbitals of interstitially doped NCs. 195
Figure B.7. Mid-gap MO energies in ground-state and excited-state geometry. 196
Figure C.1. HOMOs of Cu^+,In^{3+}:ZnS NCs with increasing Cu^+ and In^{3+} concentrations. 197
Figure C.2. LUMOs of Cu^+,In^{3+}:ZnS NCs with increasing Cu^+ and In^{3+} concentrations. 198
Figure C.3. LUMOs of Cu^+,In^{3+}:ZnS NCs with increasing Cu^+ and In^{3+} concentrations. 199
Figure C.4. LUMOs of oxidized Cu^+:ZnS NCs with increasing Cu^+ concentration. 200
Figure C.5. HOMOs of 77-cation ZnS NCs containing Cu^+ trimers. 201
Figure C.6. Mid-gap Cu-based MOs of the same $Cu_3Zn_{74}S_{77}$ NC as in Figure 4.4a. 202
Figure C.7. Mid-gap Cu-based MOs of the same $Cu_3Zn_{74}S_{77}$ NC as in Figure 4.4b. 203
Figure C.8. Mid-gap Cu-based MOs of the same $Cu_3Zn_{74}S_{77}$ NC as in Figure 4.4c. 204
Figure C.9. HOMOs of $CuInS_2$ and $CuInS_2$/ZnS core/shell NCs. 205
Figure C.10. Valence-band MO energies and selected MO surfaces for a 34-cation $CuInS_2$ NC. 206
Figure D.1. Absorption and PL spectra of $CuInS_2$ and CdSe NCs. 211
Figure D.2. Delayed luminescence decay curves for $CuInS_2$ NCs. 211
Figure D.3. Delayed luminescence decay curves for CdSe NCs. 212
Figure D.4. Delayed luminescence decay dynamics for 4x increase in power and 5x increase in pulse width. 212
Figure D.5. Pulse width dependence normalized at the longest pulse width. 213
Figure D.6. Simulated photoluminescence decay curves. 214
Figure D.7. Simulated pulse-width dependence determined from integration of PL and from excited state populations. 215
Figure D.8. Comparison of model with different Auger processes included. 216
Figure D.9. Comparison of experimental long-pulse decay curve with sum of offset short-pulse decay curves. 217
Figure E.1. XRD of $Cd_{0.87}Mn_{0.13}Se$ QDs. 219
Figure E.2. Temperature dependence of absorption and PL energies. 219
Figure E.3. Field dependence of CW PL peak energy. 220
Figure E.4. PL decay curves. 221
Figure E.5. Streak-camera PL image. 221
Figure E.6. TRFR trace showing fast oscillation. 222

Figure E.7. TRFR trace showing Mn^{2+} precession beyond 1 ns. 222
Figure E.8. Fourier transforms of TRFR traces showing dynamic phase inversion. 223
Figure E.9. Absorption spectra showing pump/probe energy dependence of TRFR phases. 223

ACKNOWLEDGMENTS

Daniel Gamelin has been a great research advisor and mentor, and over the years I've gained more and more appreciation for his approach to research, teaching, and mentorship. I am grateful to him for helping me grow as a scientist, ever since the 508 final exam in my first quarter here. I've learned so much about science, but also about how to approach problems, ask questions, and tell stories. Daniel also suggested that I take on a computational project, which turned out to be a great experience for me and which led to most of the results presented here. I appreciate his support of my endeavors outside of research, from computer science and data science coursework to my involvement in the department and university community. Beyond that, I have really valued being part of a research group in which there is so much opportunity for active discussion and collaboration, and a group that values support, camaraderie, and fun. Thanks for many Friday night beers and great conversations at Big Time!

The other members of my committee (Brandi Cossairt, David Ginger, Vince Holmberg, and Xiaosong Li) have also provided valuable and meaningful support, mentorship, and collaboration throughout my time at UW, and I appreciate their interdisciplinary expertise and varied perspectives. I have also been lucky enough to work with all of them beyond just as committee members, including my first full-time research experience as an REU student in the Ginger group, my first synthesis project making copper-doped InP nanocrystals with advice from the Cossairt group, working with Brandi in her role as faculty advisor for WCS, branching out into computational chemistry with the help of the Li group, and now the Molecular Engineering Materials Center in which my entire committee is involved.

The Gamelin group has been an awesome group of colleagues and friends over the last few years. I have really appreciated the many opportunities to learn from everyone in the group and to

share what I've learned. All of the projects I've worked on have been deeply collaborative and have built on knowledge I've gained from others in the group. Thanks to everyone who's been part of "The Concentrators", Team Copper, and EMPs. I also especially want to mention Kimberly (from getting desks in the same office during our first quarter to defending a week apart, it's been a great almost-six years), Jeff and Alina (for welcoming me into the 212 office and to their place for Packers games), and Liam (for teaching me not only how to do things in the lab, but also to understand how they work). Many past and present group members are not only my coworkers, but also my friends, and that has been a key part of my experience in graduate school.

I also really appreciate all of the great resources and opportunities that are available here at UW, within the chemistry department and beyond it. These are a few people and programs I especially want to mention: Xiaosong Li's group contributed to the development of the methods and code that enabled my DFT studies, and provided helpful answers to my questions about Gaussian. The High Performance Computing Club has greatly expanded access to supercomputing for all students, and enabled me to run more elaborate calculations on larger nanocrystals using the Hyak supercomputing cluster. The inorganic division and MEM-C have provided opportunities for me to discuss my work with different audiences and to learn about all the other cool science happening at UW. The DIRECT program and CEI enabled me to pursue my interest in data science while staying connected to materials and clean energy applications; Jim Pfaendtner and Dave Beck are great teachers and mentors, and I appreciate the effort they've put into developing and improving the program. Finally, all of the chemistry department staff members have done so much to make the department run smoothly, and it's been great to work with them.

A huge part of my experience here has been shaped by the Women in Chemical Sciences student group, which has given me the opportunity to make a difference and helped me learn a lot

about the culture and context in which we do science, and also about leadership. I'm so proud to be able to say that I co-founded this group and contributed to many projects and events that came from it. None of it would have happened without Sarah Vorpahl, who has been a great friend and an inspiration ever since we started graduate school and WCS back in 2012. I am also continually inspired by the officers and members of WCS, past and present. I hope we've been able to contribute something meaningful to the department and the community, and I hope these efforts continue for a long time. The support of the department has also been important to our success, and I appreciate everyone who has invested in the work we do.

My family has always been supportive of what I do, and always willing to listen. I'm grateful for their continuing support and encouragement, and for helping provide perspective on my experiences here. I've enjoyed their visits to Seattle, but I'm excited to be closer to home.

Finally, my partner Steve (now officially Dr. Steven Quillin) is really the most important person in my life, and his love and support have been incredibly important to me over the past four and a half years. We made it through grad school together, and I'm proud of both of us and excited for what's next!

Chapter 1. Introduction: Electronic Structure and Luminescence of Copper-Doped and Silver-Doped Semiconductor Nanocrystals

1.1 **Copper and Silver Luminescence**

Materials that emit light have been studied for centuries and have provided the foundation for many important modern-day technologies. Copper impurities have played a role in many important luminescent materials, ranging from the mysterious Bologna stones of the 1600s to the ZnS:Cu phosphors used in cathode-ray tubes throughout the 20th century. Today, copper-doped nanocrystals offer new avenues for studying, tuning, and applying copper luminescence, and many conclusions regarding the photoluminescence of copper-doped materials also extend to the less well-understood silver-doped and copper indium sulfide nanocrystals.

In the early 1600s, Italian cobbler and alchemist Vincenzo Cascariolo discovered that certain rocks from the area near Bologna could be processed in a way that caused them to emit light after being exposed to the sun.[1] These rocks were barite ($BaSO_4$) which could be converted to phosphorescent barium sulfide with calcination.[2-3] Later attempts to reproduce the glowing rocks often failed, but in the 1680s, Wilhelm Homberg discovered the importance of copper: using a bronze mortar or copper bowl to grind the barite yielded bright phosphorescence.[3] Barite found near Bologna often contained copper impurities, which were the source of the phosphorescence in the original stones. The Bologna stones were initially of interest to alchemists, who speculated that stones that incorporated the light of the sun could be used to turn other metals into gold. However, as Pierre Potier wrote in his Pharmacopoea Spagirica in 1625, the phosphorescence of the Bologna stone "…does not have any practical use, except that it delights the eyes, as usually happens to be

the case with newly found things."[1] It would be many more years before applications for luminescent minerals were developed.

Luminescent copper-doped zinc sulfide, which would later become an important commercial phosphor, was first synthesized in 1866 by Théodore Sidot, though his objective was to study crystal growth and he hadn't intentionally added copper to the material.[1,4] Spectroscopic characterization was carried out by Edmund Becquerel, who observed using a phosphoroscope that the most strongly phosphorescent crystals emitted blue light at short times and green light at much longer times, with broad emission extending into the near-infrared.[5] Other researchers eventually determined that trace metal impurities are important to luminescence in many different materials, though it wasn't until the 1920s that the use of copper and silver as luminescence activators in ZnS was established.[1,4]

Further study of ZnS revealed that it can display a variety of luminescence features depending on the presence and configuration of different impurities and defects. The characteristic "green-copper" emission originates from isolated, substitutional Cu^{+} impurities, while analogous "blue-silver" emission comes from similar Ag^{+} impurities. Both the G-Cu and B-Ag luminescence processes involve a hole localized at the dopant acceptor site, recombining with an electron which is in the semiconductor conduction band or localized at a donor co-dopant such as Al^{3+} or Cl^{-}.[4,6-9] This donor–acceptor pair mechanism is associated with a broad luminescence line width, due to the distribution of donor–acceptor pair distances and energies as well as the strong electron–phonon coupling related to the localized carriers.[6-8] The luminescence lifetime also depends on the donor–acceptor pair distance, and can extend up to seconds or minutes.[6-8] Beyond green and blue, the energy and color of copper- and silver-based PL can be tuned by varying the identity of the donor co-dopant or the host semiconductor. Phosphors for cathode-ray tubes used

in early color televisions included various alloys of $Zn_{1-x}Cd_xS$ doped with Cu^+ or Ag^+ to generate red, green, and blue light, while black-and-white televisions were based on similar phosphors that produce white light when combined.[4]

Similar luminescence has also been studied in molecular Cu^+ and Ag^+ complexes for many years.[10-15] The metal-to-ligand charge-transfer (MLCT) excited states of Cu^+ complexes are directly analogous to the excited states of semiconductors containing Cu^+ acceptors. In both cases, the copper center is oxidized and the excited electron is spatially separated (on the ligands of a molecular complex, or at a donor co-dopant in a semiconductor). The PL energy of Cu^+ and Ag^+ complexes can be tuned by varying the ligand. These systems are also of interest as phosphors for organic light-emitting diodes and for solar energy conversion.

More recently, Cu^+-doped and Ag^+-doped colloidal semiconductor nanocrystals (NCs) have been developed.[16] These materials are similar to both the bulk and molecular systems, but the electron in the charge-transfer excited state occupies the quantum-confined nanocrystal conduction band. Doped NCs offer tunability of the dopant luminescence energy by varying the nanocrystal size as well as the host semiconductor composition. Their small sizes and solution-phase synthesis methods open up many new applications,[16] including solar energy collection and concentration,[17-18] energy-efficient lighting,[19-23] and bioimaging.[24-27] This chapter discusses the photoluminescence of Cu^+-doped and Ag^+-doped NCs, focusing on recent progress in understanding the electronic structures of these materials and addressing their similarities and differences.

1.2 Copper-Doped Nanocrystals

In copper-doped nanocrystals, photoluminescence results from the recombination of a conduction-band electron with a hole localized at the Cu^+ dopant. Very similar PL has been observed for Cu^+

in a variety of different semiconductor NC hosts.[16,28-31] This mechanism, shown in Figure 1.1a, is similar to the characteristic donor–acceptor pair mechanism of the G-Cu PL in bulk Cu^+-doped ZnS, except that the electron occupies the quantum-confined conduction band of the NC rather than a donor state introduced by a co-dopant. Excitation at or above the NC band gap generates an exciton (Figure 1.1a), then the valence-band hole rapidly traps at the Cu^+ dopant, formally oxidizing it to Cu^{2+}. This excited state, which is described as a metal-to-conduction-band charge-transfer ($ML_{CB}CT$) state, can also be generated directly by photoexcitation of an electron from Cu^+ into the NC conduction band.[28,32] Because the Cu^+ defect energy level is fixed, the PL energy can be tuned across the visible and into the near-infrared region by varying the energy of the conduction-band electron—i.e., varying the NC size or composition, as illustrated in Figure 1.1b. This property has been employed to determine the band-edge energies of various NC systems.[29-31]

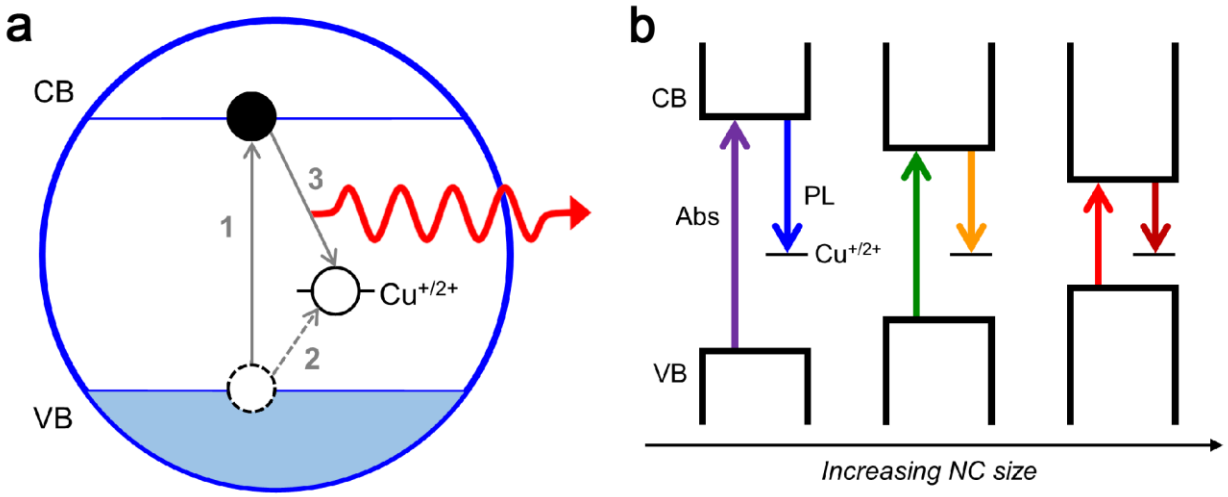

Figure 1.1. Copper PL mechanism and effect of quantum confinement on PL energy. (a) Schematic illustration of the PL mechanism in a Cu^+-doped NC. First, photoexcitation at the semiconductor band gap generates an exciton. Second, the valence-band (VB) hole rapidly traps at the Cu^+ dopant and formally oxidizes it to Cu^{2+}. Third, the conduction-band (CB) electron radiatively recombines with the copper-bound hole and a photon is emitted. (b) Illustration of how the copper PL energy depends on the NC size. The conduction-band and valence-band energies change with quantum confinement, while the copper acceptor level is fixed. The energy of the first excitonic transition (absorbance) depends on both the

conduction-band and valence-band energies, and the energy of the copper-related transition (PL) depends on the conduction-band energy only.

Figure 1.2 shows the absorption and PL spectra of undoped CdSe and Cu^+-doped CdSe nanocrystals. Excitonic luminescence in the undoped CdSe NCs is relatively narrow, with a small effective Stokes shift (difference between the first excitonic absorption peak energy and the PL peak energy); it also has a PL lifetime on the order of nanoseconds to tens of nanoseconds. In contrast, luminescence from the $ML_{CB}CT$ excited state in Cu^+-doped NCs is much broader, with a large effective Stokes shift and a longer (~100s of ns to μs) PL lifetime.

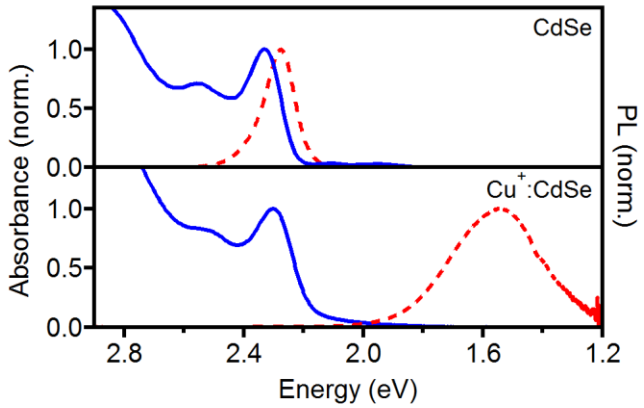

Figure 1.2. Comparison of undoped and Cu^+-doped CdSe NCs. Absorption and PL spectra of undoped (top) and Cu^+-doped CdSe NCs. While the absorption spectra (blue solid lines) are similar, the PL spectra (red dashed lines) are very different in energy and band shape.

Because of their tunable PL energies and the large effective Stokes shifts, Cu^+-doped NCs are attractive for many applications as phosphors, as discussed above.[16] Many recent synthetic advances have improved the performance of Cu^+-doped NCs for different applications as well as expanding the scope of fundamental photophysical studies. These advances include co-doping Cu^+ with other dopants,[33-39] incorporating Cu^+ into core/shell NCs and into nanomaterials with different morphologies,[18,30,40] controlling and varying the concentration of Cu^+ dopants over a broader range,[32,41-43] and more.

1.3 Silver-Doped Nanocrystals

Recently, several reports have noted strong similarities in the PL properties of Cu^+-doped and Ag^+-doped NCs. In bulk, the G-Cu and B-Ag luminescence occur via analogous donor–acceptor pair mechanisms, though the Ag^+ PL is consistently higher in energy than the Cu^+ PL.[6-8,44] Like their Cu^+-doped counterparts, Ag^+-doped NCs display broad PL with a large Stokes shift, long lifetime (100s of ns to µs), and energy that can be tuned by varying the NC size or host lattice.[37,45-51] Figure 1.3 shows the absorption and PL spectra of Ag^+-doped and Cu^+-doped CdSe NCs. Both materials have similar absorption spectra and broad PL spectra with a large effective Stokes shift. In doped NCs with the same size and host semiconductor composition, the Ag^+ PL is higher in energy than the Cu^+ PL, consistent with the trend observed in bulk materials, where Cu^+ creates a deeper acceptor state than Ag^+.[37,47-50]

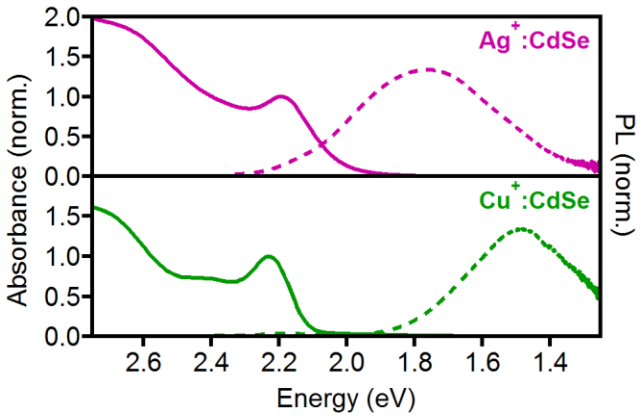

Figure 1.3. Comparison of Cu^+:CdSe and Ag^+:CdSe NCs. Absorption and PL spectra of Ag^+-doped (top) and Cu^+-doped CdSe NCs. Both samples have similar absorption spectra (solid lines) similar and broad PL (dashed lines) which is much lower in energy than the excitonic absorption peak. The PL of the Ag^+:CdSe NCs is higher in energy than the PL of the Cu^+:CdSe NCs. Differences in the width of the absorption and PL are likely related to sample inhomogeneity. This figure is adapted from ref. 50 (Chapter 3).

Some studies of Ag^+-doped NCs demonstrate signatures of electronic doping with little to no dopant-related photoluminescence.[46,52-54] In bulk materials, interstitial Ag^+ is a donor which

yields electronic doping while substitutional Ag^+ produces the characteristic B-Ag PL.[6,55-57] The same distinction seems likely to apply to Ag^+-doped NCs, supported by extended x-ray absorption fine-structure (EXAFS) studies indicating the presence of interstitial Ag^+ in NCs displaying little to no Ag^+ PL[52] and by density functional theory (DFT) calculations showing that substitutional Ag^+ introduces mid-gap acceptor states while interstitial Ag^+ is a shallower donor in both bulk materials and NCs.[50] Here, we focus on luminescent Ag^+-doped NCs with substitutional Ag^+ dopants. These materials are less well-studied than their Cu^+-doped counterparts, but recent synthetic progress has enabled more in-depth study of their luminescence.

The similarities in PL for Cu^+- and Ag^+-doped NCs suggest a similar mechanism, just as in the analogous bulk materials. A free-to-bound PL mechanism for Ag^+:CdS/ZnS NCs, involving a delocalized electron and dopant-bound hole, was proposed in ref. 45 based on the size dependence of the excitonic and dopant-related PL as well as the similarities in PL between NCs with and without Al^{3+} shallow donor co-dopants. The size dependence of the binding energy for the dopant-related excited state also suggests that Ag^+ introduces acceptor states.[46] However, the nature of the acceptor state differs significantly between Cu^+ and Ag^+. In the mechanism described above for Cu^+-doped NCs, hole trapping at Cu^+ is described as oxidizing the dopant to Cu^{2+}. In contrast, oxidation of Ag^+ to Ag^{2+} is highly unfavorable. Ionization of Ag^+ occurs ~1.2 eV higher in energy than ionization of Cu^+,[58] yet the Ag^+ PL is consistently only ~0.3 eV higher in energy than the Cu^+ PL. An excited state of Ag^+-doped NCs involving Ag^{2+} is expected to be unstable, or to be >1 eV higher in energy than the corresponding Cu^+ excited state, yet experimental observations suggest that the Ag^+ excited state is similar to that of Cu^+.

Electronic-structure calculations resolve this discrepancy and highlight the similarities and differences between the PL mechanisms of Cu^+ and Ag^+-doped NCs. Both dopants introduce

localized mid-gap molecular orbitals (MOs) above the semiconductor valence-band edge, where the hole is trapped in the excited state. These mid-gap MOs are antibonding orbitals formed from the interaction between the metal d and anion p orbitals; the corresponding bonding orbitals are located deep inside the valence band. However, differences in the relative energies of the metal d orbitals and adjacent anion p orbitals result in different atomic-orbital contributions to these MOs.[50] In Cu^+:CdSe NCs, the Cu(3d) orbitals are higher in energy than the Se(4p) orbitals, so the antibonding mid-gap MOs have primarily Cu(3d) character and the excited-state hole occupies the Cu(3d) orbitals. In contrast, Ag^+:CdSe NCs display inverted bonding: the Ag(4d) orbitals are *lower* in energy than the Se(4p) orbitals, so the antibonding mid-gap MOs have dominant Se(4p) character and the excited-state hole primarily occupies the 4p orbitals of the anions bonded to the Ag^+ dopant. The similar overall localization of the dopant-related mid-gap MOs in Cu^+- and Ag^+-doped semiconductors gives similar spectroscopic properties, but the relative amount of hole density on the metal and ligand in the excited state is reversed.[50] The similarities and differences in the electronic structures of Cu^+:CdSe and Ag^+:CdSe NCs are discussed further in Chapter 3 (ref. 50).

In luminescent molecular complexes containing Cu^+ or Ag^+, the energy of the Ag^+ and Cu^+ PL follows the same trend as in NCs: for the same ligands, the Ag^+ PL is higher in energy than the Cu^+ PL.[59-61] The calculated electronic structures also display differences in bonding: the highest occupied molecular orbital (HOMO) is Cu(3d)-based for Cu^+ complexes but primarily ligand-based for Ag^+ complexes. As a result, the excited states of Cu^+ complexes are described as metal-to-ligand charge-transfer (MLCT) states while those of Ag^+ complexes are better described as ligand-centered charge transfer (LLCT) states.[13,59-64]

1.4 Photophysics of Cu^+-Doped and Ag^+-Doped Nanocrystals

While the mechanism and basic features of PL in Cu^+-doped NCs are well-established, several recent studies have explored the photophysics of these materials in greater depth, providing new insights into their electronic structure and PL mechanism. Many of the same findings apply to Ag^+-doped NCs as well. The following sections summarize recent progress in understanding various aspects of the electronic structure and photophysical properties of these materials.

1.4.1 Dopant oxidation state and charge-transfer transitions

Ground-state and excited-state optical absorption, PL, magnetic circular dichroism (MCD), and x-ray spectroscopies show that the PL mechanism in copper-doped NCs involves the oxidation of copper from Cu^+ in the ground state to Cu^{2+} in the luminescent excited state. While Ag^+ is not formally oxidized to Ag^{2+} in the excited state, the presence of the dopant-related mid-gap acceptor state results in analogous spectroscopic features for silver-doped NCs. Several recent reports have identified and characterized the electronic transitions associated with ground-state and excited-state charge-transfer processes in these materials.

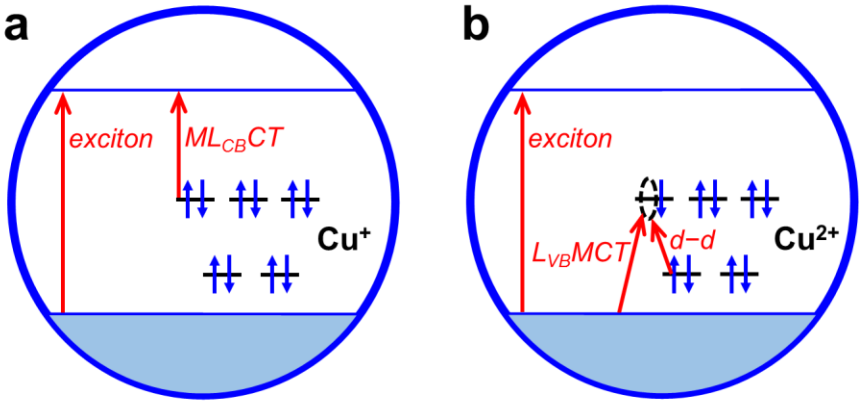

Figure 1.4. Electronic excitations in Cu+-doped and Cu2+-doped NCs. (a) Available excitations in a Cu^+-doped NC (in which copper has a $3d^{10}$ electron configuration). Besides the excitation of the host NC, electrons can be excited from the Cu^+ 3d orbitals to the conduction band ($ML_{CB}CT$ transitions, the inverse of the

Cu^+-related PL in Figure 1.1a). (b) Available excitations in a Cu^{2+}-doped NC (in which copper has a $3d^9$ electron configuration). In addition to excitation of the host NC, electrons can be excited from the valence band to the unoccupied 3d orbital of the Cu^{2+} dopant ($L_{VB}MCT$ transitions) or from its occupied 3d orbitals to the unoccupied 3d orbital (d−d transitions).

Doping NCs with Cu^+, which has a $3d^{10}$ electron configuration, introduces charge-transfer transitions involving the promotion of an electron from the Cu(3d) orbitals to the conduction band ($ML_{CB}CT$ absorption, shown in Figure 1.4a). This transition is the inverse of the Cu^+-based PL shown in Figure 1.1a. The onset of the $ML_{CB}CT$ absorption band occurs just below the energy of the first excitonic transition. This absorption feature has been predicted by DFT and observed experimentally as a "foot" in the absorption spectrum of Cu^+-doped NCs, just below the excitonic peak.[28,32,43,65] The same feature appears in the photoluminescence excitation spectrum when monitoring the Cu^+ PL intensity.[32] The magnitude of the sub-bandgap absorption foot increases with increasing Cu^+ concentration, and its extinction coefficient is similar to values predicted by DFT for the same transition in Cu^+:CdSe NCs and to estimated values for the same transition in bulk Cu^+,Al^{3+}:ZnS.[8,28,32,43,65] In transient absorption spectra of Cu^+:CdSe NCs, a bleach is observed at the same energy as the absorption foot and assigned to the same $ML_{CB}CT$ transition.[40]

Like Cu^+, Ag^+ can introduce new sub-bandgap absorption corresponding to the inverse of the PL transition. In the inverted bonding scheme discussed above, this feature represents promotion of an electron to the conduction band from primarily the anion p orbitals around the dopant, rather than a formal $ML_{CB}CT$ transition from the dopant d orbitals. Because it is higher in energy than the corresponding Cu^+ transition and thus closer to the excitonic absorption onset, identification of this Ag^+-related absorption feature is more difficult. It has been predicted by DFT and observed in experimental absorption, photoluminescence excitation, and transient transmission spectra.[50-51] In the transient transmission measurement, excitation at the sub-bandgap

Ag^+-related feature results in a bleach of the excitonic absorption, confirming that this transition involves the promotion of electrons to the NC conduction band.[51]

Some reports claim that copper exists in the Cu^{2+} oxidation state in the ground state of copper-doped NCs.[66-68] A key signature of Cu^{2+}, which has a $3d^9$ electron configuration, would be optical absorption from its d−d transitions (Figure 1.4b). This absorption and its corresponding luminescence have been observed at ~1 eV in bulk copper-doped semiconductors, in which photoexcitation can generate very long-lived Cu^{2+}.[8,69-71] The $3d^9$ electron configuration also allows charge-transfer transitions from the valence band to Cu^{2+}, as shown in Figure 1.4b. This ligand-to-valence-band charge-transfer ($L_{VB}MCT$) band occurs at energies < 1 eV in bulk copper-doped ZnS.[8,69] Time-dependent density functional theory (TD-DFT) calculations also predict broad, low-energy absorption in Cu^{2+}-doped CdSe NCs.[65] However, neither the d−d transitions nor the $L_{VB}MCT$ transitions have been observed experimentally by absorption or MCD in copper-doped NCs, indicating that copper exists in the +1 oxidation state in the ground state of these materials.[28]

In the excited state, on the other hand, Cu^+ traps a valence-band hole and is formally oxidized to Cu^{2+}. Excitation at or above the semiconductor band gap yields excitonic PL before this hole trapping occurs, which has been observed in Cu^+-doped NCs on very short timescales (<25 ps).[40,72] In transient transmission measurements on Ag^+:CdSe NCs, excitation at the band edge gave a 1.4 ps rise time of the bleach for the Ag^+ absorption feature (analogous to the Cu^+ $ML_{CB}CT$ absorption foot), corresponding to trapping of the valence-band hole at the dopant acceptor state.[51] Transient absorption dynamics of Ag^+:CdS NCs similarly show a component assigned to fast (~ps) energy transfer to the dopant state.[48]

On longer timescales, transient absorption spectra of Cu^+:CdSe/CdS NCs show a ground-state bleach as well as a broad, sub-bandgap photoinduced absorption feature attributed to

L_{VB}MCT transitions involving Cu^{2+}, suggesting the presence of Cu^{2+} in the excited state but not the ground state of these NCs. The per-hole extinction coefficient of this sub-bandgap photoinduced absorption feature between 700 and 850 nm is ~2000 $M^{-1}cm^{-1}$, similar to the value predicted by TD-DFT for the L_{VB}MCT transitions in Cu^{2+}:CdSe NCs.[40,65] The recovery of the ground-state bleach, the decay of the photoinduced absorption, and the decay of the Cu^{+} PL all follow the same dynamics, confirming that they originate from the same excited state.[40] The ground-state bleach is due to the presence of the conduction-band electron, the photoinduced absorption results from the presence of the Cu^{+}-bound hole (i.e., Cu^{2+}), and the PL originates from the recombination of these two carriers. Similar sub-bandgap absorption associated with Cu^{2+} has previously been observed in the photoinduced absorption spectrum of bulk Cu^{+},Al^{3+}:ZnS, where both the L_{VB}MCT and d−d transitions are resolved.[8] Broad, sub-bandgap photoinduced absorption features are also seen in the transient absorption spectra of Ag^{+}:CdS NCs,[48] where they likely originate from the analogous ligand-centered transitions related to the Ag^{+} acceptor state.

These optical results relating to the dopant oxidation state are supported by ground- and excited-state x-ray absorption spectroscopy studies. In Cu^{+}:CdS and Cu^{+}:CdSe NCs, Cu K-edge and L-edge x-ray absorption near-edge structure (XANES) spectra confirm that copper is in the +1 oxidation state in the ground state.[36,41,73-74] Changes in the Cu K-edge XANES spectra for photoexcited Cu^{+}:CdS NCs, including a blueshift of the absorption edge and the appearance of a new pre-edge feature associated with vacant Cu(3d) orbitals, are consistent with oxidation of Cu^{+} to Cu^{2+} in the excited state.[73]

1.4.2 Magnetic exchange in the excited state

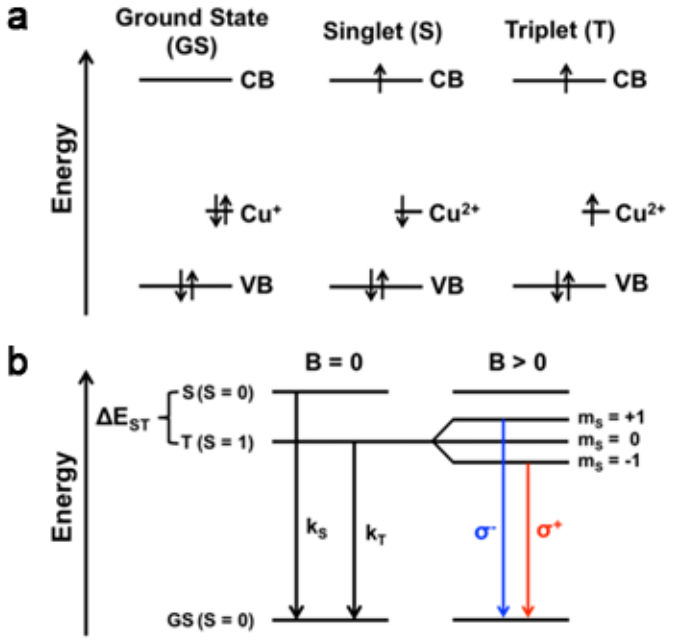

Figure 1.5. Singlet–triplet splitting in Cu^+-doped NCs. (a) Energies and occupancies of the relevant orbitals in the ground-state, singlet excited-state, and triplet excited-state configurations of a Cu^+-doped NC. The conduction-band edge, valence-band edge, and one of the Cu(3d)-based mid-gap orbitals are shown (the other four Cu(3d)-based orbitals are all doubly occupied in all configurations). (b) Energies of the singlet and triplet excited states in zero applied magnetic field (left) and with an applied magnetic field. This figure is adapted from ref. 28.

Although Cu^+ has a $3d^{10}$ electron configuration and is diamagnetic, magnetic exchange interactions are evident in the luminescent excited state. In a Cu^+-related excited state, the spins of the electron and the unpaired 3d electron of Cu^{2+} can align in a singlet (antiferromagnetic) or triplet (ferromagnetic) configuration, as shown in Figure 1.5a. The triplet state is lower in energy (Figure 1.5b), and changing the temperature shifts the thermal equilibrium between the singlet and triplet states, altering their relative populations. Recombination from the triplet state is formally spin-forbidden, so it has a much longer PL lifetime than the singlet state. With decreasing temperature, the observed lifetime lengthens dramatically, reflecting the increased amount of the excited-state population in the triplet state. Analysis of the temperature-dependent lifetimes can provide the

values of the singlet and triplet decay rate constants as well as the magnitude of the singlet−triplet splitting energy, ΔE_{ST}. Temperature-dependent PL dynamics associated with this singlet−triplet splitting have been observed and analyzed in bulk Cu^+-doped semiconductors,[75-79] molecular complexes,[11-13,15,80] and most recently in both Cu^+-doped and Ag^+-doped NCs.[28,50]

In an individual NC, the singlet−triplet splitting energy varies based on the overlap between the electron and hole wavefunctions. For a hole localized at a Cu^+ dopant closer to the NC center, where the wavefunction density of the delocalized electron is maximized, the exchange interaction will be stronger and the singlet−triplet splitting will be larger than for a hole at a Cu^+ near the NC surface. Fitting the temperature dependence of the PL lifetime to a model accounting for the distribution of Cu^+ dopant sites allows an estimation of the average singlet−triplet splitting energy for the ensemble, which is ~1 meV in Cu^+:CdSe NCs (d = 3.2 nm).[28] A similar value was found for Ag^+:CdSe NCs.[50] Density functional theory calculations on smaller NCs yield a similar dependence of ΔE_{ST} on the dopant site, and give average values that, after scaling by NC volume, are very similar to experimental results for both Cu^+-doped and Ag^+-doped CdSe NCs.[50,65]

Magneto-optical techniques can also be used to probe the triplet excited state. The triplet state emits circularly polarized light in a magnetic field, while the singlet state does not. Figure 1.5b illustrates that in an applied magnetic field, the triplet state splits into its three sublevels (m_S = +1, 0, −1). The polarization of the emitted light, measured by magnetic circularly polarized luminescence (MCPL), reflects the difference in population between the +1 and −1 sublevels of the triplet state. Because all of the circular polarization of the emission comes from the triplet state, the MCPL polarization ratio also reflects the population of the triplet state relative to the singlet state, and displays the same temperature dependence as the PL lifetime in both Cu^+-doped and Ag^+-doped NCs.[28,50] In bulk semiconductors, optically detected magnetic resonance (ODMR) has

been applied extensively to investigate the splitting of the triplet state in a magnetic field, finding a zero-field splitting between the components of the triplet and a resulting low-field level crossing.[76,78] The field dependence of the MCPL polarization ratio in Cu^+ and Ag^+-doped NCs also displays a low-field saturation feature associated with this field-dependent splitting of the triplet energy level, while the excitonic MCPL signal varies linearly in this region.[28,50,81]

In contrast with the PL lifetimes and MCPL, which provide evidence of magnetic exchange interactions in the excited states of these NCs, magnetic circular dichroism probes magnetization of the ground state. MCD studies of Cu^+:CdSe and Cu^+:InP NCs found no evidence of either sub-bandgap transitions associated with paramagnetic Cu^{2+} or magnetic exchange coupling between the exciton and Cu^{2+},[28] consistent with the optical and XANES results discussed above. However, other reports appear to show temperature- and field-dependent MCD consistent with an exchange-coupled exciton. The magnitude of the MCD signal is strongly enhanced under additional photoexcitation, interpreted as the generation of some metastable excited Cu^{2+} interacting with the exciton.[67] Similar results were also recently reported for silver-doped NCs.[51] In these cases, photoexcitation appears to generate some long-lived, magnetically active excited state, possibly involving deep trapping of charge carriers, and activate magnetic exchange in these materials.

1.4.3 **Electron–phonon coupling and the PL linewidth**

The full-width at half-maximum (fwhm) of the Cu^+ or Ag^+ PL in NCs is typically ~200-400 meV, much broader than the typical line width of excitonic PL (~50 meV).[16] For Cu^+-doped NCs, inhomogeneous broadening has often been cited to explain this broad line width. Since the Cu^+ PL energy depends on the NC size, a distribution of NC sizes will lead to a distribution of PL energies in an ensemble measurement. Besides the NC size, Cu^+ PL may also be subject to inhomogeneous broadening from differences in the local environment around the Cu^+, such as the position of the

Cu^+ relative to the NC surface (or to the interface in core–shell structures) or its proximity to other defects. However, fluorescence line narrowing measurements and single-particle PL spectra have demonstrated that removing inhomogeneous broadening does not narrow the PL line width in Cu^+-doped NCs, and the Cu^+ emission is intrinsically broad.[33,66,82]

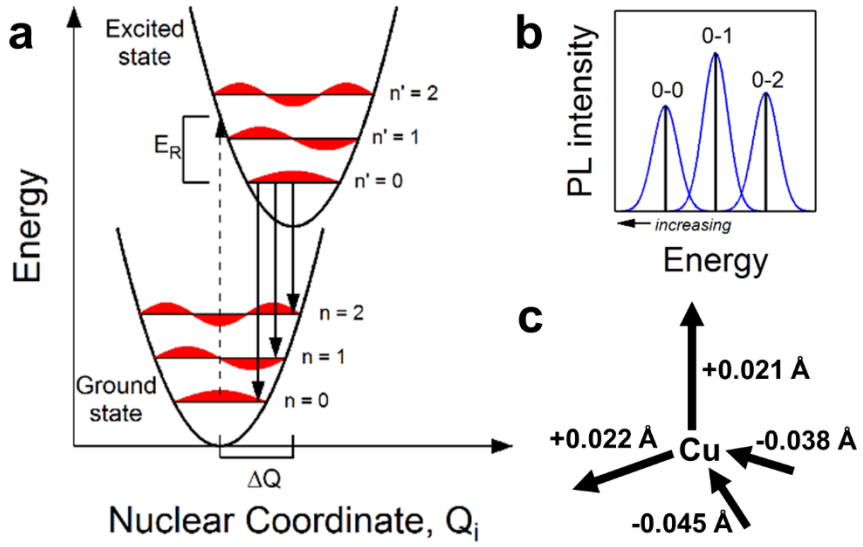

Figure 1.6. Origin of the broad PL line width and large Stokes shift in Cu^+-doped NCs. (a) Single-configurational-coordinate diagram showing the relationship between excited-state nuclear distortion and PL line width. The dashed line indicates the peak of the absorption energy for this transition, and the solid lines represent the different vibronic transitions contributing to the PL. (b) Simulated vibronic progression for the SCC diagram in (a). (c) Bond-length changes around the Cu^+ dopant in the excited state of a Cu^+:CdSe NC, calculated by DFT.[65] Unlike the simplified case shown in (a-b), the excited-state distortion here includes contributions from multiple nuclear coordinates. A full simulated PL spectrum with vibronic progressions along these multiple coordinates is shown in ref. 65 (Chapter 2).

This broad line width originates from strong electron–phonon coupling in the luminescent charge-transfer excited state, as illustrated schematically in Figure 1.6, which has been invoked for both Cu^+- and Ag^+-doped NCs.[33,45,65,82] In the case of Cu^+, hole localization at the dopant oxidizes it to Cu^{2+}. This oxidation is associated with a totally symmetric contraction and a symmetry-breaking Jahn–Teller distortion (since Cu^{2+} has a $3d^9$ electron configuration). The

excited state is stabilized by a large nuclear reorganization energy, resulting in a large Stokes shift. The emission involves vibronic progressions along multiple distortion coordinates, which combine to produce the broad PL line width. In Ag^+-doped NCs, the dopant itself is not oxidized, but similar distortions are predicted based on the strong localization of the hole and the orbital degeneracy of the excited state.[45,50]

In doped NCs, the excited-state distortion has been predicted by DFT (Figure 1.6c); simulated vibronic progressions based on the calculated geometric distortion along totally symmetric and Jahn–Teller coordinates result in a broad PL line width.[65] Excited-state EXAFS spectra, accompanied by DFT calculations, also indicate an overall shortening of Cu–S bonds in the excited state of Cu^+:CdS NCs.[73] These experimental results are complicated by heterogeneity of the local environment around Cu^+, including differences in geometric distortions for core and surface Cu^+, but the overall effect is consistent with a large excited-state nuclear distortion upon oxidation.[73] The narrowing of the single-particle PL spectrum at low temperatures also supports the attribution of the broad line width to vibronic effects.[33]

The broad linewidth of G-Cu and B-Ag luminescence in bulk semiconductors comes from strong electron–phonon coupling, combined with the distribution of donor–acceptor pair distances and energies. For each discrete donor–acceptor pair distance, the zero-phonon line is the origin of a vibronically broadened spectrum; the broad emission band thus consists of contributions from many donor–acceptor pairs coupled with varying numbers of vibrational quanta of different phonon modes.[7] Vibronic progressions have been observed directly in the dopant-related PL of materials including Cu^+:GaP[75-76,78] and Ag^+:ZnSe.[83-84] The broad PL line widths of the charge-transfer luminescence in Cu^+- and Ag^+- based molecular systems are also attributed to similar large reorganization energies, often associated with a flattening distortion of the molecule. In these

systems, the nuclear reorganization can be significantly suppressed by using bulkier ligands, by crystallization of the molecule in a rigid matrix, or by lowering the temperature, leading to narrower line widths.[85-86] Excited-state distortions have also been observed in molecular systems by optical and x-ray spectroscopies and predicted by DFT.[87-90] Overall, these results for both NCs and other systems demonstrate that the line widths of Cu^+ and Ag^+-based charge-transfer PL are intrinsically broad due to strong electron-phonon coupling.

1.4.4 **Carrier trapping and nonradiative decay pathways**

Charge-carrier trapping in Cu^+-doped NCs has been investigated by several different methods. In undoped NCs after photoexcitation, both the hole and electron can potentially trap at surface defects or other defect sites. In Cu^+-doped systems, the hole can localize at Cu^+, which can be described as an engineered hole trap that competes with other traps in the NC. Additionally, the long-lived excited state of Cu^+-doped NCs can enable more in-depth study of electron trapping.

Blinking, or fluorescence intermittency, has been studied in Cu^+:CdSe and undoped CdSe NCs to separately probe electron and hole trapping.[82] The two types of NCs displayed statistically different distributions of "on" times, indicating that they have different mechanisms of turning off or entering the dark state via carrier trapping. The "on" times were shorter in Cu^+:CdSe NCs than in undoped CdSe NCs, showing that the relevant trapping is more efficient in Cu^+:CdSe NCs. Defect-related hole trapping should be *less* efficient when Cu^+ dopants are present, because Cu^+ competes with these traps for the valence-band hole after photoexcitation. Electron trapping, however, is more efficient in Cu^+-doped NCs than in undoped NCs, because the long-lived Cu^+ excited state provides the conduction-band electron with more time to become trapped. The shorter "on" times observed for Cu^+:CdSe NCs indicate that blinking in both types of NCs is due to electron trapping. This result is also consistent with the finding that both sets of NCs displayed

statistically indistinguishable distributions of "off" times, which means they have the same mechanism of exiting the dark state (turning on, or detrapping the electron).[82]

Electron trapping and detrapping processes also lead to delayed luminescence, in which emission is observed at very long timescales due to charge carriers that become trapped, eventually detrap, and then participate in luminescence. This phenomenon has been observed in both doped and undoped NCs, but the long PL lifetime of Cu^+-doped NCs provides more time for electron trapping to compete with recombination, which can enable easier observation and more in-depth study of the characteristics of delayed luminescence.[82,91] For similar reasons, PL of Cu^+:CdSe NCs is more sensitive than PL of undoped CdSe NCs to quenching by trion Auger processes when an extra conduction-band electron is present, because the slow radiative recombination in the Cu^+-doped NCs cannot compete as effectively with the faster nonradiative Auger process.[40] The trion Auger decay involving a hole trapped at Cu^+ and two conduction-band electrons is an example of a trap-assisted Auger process.

Treatment with electron- or hole-accepting molecules or ligands can also provide insight into carrier trapping in the excited state of Cu^+-doped NCs. For example, photodoping of NCs involves photoexcitation followed by rapid transfer of the valence-band hole to a molecular hole quencher.[40] This process is slower and less efficient in Cu^+:CdSe than in undoped CdSe, because the Cu^+ dopants and the added hole quencher compete to trap the valence-band hole.[40] Various other studies have also explored the effect of different ligands and other electron- and hole-accepting molecules on the PL quantum yield (QY) and PL and transient absorption dynamics of Cu^+-doped NCs.[29,68,72,92-93] Surface chemistry of these NCs is complex, and different ligands have contrasting effects on copper and excitonic PL intensities and dynamics in various NC systems. Interpretation of these results can also be complicated by the fact that some common ligands, such

as phosphines and amines, have been shown to physically remove Cu^+ from the lattice of Cu^+:CdSe NCs.[32]

1.5 $CuInS_2$ and Related Nanocrystals

Recently, comparisons have also been drawn between Cu^+-doped and $CuInS_2$ NCs.[16,28,81] Bulk chalcopyrite $CuInS_2$ and related materials, including $CuInSe_2$ and $AgInS_2$, are structurally similar to their zinc-blende II−VI analogues. The chalcopyrite crystal structure resembles the zinc-blende structure, but with two different types of cations. The I−III−VI_2 semiconductors, however, have much narrower band gaps than their II−VI analogues due to the strong antibonding interaction between the d orbitals of the M^+ cations and the p orbitals of the anions. This "p−d repulsion" pushes the valence band up in energy and also results in significant metal d orbital character at the upper edge of the valence band.[94-98] Consequently, the electronic structure of the valence band in $CuInS_2$ resembles the mid-gap dopant levels in a Cu^+-doped II−VI semiconductor more than the valence band of a II−VI semiconductor.

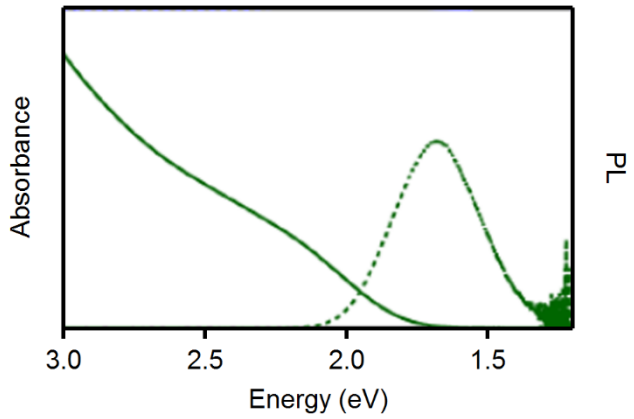

Figure 1.7. Absorption and PL of $CuInS_2$ NCs. Absorption (solid line) and PL (dashed line) spectra of $CuInS_2$ NCs. The absorption is broad with no clear excitonic feature, while the PL is broad with a large effective Stokes shift, similar to the PL of the Cu^+:CdSe NCs shown in Figure 1.2 and Figure 1.3. This figure is adapted from ref. 28.

Luminescence in bulk $CuInS_2$ includes contributions from free and bound excitons, free-to-bound transitions, and donor–acceptor pairs, with relative intensities depending on the material stoichiometry, crystal quality, and excitation conditions.[95,99-102] In $CuInS_2$ nanocrystals, on the other hand, the only PL feature observed is broad, as shown in Figure 1.7, with a large effective Stokes shift and long lifetime. Its energy is tunable by varying the NC size and stoichiometry, but it does not resemble excitonic PL in bulk $CuInS_2$ or in II–VI nanocrystals.[16,103-107] This PL is often assigned to a donor–acceptor pair or free-to-bound mechanism involving one or both carriers localized at defect sites. Several different defects have been implicated, based on the energies of the defect donor and acceptor levels in bulk $CuInS_2$ and on the dependence of the PL energy and QY on the NC composition.[104,108-110]

Based on the spectroscopic and electronic-structure similarities between $CuInS_2$ and Cu^+-doped NCs, some proposals have suggested a common PL mechanism for these classes of materials, involving hole localization at copper.[16,28,81,111-112] In addition to the broad PL linewidth, large Stokes shift, and long lifetime, both $CuInS_2$ and Cu^+-doped NCs also have similar temperature-dependent lifetimes (characteristic of a singlet–triplet splitting in the excited state) and temperature- and field-dependent MCPL.[28] In particular, exciton self-trapping has been proposed as a PL mechanism for $CuInS_2$ NCs.[28] This phenomenon, which has been observed and studied in other materials including AgCl and 2D lead–halide perovskites, occurs when strong electron–phonon coupling stabilizes a localized state relative to a delocalized one. Carrier localization causes a nuclear distortion, which supports further localization, which induces additional distortion, and so on.[113-118] This feedback loop and the creation of "excited-state defects" can occur without the presence of ground-state lattice defects, which distinguishes this proposal from other proposed PL mechanisms for $CuInS_2$ NCs. Just as in Cu^+-doped NCs, PL results from

recombination of a delocalized conduction-band electron with a hole localized at a lattice Cu^+. In this scenario, $CuInS_2$ NCs can be thought of as heavily Cu^+-doped NCs.

Comparisons between Cu^+-doped and $CuInS_2$ NCs are strengthened by the observation of similar photophysical properties in NCs with intermediate compositions: alloyed Cu–In–Zn–S NCs also display similar PL over a broad range of stoichiometries.[119-128] Density functional theory calculations on a series of NCs ranging from ZnS doped with a single Cu^+ to stoichiometric, defect-free $CuInS_2$ show that each NC's HOMO, which is relevant to the wavefunction of an excited-state hole, consists mostly of Cu(3d) atomic orbitals and is localized around 1–3 Cu^+. Further investigation of ZnS NCs doped with clusters of Cu^+ shows that the HOMOs of these NCs are rarely delocalized over all of the adjacent Cu^+ dopants. Weak electronic coupling between Cu^+ results in a strong tendency of the HOMO to localize for many different numbers and configurations of adjacent Cu^+. The site of localization depends on the symmetry and connectivity of the Cu^+ ions as well as on the local electrostatics. These results, which are presented in detail in Chapter 4 (ref. 129), support the proposal of a hole localized at a lattice Cu^+, rather than at a defect site, in the luminescent excited state of $CuInS_2$ NCs; they also reinforce the description of $CuInS_2$ NCs as resembling heavily Cu^+-doped NCs. In general, exploring the relationships among the electronic structures of Cu^+-doped NCs in the dilute limit, heavily Cu^+-doped or alloyed NCs, and stoichiometric $CuInS_2$ NCs can lead to a deeper understanding of the PL in all of these materials.[16,28,129]

1.6 **Summary**

While bulk Cu^+-doped and Ag^+-doped semiconductors have a rich history as phosphors, the nanocrystalline forms of these materials offer access to new photophysical studies, tunable properties, and novel applications. Both Cu^+-doped and Ag^+-doped NCs have been synthesized

and studied, and they display similar PL properties with key electronic-structure differences. Time-resolved photoluminescence and transient absorption measurements have established the ground-state dopant oxidation state and the nature of the charge-transfer excited state. Combined with time-resolved photoluminescence, magnetic circularly polarized luminescence and magnetic circular dichroism have been used to study the interactions between unpaired spins in the excited states of these materials. Single-particle PL and computational studies have shown that the broad PL line width is explained by strong electron–phonon coupling. The long excited-state lifetime and the behavior of these dopants as hole traps have been exploited to study different aspects of carrier trapping in NCs. Beyond doped NCs, many of the photophysical insights developed for these materials may also apply to $CuInS_2$ and related I–III–VI_2 NCs. Overall, the study of copper- and silver-based luminescence is a field with a bright past, present, and future.

Several chapters of this thesis address different aspects of Cu^+- and Ag^+-related luminescence in greater depth. Chapter 2 (ref. 65) is a computational investigation of Cu^+:CdSe NCs, addressing the copper oxidation state, excited-state distortion and PL line width, and singlet–triplet splitting. Chapter 3 (ref. 50) is a combined experimental and theoretical study of Cu^+:CdSe and Ag^+:CdSe NCs with discussion of normal vs. inverted bonding. Chapter 4 (ref. 129) compares the electronic structures of NCs ranging from Cu^+-doped ZnS to $CuInS_2$.

1.7 References

1. Harvey, E. N. *A history of luminescence from the earliest times until 1900*; American Philosophical Society: Philadelphia, 1957.
2. Lastusaari, M.; Laamanen, T.; Malkamäki, M.; Eskola, K. O.; Kotlov, A.; Carlson, S.; Welter, E.; Brito, H. F.; Bettinelli, M.; Jungner, H.; Hölsa, J. The Bologna Stone: history's first persistent luminescent material. *Eur. J. Mineral.* **2012**, *24*, 885-890.

3. Principe, L. M. Chymical Exotica in the Seventeenth Century, or, How to Make the Bologna Stone. *Ambix* **2016**, *63*, 118-144.

4. Yen, W. M.; Shionoya, S.; Yamamoto, H. *Phosphor Handbook*, 2nd ed.; CRC Press: Boca Raton, FL, USA, 2007.

5. Becquerel, E. Note sur phosphorescence de la blende hexagonal. *C. R. Hebd. Seances Acad. Sci.* **1866**, *63*, 142-146.

6. Era, K.; Shionoya, S.; Washizawa, Y. Mechanism of Broad-band Luminescences in ZnS Phosphors--I. Spectrum Shift During Decay and with Excitation Intensity. *J. Phys. Chem. Solids* **1968**, *29*, 1827-1841.

7. Era, K.; Shionoya, S.; Washizawa, Y.; Ohmatsu, H. Mechanism of Broad-band Luminescences in ZnS Phosphors--II. Characteristics of Pair Emission Type Luminescences. *J. Phys. Chem. Solids* **1968**, *29*, 1843-1857.

8. Suzuki, A.; Shionoya, S. Mechanism of the Green-Copper Luminescence in ZnS Crystals. I. Direct Evidence for the Pair Emission Mechanism. *J. Phys. Soc. Jpn.* **1971**, *31*, 1455-1461.

9. Suzuki, A.; Shionoya, S. Mechanism of the Green-Copper Luminescence in ZnS Crystals. II. Polarization Characteristics. *J. Phys. Soc. Jpn.* **1971**, *31*, 1462-1468.

10. Buckner, M. T.; McMillin, D. R. Photoluminescence from Copper(I) Complexes with Low-Lying Metal-to-Ligand Charge Transfer Excited States. *J. Chem. Soc., Chem. Commun.* **1978**, 759-761.

11. Blasse, G.; McMillin, D. R. On the Luminescence of Bis(TriPhenylPhosphine) Phenanthroline Copper(I). *Chem. Phys. Lett.* **1980**, *70*, 1-3.

12. Everly, R. M.; McMillin, D. R. Reinvestigation of the Absorbing and Emitting Charge-Transfer Excited States of $[Cu(NN)_2]+$ Systems. *J. Phys. Chem.* **1991**, *95*, 9071-9075.

13. Barbieri, A.; Accorsi, G.; Armaroli, N. Luminescent Complexes Beyond the Platinum Group: The d^{10} Avenue. *Chem. Commun.* **2008**, *44*, 2185-2193.

14. Mara, M. W.; Fransted, K. A.; Chen, L. X. Interplays of excited state structures and dynamics in copper(I) diimine complexes: Implications and perspectives. *Coord. Chem. Rev.* **2015**, *282-283*, 2-18.

15. Czerwieniec, R.; Leitl, M. J.; Homeier, H. H. H.; Yersin, H. Cu(I) Complexes – Thermally Activated Delayed Fluorescence. Photophysical Approach and Material Design. *Coord. Chem. Rev.* **2016**, *325*, 2-28.

16. Knowles, K. E.; Hartstein, K. H.; Kilburn, T. B.; Marchioro, A.; Nelson, H. D.; Whitham, P. J.; Gamelin, D. R. Luminescent Colloidal Semiconductor Nanocrystals Containing Copper: Synthesis, Photophysics, and Applications. *Chem. Rev.* **2016**, *116*, 10820-10851.

17. Bradshaw, L. R.; Knowles, K. E.; McDowall, S.; Gamelin, D. R. Nanocrystals for Luminescent Solar Concentrators. *Nano Lett.* **2015**, *15*, 1315-1323.

18. Sharma, M.; Gungor, K.; Yeltik, A.; Olutas, M.; Guzelturk, B.; Kelestemur, Y.; Erdem, T.; Delikanli, S.; McBride, J. R.; Demir, H. V. Near-Unity Emitting Copper-Doped Colloidal Semiconductor Quantum Wells for Luminescent Solar Concentrators. *Adv. Mater.* **2017**, *29*, 1700821.

19. Huang, J.; Yang, Y.; Xue, S.; Yang, B.; Liu, S.; Shen, J. Photoluminescence and electroluminescence of ZnS:Cu nanocrystals in polymeric networks. *Appl. Phys. Lett.* **1997**, *70*, 2335-2337.

20. Que, W.; Zhou, Y.; Lam, Y. L.; Chan, Y. C.; Kam, C. H. Photoluminescence and electroluminescence from copper doped zinc sulphide nanocrystals/polymer composite. *Appl. Phys. Lett.* **1998**, *73*, 2727-2729.

21. Bhaumik, S.; Ghosh, B.; Pal, A. J. Color Tunable Light-Emitting Diodes Based On Copper Doped Semiconducting Nanocrystals. *Appl. Phys. Lett.* **2011**, *99*, 083106.

22. Wang, X.; Yan, X.; Li, W.; Sun, K. Doped Quantum Dots for White-Light-Emitting Diodes Without Reabsorption of Multiphase Phosphors. *Adv. Mater.* **2012**, *24*, 2742-2747.

23. Zhang, Z.; Liu, D.; Li, D.; Huang, K.; Zhang, Y.; Shi, Z.; Xie, R.; Han, M.-Y.; Wang, Y.; Yang, W. Dual Emissive Cu:InP/ZnS/InP/ZnS Nanocrystals: Single-Source "Greener" Emitters with Flexibly Tunable Emission from Visible to Near-Infrared and Their Application in White Light-Emitting Diodes. *Chem. Mater.* **2015**, *27*, 1405-1411.

24. Wu, P.; Yan, X.-P. Doped quantum dots for chemo/biosensing and bioimaging. *Chem. Soc. Rev.* **2013**, *42*, 5489-5521.

25. Xu, S.; Wang, C.; Wang, Z.; Zhang, H.; Yang, J.; Xu, Q.; Shao, H.; Li, R.; Lei, W.; Cui, Y. Aqueous synthesis of internally doped Cu:ZnSe/ZnS core–shell nanocrystals with good stability. *Nanotechnology* **2011**, *22*, 275605.

26. Maity, A. R.; Palmal, S.; Basiruddin, S. K.; Karan, N. S.; Sarkar, S.; Pradhan, N.; Jana, N. R. Doped semiconductor nanocrystal based fluorescent cellular imaging probes. *Nanoscale* **2013**, *5*, 5506-5513.

27. Jiang, T.; Song, J.; Wang, H.; Ye, X.; Wang, H.; Zhang, W.; Yang, M.; Xia, R.; Zhu, L.; Xu, X. Aqueous synthesis of color tunable Cu doped Zn–In–S/ZnS nanoparticles in the whole visible region for cellular imaging. *J. Mater. Chem. B* **2015**, *3*, 2402-2410.

28. Knowles, K. E.; Nelson, H. D.; Kilburn, T. B.; Gamelin, D. R. Singlet−Triplet Splittings in the Luminescent Excited States of Colloidal Cu^+:CdSe, Cu^+:InP, and $CuInS_2$ Nanocrystals: Charge-Transfer Configurations and Self-Trapped Excitons. *J. Am. Chem. Soc.* **2015**, *137*, 13138–13147.

29. Grandhi, G. K.; Tomar, R.; Viswanatha, R. Study of Surface and Bulk Electronic Structure of II-VI Semiconductor Nanocrystals Using Cu as a Nanosensor. *ACS Nano* **2012**, *6*, 9751-9763.

30. Grandhi, G. K.; Viswanatha, R. Demystifying Complex Quantum Dot Heterostructures Using Photogenerated Charge Carriers. *J. Phys. Chem. Lett.* **2017**, *8*, 2043-2048.

31. Zhang, Z.; Li, D.; Xie, R.; Yang, W. Insights into the Energy Levels of Semiconductor Nanocrystals by a Dopant Approach. *Angew. Chem. Int. Ed.* **2013**, *52*, 5052-5055.

32. Yang, L.; Knowles, K. E.; Gopalan, A.; Hughes, K. E.; James, M. C.; Gamelin, D. R. One-Pot Synthesis of Monodisperse Colloidal Copper-Doped CdSe Nanocrystals Mediated by Ligand−Copper Interactions. *Chem. Mater.* **2016**, *28*, 7375–7384.

33. Ishizumi, A.; White, C. W.; Kanemitsu, Y. Space-Resolved Photoluminescence of ZnS:Cu,Al Nanocrystals Fabricated by Sequential Ion Implantation. *Appl. Phys. Lett*. **2004**, *84*, 2397-2399.

34. Ishizumi, A.; White, C. W.; Kanemitsu, Y. Photoluminescence Properties of Impurity-Doped ZnS Nanocrystals Fabricated by Sequential Ion Implantation. *Physica E* **2005**, *26*, 24-27.

35. Corrado, C.; Jiang, Y.; Oba, F.; Kozina, M.; Bridges, F.; Zhang, J. Z. Synthesis, Structural, and Optical Properties of Stable ZnS:Cu,Cl Nanocrystals. *J. Phys. Chem. A* **2009**, *113*, 3830-3839.

36. Gul, S.; Cooper, J. K.; Glans, P.-A.; Guo, J.; Yachandra, V. K.; Yano, J.; Zhang, J. Z. Effect of Al^{3+} Co-doping on the Dopant Local Structure, Optical Properties, and Exciton Dynamics in Cu^{+}-Doped ZnSe Nanocrystals. *ACS Nano* **2013**, *7*, 8680-8692.

37. Sarkar, S.; Guria, A. K.; Patra, B. K.; Pradhan, N. Synthesis and Photo-darkening/Photo-brightening of Blue Emitting Doped Semiconductor Nanocrystals. *Nanoscale* **2014**, *6*, 3786-3790.

38. Cooper, J. K.; Gul, S.; Lindley, S. A.; Yano, J.; Zhang, J. Z. Tunable Photoluminescent Core/Shell Cu^{+}-Doped ZnSe/ZnS Quantum Dots Codoped with Al^{3+}, Ga^{3+}, or In^{3+}. *ACS Appl. Mater. Interfaces* **2015**, *7*, 10055-10066.

39. Liu, M.; Yao, W.; Li, C.; Wu, Z.; Li, L. Tuning emission and Stokes shift of CdS quantum dots *via* copper and indium co-doping. *RSC Adv*. **2015**, *5*, 628-634.

40. Hughes, K. E.; Hartstein, K. H.; Gamelin, D. R. Photodoping and Transient Spectroscopies of Copper-Doped CdSe/CdS Nanocrystals. *ACS Nano* **2018**, *12*, 718-728.

41. Jawaid, A. M.; Chattopadhyay, S.; Wink, D. J.; Page, L. E.; Snee, P. T. Cluster-Seeded Synthesis of Doped CdSe:Cu_4 Quantum Dots. *ACS Nano* **2013**, *7*, 3190-3197.

42. Santiago-González, B.; Monguzzi, A.; Pinchetti, V.; Casu, A.; Prato, M.; Lorenzi, R.; Campione, M.; Chiodini, N.; Santambrogio, C.; Meinardi, F.; Manna, L.; Brovelli, S. "Quantized" Doping of Individual Colloidal Nanocrystals Using Size-Focused Metal Quantum Clusters. *ACS Nano* **2017**, *11*, 6233-6242.

43. Bhattacharyya, B.; Gahlot, K.; Viswanatha, R.; Pandey, A. Optical Signatures of Impurity−Impurity Interactions in Copper Containing II−VI Alloy Semiconductors. *J. Phys. Chem. Lett*. **2018**, *9*, 635-640.

44. Avinor, M.; Meijer, G. Emission of Activated Cadmium Selenide Phosphors. *J. Chem. Phys.* **1960**, *32*, 1456-1458.

45. Ishizumi, A.; Kanemitsu, Y. Photoluminescence Spectra and Dynamics of Al^{3+}- and Ag^{+}-Doped CdS Nanocrystals. *J. Phys. Soc. Jpn.* **2010**, *79*, 093706.

46. Sahu, A.; Kang, M. S.; Kompch, A.; Notthoff, C.; Wills, A. W.; Deng, D.; Winterer, M.; Frisbie, C. D.; Norris, D. J. Electronic Impurity Doping in CdSe Nanocrystals. *Nano Lett*. **2012**, *12*, 2587-2594.

47. Jana, S.; Manna, G.; Srivastava, B. B.; Pradhan, N. Tuning the Emission Colors of Semiconductor Nanocrystals Beyond their Bandgap Tunability: All in the Dope. *Small* **2013**, *9*, 3753-3758.

48. Liu, J.; Zhao, Q.; Liu, J.-L.; Wu, Y.-S.; Cheng, Y.; Ji, M.-W.; Qian, H.-M.; Hao, W.-C.; Zhang, L.-J.; Wei, X.-J.; Wang, S.-G.; Zhang, J.-T.; Du, Y.; Dou, S.-X.; Zhu, H.-S. Heterovalent-Doping-Enabled Efficient Dopant Luminescence and Controllable Electronic Impurity Via a New Strategy of Preparing II−VI Nanocrystals. *Adv. Mater.* **2015**, *27*, 2753-2761.

49. Wei, Q.; Zhao, Y.; Di, Q.; Liu, J.; Xu, M.; Liu, J.; Zhang, J. Good Dispersion of Large-Stokes-Shift Heterovalent-Doped CdX Quantum Dots into Bulk PMMA Matrix and Their Optical Properties Characterization. *J. Phys. Chem. C* **2017**, *121*, 6152-6159.

50. Nelson, H. D.; Hinterding, S. O. M.; Fainblat, R.; Creutz, S. E.; Li, X.; Gamelin, D. R. Mid-Gap States and Normal vs Inverted Bonding in Luminescent Cu^{+}- and Ag^{+}-Doped CdSe Nanocrystals. *J. Am. Chem. Soc.* **2017**, *139*, 6411-6421.

51. Pinchetti, V.; Di, Q.; Lorenzon, M.; Camellini, A.; Fasoli, M.; Zavelani-Rossi, M.; Meinardi, F.; Zhang, J.; Crooker, S. A.; Brovelli, S. Excitonic pathway to photoinduced magnetism in colloidal nanocrystals with nonmagnetic dopants. *Nat. Nanotechnol.* **2018**, *13*, 145-151.

52. Kompch, A.; Sahu, A.; Notthoff, C.; Ott, F.; Norris, D. J.; Winterer, M. Localization of Ag Dopant Atoms in CdSe Nanocrystals by Reverse Monte Carlo Analysis of EXAFS Spectra. *J. Phys. Chem. C* **2015**, *119*, 18762-18772.

53. Mocatta, D.; Cohen, G.; Schattner, J.; Millo, O.; Rabani, E.; Banin, U. Heavily Doped Semiconductor Nanocrystal Quantum Dots. *Science* **2011**, *332*, 77-81.

54. Almeida, A. J.; Sahu, A.; Riedinger, A.; Norris, D. J.; Brandt, M. S.; Stutzmann, M.; Pereira, R. N. Charge Trapping Defects in CdSe Nanocrystal Quantum Dots. *J. Phys. Chem. C* **2016**, *120*, 13763-13770.

55. Ivanova, G. N.; Kasiyan, V. A.; Nedeoglo, N. D.; Nedeoglo, D. D. Photoluminescence of ZnSe:Ag single crystals. *J. Lumin.* **1999**, *82*, 277-283.

56. Laiho, R.; Lashkul, A. V.; Lähderanta, E.; Nedeoglo, D. D.; Nedeoglo, N. D.; Shakhov, M. A. Shallow donor states of Ag impurity in ZnSe single crystals. *Semicond. Sci. Technol.* **2006**, *21*, 654-660.

57. Nedeoglo, N. D.; Sirkeli, V. P.; Nedeoglo, D. D.; Laiho, R.; Lähderanta, E. Electron configuration and charge state of electrically active Cu, Ag and Au ions in ZnSe. *J. Phys.: Condens. Matter* **2006**, *18*, 8113-8127.

58. *CRC Handbook of Chemistry and Physics*, 97th ed.; Boca Raton, FL, 2016.

59. Hsu, C.-W.; Lin, C.-C.; Chung, M.-W.; Chi, Y.; Lee, G.-H.; Chou, P.-T.; Chang, C.-H.; Chen, P.-Y. Systematic Investigation of the Metal-Structure−Photophysics Relationship of Emissive d^{10}-Complexes of Group 11 Elements: The Prospect of Application in Organic Light Emitting Devices. *J. Am. Chem. Soc.* **2011**, *133*, 12085-12099.

60. Osawa, M.; Kawata, I.; Ishii, R.; Igawa, S.; Hashimoto, M.; Hoshino, M. Application of Neutral d^{10} Coinage Metal Complexes with an Anionic Bidentate Ligand in Delayed Fluorescence-type Organic Light-emitting Diodes. *J. Mater. Chem. C* **2013**, *1*, 4375-4383.

61. Yersin, H.; Leitl, M. J.; Czerwieniec, R. TADF for Singlet Harvesting – Next Generation OLED Materials Based on Brightly Green and Blue Emitting Cu(I) and Ag(I) Compounds. *Proc. SPIE* **2014**, *9183*, 91830N.

62. Chen, J.; Teng, T.; Kang, L.; Chen, X.-L.; Wu, X.-Y.; Yu, R.; Lu, C.-Z. Highly Efficient Thermally Activated Delayed Fluorescence in Dinuclear Ag(I) Complexes with a Bis-Bidentate Tetraphosphane Bridging Ligand. *Inorg. Chem.* **2016**, *55*, 9528-9536.

63. Matsumoto, K.; Shindo, T.; Mukasa, N.; Tsukuda, T.; Tsubomura, T. Luminescent Mononuclear Ag(I)−Bis(diphosphine) Complexes: Correlation between the Photophysics and the Structures of Mononuclear Ag(I)−Bis(diphosphine) Complexes. *Inorg. Chem.* **2010**, *49*, 805-814.

64. Shafikov, M. Z.; Suleymanova, A. F.; Czerwieniec, R.; Yersin, H. Design Strategy for Ag(I)-Based Thermally Activated Delayed Fluorescence Reaching an Efficiency Breakthrough. *Chem. Mater.* **2017**, 10.1021/acs.chemmater.6b05175.

65. Nelson, H. D.; Li, X.; Gamelin, D. R. Computational Studies of the Electronic Structures of Copper-Doped CdSe Nanocrystals: Oxidation States, Jahn−Teller Distortions, Vibronic Bandshapes, and Singlet−Triplet Splittings. *J. Phys. Chem. C* **2016**, *120*, 5714-5723.

66. Brovelli, S.; Galland, C.; Viswanatha, R.; Klimov, V. I. Tuning Radiative Recombination in Cu-Doped Nanocrystals via Electrochemical Control of Surface Trapping. *Nano Lett.* **2012**, *12*, 4372-4379.

67. Pandey, A.; Brovelli, S.; Viswanatha, R.; Li, L.; Pietryga, J. M.; Klimov, V. I.; Crooker, S. A. Long-Lived Photoinduced Magnetization in Copper-Doped ZnSe–CdSe Core–Shell Nanocrystals. *Nat. Nanotechnol.* **2012**, *7*, 792-797.

68. Viswanatha, R.; Brovelli, S.; Pandey, A.; Crooker, S. A.; Klimov, V. I. Copper-Doped Inverted Core/Shell Nanocrystals with "Permanent" Optically Active Holes. *Nano Lett.* **2011**, *11*, 4753-4758.

69. Heitz, R.; Hoffmann, A.; Thurian, P.; Broser, I. The Copper Centre: A Transient Shallow Acceptor in ZnS and CdS. *J. Phys.: Condens. Matter* **1992**, *4*, 157-168.

70. Thurian, P.; Heitz, R.; Kaczmarczyk, G.; Hoffmann, A.; Broser, I.; Telahun, T.; Schrepel, C.; Goebel, C.; Scherz, U. Jahn-Teller Effect of Cu2+ in II–VI Compounds. *Z. Phys. Chem.* **1997**, *201*, 137-150.

71. Maier, H.; Scherz, U. Vibronic Spectra and the Dynamic Jahn-Teller Effect of Cubic ZnS:Cu^{2+}. *Phys. Status Solidi B* **1974**, *62*, 153-164.

72. Maiti, S.; Dana, J.; Jadhav, Y.; Debnath, T.; Haram, S. K.; Ghosh, H. N. Electrochemical Evaluation of Dopant Energetics and the Modulation of Ultrafast Carrier Dynamics in Cu-Doped CdSe Nanocrystals. *J. Phys. Chem. C* **2017**, *121*, 27233-27240.

73. Hassan, A.; Zhang, X.; Liu, X.; Rowland, C. E.; Jawaid, A. M.; Chattopadhyay, S.; Gulec, A.; Shamirian, A.; Zuo, X.; Klie, R. F.; Schaller, R. D.; Snee, P. T. Charge Carriers Modulate the Bonding of Semiconductor Nanoparticle Dopants As Revealed by Time-Resolved X-ray Spectroscopy. *ACS Nano* **2017**, *11*, 10070-10076.

74. Meulenberg, R. W.; van Buuren, T.; Hanif, K. M.; Willey, T. M.; Strouse, G. F.; Terminello, L. J. Structure and Composition of Cu-Doped CdSe Nanocrystals Using Soft X-ray Absorption Spectroscopy. *Nano Lett.* **2004**, *4*, 2277-2285.

75. Monemar, B.; Gislason, H. P.; Dean, P. J.; Herbert, D. C. Optical properties of the Cu-related characteristic-orange-luminescence center in GaP. *Phys. Rev. B* **1982**, *25*, 7719-7730.

76. Gislason, H. P.; Monemar, B.; Dean, P. J.; Herbert, D. C.; Depinna, S.; Cavenett, B. C.; Killoran, N. Photoluminescence studies of the 1.911-eV Cu-related complex in GaP. *Phys. Rev. B* **1982**, *26*, 827-845.

77. Bergman, P.; Monemar, B. Dynamical Studies of Triplet-Singlet Pairs for Bound Excitons Related to Complex Defects in GaP. *J. Lumin.* **1987**, *38*, 87-89.

78. Gislason, H. P. Triplet Bound Excitons in Copper-Doped Gallium Phosphide. *Appl. Phys. A* **1988**, *48*, 11-24.

79. Bergman, P.; Monemar, B.; Pistol, M.-E. Transient Characteristics of Excitons Bound at Hole-Attractive Isoelectronic Centers in GaP. *Phys. Rev. B* **1989**, *40*, 12280-12289.

80. Yersin, H.; Czerwieniec, R.; Shafikov, M. Z.; Suleymanova, A. F. TADF Material Design: Photophysical Background and Case Studies Focusing on Cu^{I} and Ag^{I} Complexes. *ChemPhysChem* **2017**, *18*, 3508-3535.

81. Rice, W. D.; McDaniel, H.; Klimov, V. I.; Crooker, S. A. Magneto-Optical Properties of $CuInS_2$ Nanocrystals. *J. Phys. Chem. Lett.* **2014**, *5*, 4105-4109.

82. Whitham, P. J.; Knowles, K. E.; Reid, P. J.; Gamelin, D. R. Photoluminescence Blinking and Reversible Electron Trapping in Copper-Doped CdSe Nanocrystals. *Nano Lett.* **2015**, *15*, 4045-4051.

83. Dean, P. J.; Fitzpatrick, B. J.; Bhargava, R. N. Optical Properties of ZnSe Doped with Ag and Au. *Phys. Rev. B* **1982**, *26*, 2016-2035.

84. Holtz, P. O.; Monemar, B.; Lozykowski, H. J. Optical Properties of Ag-related Centers in Bulk ZnSe. *Phys. Rev. B* **1985**, *32*, 986-996.

85. Everly, R. M.; Ziessel, R.; Suffert, J.; McMillin, D. R. Steric Influences on the Photoluminescence from Copper(I) Phenanthrolines in Rigid Media. *Inorg. Chem.* **1991**, *30*, 559-561.

86. Felder, D.; Nierengarten, J.-F.; Barigelletti, F.; Ventura, B.; Armaroli, N. Highly Luminescent Cu(I)-Phenanthroline Complexes in Rigid Matrix and Temperature Dependence of the Photophysical Properties. *J. Am. Chem. Soc.* **2001**, *123*, 6291-6299.

87. Chen, L. X.; Shaw, G. B.; Novozhilova, I.; Liu, T.; Jennings, G.; Attenkofer, K.; Meyer, G. J.; Coppens, P. MLCT State Structure and Dynamics of a Copper(I) Diimine Complex Characterized by Pump-Probe X-ray and Laser Spectroscopies and DFT Calculations. *J. Am. Chem. Soc.* **2003**, *125*, 7022-7034.

88. Siddique, Z. A.; Yamamoto, Y.; Ohno, T.; Nozaki, K. Structure-Dependent Photophysical Properties of Singlet and Triplet Metal-to-Ligand Charge Transfer States in Copper(I) Bis(diimine) Compounds. *Inorg. Chem.* **2003**, *42*, 6366-6378.

89. Waterland, M. R.; Howell, S. L.; Gordon, K. C.; Burrell, A. K. Structural Changes upon Photoexcitation into the Metal-to-Ligand Charge-Transfer State of $[Cu(pqx)(PPh_3)_2]^+$ Probed by Resonance Raman Spectroscopy and Density Functional Theory. *J. Phys. Chem. A* **2005**, *109*, 8826-8833.

90. Iwamura, M.; Takeuchi, S.; Tahara, T. Ultrafast Excited-State Dynamics of Copper(I) Complexes. *Acc. Chem. Res.* **2015**, *48*, 782-791.

91. Marchioro, A.; Whitham, P. J.; Knowles, K. E.; Kilburn, T. B.; Reid, P. J.; Gamelin, D. R. Tunneling in the Delayed Luminescence of Colloidal CdSe, Cu^{+}-Doped CdSe, and $CuInS_2$ Semiconductor Nanocrystals and Relationship to Blinking. *J. Phys. Chem. C* **2016**, *120*, 27040-27049.

92. Grandhi, G. K.; Viswanatha, R. Tunable Infrared Phosphors Using Cu Doping in Semiconductor Nanocrystals: Surface Electronic Structure Evaluation. *J. Phys. Chem. Lett.* **2013**, *4*, 409-415.

93. Grandhi, G. K.; Arunkumar, M.; Viswanatha, R. Understanding the Role of Surface Capping Ligands in Passivating the Quantum Dots Using Copper Dopants as Internal Sensor. *J. Phys. Chem. C* **2016**, *120*, 19785-19795.

94. Shay, J. L.; Tell, B.; Kasper, H. M.; Schiavone, L. M. *p-d* Hybridization of the Valence Bands of I-III-VI_2 Compounds. *Phys. Rev. B* **1972**, *5*, 5003-5005.

95. Tell, B.; Shay, J. L.; Kasper, H. M. Electrical Properties, Optical Properties, and Band Structure of $CuGaS_2$ and $CuInS_2$. *Phys. Rev. B* **1971**, *4*, 2463-2471.

96. Braun, W.; Goldmann, A.; Cardona, M. Partial density of valence states of amorphous and crystalline $AgInTe_2$ and $CuInS_2$. *Phys. Rev. B* **1974**, *10*, 5069-5074.

97. Jaffe, J. E.; Zunger, A. Electronic structure of the ternary chalcopyrite semiconductors $CuAlS_2$, $CuGaS_2$, $CuInS_2$, $CuAlSe_2$, $CuGaSe_2$, and $CuInSe_2$. *Phys. Rev. B* **1983**, *28*, 5822-5847.

98. Jaffe, J. E.; Zunger, A. Theory of the band-gap anomaly in ABC_2 chalcopyrite semiconductors. *Phys. Rev. B* **1984**, *29*, 1882-1906.

99. Binsma, J. J. M.; Giling, L. J.; Bloem, J. Luminescence of $CuInS_2$: I. The Broad Band Emission and its Dependence on the Defect Chemistry. *J. Lumin.* **1982**, *27*, 35-53.

100. Binsma, J. J. M.; Giling, L. J.; Bloem, J. Luminescence of $CuInS_2$: II. Exciton and Near Edge Emission. *J. Lumin.* **1982**, *27*, 55-72.

101. Ueng, H. Y.; Hwang, H. L. The Defect Structure of $CuInS_2$. Part I: Intrinsic Defects. *J. Phys. Chem. Solids* **1989**, *50*, 1297-1305.

102. Ueng, H. Y.; Hwang, H. L. The Defect Structure of $CuInS_2$. Part II: Thermal Annealing Defects. *J. Phys. Chem. Solids* **1990**, *51*, 1-10.

103. Zhong, H.; Bai, Z.; Zou, B. Tuning the Luminescence Properties of Colloidal I−III−VI Semiconductor Nanocrystals for Optoelectronics and Biotechnology Applications. *J. Phys. Chem. Lett.* **2012**, *3*, 3167-3175.

104. Castro, S. L.; Bailey, S. G.; Raffaelle, R. P.; Banger, K. K.; Hepp, A. F. Synthesis and Characterization of Colloidal $CuInS_2$ Nanoparticles from a Molecular Single-Source Precursor. *J. Phys. Chem. B* **2004**, *108*, 12429-12435.

105. Leach, A. D. P.; Macdonald, J. E. Optoelectronic Properties of $CuInS_2$ Nanocrystals and Their Origin. *J. Phys. Chem. Lett.* **2016**, *7*, 572-583.

106. Aldakov, D.; Lefrançois, A.; Reiss, P. Ternary and quaternary metal chalcogenide nanocrystals: synthesis, properties and applications. *J. Mater. Chem. C* **2013**, *1*, 3756-3776.

107. Kolny-Olesiak, J.; Weller, H. Synthesis and Application of Colloidal $CuInS_2$ Semiconductor Nanocrystals. *ACS Appl. Mater. Interfaces* **2013**, *5*, 12221-12237.

108. Uehara, M.; Watanabe, K.; Tajiri, Y.; Nakamura, H.; Maeda, H. Synthesis of $CuInS_2$ Fluorescent Nanocrystals and Enhancement of Fluorescence by Controlling Crystal Defect. *J. Chem. Phys.* **2008**, *129*, 134709.

109. Nose, K.; Omata, T.; Otsuka-Yao-Matsuo, S. Colloidal Synthesis of Ternary Copper Indium Diselenide Quantum Dots and Their Optical Properties. *J. Phys. Chem. C* **2009**, *113*, 3455-3460.

110. Chen, B.; Zhong, H.; Zhang, W.; Tan, Z.; Li, Y.; Yu, C.; Zhai, T.; Bando, Y.; Yang, S.; Zou, B. Highly Emissive and Color-Tunable $CuInS_2$-Based Colloidal Semiconductor Nanocrystals: Off-Stoichiometry Effects and Improved Electroluminescence Performance. *Adv. Funct. Mater.* **2012**, *22*, 2081-2088.

111. Fuhr, A. S.; Yun, H. J.; Makarov, N. S.; Li, H.; McDaniel, H.; Klimov, V. I. Light Emission Mechanisms in $CuInS_2$ Quantum Dots Evaluated by Spectral Electrochemistry. *ACS Photonics* **2017**, *4*, 2425-2435.

112. Pinchetti, V.; Lorenzon, M.; McDaniel, H.; Lorenzi, R.; Meinardi, F.; Klimov, V. I.; Brovelli, S. Spectro-electrochemical Probing of Intrinsic and Extrinsic Processes in Exciton Recombination in $I-III-VI_2$ Nanocrystals. *Nano Lett.* **2017**, *17*, 4508-4517.

113. Williams, R. T.; Song, K. S. The Self-Trapped Exciton. *J. Phys. Chem. Solids* **1990**, *51*, 679-716.

114. Stoneham, A. M.; Gavartin, J.; Shluger, A. L.; Kimmel, A. V.; Muñoz Ramo, D.; Rønnow, H. M.; Aeppli, G.; Renner, C. Trapping, self-trapping and the polaron family. *J. Phys.: Condens. Matter* **2007**, *19*, 255208.

115. Dohner, E. R.; Jaffe, A.; Bradshaw, L. R.; Karunadasa, H. I. Intrinsic White-Light Emission from Layered Hybrid Perovskites. *J. Am. Chem. Soc.* **2014**, *136*, 13154-13157.

116. Wu, X.; Trinh, M. T.; Niesner, D.; Zhu, H.; Norman, Z.; Owen, J. S.; Yaffe, O.; Kudisch, B. J.; Zhu, X.-Y. Trap States in Lead Iodide Perovskites. *J. Am. Chem. Soc.* **2015**, *137*, 2089-2096.

117. Yangui, A.; Garrot, D.; Lauret, J. S.; Lusson, A.; Bouchez, G.; Deleporte, E.; Pillet, S.; Bendeif, E. E.; Castro, M.; Triki, S.; Abid, Y.; Boukheddaden, K. Optical Investigation of Broadband White-Light Emission in Self-Assembled Organic−Inorganic Perovskite $(C_6H_{11}NH_3)_2PbBr_4$. *J. Phys. Chem. C* **2015**, *119*, 23638-23647.

118. Hu, T.; Smith, M. D.; Dohner, E. R.; Sher, M.-J.; Wu, X.; Trinh, M. T.; Fisher, A.; Corbett, J.; Zhu, X.-Y.; Karunadasa, H. I.; Lindenberg, A. M. Mechanism for Broadband White-Light Emission from Two-Dimensional (110) Hybrid Perovskites. *J. Phys. Chem. Lett.* **2016**, *7*, 2258-2263.

119. Nakamura, H.; Kato, W.; Uehara, M.; Nose, K.; Omata, T.; Otsuka-Yao-Matsuo, S.; Miyazaki, M.; Maeda, H. Tunable Photoluminescence Wavelength of Chalcopyrite $CuInS_2$-Based Semiconductor Nanocrystals Synthesized in a Colloidal System. *Chem. Mater.* **2006**, *18*, 3330-3335.

120. Zhang, J.; Xie, R.; Yang, W. A Simple Route for Highly Luminescent Quaternary Cu-Zn-In-S Nanocrystal Emitters. *Chem. Mater.* **2011**, *23*, 3357-3361.

121. Zhang, W.; Lou, Q.; Ji, W.; Zhao, J.; Zhong, X. Color-Tunable Highly Bright Photoluminescence of Cadmium-Free Cu-Doped Zn−In−S Nanocrystals and Electroluminescence. *Chem. Mater.* **2014**, *26*, 1204-1212.

122. Zhang, W.; Zhong, X. Facile Synthesis of ZnS−$CuInS_2$-Alloyed Nanocrystals for a Color-Tunable Fluorchrome and Photocatalyst. *Inorg. Chem.* **2011**, *50*, 4065-4072.

123. Park, J.; Kim, S.-W. $CuInS_2$/ZnS core/shell quantum dots by cation exchange and their blue-shifted photoluminescence. *J. Mater. Chem.* **2011**, *21*, 3745-3750.

124. Akkerman, Q. A.; Genovese, A.; George, C.; Prato, M.; Moreels, I.; Casu, A.; Marras, S.; Curcio, A.; Scarpellini, A.; Pellegrino, T.; Manna, L.; Lesnyak, V. From Binary Cu_2S toTernary Cu−In−S and Quaternary Cu−In−Zn−S Nanocrystals with Tunable Composition *via* Partial Cation Exchange. *ACS Nano* **2015**, *9*, 521-531.

125. De Trizio, L.; Prato, M.; Genovese, A.; Casu, A.; Povia, M.; Simonutti, R.; Alcocer, M. J. P.; D'Andrea, C.; Tassone, F.; Manna, L. Strongly Fluorescent Quaternary Cu−In−Zn−S Nanocrystals Prepared from $Cu_{1-x}InS_2$ Nanocrystals by Partial Cation Exchange. *Chem. Mater.* **2012**, *24*, 2400-2406.

126. Xiang, W.-D.; Yang, H.-L.; Liang, X.-J.; Zhong, J.-S.; Wang, J.; Luo, L.; Xie, C.-P. Direct synthesis of highly luminescent Cu–Zn–In–S quaternary nanocrystals with tunable photoluminescence spectra and decay times. *J. Mater. Chem. C* **2013**, *1*, 2014-2020.

127. Zaiats, G.; Kinge, S.; Kamat, P. V. Origin of Dual Photoluminescence States in ZnS−$CuInS_2$ Alloy Nanostructures. *J. Phys. Chem. C* **2016**, *120*, 10641-10646.

128. Dong, X.; Xu, J.; Zhang, X.; Shi, S.; Yang, H.; Mo, Z.; Li, L.; Yin, S. Investigating Photoluminescence Mechanism of Cu-doped Zn−In−Se Quantum Dots by Zn/In Ratio. *J. Phys. Chem. C* **2017**, *121*, 16978-16984.

129. Nelson, H. D.; Gamelin, D. R., Valence-Band Electronic Structures of Cu^+-Doped ZnS, Alloyed Cu−In−Zn−S, and Ternary $CuInS_2$ Nanocrystals: A Unified Description of Photoluminescence Across Compositions. **2018**, *in preparation.*

Chapter 2. Computational Studies of the Electronic Structures of Copper-Doped CdSe Nanocrystals: Oxidation States, Jahn–Teller Distortions, Vibronic Bandshapes, and Singlet–Triplet Splittings

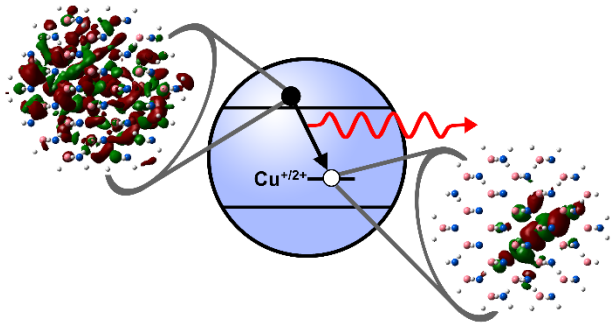

Reproduced with permission from Nelson, H. D.; Li, X.; Gamelin, D. R. *J. Phys. Chem. C* **2016**, *120*, 5714-5723. Copyright 2016 American Chemical Society.

2.1 **Overview.**

The electronic structures of copper-doped CdSe nanocrystals (NCs) are investigated using time-dependent density functional theory. Comparison of the electronic structures of Cu^{+}- and Cu^{2+}-doped NCs indicates that only the Cu^{+} ground state is consistent with the experimental absorption and photoluminescence (PL) spectra of copper-doped NCs, Cu^{2+}-doped NCs being characterized by low-energy charge-transfer and d–d excited states that quench visible PL. In the luminescent metal-to-conduction-band charge-transfer ($ML_{CB}CT$) excited state of the Cu^{+}-doped CdSe NCs, the photogenerated hole is calculated to be localized at the copper dopant. Strong electron-phonon coupling in this $ML_{CB}CT$ excited state causes substantial geometric distortion along totally symmetric and Jahn–Teller nuclear coordinates, with a correspondingly large excited-state nuclear reorganization energy. This excited-state nuclear reorganization causes the broad PL bandshape and large PL Stokes shift observed experimentally. Singlet and triplet $ML_{CB}CT$ excited-state configurations are also examined computationally. The sign and strength of the computed

magnetic exchange coupling between the conduction-band electron's spin and the copper-localized spin are both consistent with experimental results. These calculations yield fundamental insights into the electronic structures and photophysical properties of copper-doped semiconductor NCs relevant to their potential application as spectral conversion phosphors in lighting and solar technologies.

2.2 Introduction

The photoluminescence (PL) of colloidal II−VI and III−V semiconductor nanocrystals (NCs) changes dramatically when copper is introduced into the NC lattice. Instead of exhibiting the narrow near-bandgap luminescence with small Stokes shifts characteristic of exciton recombination in these direct-gap semiconductors, copper-doped semiconductor NCs display[1-10] broad mid-gap luminescence with large Stokes shifts, reminiscent of the "green" copper emission of the classic Cu^{+},Al^{3+}-co-doped ZnS phosphors long employed in display technologies.[11] In these bulk phosphors, this luminescence is attributed to donor−acceptor pair (DAP) recombination:[11-12] Photo- or electro-excitation ionizes Cu^{+} to form a metastable charge-separated state involving a hole deeply bound to the copper (Cu^{2+}-like acceptor) and an electron weakly bound to an Al^{3+} (donor). Radiative donor-acceptor pair recombination reforms the Cu^{+},Al^{3+}-co-doped ZnS ground state. In copper-doped NCs, large Stokes shifts minimize reabsorption of the NC emission, and when combined with the large absorption cross sections and spectral tunability provided by the host semiconductors, they make copper-doped NCs attractive phosphors for spectral conversion in light-emitting devices[13-14] and luminescent solar concentrators.[15]

Despite major advances by numerous laboratories over the past two decades, especially in the synthesis of copper-doped NCs, several aspects of the electronic structures of these materials remain poorly understood. At the most rudimentary level, the formal oxidation state of the copper

impurities remains a point of considerable dispute, with some data seemingly suggesting that copper incorporates as paramagnetic $Cu^{2+}(3d^9)$[7,16-17] and others suggesting that it incorporates as the closed-shell $Cu^{+}(3d^{10})$ impurity.[10,18-20] Correct identification of the ground-state electronic configuration of the active copper impurity has obvious implications for arriving at a correct interpretation of the PL and related physical properties of copper-doped NCs. Multiple interpretations have also been proposed to explain the broad PL bandshapes in copper-doped NCs. Spatially resolved PL[21-22] and fluorescence line-narrowing[23] experiments indicate that this large bandshape does not result from the NC size distribution; other broadening effects such as distributions of local structures around the copper ions[23] or distributions of DAP distances[21] have been hypothesized. The large bandshape has also been suggested to arise primarily from strong vibronic coupling in what is formally a metal-to-conduction-band charge-transfer ($ML_{CB}CT$) excited state of Cu^{+}-doped NCs.[10,22] Despite these contrasting interpretations, the experimental spectroscopic properties of different copper-doped II−VI and III−V semiconductor NCs are remarkably similar to one another, from similar PL bandshapes down to similar spin splittings of their luminescent excited states,[10] suggesting that the fundamental electronic structures of these materials are all the same. Theoretical investigation into the electronic structures of copper-doped semiconductor NCs may shed light on some of the unresolved issues, clarifying the origins and properties of the luminescence in this important class of nanophosphors.

Here, we report the results of density functional theory (DFT) calculations aimed at describing the electronic structures of copper-doped NCs pertinent to their luminescence. Although previous DFT calculations on bulk Cu^{+}:ZnSe have indicated the presence of Cu-related states in the band gap,[19,24] the properties of the luminescent excited state and the electronic structures of discrete, quantum-confined copper-doped NCs have not been explored

computationally. Using CdSe as our model system, we have examined copper-doped NCs of two different sizes. To address the experimental uncertainty in copper oxidation state, we have performed parallel calculations with copper in both its Cu^{+} and Cu^{2+} oxidation states, and have used time-dependent DFT (TD-DFT) to compute electronic absorption spectra for both Cu^{+}:CdSe and Cu^{2+}:CdSe NCs. We find major differences between the mid-gap distributions of electronic excited states in Cu^{+}:CdSe and Cu^{2+}:CdSe NCs that should make these two oxidation states readily distinguishable spectroscopically. Specifically, the calculations indicate that Cu^{2+}-doped NCs should display a broad distribution of mid-gap valence-band-to-copper charge-transfer ($L_{VB}MCT$) and ligand-field (*d*−*d*) excitations that extend from the CdSe absorption edge throughout the visible, all the way into the near-infrared. Rapid internal conversion within this manifold is therefore expected to preclude visible PL from Cu^{2+}-doped NCs. Instead, the calculations provide strong support for assignment of the experimental PL and sub-bandgap absorption to an $ML_{CB}CT$ excited state of Cu^{+}-doped NCs, describing well several key experimental observables including the large PL Stokes shift, the broad PL bandshape, and the sign and magnitude of the excited-state singlet−triplet energy splitting. These calculations indicate that the large PL Stokes shift and broad PL bandshape are both predominantly due to strong vibronic coupling in the $ML_{CB}CT$ excited state. The geometry of the copper ion in the luminescent $ML_{CB}CT$ excited state is distorted along totally symmetric and Jahn−Teller coordinates relative to the ground state, both distortions ultimately arising from extensive hole localization at the copper in this excited state. The extent of excited-state hole localization is analyzed computationally and compared with experimental estimates. These results clarify the electronic structure origins of key physical properties that make copper-doped semiconductor nanocrystals attractive as phosphors in lighting and solar energy technologies.

2.3 Computational Methods

DFT calculations were performed with Gaussian 09.[25] All calculations were performed with the PBE0 hybrid DFT functional.[26-27] The Los Alamos double-zeta pseudo-core potential and associated basis set were used for all atoms, with the Cd(4*d*, 5*s*, 5*p*), Cu(3*d*, 4*s*, 4*p*), and Se(4*s*, 4*p*) atomic orbitals described with explicit basis functions.[28-29] This method has been shown to accurately describe the electronic structures of doped ZnO, CdSe, and CdS NCs.[30-34] Fractional atomic-orbital contributions to specific molecular orbitals (MOs) of the ground-state DOS calculations are described in the text as % atomic orbital character. The full compositions of these orbitals are provided in Appendix A. . Excited states were calculated with linear-response time-dependent DFT (TD-DFT). Absorption spectra were obtained by dressing the excited-state peaks from TD-DFT calculations with Gaussian bandshape functions of arbitrary width ($\sigma = 0.3$ eV) for illustrative purposes. Natural transition orbital (NTO) analysis based on the calculated transition densities between the ground and excited states was used to visualize the excited-state electron and hole wavefunctions.[35] This approach represents the electronic transitions in terms of an expansion into single-particle orbitals (electron and hole) by diagonalizing the transition density matrix for each excitation. All NTOs and ground-state (MOs) shown here were produced with an isosurface value of 0.008.

Approximately spherical CdSe NCs ($Cd_{33}CuSe_{34}$, $d \sim 1.6$ nm; and $Cd_{76}CuSe_{77}$, $d \sim 2.1$ nm) were constructed using the bulk CdSe zinc-blende crystal structure with lattice parameter $a = 0.608$ nm.[36] Uncompensated surface Cd^{2+} and Se^{2-} ions (dangling bonds) were passivated with pseudo-hydrogen atoms with fractional charges.[30,37-38] For Cu^{2+}-doped NCs, the pseudo-hydrogen atoms passivating Cd^{2+} and Se^{2-} had nuclear charges of 1.5 and 0.5, respectively. For Cu^{+}-doped NCs, the core NC was given a charge of −1 and the total nuclear charge of the pseudo-hydrogen atoms

was increased by +1 so that the entire system remained neutral, *i.e.*, the compensating charge is distributed over the entire surface. This mean-field approach simulates charge compensation of an aliovalent dopant at the NC surface (experimentally, *via* charged ligands or surface non-stoichiometries) and accounts for dynamical fluctuations of the surfaces, *e.g.*, from ligand surface-binding equilibria or surface dipoles. We previously showed that the difference between localized and distributed countercharges in the optical spectroscopy of Al^{3+}:ZnO NCs is negligible,[34] and essentially indistinguishable results are also obtained here when no charge compensation is used. For all calculations except the site dependence of the singlet-triplet splitting, the copper dopant was substituted for a Cd^{2+} ion closest to the center of the NC. All NC structures were optimized in the ground state before other electronic structure or excited-state calculations were performed. Fully converged optimized structures could not be obtained in most cases (see Appendix A.), but increasing the precision of the optimization had little impact on the energy or geometry, indicating that the reported values are very close to the actual minima.

2.4 Results and Analysis

2.4.1 General considerations: Charge compensation and ground-state geometry.

The dominant "green" PL of bulk Cu^{+}:ZnS has been shown to involve substitutional Cu^{+} residing at a tetrahedral cation site of the host lattice.[12,39] Although substitution of Cu^{+} for a divalent II−VI host cation (Zn^{2+} or Cd^{2+}) requires charge compensation, these Cu^{+} ions possess no adjacent charge-compensating defects, and their charges are compensated remotely. Extended x-ray absorption fine structure (EXAFS) studies indicate that Cu^{+} impurities also substitute for host cations in II−VI semiconductor NCs.[18,20] In NCs, remote charge compensation is even more facile than in bulk because of the nearby NC surfaces. Experimentally, large amounts of excess charge from aliovalent dopants can be effectively compensated by surface non-stoichiometries and

charged surface ligands,[40] and similarly, the charges of multiple excess electrons within NCs can be compensated by bulky molecular counter ions outside the NCs.[41] This type of remote (surface) charge compensation is energetically more favorable than creation of high-energy internal lattice defects such as anion vacancies. With these considerations in mind, the calculations presented here on Cu^{+}-doped CdSe NCs have been performed on NCs possessing substitutional Cu^{+} dopants with no other lattice defects, analogous to the center responsible for the "green" copper-based luminescence in bulk copper-doped ZnS phosphors.[12,39] Charged pseudo-hydrogen capping ligands are then used to maintain overall NC charge neutrality. For Cu^{2+}-doped CdSe NCs, the substitution is isovalent and no additional charge compensation is needed.

Optimization of the ground-state structures of copper-doped $Cd_{33}Se_{34}$ NCs yields significant lattice distortions around the copper impurities, as expected from EXAFS studies of bulk and nanocrystalline Cu^{+}:ZnSe.[19-20,42] For Cu^{+} dopants, these ground-state distortions involve contraction of all four Cu^{+}-Se^{2-} bonds to accommodate the smaller ionic radius of Cu^{+}, but the tetrahedral cation site symmetry is maintained (see Appendix A.). This site symmetry can be broken by proximity to the NC surface, independent of the copper. For Cu^{2+} dopants, the optimized structures of ground-state Cu^{2+}:$Cd_{33}Se_{34}$ NCs also show contraction around copper, but additionally show distortion along a symmetry-breaking coordinate of approximately T_2 (T_d notation) symmetry, attributed to Jahn–Teller electron–nuclear coupling within the $Cu^{2+}(d^9)$ ground state (see Appendix A.).

2.4.2 **Orbital energies in Cu^{2+}:CdSe and Cu^{+}:CdSe nanocrystals.**

Figure 2.1 summarizes the calculated orbital energies for a series of undoped, Cu^{2+}-doped, and Cu^{+}-doped CdSe NCs ($Cd_{34}Se_{34}$, Cu^{2+}:$Cd_{33}Se_{34}$, and Cu^{+}:$Cd_{33}Se_{34}$), and broadened density-of-states plots are provided in Appendix A. . Figure 2.1a plots the results for the undoped $Cd_{34}Se_{34}$

NC. As expected, this NC shows a filled valence band (VB) and an empty conduction band (CB). The highest occupied molecular orbital (HOMO) is the $1S_h$ orbital at the VB edge and the lowest unoccupied molecular orbital (LUMO) is the $1S_e$ orbital at the CB edge; both of these orbitals are delocalized over the entire NC. Figure 2.1b plots the orbital energies of the Cu^{2+}:$Cd_{33}Se_{34}$ NC. Because this NC has an open-shell configuration, α and β spin orbitals are shown separately. As in the undoped CdSe NC, the HOMO resides at the upper edge of the VB, and a relatively unperturbed $1S_e$ orbital is also identifiable at the CB edge. The HOMO appears more localized than that of the undoped CdSe NC, due to the small but significant (~7%) Cu(3*d*) contribution at the VB edge. Of the ten α and β orbitals with dominant Cu(3*d*) character, nine are occupied and reside deep within the VB. The one unoccupied Cu(3*d*)-based orbital is the LUMO, having β spin and residing within the band gap and nearer to the VB edge. The LUMO is clearly localized around the Cu^{2+} dopant and has ~40% Cu(3*d*) character. Similarly high covalencies are observed in Cu^{2+} selenolates and related compounds.[43] Lastly, Figure 2.1c plots the calculated orbital energies for the Cu^{+}:$Cd_{33}Se_{34}$ NC. This NC has a closed-shell configuration, and each orbital in Figure 2.1c thus represents both α and β spins. Five doubly occupied orbitals with significant Cu(3*d*) character are located just above the VB edge, including the HOMO. These are clearly split by the tetrahedral ligand field into t_2 and *e* subsets, with the t_2 set ~0.6 eV above the *e* set, and the orbitals within these subsets are also not exactly degenerate due to ground-state symmetry breaking by the NC surfaces. The HOMO is again localized around the copper dopant and is highly covalent, with ~50% Cu(3*d*) character. The LUMO in this NC is the $1S_e$ orbital at the CdSe CB edge, which resembles the $1S_e$ orbital in the undoped CdSe NC but with a slight perturbation from the Cu^{+} in the lattice. Both copper-doped NCs thus have a filled VB, an empty CB, and copper-based mid-gap orbitals.

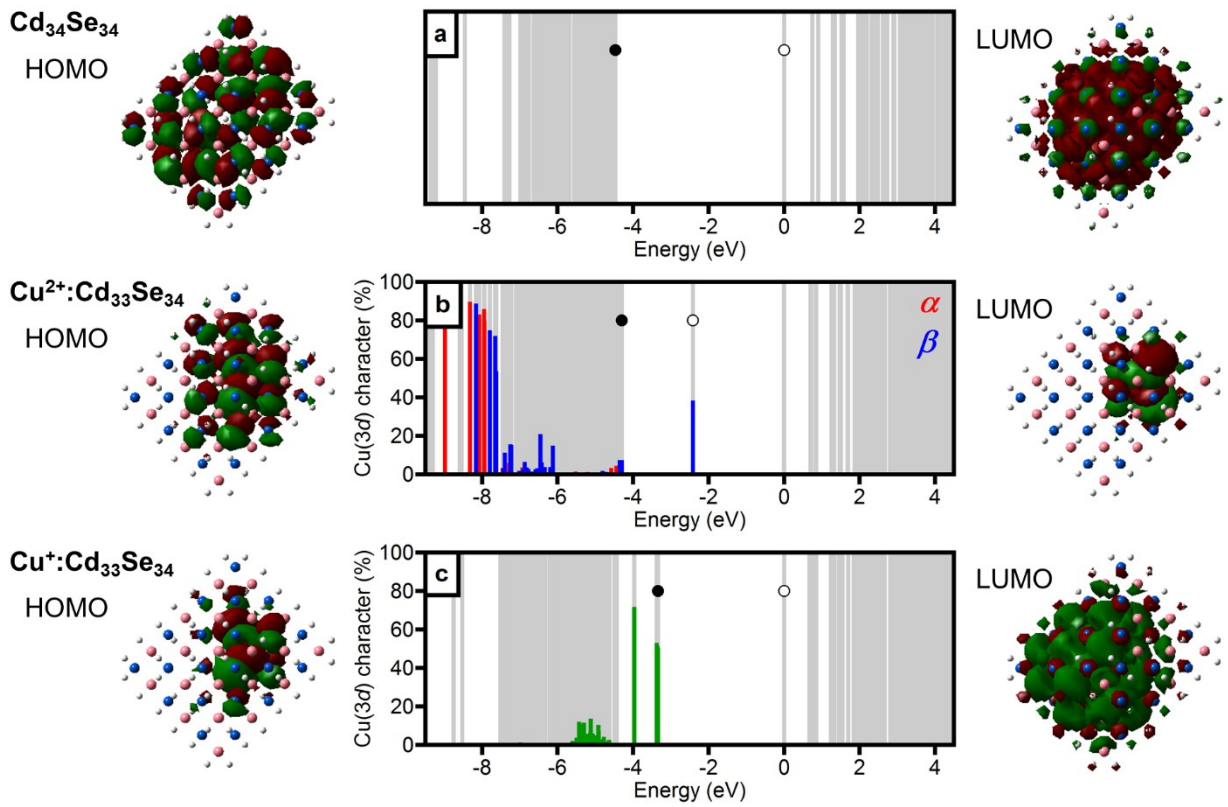

Figure 2.1. Calculated HOMO and LUMO surfaces and molecular-orbital energies for undoped, Cu^{2+}-doped, and Cu^{+}-doped NCs. The Cu(3*d*) atomic orbital contributions are highlighted in color and the HOMO and LUMO energies are indicated by closed and open circles, respectively. **(a)** Molecular-orbital energies of an undoped $Cd_{34}Se_{34}$ NC, showing the fully occupied VB and unoccupied CB. Both the HOMO and LUMO are delocalized over the entire NC. **(b)** Molecular-orbital energies of a Cu^{2+}: $Cd_{33}Se_{34}$ NC. The Cu(3*d*) character is highlighted in red for the α spin orbitals and blue for the β spin orbitals. The HOMO is VB-like, although some hybridization with the Cu(3*d*) orbitals at the VB edge makes it more localized than the HOMO of the undoped NC. The LUMO has substantial Cu(3*d*) character and is clearly localized around the Cu^{2+} dopant. The other orbitals with significant Cu(3*d*) contributions are all occupied and deep inside the VB. **(c)** Molecular-orbital energies of a Cu^{+}:$Cd_{33}Se_{34}$ NC. The Cu(3*d*) character is highlighted in green. The HOMO has significant Cu(3*d*) character and is localized around the Cu^{+} dopant, while the LUMO is delocalized.

2.4.3 Electronic absorption spectra of Cu^{+}:CdSe and Cu^{2+}:CdSe nanocrystals.

Figure 2.2 shows electronic absorption spectra calculated by TD-DFT for the same undoped, Cu^{2+}-doped, and Cu^{+}-doped CdSe NCs described in Figure 2.1. The undoped CdSe NC displays only excitonic absorption, which occurs above ~3.5 eV in these very small NCs. In contrast, both doped

NCs display mid-gap charge-transfer transitions involving copper. The calculated absorption spectrum of the Cu^{2+}-doped NC extends throughout the visible and into the near-infrared energy range, with some transitions occurring as low as <1 eV. These mid-gap transitions primarily involve promotion of electrons from the VB to the unoccupied Cu(3*d*) (LUMO) orbital, *i.e.*, they are valence-band-to-metal charge-transfer (L_{VB}MCT) transitions. Because of the high density of states in the VB, many L_{VB}MCT transitions are observed over a broad range of energies (Figure 2.2, inset) and no distinct features are predicted in the calculated absorption spectrum. Some mid-gap transitions have substantial *d*–*d* character, as anticipated for Cu^{2+}, but assignment of specific *d*–*d* transition energies from these results is complicated by the high covalencies and the presence of overlapping L_{VB}MCT transitions. Finally, the spectrum of the Cu^{2+}-doped CdSe NCs above ~3.5 eV is dominated by inter-band transitions, although L_{VB}MCT transitions originating from deep VB orbitals also still occur in this energy range. The distinct characteristic of the calculated Cu^{2+}-doped CdSe NC absorption spectrum is thus the continuous tailing mid-gap absorption throughout the visible spectral window. This result is consistent with the experimental observation of similarly broad VB $\rightarrow$ Cu^{2+} charge-transfer absorbance from the UV down to the near-infrared for photogenerated Cu^{2+} in bulk ZnS.[12] Because of the shallower valence-band-edge potential of CdSe relative to ZnS, the L_{VB}MCT transitions should extend to even lower energy in the former. The anticipated *d*–*d* transitions have also been identified in bulk II-VI semiconductors containing Cu^{2+}, for example by absorption,[12] luminescence,[44] and photoluminescence excitation (PLE)[45] spectroscopies, but they have not been reported for any copper-doped NCs. Experimentally, no L_{VB}MCT or *d*–*d* transitions could be detected by near-infrared magnetic circular dichroism (MCD) spectroscopy of copper-doped CdSe or InP NCs,[10] and sub-bandgap Cu^{2+} MCD intensity is also not observed in NCs described as containing Cu^{2+}.[16-17] In bulk Cu^{2+}:CdS and Cu^{2+}:ZnS, the ligand-

field excited states of ^{2}E parentage reside ~0.8 eV above the ground state (~1550 nm),[12,44-46] making them the lowest-energy excited states of these Cu^{2+}-doped materials. The continuous density of mid-gap states calculated in Figure 2.2, extending all the way down to the near-IR, is consistent with the experimental observation that mid-gap L_{VB}MCT photoexcitation of Cu^{2+}-doped II−VI semiconductors yields efficient nonradiative internal conversion to populate the lowest component of the ^{2}E ligand-field excited state, as illustrated by the $^2E \rightarrow {}^2T_2$ PLE spectra of bulk Cu^{2+}-doped ZnS and CdS crystals.[45] The proposal[7-8,16] of strong excitonic PL with nanosecond decay times arising from Cu^{2+}-doped II−VI semiconductor NCs is inconsistent with this electronic structure.

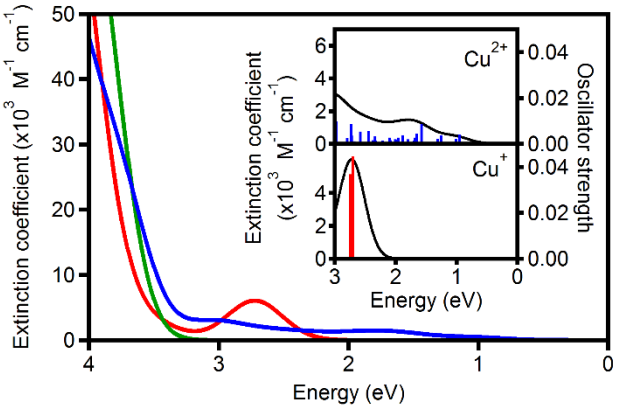

Figure 2.2. Calculated absorption spectra of undoped, Cu^{2+}-doped, and Cu^+-doped NCs. Absorption spectra are shown in green for undoped $Cd_{34}Se_{34}$, blue for Cu^{2+}:$Cd_{33}Se_{34}$, and red for Cu^+:$Cd_{33}Se_{34}$. **Inset:** Sub-bandgap energy range of the calculated absorption spectra for Cu^{2+}:$Cd_{33}Se_{34}$ (blue) and Cu^+:$Cd_{33}Se_{34}$ (red) NCs, showing oscillator strengths of the individual transitions. An arbitrary and universal Gaussian broadening factor of $\sigma = 0.3$ eV has been used to generate the spectra, which are presented for illustrative purposes.

The calculated (TD-DFT) absorption spectrum of the Cu^+-doped NC also shows mid-gap absorption, but in this case it arises from $ML_{CB}CT$ transitions. A mid-gap absorption band centered at ~2.7 eV is observed in the calculated spectrum (Figure 2.2), stemming from promotion of a $Cu^+(t_2)$ (HOMO) electron into the CdSe $1S_e$ orbital at the CB edge. Additionally, mid-gap

absorption is also evident that involves excitation of deeper $Cu^+(e)$ electrons to the same $1S_e$ orbital, as well as excitation from the $Cu^+(t_2)$ orbitals to higher CB orbitals (*e.g.*, $1P_e$). Again, the spectrum above ~3.5 eV is dominated by inter-band excitations of the CdSe itself, with smaller contributions from higher-energy $ML_{CB}CT$ transitions. There are, of course, no *d*–*d* transitions in the d^{10} configuration. These computed results are consistent with the experimental observation of an absorption "foot" just below the first band-to-band transitions in Cu^+:CdSe and related NCs.[10] As the lowest electronic excited state above the ground state, this $ML_{CB}CT$ excited state may relax to the ground state radiatively. The calculated electronic structure of Cu^+:CdSe NCs is therefore consistent with the experimental observation of slow (~400 ns at 300 K) visible PL from copper-doped NCs. Overall, this comparison shows that only the $Cu^+(d^{10})$ ground-state configuration is consistent with the experimental absorption, MCD, and PL spectroscopy of copper-doped semiconductor NCs.

2.4.4 The emissive $ML_{CB}CT$ excited states of Cu^+-doped CdSe nanocrystals.

We now examine the lowest-energy excited states of the Cu^+:CdSe NCs in more detail. In the $ML_{CB}CT$ excited state, a $Cu^+(3d^{10})$ electron is formally promoted into the CB. Ferromagnetic exchange coupling between the photogenerated d^9 copper ($S = 1/2$) and the CB electron ($S = 1/2$) generates singlet and triplet $ML_{CB}CT$ states ($^1ML_{CB}CT$ and $^3ML_{CB}CT$) split by an average of ~1 meV.[10] The formal oxidation of copper to d^9 in these $ML_{CB}CT$ excited states is expected to cause contraction of all four copper–anion bonds as well as distortion along one or more symmetry-breaking Jahn–Teller local coordinates. This excited-state nuclear reorganization defines the homogeneous PL bandshape and the PL Stokes shift. Figure 2.3a summarizes these two effects within the lowest $ML_{CB}CT$ manifold of a Cu^+:CdSe NC. The nuclear reorganization is discussed in more detail in 2.4.5 and the singlet-triplet splitting in 2.4.6.

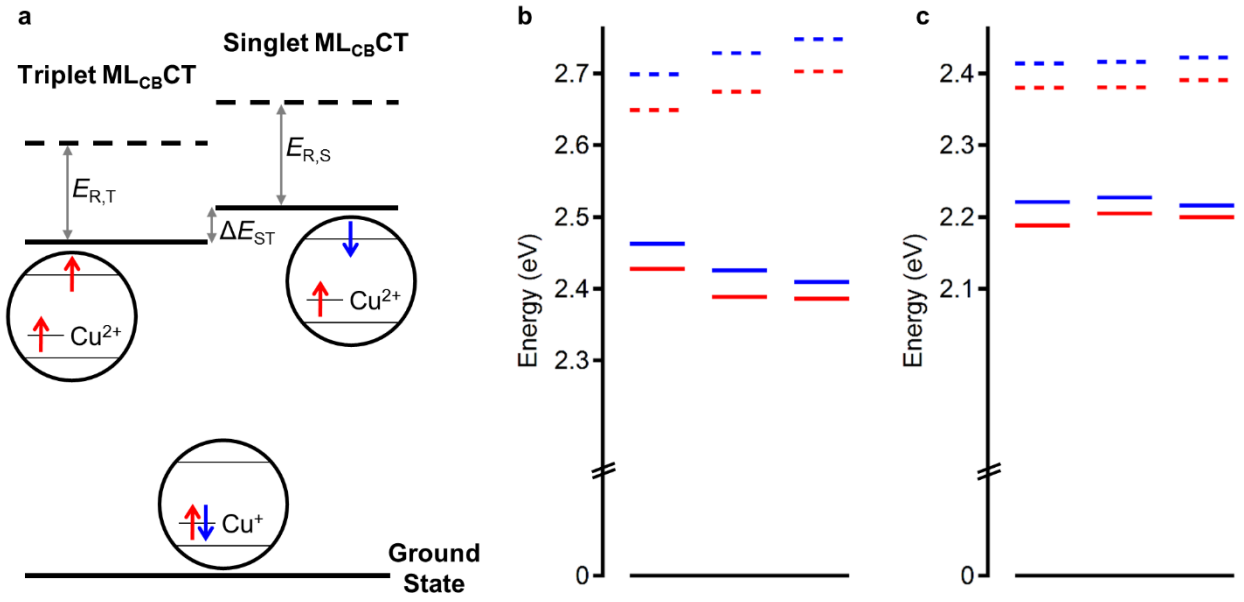

Figure 2.3. Energy levels of singlet and triplet excited states. (a) Qualitative energy levels of the lowest singlet and triplet $ML_{CB}CT$ excited states of a Cu^+:CdSe NC. The electron spin configurations for the ground state and each excited state are illustrated schematically, with only the highest-energy Cu(3*d*) orbital shown. Dashed lines represent the excited-state energies with the fixed ground-state geometry, while solid lines represent the excited-state energies after the excited-state geometry has been allowed to relax. The $^1ML_{CB}CT$ and $^3ML_{CB}CT$ nuclear reorganization energies and the singlet-triplet splitting energy are indicated. **(b)** Calculated energies of the six lowest-energy excited states of the Cu^+:$Cd_{33}Se_{34}$ NC with the Cu^+ positioned at the NC center. The dashed lines show the excited-state energies calculated with the fixed ground-state geometry. The solid lines show the excited-state energies after the excited-state geometry has been allowed to relax. $^3ML_{CB}CT$ states are shown in red and $^1ML_{CB}CT$ states in blue. **(c)** Calculated energies of the six lowest-energy excited states of the Cu^+:$Cd_{76}Se_{77}$ NC with the Cu^+ positioned at the NC center, with the same formatting as in panel (b).

Figure 2.3b shows the calculated energies of the six lowest-energy excited states of the Cu^+:$Cd_{33}Se_{34}$ NC with the Cu^+ located at the NC center. The three sets of excited states in this energy range roughly correspond to placing the copper-bound hole in each of the three Cu(3*d*) orbitals of the parent t_2 subset, while the electron occupies the CB $1S_e$ orbital. $T_2 \times T_2$ vibronic coupling yields four energy minima in the three-dimensional space of the T_2 nuclear coordinate.[47] The observation of three minima here is interpreted as a manifestation of low-symmetry effects. In tetrahedral point symmetry, the t_2 orbitals are degenerate in the Cu^+ ground state, but this

degeneracy is broken in these small NCs because of proximity to the NC surfaces. As a result, three singlet−triplet pairs of $ML_{CB}CT$ excited states are calculated with similar but not identical energies. When combined with strong electron−nuclear coupling, this remote symmetry reduction also favors a static Jahn−Teller distortion. For each singlet−triplet pair, the $^3ML_{CB}CT$ state is lower in energy than the $^1ML_{CB}CT$ state before geometry relaxation. All $ML_{CB}CT$ states are predicted to display similarly large nuclear reorganization energies (average $E_R \sim 280$ meV), computed by comparing the excited state's energy at the ground-state geometry with that obtained after geometry optimization. The singlet and triplet components of each pair also show similar reorganization energies, making the triplets lower in energy than the singlets after geometry relaxation as well.

Figure 2.3c plots the results of parallel calculations performed on the larger Cu^+:$Cd_{76}Se_{77}$ NCs. With addition of just ~1 CdSe monolayer to the Cu^+:$Cd_{33}Se_{34}$ NCs, the effects of symmetry breaking in the ground state due to the surfaces are now much weaker, and the three singlet-triplet pairs of $ML_{CB}CT$ excited states are all very close in energy to one another. For even larger NCs such as those studied experimentally, symmetry breaking by the surfaces should thus be negligible for Cu^+ dopants located within the NC internal volume, but it could still be evident for dopants located within one or two monolayers of a surface. The calculations therefore suggest that symmetry breaking by nearby NC surfaces is a likely source of inhomogeneous broadening of the experimental $ML_{CB}CT$ absorption and PL bands. The calculated reorganization energies in the larger NC (average $E_R \sim 190$ meV) are also smaller than those of the smaller NC (~280 meV), suggesting that proximity of the NC surface enables more substantial excited-state nuclear reorganization around copper, *i.e.*, the NCs are more deformable near their surfaces than in their cores. These reorganization energies correspond to Stokes shifts of 0.38 eV for the larger NC and

0.56 eV for the smaller NC, consistent with the experimental estimate of ~0.5 eV in Cu^+:CdSe and related Cu^+-doped NCs.[10]

It is interesting to consider the extent of hole localization in the $ML_{CB}CT$ excited state. Figure 2.4 presents the natural transition orbitals (NTOs) of the photogenerated electron and hole, calculated for the lowest-energy $^3ML_{CB}CT$ excited state of the Cu^+:$Cd_{76}Se_{77}$ NC after excited-state geometry relaxation. The other related singlet and triplet $ML_{CB}CT$ excited states give similar results. From these NTOs, the photoexcited electron is delocalized throughout the entire NC volume, but the photogenerated hole is contracted about the Cu^+ dopant, making the dopant Cu^{2+}-like in the $ML_{CB}CT$ excited state. Quantitatively, the orbital occupied by the hole has 46% Cu(3*d*) character, the rest being delocalized onto the neighboring Se^{2-} and even Cd^{2+} sites. This distribution is very similar to the one calculated for the ground-state LUMO of Cu^{2+}:$Cd_{33}Se_{34}$ (~40% Cu(3*d*), Figure 2.1b), reinforcing the description of copper in the $ML_{CB}CT$ excited state as Cu^{2+}-like.

$$r_B = \frac{\hbar}{\sqrt{2m^* E_b}} \tag{2.1}$$

Hole binding energies were estimated computationally as the difference between the calculated energies of the first excitonic state (in which the hole is delocalized in the valence band) and the relaxed $ML_{CB}CT$ excited state (in which the hole is bound by the copper). For the Cu^+:$Cd_{33}Se_{34}$ NC, the hole binding energy is calculated as $E_b \sim 1.4$ eV, yielding $r_B \sim 0.25$ nm from 2.1. This value of r_B is similar to the Cu–Se bond length, and is much smaller than the NC radius ($r \sim 0.8$ nm). For the Cu^+:$Cd_{76}Se_{77}$ NC, the binding energy is calculated as $E_b \sim 1.2$ eV, which gives $r_B \sim 0.27$ nm, implying a slightly increased covalency in the larger NCs. These values are consistent with the hole localization displayed in Figure 2.4. Finally, from the experimental absorption and PL peak energies measured for Cu^+:CdSe NCs with $r = 1.6$ nm,[10] the hole binding energy is estimated as $E_b \sim 0.7$ eV, which gives $r_B \sim 0.35$ nm, again much smaller than the NC radius. The

trend of greater hole delocalization with increasing NC size is consistent with the expected increase in Se(4*p*) contribution to the empty Cu(3*d*)-centered MO as the VB energy moves closer. In all of these cases, however, the NTOs (Figure 2.4) and 2.1 illustrate that the photogenerated holes in the $ML_{CB}CT$ excited states of these Cu^+:CdSe NCs are highly contracted around the copper dopants.

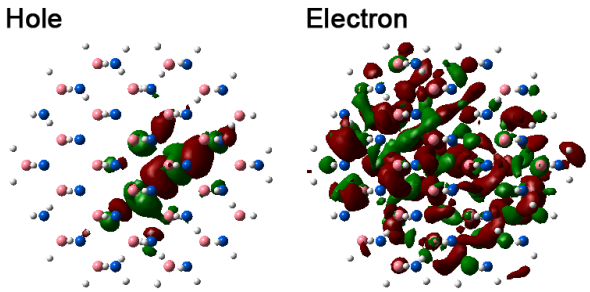

Figure 2.4. Natural transition orbitals. Electron and hole natural transition orbitals (NTOs) for the lowest-energy $^3ML_{CB}CT$ excited state of a Cu^+:$Cd_{76}Se_{77}$ NC. Cd^{2+} ions are illustrated in pink, Se^{2-} ions in blue, and capping pseudo-hydrogens in white.

2.4.5 Electron-nuclear coupling and the photoluminescence bandshape.

The large relaxation energies described by Figure 2.3 and the strong hole localization described by Figure 2.4 implicate large nuclear distortions around copper in the $ML_{CB}CT$ excited state, accompanied by correspondingly broad $ML_{CB}CT$ absorption and PL bands dominated by Franck−Condon progressions. Two kinds of nuclear distortions are expected here. First, hole trapping by the Cu^+ corresponds to a formal oxidation and should cause contraction of all copper−selenide bonds, *i.e.*, distortion along the totally symmetric breathing local coordinate. Second, the Cu^{2+}-like center of the $ML_{CB}CT$ excited state is unstable with respect to symmetry-breaking Jahn−Teller distortions. It is not clear *a priori* whether one of these two distortions dominates.

To analyze the $ML_{CB}CT$ excited-state nuclear distortion, Figure 2.5 plots the bond-length changes between the ground and relaxed $ML_{CB}CT$ excited states of the Cu^+:$Cd_{76}Se_{77}$ NC as a

function of the distance between each bond and the copper ion. Data are plotted for all six low-symmetry components of the relaxed $ML_{CB}CT$ state ($3\times[^1ML_{CB}CT] + 3\times[^3ML_{CB}CT]$). As anticipated from Figure 2.3 and Figure 2.4, the excited-state bond distortions are greatest around the copper and dissipate just a few bonds away. For all six $ML_{CB}CT$ excited states, the average Cu–Se bond length contracts, but these distortions are notably asymmetric, with some Cu–Se bonds showing a net elongation and others a net contraction. This asymmetry is a manifestation of the Jahn–Teller coupling. All other changes, for example the elongation of all Cd–Se bonds immediately surrounding the copper, are attributable primarily to relief of the strain induced by the Cu–Se localized distortions. The $ML_{CB}CT$ excited states of the Cu^+:$Cd_{33}Se_{34}$ NC show similar distortions. Moreover, the $ML_{CB}CT$ excited-state geometries of the Cu^+-doped NCs closely resemble the ground-state geometry of the Cu^{2+}:$Cd_{33}Se_{34}$ NC (see Appendix A.).

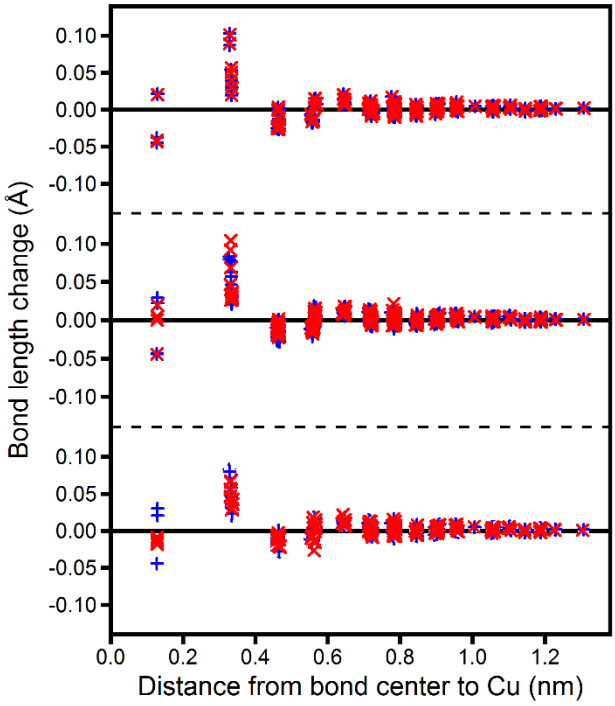

Figure 2.5. Excited-state bond length changes. Excited-state bond length changes for all Cu-Se and Cd-Se bonds in a Cu^+:$Cd_{76}Se_{77}$ NC, for the first three $^1ML_{CB}CT$ (blue + symbols) and first three $^3ML_{CB}CT$ (red × symbols) excited states. Each singlet–triplet pair is shown on a different y-axis.

More specifically, Figure 2.6 illustrates the principal distortions within the first coordination sphere around the copper ion in the lowest-energy $^1ML_{CB}CT$ excited state of the Cu^+:$Cd_{76}Se_{77}$ NC. To a good approximation, this distortion can be decomposed into a sum of a totally symmetric contraction with A_1 symmetry ($\Delta Q_{A1} = +0.020$ Å) and a Jahn-Teller distortion with T_2 symmetry ($\Delta Q_{T2} = +0.063$ Å), *i.e.*, Figure 2.6a + Figure 2.6b ≈ Figure 2.6c, with residual distortions due to other minor symmetry-allowed T_2 or E contributions. The other two lowest-energy $^1ML_{CB}CT$ states display similar distortions involving the other T_2 partner coordinates (see Appendix A.). E-symmetry Jahn−Teller distortions have also been identified in the *d*−*d* spectra of bulk Cu^{2+}-doped ZnS and CdS,[44-46] but the present calculations show relatively little if any distortion along this coordinate in the $ML_{CB}CT$ excited states of Cu^+-doped CdSe NCs. To estimate the relative contributions of the totally symmetric and T_2 Jahn−Teller distortions to the total excited-state nuclear reorganization energy, E_R, calculations were performed in which the local geometry was changed by either the A_1 or T_2 distortion of Figure 2.6a,b, the copper and nearest-neighbor Se^{2-} atom positions then frozen, and the rest of the structure allowed to relax. From these calculations, $E_{R,A1}/E_{R,T2} \sim 3$, which gives $E_{R,A1} \sim 0.156$ eV and $E_{R,T2} \sim 0.051$ eV (= E_{JT}). These reorganization energies account not just for the first-coordination-sphere distortions illustrated in Figure 2.6c, but also for the extended distortions described by Figure 2.5. Taking the energy of the A_1 vibration to be the CdSe LO phonon energy (26.0 meV)[51] and that of the T_2 vibration to be 24.3 meV based on the ratio of these two modes' energies in Cu^{2+}:ZnS,[44,46] these reorganization energies correspond to Huang−Rhys factors of $S_{A1} \sim 6.0$ and $S_{T2} \sim 2.3$ (from $E_R = Sv$). We note that the precise distribution of E_R over these nuclear coordinates may differ somewhat in real NCs that are much larger than the Cu^+:$Cd_{76}Se_{77}$ structure computed here. Nevertheless, this analysis

indicates strong electron–phonon coupling along both A_1 and T_2 (Jahn–Teller) coordinates in the luminescent $ML_{CB}CT$ excited states of Cu^+-doped NCs.

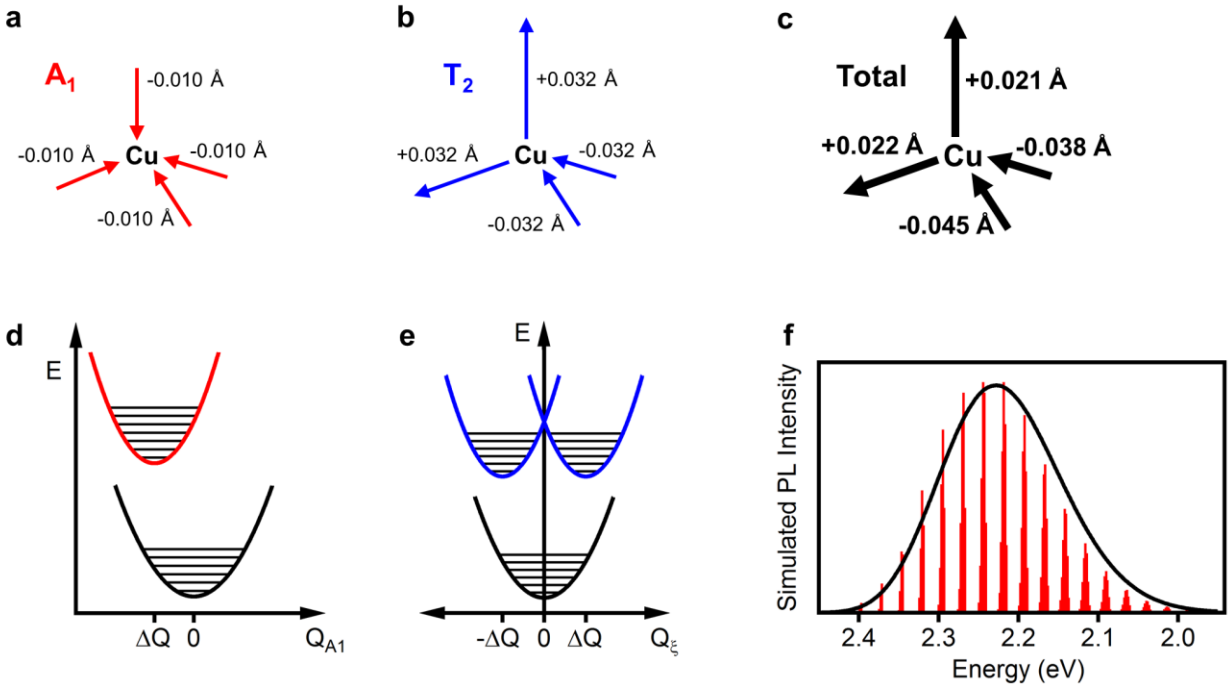

Figure 2.6. Excited-state distortions, single-configurational-coordinate diagrams, and simulated PL spectrum. (a-c) Calculated changes in Cu-Se bond lengths between the optimized ground-state geometry and optimized excited-state geometry of a Cu^+:$Cd_{76}Se_{77}$ NC for the lowest-energy $^1ML_{CB}CT$ excited state. The computed overall distortion shown in (c) is closely approximated by the sum of distortions along (a) totally symmetric and (b) T_2 Jahn–Teller nuclear coordinates (*i.e.*, a + b ≈ c). The residual distortions are small and attributable to other minor T_2- or E-symmetry contributions. **(d-e)** Potential-energy surfaces associated with the A_1 and T_2 $ML_{CB}CT$ excited-state distortion coordinates. Note that the actual three-dimensional $T_2 \times T_2$ vibronic sheet is not depicted, but instead is only represented schematically to illustrate the aspect of spontaneous symmetry breaking in the excited state by displacement along a T_2 partner coordinate ξ. **(f)** Simulated PL spectrum based on the folded A_1 and T_2 vibronic progressions resulting from the geometric distortions illustrated in (a-c) and including the extended lattice distortions, which correspond to Huang–Rhys parameters of $S_{A1} \sim 6.0$ and $S_{T2} \sim 2.3$. The smooth bandshape represents the sum of Gaussian-broadened ($\sigma = 24$ meV) vibronic transitions and simulates the experimental bandshape.

With this information, it is possible to simulate the $ML_{CB}CT$ PL bandshape predicted by these DFT calculations. Folding vibronic progressions along these two distortion coordinates

(Figure 2.6d,e) yields the simulated PL spectrum shown in Figure 2.6f. Introducing a small Gaussian line width of $\sigma = 24$ meV converts the resolved line spectrum into a smooth spectrum similar to the ones observed experimentally. This computed PL spectrum is characterized by a value of fwhm ~ 175 meV (at $T = 0$ K), which is in reasonable agreement with experimentally measured PL bandwidths for Cu^+:CdSe NCs (~370 meV for an ensemble of NCs at 15 K and ~350 meV for a single NC at 298 K).[10,22] These results demonstrate that the intrinsic $ML_{CB}CT$ PL bandshape of Cu^+-doped semiconductor NCs should be broad even without inhomogeneous contributions, because of the large nuclear reorganization associated with this electronic transition. The experimental bandshapes are also influenced by inhomogeneous contributions from NC size distributions, Cu^+ spatial distributions, and symmetry breaking by the NC surfaces as discussed above. Overall, this analysis indicates that the PL bandshapes of Cu^+-doped II−VI semiconductor NCs are intrinsically broad because of large excited-state Jahn−Teller and totally symmetric nuclear distortions around copper, both associated with hole localization at copper in the $ML_{CB}CT$ excited state. The same electron−nuclear coupling is responsible for the large Stokes shifts of the PL.

2.4.6 Singlet−triplet splittings in the $ML_{CB}CT$ excited state.

We now address another key experimental feature that characterizes the luminescence of copper-doped CdSe and related nanocrystals, namely the excited-state singlet−triplet splitting energy, ΔE_{ST}. Although the ground states of Cu^+-doped NCs are diamagnetic, photoexcitation transiently generates a CB electron and a localized Cu^{2+}-like spin, allowing the unique opportunity to study Cu^{2+}−e^-_{CB} magnetic exchange interactions in quantum-confined colloidal nanocrystals. The strength of the magnetic-exchange coupling between these two spins in the $ML_{CB}CT$ excited state, and hence the magnitude of ΔE_{ST}, depends on their spatial and energetic relationships. To describe

this exchange coupling, calculations were performed for copper ions at each symmetry-unique cation position of the Cu^+:$Cd_{33}Se_{34}$ NC, excluding surface cation sites. For uniformity, ΔE_{ST} was calculated by comparing the energies of each singlet−triplet pair of $ML_{CB}CT$ states in the geometry of the relaxed $^1ML_{CB}CT$ state. The resulting values are plotted in Figure 2.7 vs distance of the copper from the NC center. The results show that copper ions closer to the NC center yield greater values of ΔE_{ST}.

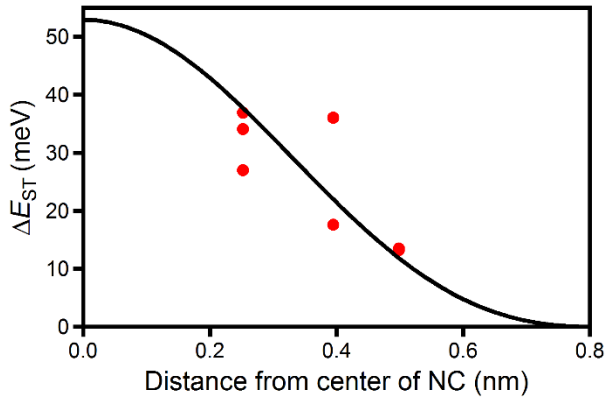

Figure 2.7. Dependence of singlet−triplet splitting on dopant location. Dependence of ΔE_{ST} on the distance between the Cu^+ dopant and the center of a Cu^+:$Cd_{33}Se_{34}$ NC. The red circles represent calculated values of ΔE_{ST} for the three lowest-energy $ML_{CB}CT$ excited states of Cu^+:$Cd_{33}Se_{34}$ NCs with the Cu^+ dopant located at different cation sites. The black line comes from fitting the computed data to a particle-in-a-spherical-well model (Eq. 2.2-2.3) and corresponds to $\Delta E_{ST}{}^{avg} = 9.0$ meV.

These results can be understood by describing the relationship between the photogenerated CB electron and the copper-bound hole analytically, approximating the quantum-confined CB electron using a particle-in-a-spherical-well model.[31,52-54] The electron density distribution is given by the square of a zeroth-order spherical Bessel function of the first kind (Eq. 2.2), where r is the distance from the center of the NC and a is the NC radius.

$$|\psi(r)|^2 = \frac{\sin^2\left(\frac{\pi r}{a}\right)}{2\pi a r^2} \qquad (2.2)$$

The singlet−triplet splitting for a copper ion located at distance r is then given by Eq. 2.3, in which n is the number of cations per NC, N_0 is the cation density (N_0 = 17.8 nm^{-3} for CdSe[36]), and ΔE_{ST}^{avg} is the average singlet-triplet splitting energy over all cation sites.

$$\Delta E_{ST}(r) = \frac{n\Delta E_{ST}^{avg}}{N_0} \cdot |\psi(r)|^2 \qquad (2.3)$$

Figure 2.7 shows the best fit of Eq. 2.3 to the DFT data for the Cu$^+$:$Cd_{33}Se_{34}$ NCs (d = 1.6 nm), which corresponds to ΔE_{ST}^{avg} = 9.0 meV. For the larger Cu$^+$:$Cd_{76}Se_{77}$ NCs (d = 2.1 nm), where the electron is more delocalized and the electron−hole overlap is smaller, a value of ΔE_{ST}^{avg} = 5.3 meV is estimated using Eq. 2.3 and the calculated ΔE_{ST} value for just the center-most copper site. A more reliable estimate of ΔE_{ST}^{avg} for the Cu$^+$:$Cd_{76}Se_{77}$ NCs, based on copper at more than one cation position, was hindered by the computational expense of excited-state geometry optimization for copper at each cation site. Experimentally, $\Delta E_{ST}^{avg} \sim$ 1 meV was estimated for d = 3.2 nm Cu$^+$:CdSe NCs from the temperature dependence of their PL lifetime and magnetic circularly polarized photoluminescence intensity.[10] The differences between these computed and experimental values are reasonable given the expected decrease in ΔE_{ST}^{avg} with increasing NC volume.

From these values, we can now estimate the mean-field s−d exchange constant $N_0\alpha$ that describes the Cu^{2+}−e^-_{CB} coupling interaction. ΔE_{ST}^{avg} is related to $N_0\alpha$ using Eq. 2.4, where $\langle S_z \rangle$ = 1/2 for the Cu^{2+} spin. Both the fitted computational value from Figure 2.7 (ΔE_{ST}^{avg} = 9.0 meV, n = 34) and the experimental value from ref. 10 ($\Delta E_{ST}^{avg} \sim$ 1 meV, $n \sim$ 300) correspond to $N_0\alpha \sim$ +0.6 eV. This value of $N_0\alpha$ is the same sign but between two and three times greater than the value of $N_0\alpha$ in Mn^{2+}-doped II−VI semiconductor NCs (*e.g.*, $N_0\alpha$ = +0.26 eV in $Cd_{1-x}Mn_xSe$).[31]

$$N_0\alpha = \frac{n\Delta E_{ST}^{avg}}{\langle S_z \rangle} \tag{2.4}$$

From our previous work,[31,55] the magnitude of $N_0\alpha$ can be interpreted in terms of a kinetic $s-s$ exchange interaction involving electron delocalization from the CB into the spin-split empty 4*s* orbitals of the paramagnetic 3*d* transition-metal impurity, as described by the perturbation expression in Eq. 2.5.

$$N_0\alpha = 2J_{KE}^{ss} = \frac{V_{ss}^2}{(S_{TM}+1/2)}\frac{I_{intra}}{(E_{4s\uparrow}-E_{CB})(E_{4s\downarrow}-E_{CB})} \tag{2.5}$$

Here, V_{ss} is the kinetic $s-s$ transfer integral, which can be estimated using Harrison's tight-binding approach,[56] I_{intra} is the intra-ion exchange energy, S_{TM} is the spin of the transition-metal center, and the energy denominators represent the energies required to transfer the CB electron to the empty 4*s* orbital of the transition metal with the indicated spin. With all other factors equal, the difference between Mn^{2+} ($S = 5/2$) and Cu^{2+} ($S = 1/2$) spins alone would lead to the expectation of $N_0\alpha(Cu^{2+}) \sim 3\times[N_0\alpha(Mn^{2+})]$, which agrees reasonably well with the computed values of $N_0\alpha(Cu^{2+}) = +0.6$ eV and $N_0\alpha(Mn^{2+}) = +0.26$ eV. This agreement suggests that the primary difference between the $N_0\alpha$ values of Mn^{2+} and Cu^{2+} in CdSe is simply the number of unpaired spins. In general, the other parameters of Eq. 2.5 should not be equal for Mn^{2+} and Cu^{2+}, and additionally the role of spin–orbit coupling in Cu^{2+} is not accounted for in Eq. 2.5 or the DFT calculations. Copper's Jahn–Teller distortion (Figure 2.6) partially quenches its orbital angular momentum in the $ML_{CB}CT$ excited state, known as the Ham effect,[57] perhaps contributing to the good agreement between experimental and spin-only computational results. Overall, the computed singlet-triplet $ML_{CB}CT$ excited-state exchange energies agree well with experimental observations, both showing stabilization of the emissive $^3ML_{CB}CT$ excited state relative to the

corresponding $^1ML_{CB}CT$ excited state by an amount consistent with expectations from the bulk *s*−*d* exchange coupling energies of other transition-metal-doped II−VI semiconductors.

2.5 Conclusion

DFT calculations have been performed on copper-doped CdSe NCs and the results related to experimental observations and physical explanations. The calculated electronic structure of Cu^{2+}-doped NCs is found to be consistent with experimental observations for bulk Cu^{2+}-doped II−VI semiconductors but inconsistent with experimental observations for copper-doped II−VI and III−V semiconductor NCs. In contrast, the calculated electronic structure of Cu^{+}-doped semiconductor NCs is consistent with experimental observations for copper-doped semiconductor nanocrystals. These calculations support identification of the luminescent excited state of Cu^{+}-doped CdSe and related NCs as an $ML_{CB}CT$ state involving an electron delocalized in the NC CB and a hole that is strongly localized at the copper dopant. The broad PL bandshapes observed in copper-doped semiconductor NCs are shown to reflect strong vibronic coupling along totally symmetric (A_1) and Jahn−Teller (T_2) local vibrational coordinates of the copper dopant. The calculated singlet−triplet splittings in the $ML_{CB}CT$ excited state agree well with experimental values in both their sign and magnitude, and can be understood using a perturbation description of the *s*−*d* exchange interaction in this excited state. Because the experimental spectroscopic properties of different copper-doped II−VI and III−V semiconductor NCs, as well as copper-based I−III−VI_2 semiconductor NCs, are mostly very similar to one another,[10,17] the conclusions drawn from these computations are likely to apply to luminescent copper-doped NCs as a class. These results improve our understanding of the electronic structures and physical properties of copper-doped semiconductor NC phosphors relevant to spectral conversion and imaging technologies.

2.6 Acknowledgments

The authors thank Dr. Kathryn E. Knowles for valuable discussions and Patrick J. Lestrange for technical assistance. Financial support from the National Science Foundation (Graduate Research Fellowship DGE-1256082 to H.D.N., CHE-1265945 to X.L., and DMR-1505901 to D.R.G.) is gratefully acknowledged. This work was facilitated through the use of advanced computational, storage, and networking infrastructure provided by the Hyak Supercomputer System at the University of Washington, funded by the UW Student Technology Fee.

2.7 Supporting Information

Appendix A. : Additional computational details, atomic orbital contributions to select copper-based molecular orbitals, densities of states and geometries for undoped, Cu^{2+}-doped, and Cu^{+}-doped NCs; comparisons of bond lengths in undoped and Cu^{+}-doped NCs, excited-state bond-length changes in Cu^{+}:$Cd_{33}Se_{34}$ NCs, geometries and energies of additional excited states.

2.8 References

1. Suyver, J. F.; van der Beek, T.; Wuister, S. F.; Kelly, J. J.; Meijerink, A. Luminescence of Nanocrystalline ZnSe:Cu. *Appl. Phys. Lett.* **2001**, *79*, 4222-4224.
2. Ishizumi, A.; White, C. W.; Kanemitsu, Y. Photoluminescence Properties of Impurity-Doped ZnS Nanocrystals Fabricated by Sequential Ion Implantation. *Physica E* **2005**, *26*, 24-27.
3. Pradhan, N.; Goorskey, D.; Thessing, J.; Peng, X. An Alternative of CdSe Nanocrystal Emitters: Pure and Tunable Impurity Emissions in ZnSe Nanocrystals. *J. Am. Chem. Soc.* **2005**, *127*, 17586-17587.
4. Corrado, C.; Jiang, Y.; Oba, F.; Kozina, M.; Bridges, F.; Zhang, J. Z. Synthesis, Structural, and Optical Properties of Stable ZnS:Cu,Cl Nanocrystals. *J. Phys. Chem. A* **2009**, *113*, 3830-3839.
5. Xie, R.; Peng, X. Synthesis of Cu-Doped InP Nanocrystals (d-dots) with ZnSe Diffusion Barrier as Efficient and Color-Tunable NIR Emitters. *J. Am. Chem. Soc.* **2009**, *131*, 10645-10651.
6. Sarkar, S.; Karan, N. S.; Pradhan, N. Ultrasmall Color-Tunable Copper-Doped Ternary Semiconductor Nanocrystal Emitters. *Angew. Chem., Int. Ed.* **2011**, *50*, 6065-6069.

7. Viswanatha, R.; Brovelli, S.; Pandey, A.; Crooker, S. A.; Klimov, V. I. Copper-Doped Inverted Core/Shell Nanocrystals with "Permanent" Optically Active Holes. *Nano Lett.* **2011**, *11*, 4753-4758.

8. Grandhi, G. K.; Tomar, R.; Viswanatha, R. Study of Surface and Bulk Electronic Structure of II-VI Semiconductor Nanocrystals Using Cu as a Nanosensor. *ACS Nano* **2012**, *6*, 9751-9763.

9. Srivastava, B. B.; Jana, S.; Pradhan, N. Doping Cu in Semiconductor Nanocrystals: Some Old and Some New Physical Insights. *J. Am. Chem. Soc.* **2010**, *133*, 1007-1015.

10. Knowles, K. E.; Nelson, H. D.; Kilburn, T. B.; Gamelin, D. R. Singlet-Triplet Splittings in the Luminescent Excited States of Colloidal Cu^+:CdSe, Cu^+:InP, and $CuInS_2$ Nanocrystals: Charge-Transfer Configurations and Self-Trapped Excitons. *J. Am. Chem. Soc.* **2015**, *137*, 13138–13147.

11. *Fundamentals of Phosphors*, ed.; Yen, W. M.; Shionoya, S.; Yamamoto, H., Eds.; CRC Press: Boca Raton, 2007.

12. Suzuki, A.; Shionoya, S. Mechanism of the Green-Copper Luminescence in ZnS Crystals. I. Direct Evidence for the Pair Emission Mechanism. *J. Phys. Soc. Jpn.* **1971**, *31*, 1455-1461.

13. Stouwdam, J. W.; Janssen, R. A. J. Electroluminescent Cu-doped CdS Quantum Dots. *Adv. Mater.* **2009**, *21*, 2916-2920.

14. Bhaumik, S.; Ghosh, B.; Pal, A. J. Color Tunable Light-Emitting Diodes Based On Copper Doped Semiconducting Nanocrystals. *Appl. Phys. Lett.* **2011**, *99*, 083106.

15. Bradshaw, L. R.; Knowles, K. E.; McDowall, S.; Gamelin, D. R. Nanocrystals for Luminescent Solar Concentrators. *Nano Lett.* **2015**, *15*, 1315-1323.

16. Pandey, A.; Brovelli, S.; Viswanatha, R.; Li, L.; Pietryga, J. M.; Klimov, V. I.; Crooker, S. A. Long-Lived Photoinduced Magnetization in Copper-Doped ZnSe–CdSe Core–Shell Nanocrystals. *Nat. Nanotechnol.* **2012**, *7*, 792-797.

17. Rice, W. D.; McDaniel, H.; Klimov, V. I.; Crooker, S. A. Magneto-Optical Properties of $CuInS_2$ Nanocrystals. *J Phys. Chem. Lett.* **2014**, *5*, 4105-4109.

18. Meulenberg, R. W.; van Buuren, T.; Hanif, K. M.; Willey, T. M.; Strouse, G. F.; Terminello, L. J. Structure and Composition of Cu-Doped CdSe Nanocrystals Using Soft X-ray Absorption Spectroscopy. *Nano Lett.* **2004**, *4*, 2277-2285.

19. Gul, S.; Cooper, J. K.; Glans, P.-A.; Guo, J.; Yachandra, V. K.; Yano, J.; Zhang, J. Z. Effect of Al^{3+} Co-doping on the Dopant Local Structure, Optical Properties, and Exciton Dynamics in Cu^+-Doped ZnSe Nanocrystals. *ACS Nano* **2013**, *7*, 8680-8692.

20. Car, B.; Medling, S.; Corrado, C.; Bridges, F.; Zhang, J. Z. Probing the Local Structure of Dilute Cu Dopants in Fluorescent ZnS Nanocrystals Using EXAFS. *Nanoscale* **2011**, *3*, 4182-4189.

21. Ishizumi, A.; White, C. W.; Kanemitsu, Y. Space-Resolved Photoluminescence of ZnS:Cu,Al Nanocrystals Fabricated by Sequential Ion Implantation. *Appl. Phys. Lett.* **2004**, *84*, 2397-2399.

22. Whitham, P. J.; Knowles, K. E.; Reid, P. J.; Gamelin, D. R. Photoluminescence Blinking and Reversible Electron Trapping in Copper-Doped CdSe Nanocrystals. *Nano Lett*. **2015**, *15*, 4045-4051.

23. Brovelli, S.; Galland, C.; Viswanatha, R.; Klimov, V. I. Tuning Radiative Recombination in Cu-Doped Nanocrystals via Electrochemical Control of Surface Trapping. *Nano Lett*. **2012**, *12*, 4372-4379.

24. Cooper, J. K.; Gul, S.; Lindley, S. A.; Yano, J.; Zhang, J. Z. Tunable Photoluminescent Core/Shell Cu^{+}-Doped ZnSe/ZnS Quantum Dots Codoped with Al^{3+}, Ga^{3+}, or In^{3+}. *ACS Appl. Mater. Interfaces* **2015**, *7*, 10055-10066.

25. Frisch, M. J.; Trucks, G. W.; Schlegel, H. B.; Scuseria, G. E.; Robb, M. A.; Cheeseman, J. R.; Scalmani, G.; Barone, V.; Mennucci, B.; Petersson, G. A.; Nakatsuji, H.; Caricato, M.; Li, X.; Hratchian, H. P.; Izmaylov, A. F.; Bloino, J.; Zheng, G.; Sonnenberg, J. L.; Hada, M.; Ehara, M.; Toyota, K.; Fukuda, R.; Hasegawa, J.; Ishida, M.; Nakajima, T.; Honda, Y.; Kitao, O.; Nakai, H.; Vreven, T.; Montgomery Jr., J. A.; Peralta, J. E.; Ogliaro, F.; Bearpark, M. J.; Heyd, J.; Brothers, E. N.; Kudin, K. N.; Staroverov, V. N.; Kobayashi, R.; Normand, J.; Raghavachari, K.; Rendell, A. P.; Burant, J. C.; Iyengar, S. S.; Tomasi, J.; Cossi, M.; Rega, N.; Millam, N. J.; Klene, M.; Knox, J. E.; Cross, J. B.; Bakken, V.; Adamo, C.; Jaramillo, J.; Gomperts, R.; Stratmann, R. E.; Yazyev, O.; Austin, A. J.; Cammi, R.; Pomelli, C.; Ochterski, J. W.; Martin, R. L.; Morokuma, K.; Zakrzewski, V. G.; Voth, G. A.; Salvador, P.; Dannenberg, J. J.; Dapprich, S.; Daniels, A. D.; Farkas, Ö.; Foresman, J. B.; Ortiz, J. V.; Cioslowski, J.; Fox, D. J. *Gaussian 09*, Gaussian, Inc.: Wallingford, CT, USA, 2009.

26. Perdew, J. P.; Burke, K.; Ernzerhof, M. Generalized Gradient Approximation Made Simple. *Phys. Rev. Lett*. **1996**, *77*, 3865-3868.

27. Adamo, C.; Barone, V. Toward Reliable Density Functional Methods without Adjustable Parameters: The PBE0 Model. *J. Chem. Phys*. **1999**, *110*, 6158-6170.

28. Hay, P. J.; Wadt, W. R. Ab Initio Effective Core Potentials for Molecular Calculations. Potentials for the Transition Metal Atoms Sc to Hg. *J. Chem. Phys*. **1985**, *82*, 270-283.

29. Wadt, W. R.; Hay, P. J. Ab Initio Effective Core Potentials for Molecular Calculations. Potentials for Main Group Elements Na to Bi. *J. Chem. Phys*. **1985**, *82*, 284-298.

30. Badaeva, E.; Feng, Y.; Gamelin, D. R.; Li, X. Investigation of Pure and Co^{2+}-Doped ZnO Quantum Dot Electronic Structures Using the Density Functional Theory: Choosing the Right Functional. *New J. Phys*. **2008**, *10*, 055013.

31. Beaulac, R.; Feng, Y.; May, J. W.; Badaeva, E.; Gamelin, D. R.; Li, X. Orbital Pathways for Mn2+-Carrier sp-d Exchange in Diluted Magnetic Semiconductor Quantum Dots. *Phys. Rev. B* **2011**, *84*, 195324.

32. Badaeva, E.; Isborn, C. M.; Feng, Y.; Ochsenbein, S. T.; Gamelin, D. R.; Li, X. Theoretical Characterization of Electronic Transitions in Co^{2+}- and Mn^{2+}-Doped ZnO Nanocrystals. *J. Phys. Chem. C* **2009**, *113*, 8710-8717.

33. Peng, B.; Liang, W.; White, M. A.; Gamelin, D. R.; Li, X. Theoretical Evaluation of Spin-Dependent Auger De-Excitation in Mn^{2+}-Doped Semiconductor Nanocrystals. *J. Phys. Chem. C* **2012**, *116*, 11223-11231.

34. Goings, J. J.; Schimpf, A. M.; May, J. W.; Johns, R. W.; Gamelin, D. R.; Li., X. Theoretical Characterization of Conduction-Band Electrons in Photodoped and Aluminum-Doped Zinc Oxide (AZO) Quantum Dots. *J. Phys. Chem. C* **2014**, *118*, 26584−26590.

35. Martin, R. L. Natural Transition Orbitals. *J. Chem. Phys.* **2003**, *118*, 4775-4777.

36. Madelung, O. *Semiconductors: Data Handbook*, 3rd ed. ed.; Springer: Berlin, 2004.

37. Wang, L.-W.; Li, J. First-Principles Thousand-Atom Quantum Dot Calculations. *Phys. Rev. B* **2004**, *69*, 153302.

38. Huang, X.; Lindgren, E.; Chelikowsky, J. R. Surface Passivation Method for Semiconductor Nanostructures. *Phys. Rev. B* **2005**, *71*, 165328.

39. Suzuki, A.; Shionoya, S. Mechanism of the Green-Copper Luminescence in ZnS Crystals. II. Polarization Characteristics. *J. Phys. Soc. Jpn.* **1971**, *31*, 1462-1468.

40. Schimpf, A. M.; Ochsenbein, S. T.; Buonsanti, R.; Milliron, D. J.; Gamelin, D. R. Comparison of Extra Electrons in Colloidal n-Type Al^{3+}-doped and Photochemically Reduced ZnO Nanocrystals. *Chem. Commun.* **2012**, *48*, 9352−9354.

41. Valdez, C. N.; Braten, M.; Soria, A.; Gamelin, D. R.; Mayer, J. M. Effect of Protons on the Redox Chemistry of Colloidal Zinc Oxide Nanocrystals. *J. Am. Chem. Soc.* **2013**, *135*, 8492-8495.

42. Goldman, A. I.; Canova, E.; Kao, Y. H.; Fitzpatrick, B. J.; Bhargava, R. N.; Phillips, J. C. Extended X-ray Absorption Fine Structure Studies of Diffused Copper Impurities in ZnSe. *Appl. Phys. Lett.* **1983**, *43*, 836-838.

43. Sarangi, R.; Gorelsky, S. I.; Basumallick, L.; Hwang, H. J.; Pratt, R. C.; Stack, T. D. P.; Lu, Y.; Hodgson, K. O.; Hedman, B.; Solomon, E. I. Spectroscopic and Density Functional Theory Studies of the Blue−Copper Site in M121SeM and C112SeC Azurin: Cu−Se Versus Cu−S Bonding. *J. Am. Chem. Soc.* **2008**, *130*, 3866-3877.

44. Thurian, P.; Heitz, R.; Kaczmarczyk, G.; Hoffmann, A.; Broser, I.; Telahun, T.; Schrepel, C.; Goebel, C.; Scherz, U. Jahn-Teller Effect of Cu2+ in II–VI Compounds. *Z. Phys. Chem.* **1997**, *201*, 137-150.

45. Heitz, R.; Hoffmann, A.; Thurian, P.; Broser, I. The Copper Centre: A Transient Shallow Acceptor in ZnS and CdS. *J. Phys.: Condens. Matter* **1992**, *4*, 157-168.

46. Maier, H.; Scherz, U. Vibronic Spectra and the Dynamic Jahn-Teller Effect of Cubic $ZnS:Cu^{2+}$. *Phys. Status Solidi B* **1974**, *62*, 153-164.

47. Bersuker, I. B.; Polinger, V. Z. *Vibronic Interactions in Molecules and Crystals*; Springer: Berlin, 1989, 10.1007/978-3-642-83479-0.

48. Heitz, R.; Hoffmann, A.; Broser, I. Magneto-Optics of Ni-Bound Shallow States in ZnS and CdS. *Phys. Rev. B* **1993**, *48*, 8672-8682.

49. Fleurov, V. N.; Kikoin, K. A. Amphoteric Exciton Trapping by 3d-Impurities in A_2B_6 Semiconductors. *Solid State Commun.* **1982**, *42*, 353-357.

50. Kittilstved, K. R.; Liu, W. K.; Gamelin, D. R. Electronic Structure Origins of Polarity-Dependent High-T_C Ferromagnetism in Oxide-Diluted Magnetic Semiconductors. *Nat. Mater.* **2006**, *5*, 291-297.

51. Trallero-Giner, C.; Debernardi, A.; Cardona, M.; Menéndez-Proupín, E.; Ekimov, A. I. Optical Vibrons in CdSe Dots and Dispersion Relation of the Bulk Material. *Phys. Rev. B* **1998**, *57*, 4664-4669.

52. Bhattacharjee, A. K. Nanocrystals of Diluted Magnetic Semiconductors: Model for Magnetic Polaron. *Phys. Rev. B* **1995**, *51*, 9912-9916.

53. Bhattacharjee, A. K.; Benoit à la Guillaume, C. Exciton Magnetic Polaron in Semimagnetic Semiconductor Nanocrystals. *Phys. Rev. B* **1997**, *55*, 10613-10620.

54. Bhattacharjee, A. K. Confinement-Induced Reduction of the Effective Exchange Parameters in Semimagnetic Semiconductor Nanostructures. *Phys. Rev. B* **1998**, *58*, 15660-15665.

55. Beaulac, R.; Gamelin, D. R. Two-Center Formulation of Mn^{2+}-Electron s-d Exchange Coupling in Bulk and Quantum-Confined Diluted Magnetic Semiconductors. *Phys. Rev. B* **2010**, *82*, 224401.

56. Harrison, W. A. *Electronic Structure and the Properties of Solids*; Dover: New York, 1989.

57. Ham, F. S. Dynamical Jahn-Teller Effect in Paramagnetic Resonance Spectra: Orbital Reduction Factors and Partial Quenching of Spin-Orbit Interaction. *Phys. Rev.* **1965**, *138*, A1727-A1740.

Chapter 3. Mid-Gap States and Normal *vs* Inverted Bonding in Luminescent Cu^+- and Ag^+-Doped CdSe Nanocrystals

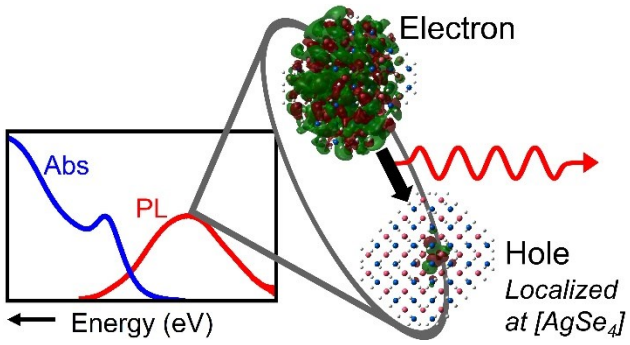

Reproduced with permission from Nelson, H. D.; Hinterding, S. O. M.; Fainblat, R.; Creutz, S. E.; Li, X.; Gamelin, D. R. *J. Am. Chem. Soc.* **2017**, *139*, 6411-6421. Copyright 2017 American Chemical Society.

3.1 **Overview**

Mid-gap luminescence in copper (Cu^+)-doped semiconductor nanocrystals (NCs) involves recombination of delocalized conduction-band electrons with copper-localized holes. Silver (Ag^+)-doped semiconductor NCs show similar mid-gap luminescence at slightly (~0.3 eV) higher energy, suggesting a similar luminescence mechanism, but this suggestion appears inconsistent with the large difference between Ag^+ and Cu^+ ionization energies (~1.5 eV), which should make hole trapping by Ag^+ highly unfavorable. Here, Ag^+-doped CdSe NCs (Ag^+:CdSe) are studied using time-resolved variable-temperature photoluminescence (PL) spectroscopy, magnetic circularly polarized luminescence (MCPL) spectroscopy, and time-dependent density functional theory (TD-DFT) to address this apparent paradox. In addition to confirming that Ag^+:CdSe and Cu^+:CdSe NCs display similar broad PL with large Stokes shifts, we demonstrate that both also show very similar temperature-dependent PL lifetimes and magneto-luminescence. Electronic-structure calculations further predict that both dopants generate similar localized mid-gap states. Despite

these strong similarities, we conclude that these materials possess significantly different electronic structures. Specifically, whereas photogenerated holes in Cu^+:CdSe NCs localize primarily in Cu(3*d*) orbitals, formally oxidizing Cu^+ to Cu^{2+}, in Ag^+:CdSe NCs they localize primarily in 4*p* orbitals of the four neighboring Se^{2-} ligands, and Ag^+ is not oxidized. This difference reflects a shift from "normal" to "inverted" bonding going from Cu^+ to Ag^+. The spectroscopic similarities are explained by the fact that, in both materials, photogenerated holes are localized primarily within covalent [MSe_4] dopant clusters (M = Ag^+, Cu^+). These findings reconcile the similar spectroscopies of Ag^+- and Cu^+-doped semiconductor NCs with the vastly different ionization potentials of their Ag^+ and Cu^+ dopants.

3.2 Introduction

Silver- and copper-doped semiconductors are technologically important phosphors that have been employed in cathode-ray tubes and other devices for many years.[1-3] Most common are Ag^+- and Cu^+-doped ZnS, which give rise to the well-known blue-silver ("B-Ag") and green-copper ("G-Cu") luminescence. The "B-Ag" and "G-Cu" luminescence features are both broad and red-shifted from the semiconductor band-to-band absorption edge, and both typically display very long decay times. The colors of these luminescence bands can be tuned across the visible by varying the compositions of the host lattices, an advantage for many applications. For a given host composition, however, the "B-Ag" luminescence is always ~0.3−0.5 eV higher in energy than the "G-Cu" luminescence.[2-4] The mechanisms of "B-Ag" and "G-Cu" photoluminescence (PL) have been thoroughly investigated: photogenerated valence-band (VB) holes generated by above-band-gap photoexcitation rapidly localize in deep acceptor states induced by Cu^+ or Ag^+ doping, and the electrons are loosely bound by charge-compensating codopants such as Al^{3+} or In^{3+}, forming shallow donors. "B-Ag" and "G-Cu" PL then results from recombination of the shallow-donor

electrons with the deeply bound holes, i.e., donor−acceptor pair (DAP) recombination.[2-3,5-7]

Recently, Ag^+- and Cu^+-doped II−VI, III−V, and related semiconductor nanocrystals (NCs) have also attracted broad interest.[8-17] The solution processability of these NCs offers new opportunities for imaging and spectral-conversion applications of these classic phosphor materials, for example for luminescent solar concentration.[18-19] Most authors agree that a mechanism analogous to the "G-Cu" PL also applies for Cu^+-doped semiconductor NCs.[17] Specifically, upon NC photoexcitation, the photogenerated hole is rapidly localized at the Cu^+ to make it formally Cu^{2+}-like. Luminescence then arises from radiative "free-to-bound"-type recombination of this deeply trapped hole with the delocalized photogenerated conduction-band (CB) electron. The luminescent excited state can thus be described as a Cu^+-to-CB charge-transfer ($ML_{CB}CT$) excited state of the Cu^+-doped NC.[17,20-21] In contrast, the PL of Ag^+-doped NCs has not been very extensively studied, but in many ways appears similar to that of Cu^+-doped NCs.[10,12-13] Ag^+- and Cu^+-doped NCs both display broad, composition-tunable PL with large effective Stokes shifts and slow (~100s of ns to μs) decay,[10,13-15,17] and for the same host NCs, the Ag^+-activated PL is again higher in energy than the Cu^+-activated PL.[13] Picosecond relaxation from the first excitonic state to the emissive state consistent with rapid hole localization has been observed in Ag^+:CdS NCs via transient absorption spectroscopy.[15] These very strong spectroscopic similarities suggest a nearly identical "free-to-bound"-type luminescence mechanism in Ag^+-doped NCs as found in Cu^+-doped NCs.

It would be rather surprising for the luminescence of Ag^+- and Cu^+-doped NCs to both arise from $ML_{CB}CT$ excited states, however, because $ML_{CB}CT$ excitations formally involve ionization of the cation (Ag^+ or Cu^+), and Ag^+ is much more difficult to oxidize than Cu^+ is. Although the ~0.3−0.5 eV difference in energy between otherwise analogous Ag^+- and Cu^+-doped NC PL is

indeed consistent with the expectation that Ag^+ is more difficult to oxidize, this energy difference is far smaller than anticipated based on the relative ionization energies of the dopants themselves. For example, the second ionization potential of elemental Ag is ~1.2 eV greater than that of elemental Cu, the standard reduction potential for aqueous Ag^{2+} ions ($Ag^{2+} + e^- \leftrightarrows Ag^+$, 25 °C) is ~1.85 V more positive than that for Cu^{2+} ions, and isostructural Ag^+ and Cu^+ molecular compounds display similarly disparate redox potentials.[22-23] This striking contrast in ionization potentials suggests that there should be more substantial differences between the electronic structures of Ag^+- and Cu^+-doped semiconductor NCs. The strong similarity between Ag^+- and Cu^+-doped NC spectroscopic properties despite this large contrast in ionization potentials is paradoxical, and it highlights the fact that the acceptor states responsible for the luminescence of Ag^+- and Cu^+-doped semiconductors, and particularly Ag^+, have not yet been sufficiently characterized in either bulk or nanocrystalline form. A thorough description of the electronic structures of Ag^+- and Cu^+-doped semiconductor NCs that reconciles their very similar PL with the vastly different chemical properties of these two dopants would greatly improve the fundamental understanding of these materials and their photophysics.

Here, we report the results of spectroscopic and computational investigations of Ag^+- and Cu^+-doped NCs, using CdSe as our model semiconductor host lattice. Experimentally, we illustrate the known similarities between these materials and identify new similarities in their temperature-dependent PL lifetimes and magneto-photoluminescence that have not been previously described. Density functional theory (DFT) calculations are then used to examine the electronic structures of these materials and compare with experiment. Our DFT results confirm that both dopants introduce localized mid-gap levels just above the NC VB, but also identify key differences between these impurity levels. We show that in Cu^+:CdSe NCs, the impurity level has predominantly copper 3*d*

character, with substantial selenide 4*p* covalency. On the other hand, we find that the impurity level in Ag^+:CdSe NCs consists primarily of 4*p* orbitals on the four Se^{2-} anions bonded to the Ag^+ dopant, with only a small contribution from the Ag(4*d*) atomic orbitals. These differences reflect a shift from so-called "normal" bonding in the Cu^+:CdSe NCs (in which the impurity valence *d* orbitals are shallower than the anion valence *p* orbitals) to "inverted" bonding in the Ag^+:CdSe NCs (in which the impurity valence *d* orbitals are deeper than the anion valence *p* orbitals). Despite this major fundamental electronic-structure distinction, both NCs show qualitatively similar localization of photogenerated holes within the $[MSe_4]$ clusters (M = Cu^+ or Ag^+) formed by the dopant and its four nearest-neighbor Se^{2-} anions. With such similar cluster localization, DFT calculations predict many other similarities between Ag^+:CdSe and Cu^+:CdSe NCs, including similar electronic absorption spectra, excited-state nuclear reorganization, and excited-state singlet−triplet splittings, all supported by experiment. Together, these experimental and theoretical findings resolve the apparent paradox of the very similar spectroscopies despite vastly different dopant ionization potentials in Ag^+- and Cu^+-doped semiconductor NCs, advancing our understanding of this important class of luminescent materials.

3.3 Methods

3.3.1 Synthesis and Characterization

The Cu^+:CdSe NCs were synthesized according to the procedure detailed in ref. 20. The synthesis procedure for Ag^+:CdSe NCs was adapted from the same method. Here, cadmium oleate (0.135 g, 0.2 mmol), selenium dioxide (0.022 g, 0.2 mmol), and octadecene (8.8 g) were degassed under vacuum at 55 °C for 30 min and then heated to 235 °C under N_2 flow at a heating rate of 14 °C/min. After 5 min, a degassed solution of silver iodide (0.043 g, 0.18 mmol) and trioctylphosphine (0.1 mL) in octadecene (2.4 g) was injected into the CdSe reaction mixture. The temperature was

lowered to 190 °C and the reaction was allowed to continue for 2.5−4 h. The NCs were purified by precipitation with methanol and acetone followed by centrifugation, then a second cycle of precipitation and centrifugation with acetone. The NCs were redispersed in toluene.

Room-temperature absorption spectra of NCs dispersed in toluene were recorded on a Varian Cary 500 spectrometer. Room-temperature photoluminescence spectra were recorded with an Ocean Optics USB-2000+ spectrometer, using a 405 nm laser as the excitation source. Relative atomic concentrations were obtained by analysis of dried nanocrystals digested in ultrapure nitric acid using inductively coupled plasma atomic emission spectrometry (ICP-AES; PerkinElmer). Due to the likely formation of Ag_2Se particles during the Ag^+:CdSe synthesis,[20] the possibility of incomplete purification of the Ag^+:CdSe NCs, and the instability of the Ag^+:CdSe NCs with respect to Ag^+ out-diffusion over several months of storage,[20] the dopant concentrations determined by ICP-AES for the Ag^+:CdSe NCs represent upper limits. X-ray diffraction (XRD) data were collected from evaporated NC films on silicon substrates using a Bruker D8 Discover spectrometer at the University of Washington Molecular Analysis Facility.

3.3.2 **Temperature-Dependent Photoluminescence and Magneto-photoluminescence**

Temperature-dependent PL data were measured on films of NCs sandwiched between quartz discs in a Janis STVP-100 continuous-flow optical cryostat, closed-cycle helium cryostat, or Cryo-Industries SMC-1659 OVT superconducting magneto-optical cryostat. For all PL measurements, the nanocrystals were excited using a 405 nm diode laser. Emitted light was collected and focused into a monochromator with a 150 g/mm grating blazed at 500 nm. For magnetic circularly polarized luminescence (MCPL) and for time-resolved PL measurements at $T < 40$ K, the emitted light was collected through a multimode fiber coupled to the same monochromator. Continuous-wave PL spectra, including MCPL spectra, were recorded with a liquid-nitrogen-cooled CCD. For

time-resolved PL, the excitation was modulated at 100 Hz using the square-wave output of a function generator. The emission was detected with a photomultiplier tube connected to a multichannel scaler. The time resolution of this setup is 5 ns. For MCPL, emission was collected along the magnetic field axis (Faraday geometry). The emission was passed through a liquid-crystal variable retardation plate set to λ/4 at the emission maximum, followed by a linear polarizer to separate left (LCP) and right (RCP) circularly polarized components. MCPL polarization ratios are reported as $\Delta I/I = (I_L - I_R)/(I_L + I_R)$, where I_L and I_R refer to the intensity of LCP (σ^-) and RCP (σ^+) emission according to the sign convention outlined in Piepho and Schatz.[24]

3.3.3 **Computations**

DFT calculations were performed using Gaussian 09[25] with the PBE0 hybrid DFT functional.[26-27] All atoms were described using the Los Alamos double-ζ pseudocore potential and corresponding basis set, with explicit basis functions used to describe the Se(4*s*, 4*p*), Cd(4*d*, 5*s*, 5*p*), Cu(3*d*, 4*s*, 4*p*), and Ag(4*d*, 5*s*, 5*p*) atomic orbitals.[28-30] This method has previously been applied to other doped NCs, including Cu^+:CdSe NCs.[31-35] Excited states were calculated using linear-response time-dependent DFT (TD-DFT).[36] Excited-state energies obtained from the TD-DFT calculations were dressed with Gaussian bandshapes of arbitrary width (σ = 0.2 eV) to simulate absorption spectra. Electron and hole wavefunctions were visualized using natural transition orbital (NTO) analysis, which diagonalizes the transition density matrix of each excitation to represent the electronic transitions with single-particle (electron and hole) orbitals.[37]

Small CdSe NCs ($Cd_{34}Se_{34}$, $d \approx 1.6$ nm; $Cd_{77}Se_{77}$, $d \approx 2.1$ nm; and $Cd_{134}Se_{134}$, $d \approx 3.0$ nm) were constructed based on the bulk zinc-blende CdSe crystal structure with lattice parameter a = 0.608 nm.[38] These NC structures are roughly spherical, but clearly faceted, and their volumes are smaller than the volumes of spherical NCs with the same diameters. Dangling bonds on

uncompensated surface Cd^{2+} and Se^{2-} ions were passivated by pseudohydrogen atoms with fractional charges (+1.5 and +0.5, respectively, in undoped CdSe NCs).[39-40] For substitutionally doped NCs, the Cu^{+} or Ag^{+} dopant ion replaced the most centrally located Cd^{2+} ion in the NC. In these NCs, the charge of the NC core was set to −1 and a compensating charge of +1 was distributed over all pseudohydrogen atoms on the surface, giving the dopant a +1 charge while leaving the overall system neutral. This mean-field approach represents charge compensation of the aliovalent dopant by the NC surface.[31,34] For interstitially doped Ag^{+}:CdSe NCs (see Appendix B.), the Ag^{+} dopant was located at the most centrally located tetrahedral or octahedral interstitial site in the NC, the charge of the NC core was set to +1, and a compensating charge of −1 was distributed over the pseudohydrogen surface atoms. All NC structures were optimized in the ground state before other electronic-structure or excited-state calculations were performed.

3.4 Results and Analysis

3.4.1 Absorption, Luminescence, and Magneto-luminescence

Figure 3.1 presents absorption and photoluminescence spectra of zinc-blende Cu^{+}:CdSe (d = 3.1 nm, 0.6% Cu^{+}) and Ag^{+}:CdSe (d = 3.5 nm, ≤ 3.5% Ag^{+}) NCs. Both types of NCs display absorption spectra very similar to that of the parent CdSe NCs. A weak, broad sub-bandgap "foot" in the absorption spectrum of Cu^{+}:CdSe NCs has been described previously and attributed to the $ML_{CB}CT$ excitation that is the inverse of the Cu^{+}-activated PL.[19-20] Identification of an analogous feature in the Ag^{+}:CdSe absorption spectrum of Figure 3.1 is complicated by its even greater proximity to the excitonic absorption edge, and by greater inhomogeneous spectral broadening in this sample. Both types of NCs also display similarly broad PL bands with large effective Stokes shifts. Although the PL of both NCs is significantly red-shifted from the excitonic absorption, the Cu^{+}:CdSe PL displays a larger effective Stokes shift (E_g(CdSe) – E_{PL} ≈ 0.75 eV) than the Ag^{+}:CdSe

PL (E_g(CdSe) – E_{PL} ≈ 0.42 eV), consistent with the ordering of Ag^+- and Cu^+-activated PL in bulk CdSe.[4] Here, the effective Stokes shift (E_g(CdSe) – E_{PL}) describes the difference between the energies of the first excitonic absorption maximum and dopant-activated PL maximum, as opposed to the true Stokes shift, which is defined as the energy difference between absorption and PL maxima for the same electronic transition.[17] In both their bulk and nanocrystalline forms, the PL band shapes of Cu^+-doped semiconductors are intrinsically broad due to Franck−Condon progressions, i.e., homogeneous effects. These broad band shapes thus show characteristic thermal broadening and are observed even in single-NC/single-dopant PL measurements.[41] The PL band shape of the Ag^+:CdSe NCs also broadens with increasing temperature (see Appendix B.), consistent with this interpretation in this case as well, but this band is clearly broadened by the less uniform NC size distribution, too. We note that resolved Franck−Condon progressions are observed experimentally in the analogous DAP PL spectra of bulk Ag^+:ZnSe,[42-43] with Huang−Rhys factors of $S \approx 4$ and $h\nu \approx 30$ meV in the dominant progression, reflecting overall nuclear reorganization energies of $E_R \approx 0.14$ eV. As described previously,[31] such nuclear reorganization energies likely increase with proximity of the dopant to the NC surfaces because of symmetry breaking and greater lattice deformability near the surfaces, representing one of several sources of inhomogenous broadening within such NC ensembles.

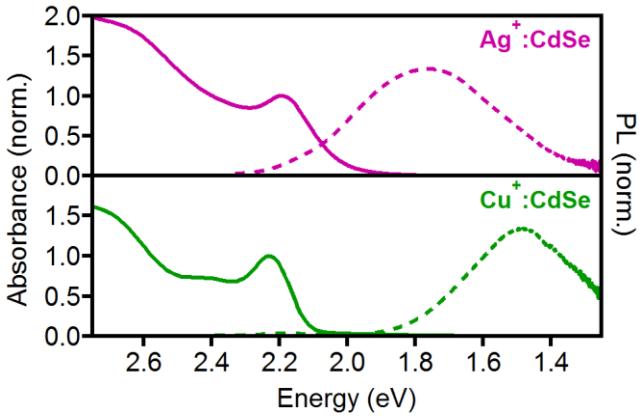

Figure 3.1. Absorption and PL of Ag^+- and Cu^+-doped CdSe NCs. Normalized experimental room-temperature absorption (solid lines) and PL (dashed lines) spectra of d = 3.5 nm Ag^+:CdSe (purple) and d = 3.1 nm Cu^+:CdSe (green) NCs. The absorption spectra are similar, but the first excitonic absorption band of the Ag^+:CdSe NCs is broader, suggesting more inhomogeneity in this sample. The dopant-activated PL occurs ~0.3 eV higher in energy in the Ag^+:CdSe NCs than in the Cu^+:CdSe NCs.

For Cu^+:CdSe NCs, magnetic circularly polarized luminescence (MCPL) and temperature-dependent time-resolved PL have previously provided insight into the nature of the luminescent excited state. Applying the same experimental techniques to Ag^+:CdSe NCs can help reveal similarities and differences between these materials. Figure 3.2a shows circularly polarized luminescence spectra for Ag^+:CdSe NCs (d = 3.1 nm, ≤ 3.9% Ag^+), measured at T = 1.7 K and B = 0 and 6 T. In an applied magnetic field, I_L decreases and I_R increases. These effects originate from a Zeeman splitting of the emissive excited state, which lowers the energy of the LCP-emitting sublevel while increasing the energy of the RCP-emitting sublevel. The MCPL polarization ratio $\Delta I/I = (I_L - I_R)/(I_L + I_R)$ reflects the population of the magnetically active state and the relative populations of its LCP- and RCP-emitting components. The MCPL polarization ratio measured for Ag^+:CdSe NCs, shown in Figure 3.2b, has the same sign and similar magnitude as that of Cu^+:CdSe NCs, as well as a similar temperature and field dependence.[21] The origin of this polarization is discussed below.

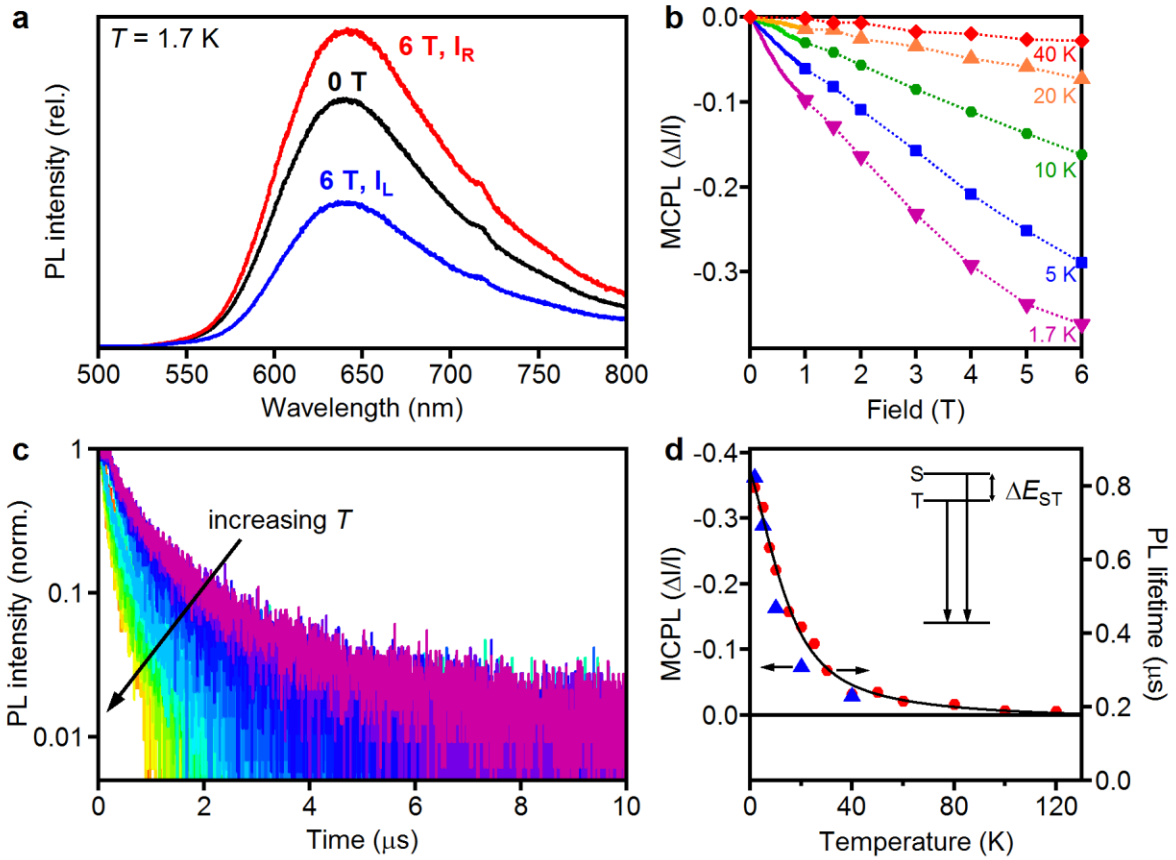

Figure 3.2. MCPL and TRPL of Ag^+:CdSe NCs. (a) Experimental circularly polarized PL spectra of $d = 3.1$ nm Ag^+:CdSe NCs measured at 1.7 K with applied magnetic fields of 0 (black) and 6 T (blue: LCP emission; red: RCP emission). The feature at ~720 nm is an artifact related to the optical fiber. **(b)** Field and temperature dependence of the MCPL polarization ratio, $\Delta I/I$, for the same Ag^+:CdSe NCs, measured at the PL peak energy. The dotted lines are guides to the eye. **(c)** PL decay traces for the same Ag^+:CdSe NCs, normalized at $t = 0$ and measured at temperatures between 1.7 and 300 K. **(d)** MCPL polarization ratio at 6 T (shown in (b)) and PL lifetimes (obtained from biexponential fits to the decay curves in (c)) plotted versus temperature. The solid line represents the best fit to the singlet–triplet splitting model of ref. 21 and yields a value of $\Delta E_{ST}{}^{avg} \approx 1.0$ meV. Inset: schematic illustration of the singlet and triplet energy levels.

Figure 3.2c plots PL decay curves measured for the dopant-activated PL in the same Ag^+:CdSe NCs as a function of sample temperature. Between room temperature and ~60 K, the PL lifetime is nearly temperature independent at ~200 ns. Below ~60 K, the PL lifetime increases dramatically with decreasing temperature, rising to ~800 ns at 1.7 K, as shown in Figure 3.2d. Similar behavior was observed in Cu^+:CdSe, Cu^+:InP, and $CuInS_2$ NCs, where it was attributed to

the existence of a singlet−triplet splitting in the luminescent excited state, resulting from exchange coupling between the spins of the CB electron and the Cu^+-bound hole.[21,31] The triplet state is lower in energy, but recombination from this state is spin-forbidden and its decay rate constant is consequently smaller than that of the singlet state. At low temperatures, the relative population of the triplet state increases, and this state therefore contributes more to the observed luminescence. The MCPL in these Cu^+-doped materials also originates from the triplet state, which splits into m_S = −1, 0, and +1 sublevels in an applied magnetic field. Although the PL intensities and lifetimes have contributions from both singlet and triplet excited states, the difference between I_L and I_R comes solely from the triplet excited state to first order. The MCPL polarization ratio thus reflects the total contribution of triplet-state emission as well as the relative populations and wavefunctions of the Zeeman-split sublevels of the triplet state.[21] Figure 3.2d shows that the MCPL polarization ratio and the PL lifetimes of the Ag^+:CdSe NCs both display the same temperature and field dependence, confirming that both effects originate from freezing of the population in the emissive triplet state. Excited-state singlet−triplet splittings have not been reported previously for any Ag^+-doped semiconductor NCs, but have been described in molecular Ag^+ complexes.[44-49] Fitting the luminescence decay temperature dependence in Figure 3.2d to a kinetic model[21] yields $\Delta E_{ST}{}^{avg} \approx$ 1.0 meV in these Ag^+:CdSe NCs. This value is similar to the singlet−triplet splittings observed in other Cu^+-doped and Cu^+-based semiconductor NCs (*e.g.*, ~0.85 meV in similar Cu^+:CdSe NCs).[21,31]

Overall, these spectroscopic results for the Ag^+:CdSe NCs strongly parallel those obtained for Cu^+-doped NCs.[21] In the latter, many of the analogous observations can be explained by invoking hole trapping by Cu^+ in the emissive excited state, which causes a large nuclear reorganization (large Stokes shift and vibronic bandwidth), and defines the magnitude of the

excited-state singlet−triplet exchange splitting. Despite the fact that hole trapping by Ag^+ is very unfavorable because of its large ionization energy, the spectroscopic results presented here nonetheless indicate very similar emissive excited states in Ag^+:CdSe and Cu^+:CdSe NCs. This apparent paradox is resolved by the electronic-structure calculations presented below.

3.4.2 Electronic-Structure Calculations

3.4.2.1 Ground-state molecular orbitals

Figure 3.3 plots the ground-state molecular-orbital (MO) energies and their breakdown into individual atomic-orbital contributions (plotted as percentages) calculated for undoped CdSe and substitutionally doped Cu^+:CdSe and Ag^+:CdSe NCs, each with 134 lattice cations (d = 3.0 nm). Binned density-of-states (DOS) plots and orbital energies for this and other NC sizes are provided in Appendix B. . All three NCs show a fully occupied VB with mostly Se^{2-} character and an unoccupied CB with mostly Cd^{2+} character, as seen for undoped CdSe (Figure 3.3a). The Cu^+-doped NC (Figure 3.3b) additionally displays five doubly occupied mid-gap orbitals with ~50% Cu(3d) character each. These copper 3d orbitals are split into t_2 and e orbital subsets by the tetrahedral ligand field provided by the zinc-blende CdSe lattice. The orbital degeneracy of each tetrahedral subset is additionally broken by the proximity of the NC surface, which further reduces the cation point symmetry. This symmetry-breaking influence of the surface becomes more important in smaller NCs.[31] The Ag^+-doped CdSe NC (Figure 3.3c) also shows doubly occupied mid-gap orbitals just above the VB. In this case, however, there is only one quasi-3-fold-degenerate set of occupied mid-gap orbitals, and these three orbitals are all predominantly Se(4p) in character, with only a small admixture (~15%) of Ag(4d) character. As expected from the much greater ionization energy of Ag^+, the Ag(4d) orbitals primarily appear only deep within the VB (at ~ −9 eV in Figure 3.3c). It is evident that Ag^+ and Cu^+ doping introduces new mid-gap electronic

transitions involving promotion of electrons from these mid-gap orbitals into the CdSe NC CB, and that these mid-gap transitions occur at higher energy in Ag^+:CdSe NCs than in Cu^+:CdSe NCs.

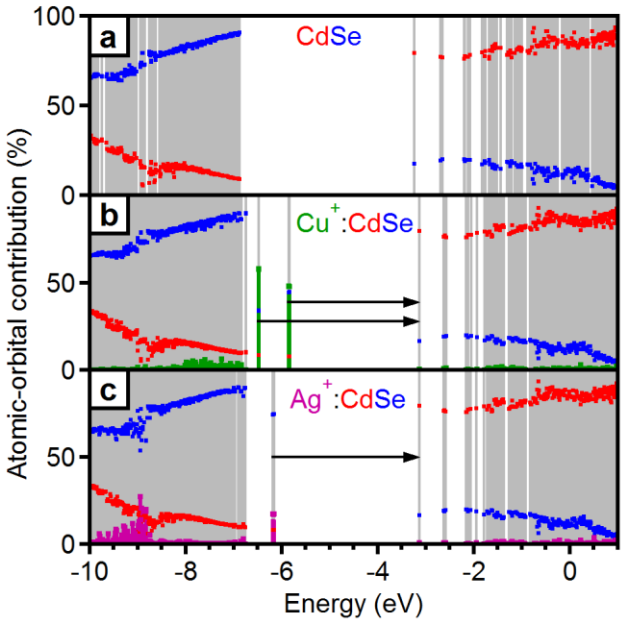

Figure 3.3. MO energies and compositions for undoped, Cu^+-doped, and Ag^+-doped CdSe NCs. Calculated molecular-orbital energies for **(a)** $Cd_{134}Se_{134}$, **(b)** Cu^+:$Cd_{133}Se_{134}$, and **(c)** Ag^+:$Cd_{133}Se_{134}$ NCs with the breakdown of atomic-orbital contributions to each shown as red dots for Cd^{2+}, blue dots for Se^{2-}, green (Cu^+) or purple (Ag^+) dots for the total dopant orbital contribution, and green (Cu^+) or purple (Ag^+) lines for the dopant valence *d*-orbital contributions. The arrows indicate new sub-bandgap electronic transitions introduced upon doping; the dopant-activated PL is attributed to the inverse of the lowest-energy electronic excitations shown here.

In previous studies of Ag^+:CdSe NCs, some results have suggested that Ag^+ incorporates as an interstitial dopant rather than substituting for a host Cd^{2+} cation.[12,50] Substitutional and interstitial Ag^+ defects have been observed in bulk semiconductors, but the characteristic blue-Ag PL in bulk ZnS is known to originate from a substitutional Ag^+ acceptor.[7,43] Density-of-states plots for interstitially doped Ag^+:CdSe NCs (see Appendix B.) show no mid-gap acceptor states. These results do not rule out the possibility of interstitial Ag^+ in Ag^+-doped CdSe NCs, but they do

support association of the dopant-activated PL in these NCs to substitutional rather than interstitial Ag^+ doping.

Although the contributions of the Ag^+ and Cu^+ valence *d* orbitals to the mid-gap orbitals differ substantially, all of the mid-gap orbitals shown in Figure 3.3 are strongly localized around the dopant ions. Figure 3.4 shows the breakdown of atomic-orbital contributions to the three highest-energy mid-gap orbitals of the Cu^+:CdSe NC (*i.e.*, the Cu^+ t_2 set) and the Ag^+:CdSe NC. The atomic-orbital contributions are shown separately for the Cu^+ or Ag^+ dopant, the four Se^{2-} anions bound to the dopant, all other Se^{2-} anions, and all Cd^{2+} cations. For both doped NCs, valence orbitals from the $[MSe_4]$ clusters (*i.e.*, the dopant *d* orbitals and nearest-neighbor Se(4*p*) orbitals) account for a similar ~75−80% of the mid-gap MOs. Whereas Cu(3*d*) orbitals account for over half of the $[MSe_4]$ cluster contribution to the mid-gap orbitals in the Cu^+:CdSe NCs, however, the Ag(4*d*) orbitals account for only ~20% of the $[MSe_4]$ cluster contribution to the mid-gap orbitals in the Ag^+:CdSe NCs. Instead, the Se(4*p*) atomic orbitals of the $[MSe_4]$ cluster dominate the mid-gap MOs in the Ag^+:CdSe NC.

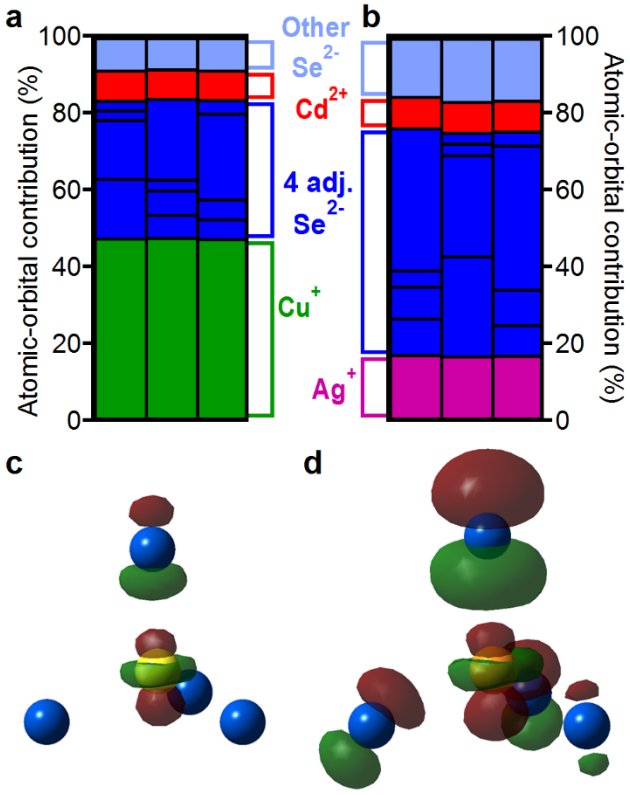

Figure 3.4. Mid-gap MOs of Cu^+-doped and Ag^+-doped CdSe NCs. (a,b) Calculated atomic-orbital contributions to the three highest-energy mid-gap orbitals in **(a)** the Cu^+:$Cd_{133}Se_{134}$ NC and **(b)** the Ag^+:$Cd_{133}Se_{134}$ NC. The dopant atomic-orbital contributions are shown in green for Cu^+ and purple for Ag^+, Se^{2-} atomic-orbital contributions are shown in dark blue for the four Se^{2-} bonded to the dopant and light blue for all other Se^{2-} atoms in the NC, and Cd^{2+} atomic-orbital contributions are shown in red. Due to small contributions from the atomic orbitals of the pseudohydrogen capping ligands, the atomic-orbital contributions shown here add up to just less than 100%. **(c,d)** Visualization of the highest-energy mid-gap MO surfaces for (c) the Cu^+:$Cd_{133}Se_{134}$ NC and (d) the Ag^+:$Cd_{133}Se_{134}$ NC, showing only the dopant and four adjacent Se^{2-} ions. These surfaces represent the region of the MOs with the highest electron density. The atomic-orbital contributions from the dopant *d* orbitals and Se(4*p*) orbitals are clearly recognizable. These depictions correspond to the orbitals described by the right columns of panels (a) and (b).

Despite this very large difference in dopant contribution, the highest-energy mid-gap orbitals (HOMOs) in Ag^+- and Cu^+-doped CdSe NCs are remarkably similar. This similarity is evident from Figure 3.4c,d, which shows isosurface plots of each, generated at values corresponding to 50% of the HOMO wavefunction density. The relative contributions of the

dopant *d* orbitals and Se(4*p*) orbitals are reflected by the relative sizes of these atomic orbitals in Figure 3.4c,d, and are consistent with the breakdown described in Figure 3.4a,b. Importantly, these mid-gap orbitals are the ones occupied by the photogenerated holes in the luminescent excited states of Ag^+- and Cu^+-doped CdSe NCs. The similar localization of these orbitals within the [MSe_4] clusters of each NC explains the strong resemblance of the spectroscopic properties of Cu^+-doped and Ag^+-doped NCs. At the same time, the stark difference in metal *d vs* Se(4*p*) character points to a substantial electronic-structure difference between the two materials. The large Cu^+ *d*-orbital character of the Cu^+:$Cd_{133}Se_{134}$ HOMO supports description of copper as Cu^{2+}-like in the luminescent excited state of Cu^+-doped NCs. In contrast, the small Ag^+ *d*-orbital character of the Ag^+:$Cd_{133}Se_{134}$ HOMO indicates that it would be inappropriate to draw the analogous conclusion of Ag^{2+}-like character in the luminescent excited state of Ag^+-doped NCs. This contrast is explored in more detail below using excited-state computational methods.

3.4.2.2 **Excited-state energies**

Investigation of the excited states of these doped NCs using time-dependent DFT (TD-DFT) provides additional insight into their electronic structures and photophysical properties. Figure 3.5 presents absorption spectra calculated by TD-DFT for Cu^+:$Cd_{33}Se_{34}$ and Ag^+:$Cd_{33}Se_{34}$ NCs (d = 1.6 nm for both). For illustrative purposes, smooth spectra have been generated from the oscillator strengths and energies of the individual line transitions using a uniform arbitrary Gaussian linewidth (σ = 0.2 eV) for each transition. From these computed TD-DFT spectra, both NCs show similar absorption above ~3.75 eV that arises primarily from the onset of band-to-band transitions within the CdSe lattice itself. Both NCs also show additional mid-gap absorption features. The mid-gap transitions of the Ag^+-doped CdSe NC occur ~0.45 eV higher in energy than those of the Cu^+-doped NC, consistent with the trend in ground-state molecular-orbital energies described in

Figure 3.3. In both cases, these mid-gap transitions arise from excitation of electrons from the mid-gap [MSe_4] cluster orbitals to the CB, as discussed above. This mid-gap absorption has been identified experimentally in Cu^+:CdSe NCs,[20-21] but analogous absorption in Ag^+:CdSe NCs has not been definitively identified experimentally.

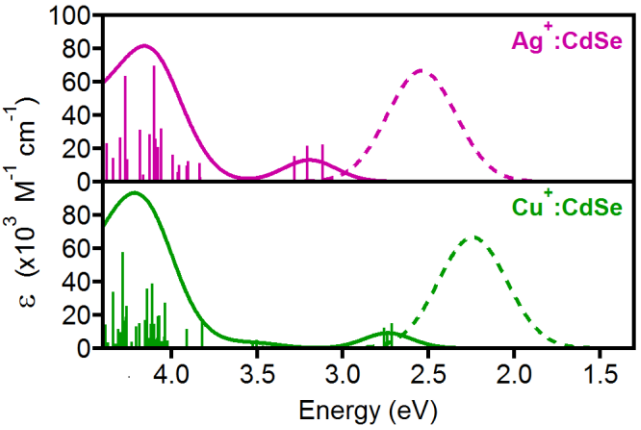

Figure 3.5. Calculated absorption and PL spectra for Cu^+-doped and Ag^+-doped CdSe NCs. Calculated TD-DFT absorption spectra (solid lines) for Cu^+:$Cd_{33}Se_{34}$ (green) and Ag^+:$Cd_{33}Se_{34}$ (purple) NCs. The oscillator strengths of the individual transitions are shown as vertical lines. PL spectra (dashed lines) with Stokes shifts based on the computed nuclear reorganization energies of the lowest-energy singlet excited states are also shown. For illustrative purposes, these absorption and luminescence spectra were generated using an arbitrary Gaussian broadening factor of σ = 0.2 eV, and they are not intended to reflect actual bandshapes.

Figure 3.5 also includes simulated PL spectra, accounting for the nuclear reorganization energies (E_R) computed for the lowest-energy excited states using geometry-relaxed TD-DFT. Both NCs show large nuclear reorganization energies upon photoexcitation: E_R = 0.24 eV for Cu^+:$Cd_{33}Se_{34}$, and 0.29 eV for Ag^+:$Cd_{33}Se_{34}$. The true Stokes shifts for the PL from these NCs are twice these reorganization energies: $E_{Stokes} = 2E_R$. From the experimental absorption spectra of Cu^+:CdSe NCs, the true Stokes shift was previously estimated to be ~0.55 eV,[21] which gives a reorganization energy similar to the value calculated here. Estimation of the true Stokes shift for

the Ag^+:CdSe NCs described here is more difficult because of greater inhomogeneous broadening and the small energy difference between the Ag^+-centered and excitonic absorption origins.

Because of their large reorganization energies, both predicted PL spectra also display large effective Stokes shifts similar to those observed in the experimental spectra of Figure 3.1. The resulting PL peak energies are calculated to be ~2.24 eV for the Cu^+:CdSe NC and ~2.54 eV for the Ag^+:CdSe NC, which reproduces the ordering and approximate energy differences between Ag^+- and Cu^+-activated PL observed experimentally (Figure 3.1). Such large nuclear reorganization also generates PL bandshapes that are broadened by Franck–Condon progressions along the nuclear distortion coordinates, shown in Cu^+:CdSe NCs to involve totally symmetric and Jahn–Teller displacements.[31] Such homogeneously broadened PL bandshapes are consistent with the broad PL bandshapes observed experimentally (Figure 3.1), even at the single-NC single-dopant level.[41]

3.4.2.3 **Excited-state hole localization and electron–hole magnetic exchange coupling**

Figure 3.6 shows the excited-state hole wavefunctions (natural transition orbitals) generated for the relaxed-geometry lowest excited states of the Cu^+:CdSe and Ag^+:CdSe NCs. The hole is strongly localized at the dopant in both NCs, as expected from the HOMOs shown in Figure 3.4, whereas the electron is highly delocalized in both NCs. The hole appears more localized in Cu^+:CdSe than in Ag^+:CdSe, consistent with localization primarily at the Cu^+ dopant rather than at the four neighboring Se^{2-} (Figure 3.4). The hole Bohr radii (r_B) in these NCs can be estimated independently from the computed hole-binding energies (E_b, defined as the energy difference between the first excitonic state (delocalized hole) and the relaxed-geometry first excited state (localized hole)) using $r_B = \hbar/\sqrt{(2m^*E_b)}$, where m^* is the effective mass of the hole in CdSe.[31,51] For the Cu^+:$Cd_{76}Se_{77}$ NC, E_b = 1.18 eV, corresponding to r_B = 0.27 nm. For the Ag^+:$Cd_{76}Se_{77}$ NC,

E_b = 1.05 eV, corresponding to r_B = 0.29 nm. These Bohr radii are similar in magnitude to the dopant−Se bond lengths and are consistent with the hole wavefunctions depicted in Figure 3.6. The smaller E_b in the Ag^+:CdSe NC than in the Cu^+:CdSe NC is consistent with the experimental PL energies of Ag^+:CdSe and Cu^+:CdSe NCs (Figure 3.1), and with the difference in experimental photoionization energies of bulk Ag^+- and Cu^+-doped ZnS.[5]

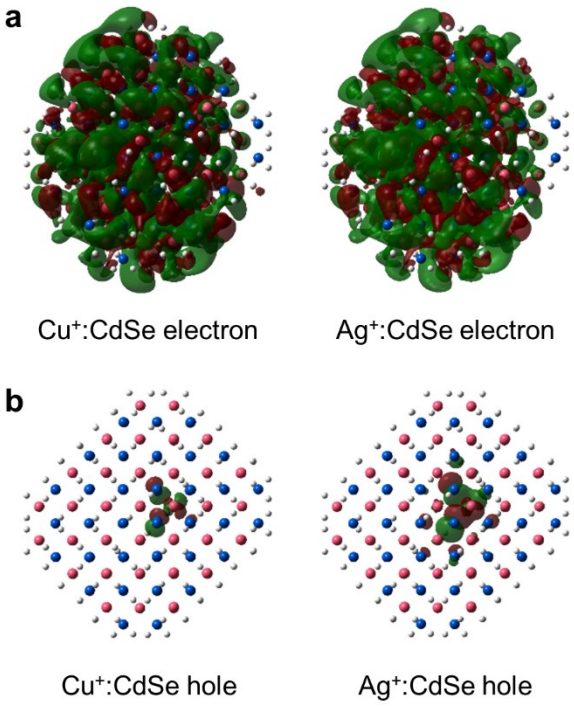

Figure 3.6. Natural transition orbitals for Cu^+:CdSe and Ag^+:CdSe NCs. (a) Electron and **(b)** hole natural transition orbitals for the lowest-energy singlet transitions of Cu^+:$Cd_{76}Se_{77}$ and Ag^+:$Cd_{76}Se_{77}$ NCs, showing the electron and hole wavefunctions in the excited state. Isosurface values were chosen to enclose 70% of the total electron or hole wavefunction density.

Finally, TD-DFT calculations also reproduce the experimental observation that the lowest-energy excited states of both Ag^+- and Cu^+-doped CdSe NCs have a triplet spin configuration. From the energies of the lowest-energy singlet and triplet excited states in their relaxed excited-state geometries, the singlet−triplet splitting ΔE_{ST} can be determined. For the Ag^+:$Cd_{76}Se_{77}$ and Cu^+:$Cd_{76}Se_{77}$ NCs (d = 2.1 nm) with their dopants located at a central cation site, the computed

values of ΔE_{ST} are 34 and 30 meV, respectively. The lower energy of the triplet state in both cases, as well as the similar Ag^+:$Cd_{76}Se_{77}$ and Cu^+:$Cd_{76}Se_{77}$ singlet−triplet splitting magnitudes, are both consistent with experiment. Experiment measures an average value ($\Delta E_{ST}{}^{avg}$) that also reflects the distribution of cation sites throughout the NC ensemble, and moreover reflects the larger volumes of the experimental NCs.[21] Estimating $\Delta E_{ST}{}^{avg}$ from the calculated value of ΔE_{ST} for the centrally located dopant, and scaling to account for NC volume,[21,31] yields predicted $\Delta E_{ST}{}^{avg}$ values of 2.0 and 1.8 meV for spherical $d = 3.1$ nm Ag^+:CdSe and Cu^+:CdSe NCs, respectively. These predicted values are similar to the experimental ones obtained from analysis of the PL lifetime temperature dependence (Figure 3.2 and ref. 21). A more reliable computational estimate of $\Delta E_{ST}{}^{avg}$ can be obtained by calculating ΔE_{ST} for each individual cation site, but this approach was not taken here because of the expense of such excited-state geometry optimization calculations. Nevertheless, the excellent agreement in both sign and magnitude allows the conclusion that these calculations describe the spin-exchange coupling interactions of the luminescent excited states in these NCs well.

3.4.2.4 **Nuclear reorganization in the luminescent excited state**

The strong hole localization in the luminescent excited states of these NCs is accompanied by substantial excited-state nuclear reorganization. Figure 3.7 summarizes the geometric changes predicted by DFT upon excitation to the lowest-energy singlet excited states of the Ag^+:$Cd_{76}Se_{77}$ and Cu^+:$Cd_{76}Se_{77}$ NCs. In the ground state (closed circles), the Cu^+-doped NC lattice is significantly contracted around the Cu^+ dopant, whereas the Ag^+-doped NC lattice is slightly expanded around the Ag^+ dopant. This difference is a reflection of the fact that Cu^+ and Ag^+ tetrahedral ionic radii (0.60 and 1.00 Å) straddle the Cd^{2+} tetrahedral ionic radius (0.78 Å).[23] In the excited state (open triangles), both NCs undergo large nuclear reorganization around the

dopant. The insets in Figure 3.7 illustrate the excited-state bond-length changes within the [MSe_4] cluster of each doped NC. Both NCs display net contraction of the M−Se bonds, as well as symmetry-breaking distortions along other nuclear coordinates. In the Cu^+:CdSe NC, the contraction is small relative to the symmetry-breaking distortion, whereas, in the Ag^+:CdSe NC, the contraction is larger. This contrast reflects the difference in the ground-state bond lengths: the NC lattice is significantly contracted around the Cu^+ even in the ground state, so further contraction is unfavorable, but there is no such ground-state contraction around Ag^+ in the Ag^+:CdSe NC, so this component of the excited-state distortion is more facile. In both cases, however, the excited-state reorganization involves both a net contraction and breaking of the tetrahedral cation site symmetry. The bonds from the first-coordination-sphere Se^{2-} anions to the next shell of Cd^{2+} cations also distort to accommodate the [MSe_4] distortions.

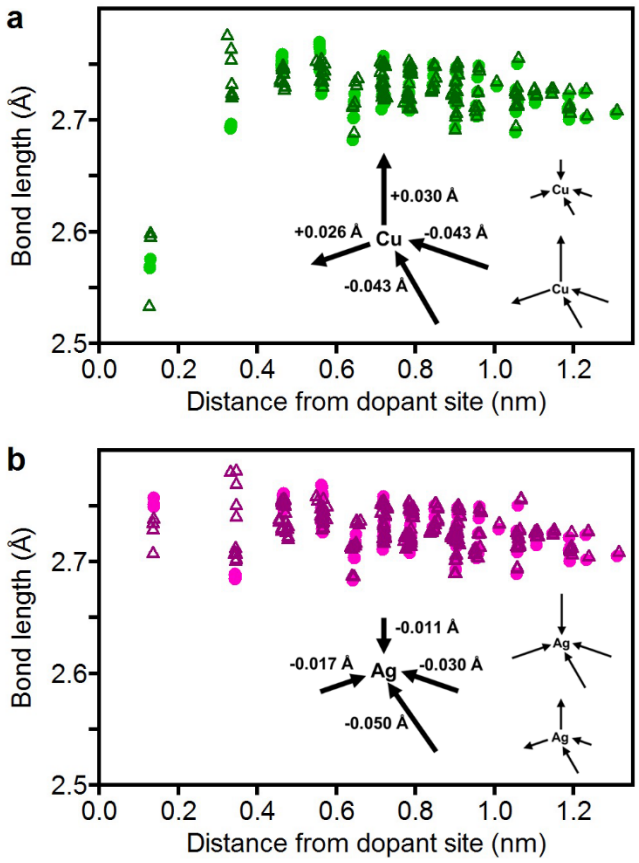

Figure 3.7. Excited-state bond lengths for Cu^+:CdSe and Ag^+:CdSe NCs. Comparison of computed M−Se bond lengths for the ground states (closed circles) and lowest-energy singlet excited states (open triangles) of **(a)** Cu^+:$Cd_{76}Se_{77}$ and **(b)** Ag^+:$Cd_{76}Se_{77}$ NCs, plotted vs distance from the dopant. Insets: first-coordination-sphere bond-length changes at the dopants for the same NCs upon excitation to the same lowest-energy singlet excited states (left) and illustration of the relative magnitudes of the totally symmetric contraction and symmetry-breaking distortion that contribute to these bond-length changes (right). In the Cu^+:CdSe NC, the totally symmetric contraction (top) is smaller than the symmetry-breaking distortion (bottom), whereas the opposite is true in the Ag^+:CdSe NC, attributable primarily to the different lattice strain in the ground states of these NCs arising from the difference between Cu^+ and Ag^+ ionic radii.

We can understand these specific excited-state geometric distortions by considering the orbital excitations involved. In both NCs, the dopant is in a pseudotetrahedral environment in its ground state, and the HOMO is one of three doubly occupied, nearly degenerate MOs. These three MOs are associated with the three metal t_2 *d* orbitals of tetrahedral symmetry in antibonding interactions with the appropriate symmetry-adapted linear combinations of Se^{2-} orbitals, and all

three are highly localized within the [MSe_4] cluster unit. In the luminescent excited state, an electron has been removed from one of these three MOs. Removal of this antibonding electron from the [MSe_4] cluster strengthens M−Se bonding, causing a totally symmetric contraction of the four M−Se bonds. The resulting open-shell configuration is also susceptible to a Jahn−Teller-like distortion that lowers the symmetry of the [MSe_4] cluster in order to stabilize the photogenerated hole. Just the MO possessing the photogenerated hole is destabilized in the excited state (see Appendix B.). Interestingly, removal of an antibonding electron has essentially the same effect on the overall nuclear reorganization of the [MSe_4] clusters of both Ag^+:CdSe and Cu^+:CdSe NCs, despite the rather large differences in relative contributions of metal *d* and Se(4*p*) atomic orbitals to that MO in these two NCs. The totally symmetric and symmetry-breaking distortions combine to generate the large overall nuclear reorganization energies of ~0.2−0.3 eV calculated in each NC, and should result in similar Franck−Condon-broadened homogeneous PL bandshapes for both Cu^+:CdSe and Ag^+:CdSe NCs. These conclusions are consistent with the experimental PL spectra in Figure 3.1 and with previous interpretations of experimental PL bandshapes in both bulk and nanocrystalline Ag^+- and Cu^+-doped semiconductors.[5,10,31,41,43]

3.5 **Discussion**

The contrasting electronic structures of Ag^+:CdSe and Cu^+:CdSe NCs represent an example of a shift between "normal" and "inverted" bonding schemes in these two materials. Figure 3.8 illustrates this shift schematically, by plotting the MOs formed from the interaction of Cu^+ and Ag^+ valence *d* orbitals with the surrounding Se(4*p*) orbitals of the respective [MSe_4] clusters (effectively, the same MOs pictured in Figure 3.4c,d). In both cases, the M−Se interaction pushes one antibonding cluster MO up in energy while stabilizing a corresponding bonding MO. Similar interactions occur for all three metal t_2 *d* orbitals with the appropriate combination of Se(4*p*)

orbitals, creating the three highest-energy mid-gap MOs shown for both NCs in Figure 3.3 and Figure 3.4.

The key difference between Ag^+:CdSe and Cu^+:CdSe electronic structures rests in the different ionization energies of the dopant valence *d* orbitals relative to the lattice Se(4*p*) orbitals. In Cu^+:CdSe NCs, as in most 3*d* transition-metal coordination complexes, the ionization energy of the Cu^+ valence shell (3*d*) is smaller than that of the ligand's valence shell (Se(4*p*)), *i.e.*, the metal is more easily oxidized than the ligand. This ordering positions the Cu(3*d*) atomic orbitals above the Se(4*p*) orbitals in the MO diagram of Figure 3.8a. Hybridization then generates bonding MOs with mostly Se(4*p*) character located within the VB, and antibonding MOs with mostly Cu(3*d*) character located above the VB edge. In bulk Cu^+-doped semiconductors, strong interactions between the Cu(3*d*) and anion *p* orbitals, often referred to as "*p*−*d* repulsion", have been invoked to explain the unexpected depth of the Cu^+ acceptor level,[52] which is the copper-based antibonding MO pushed up in energy by this interaction.

In contrast with Cu^+, the ionization energy of the Ag^+ valence shell (4*d*) is ~1.5 eV greater than that of Cu^+.[23] Consequently, the Ag(4*d*) atomic orbitals are now located below the Se(4*p*) orbitals in the MO diagram of Figure 3.8b. In this case, hybridization generates bonding MOs with primarily Ag(4*d*) character that reside deep within the VB (Figure 3.3), and antibonding MOs with primarily Se(4*p*) character that occur above the VB edge. The bonding scheme for silver is thus inverted relative to the normal scheme displayed by copper. In both the Ag^+:CdSe and Cu^+:CdSe NCs, extensive M−Se hybridization in the antibonding MOs split off from the VB edge allows the $[MSe_4]$ units to behave qualitatively similarly upon photoexcitation, despite this shift from normal to inverted bonding.

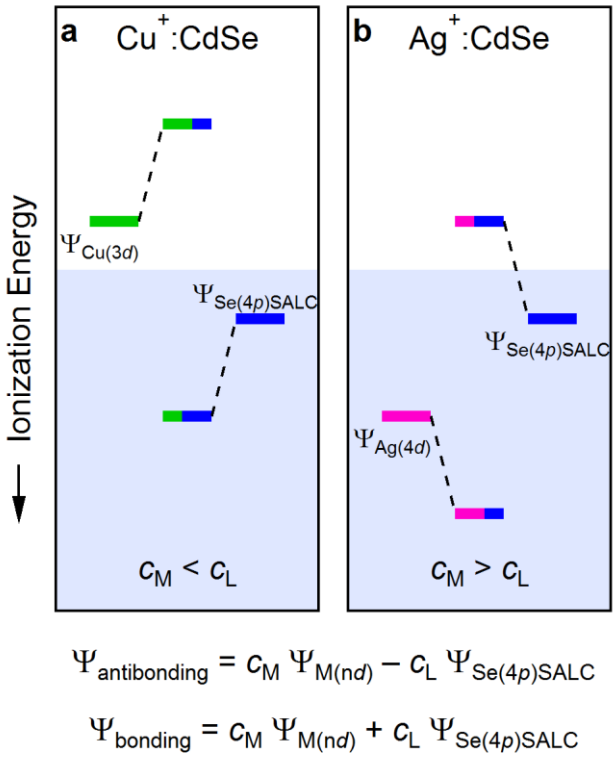

Figure 3.8. Molecular-orbital diagrams illustrating normal and inverted bonding. Schematic molecular-orbital diagrams illustrating the relative energy levels of the dopant (metal) *d* orbitals and symmetry-adapted linear combinations (SALCs) of the four nearest-neighbor anion (ligand) *p* orbitals in **(a)** Cu^+:CdSe and **(b)** Ag^+:CdSe NCs, as well as their relative contributions to the mid-gap and deep valence-band orbitals. The dashed lines are included to emphasize the dominant parent atomic orbitals of each cluster MO. The shaded area represents the filled VB of the CdSe NC. In the Cu^+:CdSe NCs, the Cu(3*d*) atomic orbitals reside above the Se(4*p*) atomic orbitals, and the antibonding (mid-gap) molecular orbital therefore has predominantly Cu(3*d*) character. In the Ag^+:CdSe NCs, the Ag(4*d*) atomic orbitals reside *below* the Se(4*p*) atomic orbitals, and the antibonding (mid-gap) molecular orbital therefore has predominantly anion *p* character (inverted bonding). The mid-gap orbitals are higher in energy (farther from the VB edge) for the Cu^+:CdSe NCs than for the Ag^+:CdSe NCs in both the experimental and computational results.

Inverted bonding has been observed in some molecules[53-54] and is also invoked to describe the VB structure of undoped II−VI semiconductors, as defined by photoemission spectroscopy and computational methods.[52,55] Here, the valence *d* orbitals of metal cations such as Cd^{2+} or Zn^{2+} are deeper (greater ionization energy) than the valence *p* orbitals of anions such as Se^{2-} or S^{2-}.

Cation−anion hybridization then generates bonding orbitals with primarily metal *d* character located deep in the VB, while the corresponding antibonding orbitals with primarily anion *p* character appear at the VB edge. Given the appearance of mid-gap levels upon Ag^+ doping by this mechanism, we can conclude that the antibonding interactions within the [$AgSe_4$] cluster are stronger than the corresponding antibonding interactions in CdSe. Cu^+ and Ag^+ are not unique in this behavior; the *d* orbitals of other transition-metal impurities in II−VI and III−V semiconductors show a variety of energies relative to the anion *p* orbitals, depending on the identity of the impurity, and consequently yield a variety of mid-gap defect states that traverse from predominantly metal *d* character to predominantly anion *p* character.[42,52,56]

It is also interesting to compare the electronic structures of the Ag^+- and Cu^+-doped II−VI semiconductor examined here to those of related I−III−VI_2 semiconductors such as $CuInSe_2$ and $AgInSe_2$. In most I−III−VI_2 materials, the upper VB consists of strongly hybridized *d* orbitals from the group I metal cations and *p* orbitals from the group VI anions. Because of strong *p*−*d* repulsion pushing antibonding orbitals high in energy, I−III−VI_2 chalcopyrite semiconductors typically have narrower band gaps than their II−VI zinc-blende analogues.[57-59] Consistent with the relative energies of the Cu^+ and Ag^+ *d* orbitals and those of the resulting antibonding MOs shown in Figure 3.8, Cu^+-based I−III−VI_2 semiconductors have higher VB edges and smaller band gaps than their Ag^+-based analogues.[38,57-60] Covalency at the VB edge in these materials can be probed using X-ray photoemission spectroscopy, analysis of spin-orbit splittings at the VB edge, and computational methods, and these techniques consistently indicate substantially more metal *d* character at the VB edge in Cu^+-based I−III−VI_2 materials than in their Ag^+-based analogues.[59-64] For example, the VB edge in $CuInSe_2$ possesses ~50% Cu(3*d*) character, while in $AgInSe_2$ it has only ~20% Ag(4*d*) character.[59,64] These experimental values agree very well with the atomic-

orbital contributions calculated for the mid-gap MOs of Cu^+:CdSe and Ag^+:CdSe NCs shown in Figure 3.3 and Figure 3.4. Interestingly, the emissive excited states of $CuInS_2$ and $CuInSe_2$ NCs also appear to be very similar to those of Cu^+-doped II−VI and III−V NCs such as those described here.[17,21,65-66] One hypothesis that has been proposed[17,21] to explain this spectroscopic similarity invokes hole self-trapping within a very similar $[MSe_4]$ cluster as described here, driven by strong electron−nuclear coupling of the type illustrated in Figure 3.7. In this scenario, these I−III−VI2 NCs behave simply as heavily Cu+- or Ag+-doped semiconductors, an interpretation supported by observations of preserved spectral properties when going from stoichiometric to heavily group-I-deficient compositions.[17]

Similar spectroscopic properties but different electronic structures also occur in many luminescent Cu^+ and Ag^+ molecular complexes, often with diimine and/or diphosphine ligands, which have been of interest for organic light-emitting diodes.[44-49,67-68] Both frequently show large Stokes shifts, broad PL bandshapes, and ferromagnetic excited-state singlet−triplet splittings.[45-47] For many of these Cu^+ complexes, DFT shows dominant Cu(3*d*) character in their HOMOs, generally with substantial covalency, and significant MLCT character in their luminescent excited states.[44-46,68] Computational studies of the analogous Ag^+ complexes indicate very little metal 4*d* character in their HOMOs and correspondingly small MLCT character in their luminescent excited states, and their luminescence is thus better described as ligand-based.[45-49,67-68] These relationships between Cu^+- and Ag^+ molecular complexes thus parallel those described above for Cu^+- and Ag^+-doped semiconductor NCs.

3.6 **Conclusion**

Experimental studies of Ag^+:CdSe and Cu^+:CdSe NCs demonstrate many spectroscopic similarities between these materials. Both display broad, dopant-activated PL with a large effective

Stokes shift and comparable singlet−triplet splitting energies. Their calculated electronic structures are both characterized by mid-gap MOs localized within [MSe_4] dopant clusters ($M = Ag^+$, Cu^+), and both show luminescence involving recombination of delocalized CB electrons with holes that are strongly localized within these [MSe_4] clusters. Despite these similarities, the electronic structures of these two materials show a major qualitative difference: Cu^+ dopants in CdSe NCs follow a "normal" bonding scheme, while Ag^+ dopants in CdSe NCs display "inverted" bonding. This fundamental difference stems from the far greater ionization energy of Ag^+, which places its 4*d* orbitals well below the Se(4*p*) atomic valence orbitals that form the VB. As a consequence of this difference, the mid-gap MOs in Cu^+:CdSe NCs have predominantly Cu(3*d*) character, whereas those of Ag^+:CdSe NCs have predominantly Se(4*p*) character. Our DFT calculations accurately reproduce the experimental trend in Cu^+ and Ag^+ acceptor-level energies (and luminescence energies), as well as the signs and magnitudes of the experimental singlet−triplet splittings. For both types of NCs, our calculations predict similarly large excited-state nuclear reorganization involving a totally symmetric contraction and symmetry-breaking Jahn−Teller distortion within the [MSe_4] dopant cluster. This strong vibronic coupling results in the characteristically broad PL bandshapes of both the Ag^+- and Cu^+-doped semiconductors. The shift from normal bonding in Cu^+:CdSe NCs to inverted bonding in Ag^+:CdSe NCs identified here resolves the apparent paradox of similar spectroscopic properties coexisting with very large differences in Cu^+ and Ag^+ ionization energies. In the broader picture, the challenge of correctly describing the different electronic structures of Ag^+- and Cu^+-doped CdSe NCs despite their nearly indistinguishable optical properties emphasizes the value of combined experimental and computational investigations such as presented here.

3.7 Acknowledgments

The authors thank Kira E. Hughes, Dr. Arianna Marchioro, and Dr. Patrick J. Whitham for experimental assistance. Financial support from the National Science Foundation (Graduate Research Fellowship DGE-1256082 to H.D.N., CHE-1565520 to X.L., and DMR-1505901 to D.R.G.) is gratefully acknowledged. S.O.M.H. gratefully acknowledges the Stichting Fundatie van de Vrijvrouwe van Renswoude te 's-Gravenhage and the Stichting dr. Hendrik Muller's Vaderlandsch Fonds for their financial support. R.F. was also supported by the German Academic Exchange Service (DAAD) with funds from the German Federal Ministry of Education and Research (BMBF) and the People Programme (Marie Curie Actions) of the European Union's Seventh Framework Programme (FP7/2007-2013) under REA grant agreement n° 605728 (P.R.I.M.E. – Postdoctoral Researchers International Mobility Experience). This work was facilitated through the use of advanced computational, storage, and networking infrastructure provided by the Hyak Supercomputer System at the University of Washington, funded by the UW Student Technology Fee.

3.8 Supporting Information

Appendix B. : Temperature-dependent PL spectra of Ag^+:CdSe NCs, calculated densities of states for Cu^+:CdSe and Ag^+:CdSe NCs, calculated ground-state molecular-orbital energies and excited-state energies for Cu^+:CdSe and Ag^+:CdSe NCs of different sizes, natural transition orbitals and ground- and excited-state geometries for smaller Cu^+:CdSe and Ag^+:CdSe NCs, calculated MO energies and compositions for interstitially doped Ag^+:CdSe NCs, mid-gap MO energies for Cu^+:CdSe and Ag^+:CdSe NCs before and after the symmetry-breaking excited-state geometric distortion.

3.9 References

1. *Fundamentals of Phosphors*, 2nd ed.; Yen, W. M.; Shionoya, S.; Yamamoto, H., Eds.; CRC Press: Boca Raton, FL, 2007.
2. Era, K.; Shionoya, S.; Washizawa, Y. Mechanism of Broad-band Luminescences in ZnS Phosphors--I. Spectrum Shift During Decay and with Excitation Intensity. *J. Phys. Chem. Solids* **1968**, *29*, 1827-1841.
3. Era, K.; Shionoya, S.; Washizawa, Y.; Ohmatsu, H. Mechanism of Broad-band Luminescences in ZnS Phosphors--II. Characteristics of Pair Emission Type Luminescences. *J. Phys. Chem. Solids* **1968**, *29*, 1843-1857.
4. Avinor, M.; Meijer, G. Emission of Activated Cadmium Selenide Phosphors. *J. Chem. Phys.* **1960**, *32*, 1456-1458.
5. Schwenkenbecher, K.; Boyn, R.; Resagk, H. Optical Transitions at Ag Centers in ZnS Crystals. *Phys. Status Solidi B* **1980**, *101*, 215-220.
6. Suzuki, A.; Shionoya, S. Mechanism of the Green-Copper Luminescence in ZnS Crystals. I. Direct Evidence for the Pair Emission Mechanism. *J. Phys. Soc. Jpn.* **1971**, *31*, 1455-1461.
7. Swaminathan, V.; Greene, L. C. Low Temperature Photoluminescence in Ag-doped ZnSe. *J. Lumin.* **1976**, *14*, 357-363.
8. Suyver, J. F.; van der Beek, T.; Wuister, S. F.; Kelly, J. J.; Meijerink, A. Luminescence of Nanocrystalline ZnSe:Cu. *Appl. Phys. Lett.* **2001**, *79*, 4222−4224.
9. Xie, R.; Peng, X. Synthesis of Cu-Doped InP Nanocrystals (d-dots) with ZnSe Diffusion Barrier as Efficient and Color-Tunable NIR Emitters. *J. Am. Chem. Soc.* **2009**, *131*, 10645−10651.
10. Ishizumi, A.; Kanemitsu, Y. Photoluminescence Spectra and Dynamics of Al^{3+}- and Ag^{+}-Doped CdS Nanocrystals. *J. Phys. Soc. Jpn.* **2010**, *79*, 093706.
11. Viswanatha, R.; Brovelli, S.; Pandey, A.; Crooker, S. A.; Klimov, V. I. Copper-Doped Inverted Core/Shell Nanocrystals with "Permanent" Optically Active Holes. *Nano Lett.* **2011**, *11*, 4753–4758.
12. Sahu, A.; Kang, M. S.; Kompch, A.; Notthoff, C.; Wills, A. W.; Deng, D.; Winterer, M.; Frisbie, C. D.; Norris, D. J. Electronic Impurity Doping in CdSe Nanocrystals. *Nano Lett.* **2012**, *12*, 2587-2594.
13. Jana, S.; Manna, G.; Srivastava, B. B.; Pradhan, N. Tuning the Emission Colors of Semiconductor Nanocrystals Beyond their Bandgap Tunability: All in the Dope. *Small* **2013**, *9*, 3753-3758.
14. Sarkar, S.; Guria, A. K.; Patra, B. K.; Pradhan, N. Synthesis and Photo-darkening/Photo-brightening of Blue Emitting Doped Semiconductor Nanocrystals. *Nanoscale* **2014**, *6*, 3786-3790.
15. Liu, J.; Zhao, Q.; Liu, J.-L.; Wu, Y.-S.; Cheng, Y.; Ji, M.-W.; Qian, H.-M.; Hao, W.-C.; Zhang, L.-J.; Wei, X.-J.; Wang, S.-G.; Zhang, J.-T.; Du, Y.; Dou, S.-X.; Zhu, H.-S. Heterovalent-Doping-Enabled Efficient Dopant Luminescence and Controllable Electronic

Impurity Via a New Strategy of Preparing II−VI Nanocrystals. *Adv. Mater.* **2015**, *27*, 2753-2761.

16. Gopal, M. B. Ag and Cu Doped Colloidal CdSe Nanocrystals: Partial Cation Exchange and Luminescence. *Mater. Res. Express* **2015**, *2*, 085004.
17. Knowles, K. E.; Hartstein, K. H.; Kilburn, T. B.; Marchioro, A.; Nelson, H. D.; Whitham, P. J.; Gamelin, D. R. Luminescent Colloidal Semiconductor Nanocrystals Containing Copper: Synthesis, Photophysics, and Applications. *Chem. Rev.* **2016**, *116*, 10820-10851.
18. Bradshaw, L. R.; Knowles, K. E.; McDowall, S.; Gamelin, D. R. Nanocrystals for Luminescent Solar Concentrators. *Nano Lett.* **2015**, *15*, 1315-1323.
19. Knowles, K. E.; Kilburn, T. B.; Alzate, D. G.; McDowall, S.; Gamelin, D. R. Bright $CuInS_2$/CdS Nanocrystal Phosphors for High-gain Full-spectrum Luminescent Solar Concentrators. *Chem. Commun.* **2015**, *51*, 9129-9132.
20. Yang, L.; Knowles, K. E.; Gopalan, A.; Hughes, K. E.; James, M. C.; Gamelin, D. R. One-Pot Synthesis of Monodisperse Colloidal Copper-Doped CdSe Nanocrystals Mediated by Ligand−Copper Interactions. *Chem. Mater.* **2016**, *28*, 7375–7384.
21. Knowles, K. E.; Nelson, H. D.; Kilburn, T. B.; Gamelin, D. R. Singlet−Triplet Splittings in the Luminescent Excited States of Colloidal Cu^+:CdSe, Cu^+:InP, and $CuInS_2$ Nanocrystals: Charge-Transfer Configurations and Self-Trapped Excitons. *J. Am. Chem. Soc.* **2015**, *137*, 13138–13147.
22. Grochala, W.; Mazej, Z. Chemistry of Silver(II): A Cornucopia of Peculiarities. *Philos. Trans. R. Soc., A* **2015**, *373*, 20140179.
23. *CRC Handbook of Chemistry and Physics*, 97th ed.; Boca Raton, FL, 2016.
24. Piepho, S. B.; Schatz, P. N. *Group Theory in Spectroscopy with Applications to Magnetic Circular Dichroism*; Wiley: New York, 1983.
25. Frisch, M. J.; Trucks, G. W.; Schlegel, H. B.; Scuseria, G. E.; Robb, M. A.; Cheeseman, J. R.; Scalmani, G.; Barone, V.; Mennucci, B.; Petersson, G. A.; Nakatsuji, H.; Caricato, M.; Li, X.; Hratchian, H. P.; Izmaylov, A. F.; Bloino, J.; Zheng, G.; Sonnenberg, J. L.; Hada, M.; Ehara, M.; Toyota, K.; Fukuda, R.; Hasegawa, J.; Ishida, M.; Nakajima, T.; Honda, Y.; Kitao, O.; Nakai, H.; Vreven, T.; Montgomery Jr., J. A.; Peralta, J. E.; Ogliaro, F.; Bearpark, M. J.; Heyd, J.; Brothers, E. N.; Kudin, K. N.; Staroverov, V. N.; Kobayashi, R.; Normand, J.; Raghavachari, K.; Rendell, A. P.; Burant, J. C.; Iyengar, S. S.; Tomasi, J.; Cossi, M.; Rega, N.; Millam, N. J.; Klene, M.; Knox, J. E.; Cross, J. B.; Bakken, V.; Adamo, C.; Jaramillo, J.; Gomperts, R.; Stratmann, R. E.; Yazyev, O.; Austin, A. J.; Cammi, R.; Pomelli, C.; Ochterski, J. W.; Martin, R. L.; Morokuma, K.; Zakrzewski, V. G.; Voth, G. A.; Salvador, P.; Dannenberg, J. J.; Dapprich, S.; Daniels, A. D.; Farkas, Ö.; Foresman, J. B.; Ortiz, J. V.; Cioslowski, J.; Fox, D. J. *Gaussian 09*, Gaussian, Inc.: Wallingford, CT, USA, 2009.
26. Perdew, J. P.; Burke, K.; Ernzerhof, M. Generalized Gradient Approximation Made Simple. *Phys. Rev. Lett.* **1996**, *77*, 3865-3868.
27. Adamo, C.; Barone, V. Toward Reliable Density Functional Methods without Adjustable Parameters: The PBE0 Model. *J. Chem. Phys.* **1999**, *110*, 6158-6170.

28. Hay, P. J.; Wadt, W. R. *Ab initio* Effective Core Potentials for Molecular Calculations. Potentials for K to Au Including the Outermost Core Orbitals. *J. Chem. Phys.* **1985**, *82*, 299-310.

29. Wadt, W. R.; Hay, P. J. *Ab initio* Effective Core Potentials for Molecular Calculations. Potentials for Main Group Elements Na to Bi. *J. Chem. Phys.* **1985**, *82*, 284-298.

30. Hay, P. J.; Wadt, W. R. *Ab initio* Effective Core Potentials for Molecular Calculations. Potentials for the Transition Metal Atoms Sc to Hg. *J. Chem. Phys.* **1985**, *82*, 270-283.

31. Nelson, H. D.; Li, X.; Gamelin, D. R. Computational Studies of the Electronic Structures of Copper-Doped CdSe Nanocrystals: Oxidation States, Jahn−Teller Distortions, Vibronic Bandshapes, and Singlet−Triplet Splittings. *J. Phys. Chem. C* **2016**, *120*, 5714-5723.

32. Beaulac, R.; Feng, Y.; May, J. W.; Badaeva, E.; Gamelin, D. R.; Li, X. Orbital Pathways for Mn^{2+}-carrier *s p-d* Exchange in Diluted Magnetic Semiconductor Quantum Dots. *Phys. Rev. B* **2011**, *84*, 195324.

33. Badaeva, E.; Feng, Y.; Gamelin, D. R.; Li, X. Investigation of Pure and Co^{2+}-Doped ZnO Quantum Dot Electronic Structures Using the Density Functional Theory: Choosing the Right Functional. *New J. Phys.* **2008**, *10*, 055013.

34. Goings, J. J.; Schimpf, A. M.; May, J. W.; Johns, R. W.; Gamelin, D. R.; Li., X. Theoretical Characterization of Conduction-Band Electrons in Photodoped and Aluminum-Doped Zinc Oxide (AZO) Quantum Dots. *J. Phys. Chem. C* **2014**, *118*, 26584−26590.

35. Badaeva, E.; Isborn, C. M.; Feng, Y.; Ochsenbein, S. T.; Gamelin, D. R.; Li, X. Theoretical Characterization of Electronic Transitions in Co^{2+}- and Mn^{2+}-Doped ZnO Nanocrystals. *J. Phys. Chem. C* **2009**, *113*, 8710-8717.

36. Liang, W.; Fischer, S. A.; Frisch, M. J.; Li, X. Energy-Specific Linear Response TDHF/TDDFT for Calculating High-Energy Excited States. *J. Chem. Theory Comput.* **2011**, *7*, 3540-3547.

37. Martin, R. L. Natural Transition Orbitals. *J. Chem. Phys.* **2003**, *118*, 4775-4777.

38. Madelung, O. *Semiconductors: Data Handbook*, 3rd ed.; Springer: Berlin, 2004.

39. Huang, X.; Lindgren, E.; Chelikowsky, J. R. Surface Passivation Method for Semiconductor Nanostructures. *Phys. Rev. B* **2005**, *71*, 165328.

40. Wang, L.-W.; Li, J. First-Principles Thousand-Atom Quantum Dot Calculations. *Phys. Rev. B* **2004**, *69*, 153302.

41. Whitham, P. J.; Knowles, K. E.; Reid, P. J.; Gamelin, D. R. Photoluminescence Blinking and Reversible Electron Trapping in Copper-Doped CdSe Nanocrystals. *Nano Lett.* **2015**, *15*, 4045-4051.

42. Dean, P. J.; Fitzpatrick, B. J.; Bhargava, R. N. Optical Properties of ZnSe Doped with Ag and Au. *Phys. Rev. B* **1982**, *26*, 2016-2035.

43. Holtz, P. O.; Monemar, B.; Lozykowski, H. J. Optical Properties of Ag-related Centers in Bulk ZnSe. *Phys. Rev. B* **1985**, *32*, 986-996.

44. Czerwieniec, R.; Leitl, M. J.; Homeier, H. H. H.; Yersin, H. Cu(I) Complexes – Thermally Activated Delayed Fluorescence. Photophysical Approach and Material Design. *Coord. Chem. Rev.* **2016**, *325*, 2-28.

45. Osawa, M.; Kawata, I.; Ishii, R.; Igawa, S.; Hashimoto, M.; Hoshino, M. Application of Neutral d^{10} Coinage Metal Complexes with an Anionic Bidentate Ligand in Delayed Fluorescence-type Organic Light-emitting Diodes. *J. Mater. Chem. C* **2013**, *1*, 4375-4383.

46. Yersin, H.; Leitl, M. J.; Czerwieniec, R. TADF for Singlet Harvesting – Next Generation OLED Materials Based on Brightly Green and Blue Emitting Cu(I) and Ag(I) Compounds. *Proc. SPIE* **2014**, *9183*, 91830N.

47. Chen, J.; Teng, T.; Kang, L.; Chen, X.-L.; Wu, X.-Y.; Yu, R.; Lu, C.-Z. Highly Efficient Thermally Activated Delayed Fluorescence in Dinuclear Ag(I) Complexes with a Bis-Bidentate Tetraphosphane Bridging Ligand. *Inorg. Chem.* **2016**, *55*, 9528-9536.

48. Barbieri, A.; Accorsi, G.; Armaroli, N. Luminescent Complexes Beyond the Platinum Group: The d^{10} Avenue. *Chem. Commun.* **2008**, *44*, 2185-2193.

49. Shafikov, M. Z.; Suleymanova, A. F.; Czerwieniec, R.; Yersin, H. Design Strategy for Ag(I)-Based Thermally Activated Delayed Fluorescence Reaching an Efficiency Breakthrough. *Chem. Mater.* **2017**, 10.1021/acs.chemmater.6b05175.

50. Kompch, A.; Sahu, A.; Notthoff, C.; Ott, F.; Norris, D. J.; Winterer, M. Localization of Ag Dopant Atoms in CdSe Nanocrystals by Reverse Monte Carlo Analysis of EXAFS Spectra. *J. Phys. Chem. C* **2015**, *119*, 18762-18772.

51. Kittilstved, K. R.; Liu, W. K.; Gamelin, D. R. Electronic Structure Origins of Polarity-Dependent High-T_C Ferromagnetism in Oxide-Diluted Magnetic Semiconductors. *Nat. Mater.* **2006**, *5*, 291-297.

52. Wei, S.-H.; Zunger, A. Role of Metal *d* States in II-VI Semiconductors. *Phys. Rev. B* **1988**, *37*, 8958-8981.

53. Hoffmann, R.; Alvarez, S.; Mealli, C.; Falceto, A.; Cahill, T. J.; Zeng, T.; Manca, G. From Widely Accepted Concepts in Coordination Chemistry to Inverted Ligand Fields. *Chem. Rev.* **2016**, *116*, 8173-8192.

54. Walroth, R. C.; Lukens, J. T.; MacMillan, S. N.; Finkelstein, K. D.; Lancaster, K. M. Spectroscopic Evidence for a $3d^{10}$ Ground State Electronic Configuration and Ligand Field Inversion in $[Cu(CF_3)_4]^{1-}$. *J. Am. Chem. Soc.* **2016**, *138*, 1922-1931.

55. Ley, L.; Pollak, R. A.; McFeely, F. R.; Kowalczyk, S. P.; Shirley, D. A. Total Valence-Band Densities of States of III-V and II-VI Compounds from X-ray Photoemission Spectroscopy. *Phys. Rev. B* **1974**, *9*, 600-621.

56. Hemstreet, L. A. Trends in the Electronic Properties of Substitutional 3*d* Transition-metal Impurities in GaAs. *Phys. Rev. B* **1980**, *22*, 4590-4599.

57. Jaffe, J. E.; Zunger, A. Theory of the Band-gap Anomaly in ABC_2 Chalcopyrite Semiconductors. *Phys. Rev. B* **1984**, *29*, 1882-1906.

58. Shay, J. L.; Kasper, H. M. Direct Observation of Cu *d* Levels in I-III-VI_2 Compounds. *Phys. Rev. Lett.* **1972**, *29*, 1162-1164.

59. Shay, J. L.; Tell, B.; Kasper, H. M.; Schiavone, L. M. *p-d* Hybridization of the Valence Bands of I-III-VI_2 Compounds. *Phys. Rev. B* **1972**, *5*, 5003-5005.

60. Rife, J. C.; Dexter, R. N.; Bridenbaugh, P. M.; Veal, B. W. Optical Properties of the Chalcopyrite Semiconductors $ZnGeP_2$, $ZnGeAs_2$, $CuGaS_2$, $CuAlS_2$, $CuInSe_2$, and $AgInSe_2$. *Phys. Rev. B* **1977**, *16*, 4491-4500.

61. Braun, W.; Goldmann, A.; Cardona, M. Partial Density of Valence States of Amorphous and Crystalline $AgInTe_2$ and $CuInS_2$. *Phys. Rev. B* **1974**, *10*, 5069-5074.

62. Lavrentyev, A. A.; Nikiforov, I. Y.; Gabrelian, B. V. The Chemical Bonding in Crystals with Chalcopyrite Structure. *J. Phys. IV* **1997**, *7*, 283-284.

63. Takarabe, K.; Kawai, K.; Minomura, S.; Irie, T.; Taniguchi, M. Electronic Structure of Some I−III−VI_2 Chalcopyrite Semiconductors Studied by Synchrotron Radiation. *J. Appl. Phys.* **1992**, *71*, 441-447.

64. Löher, T.; Klein, A.; Pettenkofer, C.; Jaegermann, W. Partial Density of States in the $CuInSe_2$ Valence Bands. *J. Appl. Phys.* **1997**, *81*, 7806-7809.

65. Rice, W. D.; McDaniel, H.; Klimov, V. I.; Crooker, S. A. Magneto-Optical Properties of $CuInS_2$ Nanocrystals. *J Phys. Chem. Lett.* **2014**, *5*, 4105-4109.

66. Berends, A. C.; Rabouw, F. T.; Spoor, F. C. M.; Bladt, E.; Grozema, F. C.; Houtepen, A. J.; Siebbeles, L. D. A.; de Mello Donegá, C. Radiative and Nonradiative Recombination in $CuInS_2$ Nanocrystals and $CuInS_2$-Based Core/Shell Nanocrystals. *J Phys. Chem. Lett.* **2016**, *7*, 3503-3509.

67. Matsumoto, K.; Shindo, T.; Mukasa, N.; Tsukuda, T.; Tsubomura, T. Luminescent Mononuclear Ag(I)−Bis(diphosphine) Complexes: Correlation between the Photophysics and the Structures of Mononuclear Ag(I)−Bis(diphosphine) Complexes. *Inorg. Chem.* **2010**, *49*, 805-814.

68. Hsu, C.-W.; Lin, C.-C.; Chung, M.-W.; Chi, Y.; Lee, G.-H.; Chou, P.-T.; Chang, C.-H.; Chen, P.-Y. Systematic Investigation of the Metal-Structure−Photophysics Relationship of Emissive d^{10}-Complexes of Group 11 Elements: The Prospect of Application in Organic Light Emitting Devices. *J. Am. Chem. Soc.* **2011**, *133*, 12085-12099.

Chapter 4. Valence-Band Electronic Structures of Cu^+-Doped ZnS, Alloyed Cu–In–Zn–S, and Ternary $CuInS_2$ Nanocrystals: A Unified Description of Photoluminescence Across Compositions

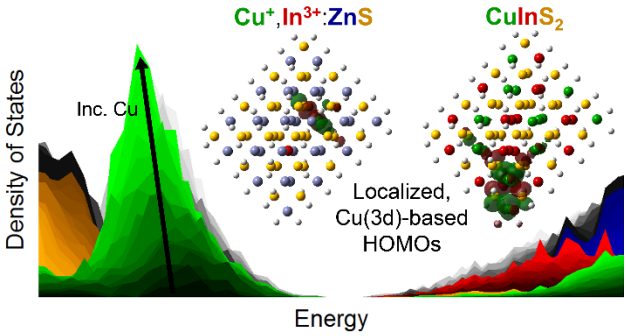

4.1 **Overview**

Copper-doped and copper-based colloidal semiconductor nanocrystals have attracted broad attention as phosphors in many contexts, but fundamental aspects of their electronic structures that give rise to their photoluminescence are not understood. Here, we report a detailed systematic investigation of the electronic structures of Cu^+-doped ZnS, alloyed Cu–In–Zn–S, and $CuInS_2$ nanocrystals (NCs) using density functional theory. These calculations demonstrate a continuous evolution in electronic structure from lightly doped to ternary compositions. As an impurity, Cu^+ introduces isolated mid-gap *d* orbitals above the valence-band edge, with large Cu(3*d*)–S(3*p*) covalency. As the Cu^+ content is increased in Cu–In–Zn–S alloys, these orbitals evolve to become the $CuInS_2$ valence band in the ternary limit. The calculations further describe the highest occupied molecular orbital (HOMO) as localized and Cu(3*d*)-based for all compositions from Cu^+-doped ZnS to stoichiometric $CuInS_2$. The calculations predict that the Cu(3*d*)-based HOMOs can only delocalize over ca. 2 or 3 adjacent Cu^+ ions but not more, reflecting weak Cu^+–Cu^+ electronic coupling, attributable in large measure to the directionality of the *d*-orbitals. HOMO localization

is also sensitive to the local Cu^+ environment, Cu^+–Cu^+ geometric connectivity, and electrostatics. We conclude that the Cu(3*d*)-based HOMO of chalcopyrite $CuInS_2$ makes localization likely even in defect-free $CuInS_2$ NCs, placing this material in stark contrast with structurally analogous II–VI semiconductor NCs that have anion *p*-orbital-based HOMOs and show facile HOMO delocalization. The strong tendency for HOMO localization in both Cu^+-doped II–VI and Cu^+-based chalcopyrite NCs has significant implications for interpretation of the photophysical properties of such materials.

4.2 Introduction

Copper-doped and ternary copper-based semiconductor nanocrystals (NCs) have recently attracted attention as bright, tunable phosphors for applications including solar-energy conversion, energy-efficient lighting, and bioimaging.[1-6] Very similar photoluminescence (PL) has been observed in materials ranging from II–VI NCs doped with single Cu^+ ions to stoichiometric I–III–VI_2 $CuInS_2$ NCs,[1,7-8] including emission energies that depend on both the NC size and composition. Compared to the excitonic PL of II–VI NCs, emission from these copper-containing NCs is also much broader (fwhm > 100 meV) and shows larger effective Stokes shifts and longer PL lifetimes (~100s of ns). In Cu^+-doped NCs, the PL mechanism involves recombination of a photogenerated delocalized conduction-band (CB) electron with a photogenerated hole that has been captured by the Cu^+ dopant, formally oxidizing it to Cu^{2+}. The PL mechanism is less clear in $CuInS_2$ NCs and related I–III–VI_2 materials, but most proposals invoke localization of one or both charge carriers, and many suggest that recombination occurs between a delocalized CB electron and a localized hole.[1-2] Many reports have concluded that the hole is trapped at a lattice defect, often suggested to be a copper vacancy (V_{Cu}).[1-2,9-11] Based on the similarities between the PL of Cu^+-doped and $CuInS_2$ NCs, some recent studies have suggested that $CuInS_2$ PL actually involves a hole localized at a

copper defect, such as Cu^{2+} with an adjacent charge-compensating defect or Cu^{+} located at an In^{3+} site (Cu_{In} anti-site defect).[7,12-13]

An alternative mechanism that has been proposed for explaining the PL of $CuInS_2$ NCs is exciton self-trapping.[8] In this scenario, the potential energy associated with hole localization outcompetes the kinetic energy associated with hole delocalization, reflecting weak Cu^{+}–Cu^{+} electronic coupling relative to localization forces such as electron–phonon coupling. In bulk exciton self-trapping, hole contraction drives a local nuclear distortion that favors further hole localization until a distorted equilibrium structure is reached. Exciton self-trapping has been studied in many semiconductors, including the classic example of $AgCl_{1-x}Br_x$ and the more recent example of 2D lead-halide perovskites.[14-19] In the exciton self-trapping picture, $CuInS_2$ NCs can be described as Cu^{+}-doped NCs in the heavy doping limit (*i.e.*, 50% Cu^{+}). Transient optical[20] and x-ray absorption[21] data appear to support hole localization at copper in $CuInS_2$ NCs, accompanied by partial copper oxidation, although it remains unclear whether the participating copper is a native defect (*e.g.*, Cu_{In} anti-site, unpassivated surface Cu^{+}) or a bulk-like lattice Cu^{+}. Further work to understand where and why holes localize in $CuInS_2$ NCs would improve our understanding of the PL of these important materials.

Alloyed Cu–In–Zn–S NCs offer a bridge between Cu^{+}-doped and $CuInS_2$ NCs that can help to consolidate our understanding of these materials. In bulk, $CuInS_2$ and ZnS form a continuous solid solution.[22] NCs in this family have been synthesized with compositions ranging from Cu^{+}-doped Zn–In–S to "Zn^{2+}-alloyed" $CuInS_2$.[23-34] Alloyed NCs can also be formed by cation exchange with $CuInS_2$ NCs,[35-37] and alloying often occurs during ZnS shell growth on $CuInS_2$ NCs,[24,35,38-41] controlled by the NC surface chemistry and synthesis conditions.[41] In general, the PL of Cu–In–Zn–S alloy NCs resembles that of both Cu^{+}-doped and $CuInS_2$ NCs,

showing broad PL line widths, large effective Stokes shifts, and long lifetimes. The PL energy depends on the NC composition, with a higher Zn^{2+} concentration generally yielding higher-energy emission.[23-25,29-37,42] This PL has been attributed variously to Cu^{+}-centered and defect-based mechanisms.

Here, we present results from density functional theory (DFT) calculations on a systematic series of NCs spanning from undoped ZnS to $CuInS_2$ *via* Cu^{+}-doped and Cu–In–Zn–S alloy compositions. The calculated densities of states of these NCs are consistent with the known electronic structures of bulk Cu^{+}-doped II–VI and $CuInS_2$ semiconductors, and with the expected properties of the intermediate compositions. Upon closer inspection, however, the valence-band-edge (VB-edge) MOs of $CuInS_2$ NCs are consistently found to localize within small clusters of lattice Cu^{+} ions, thus closely resembling the HOMOs of Cu^{+}-doped NCs, which are localized at individual Cu^{+} ions. The specifics of this localization are sensitive to symmetry-breaking and electrostatic perturbations, but localization is still observed even in the absence of lattice defects. The strong propensity for hole localization reflects relatively weak Cu^{+}–Cu^{+} electronic coupling within the copper *d* band that defines the $CuInS_2$ NC VB edge.

4.3 Methods

DFT calculations were performed using Gaussian 09[43] with the PBE0 hybrid DFT functional.[44-45] Atoms were described with the Los Alamos double-ζ pseudocore potential and corresponding basis set, with explicit basis functions used to describe the Cu(3*d*, 4*s*, 4*p*), In(5*s*, 5*p*), Zn(3*d*, 4*s*, 4*p*), and S(3*s*, 3*p*) atomic orbitals.[46-48] The electronic structures of other doped and undoped semiconductor NCs, including Cu^{+}:CdSe NCs, have been previously described by this method.[49-53]

All NC structures were constructed with 34, 77, or 134 total cations, with atomic positions based on the bulk zinc-blende crystal structure. Ground-state geometric relaxation was performed

for all structures before any other electronic-structure calculations were performed. Dangling bonds on uncompensated surface ions were passivated by pseudo-atoms with fractional charges (+1.75 for Cu^+, +1.25 for In^{3+}, +1.5 for Zn^{2+}, and +0.5 for S^{2-}).[54-55]

For each structure in the series of alloyed $Zn_{34-2n}Cu_nIn_nS_{34}$ NCs, $2n$ Zn^{2+} cations were randomly replaced by n Cu^+ and n In^{3+} cations (n = 1 to 16), maintaining charge neutrality of the overall structure. Cu^+ and In^{3+} cations were placed according to the sites they would occupy if the entire NC had the ordered chalcopyrite $CuInS_2$ crystal structure. With the pseudo-atom surface capping scheme, surface charge neutrality must also be maintained, so the number of surface Cu^+ and surface In^{3+} (more specifically, the number of surface pseudo-atoms bound to Cu^+ and the number of surface pseudo-atoms bound to In^{3+}) was also constrained to be equal. Ten structures were generated for each intermediate composition. Two different ordered chalcopyrite $Cu_{17}In_{17}S_{34}$ structures were also generated. In total, 163 NC structures were generated for this series.

For other doped structures, Cu^+ and In^{3+} were placed in different configurations near the NC center according to the chalcopyrite crystal structure, except where indicated. For Cu^+-doped structures without charge-compensating In^{3+}, the charge of the NC core was set to $-n$ (where n is the number of Cu^+ dopants) and a compensating charge of $+n$ was distributed equally over the pseudo-atoms on the surface, representing charge compensation by ligands or defects on the NC surface.[49,52]

4.4 Results and Analysis

4.4.1 Overview of $Zn_{2-2x}(Cu,In)_xS_2$ NC Electronic Structure

Figure 4.1 illustrates the calculated electronic structures of a series of alloyed $Zn_{2-2x}(Cu,In)_xS_2$ NCs. Figure 4.1a shows the progression of the density of states (DOS) from ZnS to $CuInS_2$ as more Cu^+ and In^{3+} are added in place of Zn^{2+}. After introduction of a single Cu^+ dopant to the

starting ZnS NC, the DOS shows a small contribution from Cu^+ well above the ZnS VB edge, arising from five doubly occupied mid-gap MOs dominated by Cu(3*d*) character. These MOs are similar to the dopant-centered MOs previously described in depth by DFT for Cu^+:CdSe NCs.[49] With increasing Cu^+ concentration, the Cu^+-based DOS above the VB increases, eventually becoming the VB of $CuInS_2$. In bulk $CuInS_2$, DFT calculations and x-ray photoelectron spectroscopy show that the upper region of the VB has ~45−60% Cu(3*d*) character and a high covalency with the S(2*p*) orbitals, whereas the deeper part of the VB has primarily S(2*p*) character.[56-59] This description is reproduced well by the NC calculations summarized in Figure 4.1a. Interestingly, the width of the Cu(3*d*) band does not change substantially with increasing Cu^+ concentration, suggesting low dispersion within this copper *d*-band. The CB changes more gradually than the VB across this alloy series, with contributions from Zn(4*s*) orbitals being replaced by those from In(5*s*) and Cu(4*s*) orbitals. Unlike Cu^+, In^{3+} does not generate a distinct impurity band in these NCs, although it does dominate the CB edge at high concentrations.

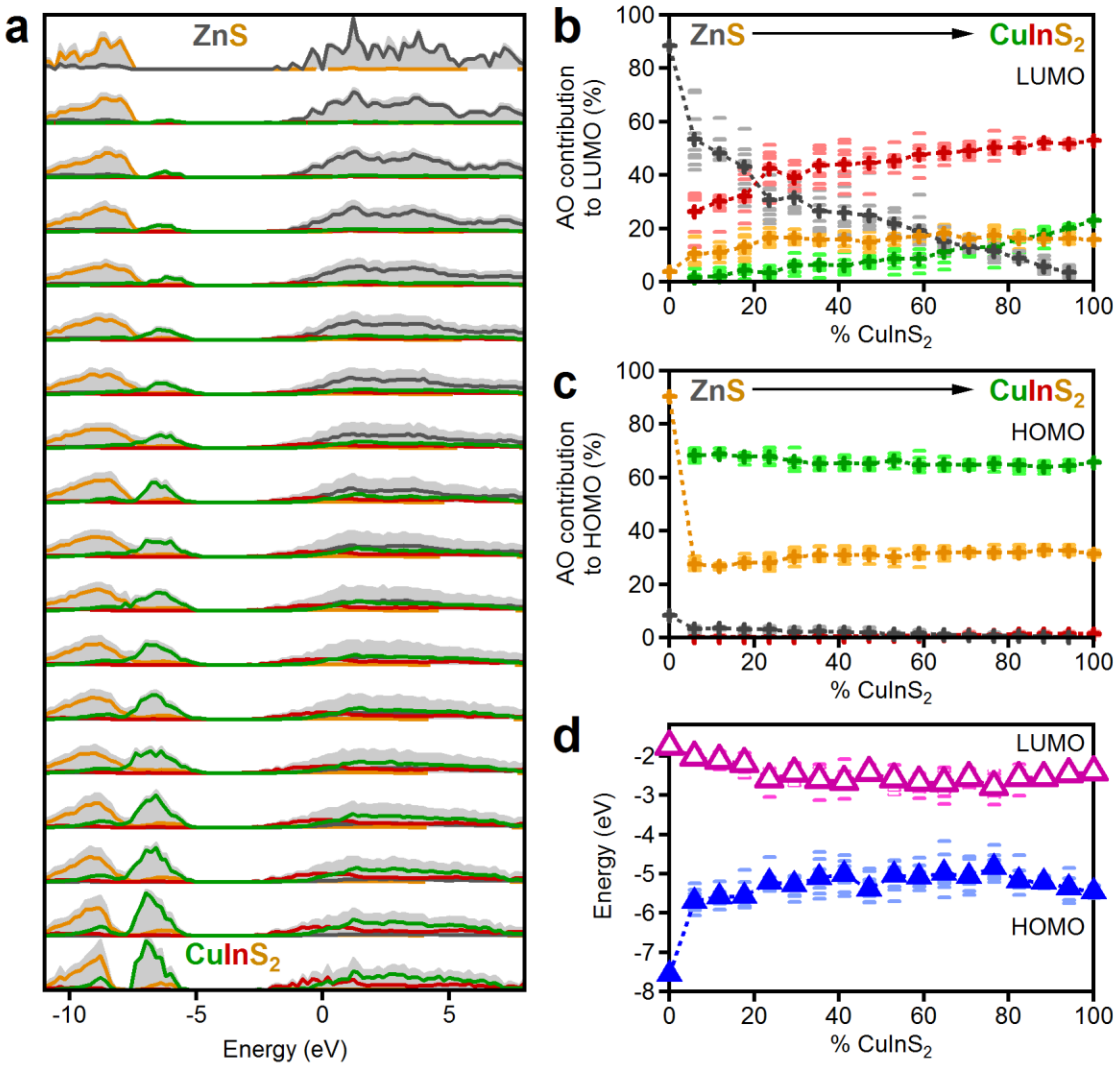

Figure 4.1. Calculated electronic structures of randomly alloyed Cu–In–Zn–S NCs. (a) Density-of-states (DOS) diagrams for $Zn_{34-2n}Cu_nIn_nS_{34}$ random-alloy NCs (n = 0 to 17), ranging from undoped ZnS (top) to $CuInS_2$ (bottom). The total DOS is shown in solid gray, and contributions from Cu^+ are shown in green, In^{3+} in red, Zn in dark gray, and S^{2-} in yellow. Each intermediate composition (n = 1 to 16) represents the average DOS from 10 different NC structures with Cu^+ and In^{3+} cations replacing random Zn^{2+} cations but following the chalcopyrite crystal structure. **(b-c)** Atomic-orbital (AO) contributions to the LUMO (b) and HOMO (c) of each NC in this alloy series. Contributions from Cu^+ are shown in green, In^{3+} in red, Zn^{2+} in gray, and S^{2-} in yellow. Horizontal dashes show the calculated values for each individual structure; + symbols show the average values for each composition. **(d)** HOMO (blue, filled triangles) and LUMO (purple, open triangles) energies of each NC. Horizontal dashes show the calculated values for each individual structure; triangles show the average values for each composition. The dotted lines in (b-d) are guides to the eye.

Figure 4.1b,c plots the atomic-orbital contributions to the LUMO (CB edge) and HOMO (VB edge or Cu^+ impurity level) of each NC in this alloy series, respectively. Figure 4.1b shows a gradual change in the LUMO from primarily Zn(4*s*) character to primarily In(5*s*) character. The changes in the HOMO (Figure 4.1c) are qualitatively very different from those in the LUMO. In ZnS, the HOMO has primarily S(3*p*) character. In all Cu^+-containing NCs, however, the HOMO has ~65% Cu(3*d*) character, with the rest coming from S(3*p*). The Cu^+(3*d*) character of the HOMO remains nearly constant throughout the entire alloy series from doped ZnS to stoichiometric $CuInS_2$.

Figure 4.1d plots the HOMO and LUMO energies across this alloy series. The LUMO gradually shifts lower with increasing In^{3+} concentration. Addition of a single Cu^+ also raises the HOMO by ~2 eV relative to the ZnS VB edge, but the HOMO energy then remains almost constant with increased alloying. The calculations suggest that the HOMO and LUMO energies can vary by as much as 1 eV within a set of NCs with the same composition but different Cu^+ and In^{3+} spatial positions. This variation, obtained from calculations on numerous randomly generated individual structures, is illustrated in Figure 4.1d by the set of horizontal lines at each specific composition. Although likely exaggerated in these very small NCs, this variance suggests significant inhomogeneous broadening in the spectroscopy of alloyed NC ensembles, even if all NCs had identical sizes and compositions.

Figure 4.2 illustrates the HOMO and LUMO of representative NCs with $Zn_{2-2x}(Cu,In)_xS_2$ compositions ranging from ZnS to $CuInS_2$. In the undoped ZnS NC (Figure 4.2a), both the HOMO and LUMO are delocalized over the entire NC. Addition of just one Cu^+ and one In^{3+} results in a highly localized HOMO and slightly contracted LUMO (Figure 4.2b), consistent with the introduction of a deep Cu^+ mid-gap level above the VB edge and a shallow In^{3+} level near the CB

edge. Increasing the Cu^+ and In^{3+} concentrations does not change the spatial extent of the HOMO or LUMO substantially. Even for stoichiometric $CuInS_2$ (Figure 4.2f), the HOMO is still localized and the LUMO is still delocalized. From the DOS and atomic-orbital contributions shown in Figure 4.1 and the HOMO/LUMO illustrations in Figure 4.2, we conclude that the DFT calculations yield very similar, localized Cu^+-based HOMOs and largely delocalized LUMOs for all Cu−In−Zn−S NC compositions from Cu^+-doped ZnS to $CuInS_2$. These results are consistent with the proposal from experimental studies that all of these materials display a similar PL mechanism involving recombination of a delocalized electron with a copper-localized hole.

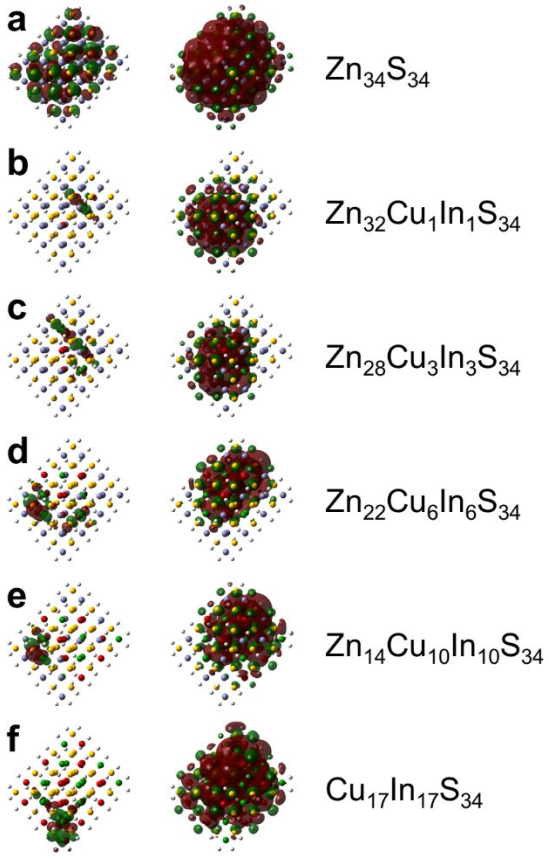

Figure 4.2. HOMOs and LUMOs of randomly alloyed Cu−In−Zn−S NCs. HOMO and LUMO surfaces for a series of 34-cation NCs ranging from ZnS to $CuInS_2$, including **(a)** undoped ZnS, **(b-e)** $Zn_{34-2n}Cu_nIn_nS_{34}$ with increasing n, and **(f)** stoichiometric $CuInS_2$. In this series, Cu^+ and In^{3+} dopants are placed in adjacent cation sites near the center of the NC, following the chalcopyrite crystal structure.

HOMO and LUMO surfaces are visualized at 80% density (*i.e.*, 80% probability that an electron occupying this orbital is inside the pictured surface).

4.4.2 Analysis of HOMOs in $Zn_{2-2x}(Cu,In)_xS_2$ NCs

To investigate the HOMO localization revealed in Figure 4.2, calculations were performed on a series of larger (77-cation) ZnS NCs with increasing numbers of adjacent Cu^+ and In^{3+} dopants. Figure 4.3 shows zoomed-in portions of the HOMO surfaces calculated for these NCs, depicting only the dopant-containing fragments of the structures (depictions of the full HOMOs are provided in Appendix C.). Figure 4.3 also details the atomic-orbital contributions to these HOMOs. From Figure 4.3a, the HOMO of the NC doped with just 1 Cu^+ and 1 In^{3+} is localized around the Cu^+ dopant, whose 3*d* orbitals make up ~60% of the HOMO. This HOMO is very similar to that of the same NC doped with 1 Cu^+ only; In^{3+} does not have any significant effect on the HOMO. Figure 4.3b shows that addition of a second adjacent Cu^+ dopant causes delocalization of the HOMO over both Cu^+ ions. The overall contribution from Cu^+ to the HOMO remains ~60%, but both dopants now contribute equally. Figure 4.3c,d shows that the HOMO does not delocalize further upon adding a third or fourth adjacent Cu^+ dopant. Instead, the HOMO remains primarily localized on just two Cu^+ dopants. After delocalization over one pair of Cu^+–Cu^+ nearest neighbors, the HOMO thus does not change significantly at higher Cu^+ concentrations.

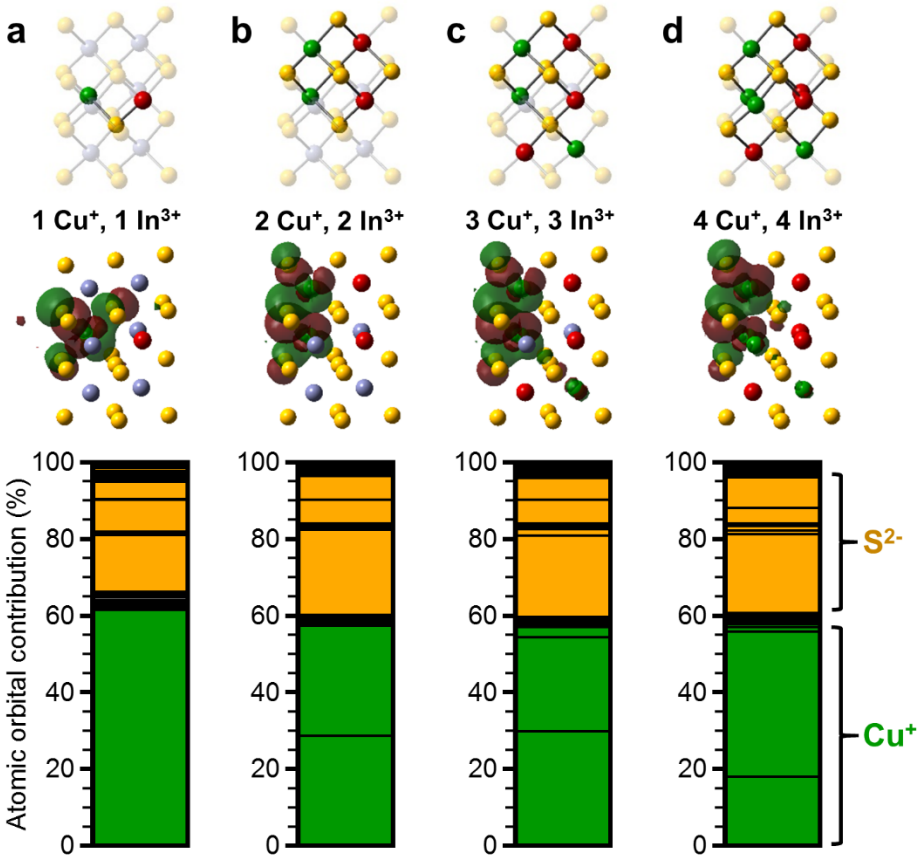

Figure 4.3. HOMOs of Cu^+,In^{3+}:ZnS NCs with increasing Cu^+ and In^{3+} concentrations. HOMO surfaces and atomic-orbital contributions for 77-cation ZnS NCs with **(a)** 1 Cu^+ and 1 In^{3+}; **(b)** 2 Cu^+ and 2 In^{3+}; **(c)** 3 Cu^+ and 3 In^{3+}; and **(d)** 4 Cu^+ and 4 In^{3+} dopants. Top: depiction of the relevant portion of the NC, showing only the 8 cation sites doped with Cu^+ or In^{3+} and their adjacent S^{2-} anions. Cu^+ are shown in green, In^{3+} in red, Zn^{2+} in gray, and S^{2-} in yellow. For each structure, the Cu^+ and In^{3+} dopants and their bridging S^{2-} anions are highlighted. Middle: HOMO surfaces visualized at 80% density, showing the same fragment of the NC as above. Bottom: Breakdowns of atomic-orbital contributions (%) for the same HOMOs. Contributions from each individual atom are shown separately (Cu^+: green, S^{2-}: yellow, In^{3+} and Zn^{2+} contributions to these orbitals are negligible).

One-electron oxidation of these NCs (*i.e.*, placing holes in the HOMOs shown in Figure 4.3) followed by geometry relaxation also does not yield significant changes in these HOMOs (see Appendix C.), indicating that these HOMOs provide reasonable representations of hole wavefunctions in these materials. Oxidation does cause a geometric distortion that further

stabilizes the localized hole, similar to the excited-state nuclear reorganization described previously for Cu^+-doped CdSe NCs.[49]

4.4.3 Cu^+ Clusters and the Effect of In^{3+} Co-Doping

To probe the generality of the observation in Figure 4.3 that holes only partially delocalize within Cu^+ clusters, we investigated a series of NCs containing Cu^+ trimers in various geometric configurations, with no In^{3+} co-dopants. Figure 4.4 illustrates the HOMOs of three different 77-cation ZnS NCs containing Cu^+ trimers, focusing on only the Cu^+ and S^{2-} atoms that make significant contributions to these MOs. The HOMOs of two more NCs with different trimer configurations are shown in Appendix C. . Figure 4.4a and Figure 4.4b represent Cu^+–Cu^+–Cu^+ configurations that occur in the ordered chalcopyrite crystal structure. For example, Figure 4.4a involves the same Cu^+ dopants as in Figure 4.3c, but without In^{3+}. The HOMO in Figure 4.4a appears more delocalized than that in Figure 4.3c, but the atomic-orbital breakdown shows that it is in fact dominated by the central Cu^+. Similarly, the HOMO in Figure 4.4b contains a disproportionate contribution from just the central Cu^+ dopant. These results illustrate that hole delocalization is inefficient in the chalcopyrite configuration of Cu^+ ions. Inspection of deeper Cu(3*d*)-based mid-gap MOs reveals that some are more evenly distributed over all three Cu^+ ions (see Appendix C.), but the HOMO is consistently localized.

Figure 4.4c shows the HOMO of a NC containing a closed-ring Cu^+ trimer, in which each Cu^+ is a nearest neighbor to both of the other Cu^+ ions. This closed-ring trimer does not occur in the ordered chalcopyrite structure but forms with Cu_{In} anti-site defects. The HOMO for this closed-ring trimer is evenly delocalized over all three Cu^+ ions. In this case, delocalization is assisted by the increased symmetry and added nearest-neighbor interactions. Although always quite localized,

the specific number and geometric arrangement of nearest-neighbor Cu^+ ions clearly influence the precise extent of HOMO localization.

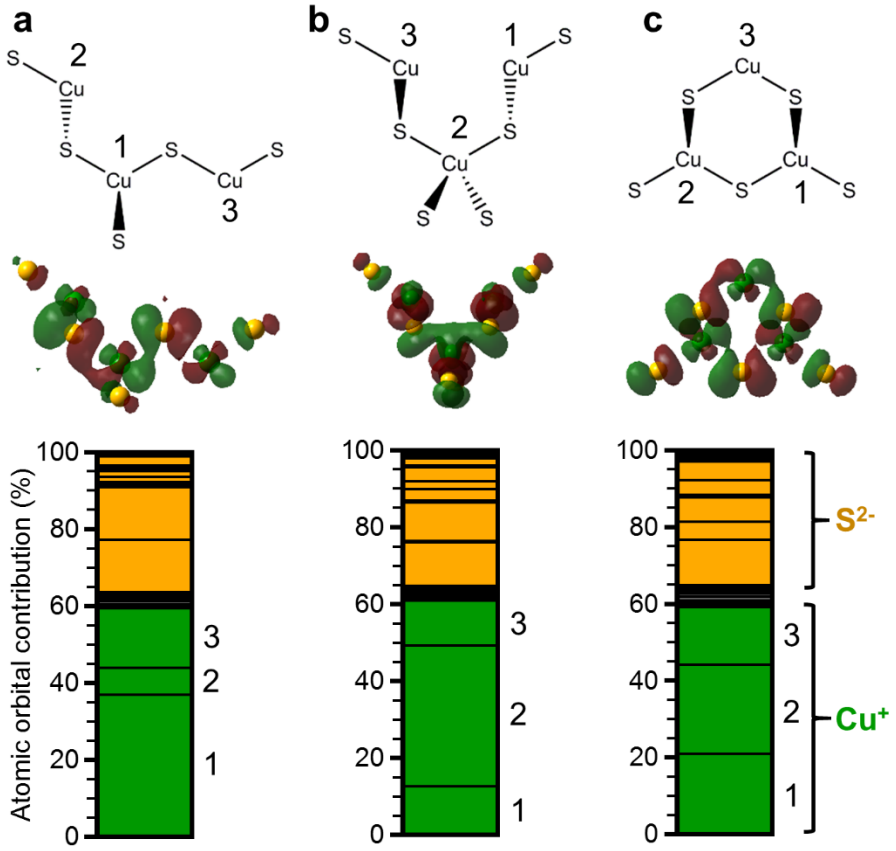

Figure 4.4. HOMOs of 77-cation ZnS NCs containing Cu^+ trimers. (a), (b), and **(c)** represent NCs with different trimer configurations. Top: schematic illustrations of the Cu^+ trimer configurations. Middle: HOMO surfaces visualized at 80% density, showing the same atoms as above. Bottom: Breakdowns of atomic-orbital contributions (%) for the same HOMOs. Contributions from each individual atom are shown separately (Cu^+: green, S^{2-}: yellow, Zn^{2+} contributions to these orbitals are negligible). The numbers next to these plots correspond to the numbered Cu^+ ions in the trimer configurations above.

The presence and position of In^{3+} co-dopants can also influence the Cu^+-based HOMO. Figure 4.5 shows the HOMOs of three different 77-cation NCs containing identical Cu^+ dimers near the NC center. In the absence of In^{3+} (Figure 4.5a), the dimer is symmetric and the HOMO is evenly distributed over both Cu^+ ions. Adding In^{3+} while maintaining the symmetry equivalence of the two Cu^+ ions (Figure 4.5b, same NC as in Figure 4.3b) results in a similar delocalized

HOMO. Adding In^{3+} in a position that breaks the dimer symmetry causes the HOMO to localize primarily on the Cu^{+} farther from the In^{3+} (Figure 4.5c); the excess positive charge on In^{3+} relative to Zn^{2+} lowers the energy of the proximal Cu(3*d*) orbital and reduces its contribution to the HOMO. By extension, this result indicates that a photogenerated hole would be localized primarily on the Cu^{+} farther from the In^{3+}. This comparison shows that even HOMO delocalization over nearest-neighbor Cu^{+}–Cu^{+} pairs can be disrupted by symmetry-breaking perturbations.

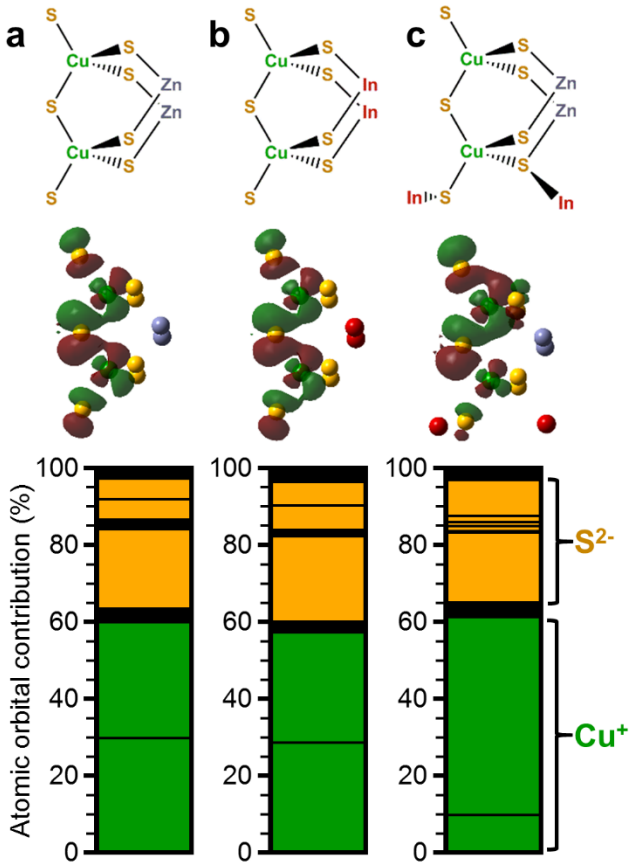

Figure 4.5. HOMO surfaces and atomic-orbital contributions for 77-cation ZnS NCs containing Cu^{+} dimers with different In^{3+} positions. All three NCs have the same two Cu^{+} dopants located in the same nearest-neighbor sites. Top: Schematic illustration of the relative positions and connectivity of the Cu^{+} and In^{3+} dopants in each NC. Middle: HOMO surfaces visualized at 80% density, showing the same atoms as above. Cu^{+} are shown in green, In^{3+} in red, Zn^{2+} in gray, and S^{2-} in yellow. Bottom: Breakdowns of atomic-orbital contributions (%) for the same HOMOs. Contributions from each individual atom are shown separately (Cu^{+}: green, S^{2-}: yellow, In^{3+} and Zn^{2+} contributions to these orbitals are negligible). **(a)** NC doped with 2 Cu^{+} in adjacent cation sites. **(b)** NC doped with 2 Cu^{+} in the same

sites and with 2 In^{3+}. Both In^{3+} are nearest-neighbors of both Cu^{+}. **(c)** NC doped with 2 Cu^{+} in the same sites and with 2 In^{3+}. Both In^{3+} are nearest-neighbors of one Cu^{+} (the lower Cu^{+} in both the dimer structure and the atomic-orbital contributions plot) and are not nearest-neighbors of the other Cu^{+}.

Hole delocalization requires inter-Cu^{+} electronic coupling (H_{AB}) to outweigh vibronic trapping energies (E_R). The electronic-coupling strength between nearest-neighbor Cu^{+} ions in the doped ZnS or chalcopyrite structures can be estimated from the energy difference between symmetric and antisymmetric linear combinations of the 3*d* orbitals that dominate the HOMO ($2H_{AB}$). For the dimer in Figure 4.5b, identification of the deeper partner orbital gives $H_{AB} = 0.38$ eV. Similarly, geometry relaxation after addition of a hole to this NC yields $E_R = 0.57$ eV. Although the magnitudes of H_{AB} and E_R depend on the specific positions of the Cu^{+} dopants, these numbers confirm that Cu^{+}–Cu^{+} electronic coupling is relatively weak in these NCs.

4.4.4 $CuInS_2$ NCs, Surfaces, and Anti-Site Defects

Replacing all Zn^{2+} ions of ZnS with Cu^{+}/In^{+} ions yields $CuInS_2$ NCs. Even in the ternary limit, these DFT calculations consistently predict HOMO localization on just 1-3 lattice Cu^{+} ions. Figure 4.6a shows that for a 34-cation $CuInS_2$ NC, the HOMO is predicted to localize at the NC surface. HOMO localization is also predicted in $CuInS_2$/ZnS core/shell structures (see Appendix C.), indicating that this localization does not stem from the presence of unsaturated bonds. Instead, the DFT results suggest that this HOMO localizes in a way that would minimize proximity of an excited-state hole to In^{3+}. The HOMO in Figure 4.6a consists primarily of Cu(3*d*) character from one Cu^{+} ion that is bonded to two S^{2-} anions and two surface pseudo-atoms. This Cu^{+} ion has only two In^{3+} and two Cu^{+} nearest neighbors, in contrast with a Cu^{+} in the NC core that would have eight In^{3+} and four Cu^{+} nearest neighbors. To illustrate the strong effect of electrostatics, Figure 4.6b shows the HOMO obtained for the same NC after modifying the local environment around

this Cu^+ by changing the charges of the adjacent surface pseudo-atoms. When the charges of these two pseudo-atoms are increased from +1.75 to +1.99 and the molecular orbitals are recomputed, the new calculated HOMO involves a completely different cluster of Cu^+ cations on the opposite side of the NC. The excess positive charge on the surface stabilizes nearby 3*d* orbitals and thereby lowers the energy of the original HOMO, shifting the HOMO to a different region of the NC. In experimental NCs, similar effects could arise from the presence or absence of passivating surface ligands, cation- or anion-rich NC surfaces, or other surface charges.

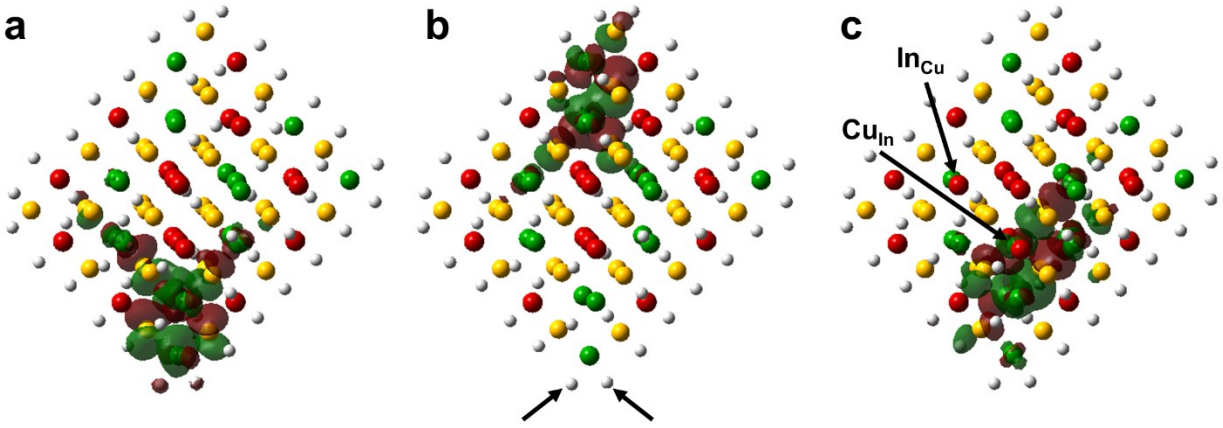

Figure 4.6. Comparison of the HOMOs of modified $CuInS_2$ NCs. HOMO wavefunction surfaces (visualized at 80% density) for three different $CuInS_2$ NC structures. Cu^+ are shown in green, In^{3+} in red, Zn^{2+} in gray, and S^{2-} in yellow. **(a)** HOMO of the stoichiometric, chalcopyrite 34-cation $CuInS_2$ NC shown in Figure 4.2f. **(b)** HOMO of the same NC as in (a), but with the charges of two surface pseudo-atoms (indicated by arrows) increased from +1.75 to +1.99. **(c)** HOMO of the same NC as in (a), but with a Cu_{In} + In_{Cu} anti-site defect pair.

Switching the positions of one Cu^+ and one In^{3+} near the NC center creates a Cu_{In} + In_{Cu} anti-site defect pair that also changes the HOMO. The anti-site Cu^+, which has more Cu^+ neighbors and fewer In^{3+} neighbors than the other lattice Cu^+ ions, makes a significant contribution to the new HOMO (Figure 4.6c). This result is consistent with the proposal that Cu_{In} anti-site defects act as hole traps: this defect represents a more stable location for the hole than a typical lattice Cu^+ in

the chalcopyrite structure because it has fewer neighboring In^{3+} ions. Importantly, however, the presence of a Cu_{In} defect in these calculations only affects *where* the HOMO is localized, but not *whether* it is localized. The HOMO is still localized at a small cluster of Cu^+ ions even in the absence of anti-site defects.

Overall, these DFT calculations consistently predict HOMO (or hole) localization at only a few lattice Cu^+ cations in $CuInS_2$ NCs, with sensitivity to local electrostatics. Because of this propensity for localization, the computed HOMOs of $CuInS_2$ NCs are extremely similar to those of Cu^+-doped NCs described above.

4.5 **Discussion**

The computational results presented here allow the strong spectroscopic similarities between Cu^+-doped, Cu–In–Zn–S alloy, and $CuInS_2$ NCs to be interpreted. In Cu^+-doped NCs, it is now well established that photogenerated holes localize in mid-gap Cu(3*d*) orbitals and that PL occurs *via* the mechanism illustrated in Figure 4.7(left). With increasing Cu^+ concentration, more mid-gap 3*d* orbitals are introduced, but the HOMOs remain localized within small clusters of Cu^+ ions (only 2−3 Cu^+) instead of resembling delocalized Bloch-like bands. Strikingly, the DFT results suggest that added holes have a strong tendency to localize even in defect-free chalcopyrite $CuInS_2$ NCs. In this limit, the $CuInS_2$ NC VB is described well as a collection of many localized Cu(3*d*)-based MOs (Figure 4.7(right)), and this material is adequately described as a heavily Cu^+-doped semiconductor NC, with 50% Cu^+ "doping". Just like in lightly Cu^+-doped semiconductor NCs, $CuInS_2$ NC PL involves recombination of a delocalized CB electron and a hole localized in the highest of these Cu(3*d*)-based MOs.

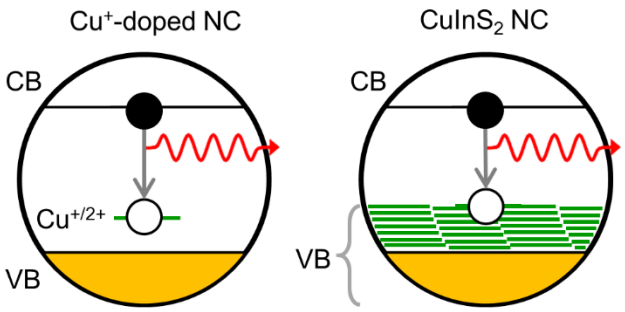

Figure 4.7. Schematic illustration of the electronic structure and radiative recombination mechanism in Cu^+-doped and $CuInS_2$ NCs. In the Cu^+-doped NC (left), the CB electron recombines with a hole bound at the single Cu^+ dopant. The $CuInS_2$ NC (right) resembles a heavily-Cu^+-doped NC, with many localized copper-based mid-gap orbitals (*i.e.*, the $CuInS_2$ valence band). In the luminescent excited state, the hole occupies the highest of these copper-based levels, and PL involves recombination of this copper-localized hole with a delocalized CB electron.

The strong propensity for HOMO localization in $CuInS_2$ NCs contrasts with the delocalized HOMOs predicted for ZnS and other II–VI NCs by the same methods (*e.g.*, Figure 4.2a). The key difference between $CuInS_2$ and ZnS is the large contribution of Cu(3*d*) orbitals at the $CuInS_2$ VB edge in the former. The directionality and poor radial extension of the 3*d* orbitals, combined with the relatively sparse Cu^+ content and their non-colinear geometric arrangement in the $CuInS_2$ lattice, leads to weak Cu^+–Cu^+ electronic coupling and hence poor delocalization. This weak Cu^+–Cu^+ electronic coupling is exacerbated by symmetry-breaking effects of surfaces and lattice defects and by the large vibronic reorganization energy associated with hole localization at copper.

The predicted HOMO localization in defect-free $CuInS_2$ NCs is closely related to exciton self-trapping, which has been proposed[8] to explain the striking similarity between $CuInS_2$ and Cu^+-doped NC PL. In this proposal, photogenerated holes in $CuInS_2$ NCs localize spontaneously even in the absence of lattice defects, resulting in free-to-bound electron–hole radiative recombination. In general, self-trapping occurs when the potential energy gain associated with localization exceeds the kinetic energy gain associated with delocalization. Here, $CuInS_2$ NCs are described

by DFT as being in the regime of strong electron–phonon coupling (which drives localization) and weak inter-Cu^+ electronic coupling (which limits delocalization). Indeed, in these calculations, the Cu^+-based HOMO of $CuInS_2$ is prone to localization even *before* nuclear reorganization, just based on symmetry breaking and electrostatics. Even without direct participation of a defect-localized state, defects can influence the hole localization electrostatically, helping to explain some of the stoichiometry-dependent trends in the PL energy and QY of $CuInS_2$ and Cu–In–Zn–S NCs, which were previously attributed to changing the concentrations of defects that participate in PL.[9,11,25,27,29,33,40] Overall, these findings identify the relatively weak electronic coupling between Cu^+ ions in $CuInS_2$ as a major factor leading to exciton self-trapping in this lattice.

As discussed previously,[1,8] hole self-trapping in $CuInS_2$ NCs parallels hole trapping in Cu^+-doped NCs (Figure 4.7), and both are described by similar single-configurational-coordinate diagrams. Consequently, both scenarios yield similar absorption and PL spectra. This analogy is supported by the present calculations, in which the lowest-energy band-to-band electronic excitations of $CuInS_2$ NCs involve promotion of a localized Cu(3*d*)-based electron into a delocalized CB orbital, directly analogous to the mid-gap $ML_{CB}CT$ absorption "foot" observed in Cu^+-doped NCs.[8,60] Both have similar experimental per-copper extinction coefficients.[8] Because of the presence of many different localized Cu(3*d*)-based MOs at the $CuInS_2$ NC VB edge, the onset of band-to-band absorption in $CuInS_2$ NCs is broad, even for narrow NC size distributions,[40,61] and it does not display a resolved excitonic maximum.

4.6 **Conclusion**

DFT calculations have been used to examine the electronic structures of luminescent copper-containing semiconductor NCs, ranging from Cu^+-doped ZnS to $CuInS_2$ and including the full continuum of $Zn_{2-2x}(Cu,In)_xS_2$ alloy compositions. These calculations predict localized HOMOs

with dominant Cu(3*d*) character for all of these NC compositions, consistent with experimental observations of similar absorption and PL in Cu^+-doped, Cu–In–Zn–S, and $CuInS_2$ NCs. The calculations show the evolution of localized Cu(3*d*) orbitals into the Cu(3*d*)-based upper valence band of $CuInS_2$ NCs, with similar $Cu^+–S^{2-}$ covalency in the HOMO across the entire series. As expected from previous work, the calculations predict hole capture by Cu^+ in lightly copper-doped ZnS NCs. Even in alloyed $Zn_{2-2x}(Cu,In)_xS_2$ and $CuInS_2$ NCs, however, the HOMO is still predicted to be localized at small clusters of lattice Cu^+ ions, rather than delocalized to form a true band. Careful computational investigation shows that the HOMO delocalizes over pairs of adjacent Cu^+ ions but does not continue to delocalize when more adjacent Cu^+ ions are added. Perhaps most strikingly, even in defect-free $CuInS_2$ NCs, the HOMO is consistently predicted to localize at clusters of 2 or 3 Cu^+ ions. In all cases, the specific HOMO characteristics are easily perturbed by the presence of surface or lattice charges.

These findings have important implications for understanding the PL mechanisms of Cu^+-doped, Cu–In–Zn–S, and $CuInS_2$ NCs. Specifically, the DFT results suggest that photogenerated holes localize at lattice Cu^+ cations (up to 2–3 cations) in the luminescent excited states of all of these materials, and that the PL always involves recombination of these copper-bound holes with delocalized CB electrons. In particular, the tendency for Cu(3*d*) hole localization in $CuInS_2$ NCs predicted by DFT supports the same conclusion drawn from experimental spectroscopic results. These computational results further provide insight into why such holes tend to localize, relating localization to poor inter-Cu^+ electronic coupling and electrostatic perturbations. Overall, these results present a unified understanding of the PL mechanisms active in Cu^+-doped, Cu–In–Zn–S alloy, and $CuInS_2$ NCs, and explain at a fundamental level the experimental similarities observed among these materials.

4.7 Acknowledgments

Financial support from the National Science Foundation (DMR-1807394 to DRG) is gratefully acknowledged. This work was facilitated by the advanced computational, storage, and networking infrastructure provided by the Hyak Supercomputer System at the University of Washington, funded by the UW Student Technology Fee.

4.8 Supporting Information

Appendix C. : HOMO visualizations showing full NC structures, LUMO visualizations and atomic-orbital contributions, LUMOs of oxidized NCs, HOMOs of NCs containing different Cu^+ trimer configurations, atomic-orbital contributions to deeper Cu^+-based MOs for NCs containing Cu^+ trimers, HOMOs of different $CuInS_2$ and $CuInS_2$/ZnS core/shell NCs, energies and visualizations of deeper valence-band MOs for $CuInS_2$ NCs.

4.9 References

1. Knowles, K. E.; Hartstein, K. H.; Kilburn, T. B.; Marchioro, A.; Nelson, H. D.; Whitham, P. J.; Gamelin, D. R. Luminescent Colloidal Semiconductor Nanocrystals Containing Copper: Synthesis, Photophysics, and Applications. *Chem. Rev.* **2016**, *116*, 10820-10851.
2. Leach, A. D. P.; Macdonald, J. E. Optoelectronic Properties of $CuInS_2$ Nanocrystals and Their Origin. *J. Phys. Chem. Lett.* **2016**, *7*, 572-583.
3. van der Stam, W.; Berends, A. C.; de Mello Donega, C. Prospects of Colloidal Copper Chalcogenide Nanocrystals. *ChemPhysChem* **2016**, *17*, 559-581.
4. Sandroni, M.; Wegner, K. D.; Aldakov, D.; Reiss, P. Prospects of Chalcopyrite-Type Nanocrystals for Energy Applications. *ACS Energy Lett.* **2017**, *2*, 1076-1088.
5. Coughlan, C.; Ibáñez, M.; Dobrozhan, O.; Singh, A.; Cabot, A.; Ryan, K. M. Compound Copper Chalcogenide Nanocrystals. *Chem. Rev.* **2017**, *117*, 5865-6109.
6. Chen, B.; Pradhan, N.; Zhong, H. From Large-Scale Synthesis to Lighting Device Applications of Ternary I−III−VI Semiconductor Nanocrystals: Inspiring Greener Material Emitters. *J. Phys. Chem. Lett.* **2018**, *9*, 435-445.
7. Rice, W. D.; McDaniel, H.; Klimov, V. I.; Crooker, S. A. Magneto-Optical Properties of $CuInS_2$ Nanocrystals. *J. Phys. Chem. Lett.* **2014**, *5*, 4105-4109.

8. Knowles, K. E.; Nelson, H. D.; Kilburn, T. B.; Gamelin, D. R. Singlet−Triplet Splittings in the Luminescent Excited States of Colloidal Cu^+:CdSe, Cu^+:InP, and $CuInS_2$ Nanocrystals: Charge-Transfer Configurations and Self-Trapped Excitons. *J. Am. Chem. Soc.* **2015**, *137*, 13138–13147.

9. Uehara, M.; Watanabe, K.; Tajiri, Y.; Nakamura, H.; Maeda, H. Synthesis of $CuInS_2$ Fluorescent Nanocrystals and Enhancement of Fluorescence by Controlling Crystal Defect. *J. Chem. Phys.* **2008**, *129*, 134709.

10. Nose, K.; Omata, T.; Otsuka-Yao-Matsuo, S. Colloidal Synthesis of Ternary Copper Indium Diselenide Quantum Dots and Their Optical Properties. *J. Phys. Chem. C* **2009**, *113*, 3455-3460.

11. Chen, B.; Zhong, H.; Zhang, W.; Tan, Z.; Li, Y.; Yu, C.; Zhai, T.; Bando, Y.; Yang, S.; Zou, B. Highly Emissive and Color-Tunable $CuInS_2$-Based Colloidal Semiconductor Nanocrystals: Off-Stoichiometry Effects and Improved Electroluminescence Performance. *Adv. Funct. Mater.* **2012**, *22*, 2081-2088.

12. Fuhr, A. S.; Yun, H. J.; Makarov, N. S.; Li, H.; McDaniel, H.; Klimov, V. I. Light Emission Mechanisms in $CuInS_2$ Quantum Dots Evaluated by Spectral Electrochemistry. *ACS Photonics* **2017**, *4*, 2425-2435.

13. Pinchetti, V.; Lorenzon, M.; McDaniel, H.; Lorenzi, R.; Meinardi, F.; Klimov, V. I.; Brovelli, S. Spectro-electrochemical Probing of Intrinsic and Extrinsic Processes in Exciton Recombination in I−III−VI_2 Nanocrystals. *Nano Lett.* **2017**, *17*, 4508-4517.

14. Williams, R. T.; Song, K. S. The Self-Trapped Exciton. *J. Phys. Chem. Solids* **1990**, *51*, 679-716.

15. Stoneham, A. M.; Gavartin, J.; Shluger, A. L.; Kimmel, A. V.; Muñoz Ramo, D.; Rønnow, H. M.; Aeppli, G.; Renner, C. Trapping, Self-Trapping and the Polaron Family. *J. Phys.: Condens. Matter* **2007**, *19*, 255208.

16. Dohner, E. R.; Jaffe, A.; Bradshaw, L. R.; Karunadasa, H. I. Intrinsic White-Light Emission from Layered Hybrid Perovskites. *J. Am. Chem. Soc.* **2014**, *136*, 13154-13157.

17. Wu, X.; Trinh, M. T.; Niesner, D.; Zhu, H.; Norman, Z.; Owen, J. S.; Yaffe, O.; Kudisch, B. J.; Zhu, X.-Y. Trap States in Lead Iodide Perovskites. *J. Am. Chem. Soc.* **2015**, *137*, 2089-2096.

18. Yangui, A.; Garrot, D.; Lauret, J. S.; Lusson, A.; Bouchez, G.; Deleporte, E.; Pillet, S.; Bendeif, E. E.; Castro, M.; Triki, S.; Abid, Y.; Boukheddaden, K. Optical Investigation of Broadband White-Light Emission in Self-Assembled Organic−Inorganic Perovskite $(C_6H_{11}NH_3)_2PbBr_4$. *J. Phys. Chem. C* **2015**, *119*, 23638-23647.

19. Hu, T.; Smith, M. D.; Dohner, E. R.; Sher, M.-J.; Wu, X.; Trinh, M. T.; Fisher, A.; Corbett, J.; Zhu, X.-Y.; Karunadasa, H. I.; Lindenberg, A. M. Mechanism for Broadband White-Light Emission from Two-Dimensional (110) Hybrid Perovskites. *J. Phys. Chem. Lett.* **2016**, *7*, 2258-2263.

20. Berends, A. C.; Rabouw, F. T.; Spoor, F. C. M.; Bladt, E.; Grozema, F. C.; Houtepen, A. J.; Siebbeles, L. D. A.; de Mello Donegá, C. Radiative and Nonradiative Recombination in

$CuInS_2$ Nanocrystals and $CuInS_2$-Based Core/Shell Nanocrystals. *J. Phys. Chem. Lett.* **2016**, *7*, 3503-3509.

21. Hu, W.; Ludwig, J.; Pattengale, B.; Yang, S.; Liu, C.; Zuo, X.; Zhang, X.; Huang, J. Unravelling the Correlation of Electronic Structure and Carrier Dynamics in $CuInS_2$ Nanoparticles. *J. Phys. Chem. C* **2018**, *122*, 974-980.
22. Parasyuk, O. V.; Voronyuk, S. V.; Gulay, L. D.; Davidyuk, G. Y.; Halka, V. O. Phase Diagram of the CuInS –ZnS System and Some Physical Properties of Solid Solutions Phases. *J. Alloys Compd.* **2003**, *348*, 57-64.
23. Nakamura, H.; Kato, W.; Uehara, M.; Nose, K.; Omata, T.; Otsuka-Yao-Matsuo, S.; Miyazaki, M.; Maeda, H. Tunable Photoluminescence Wavelength of Chalcopyrite $CuInS_2$-Based Semiconductor Nanocrystals Synthesized in a Colloidal System. *Chem. Mater.* **2006**, *18*, 3330-3335.
24. Zhang, W.; Zhong, X. Facile Synthesis of ZnS−$CuInS_2$-Alloyed Nanocrystals for a Color-Tunable Fluorchrome and Photocatalyst. *Inorg. Chem.* **2011**, *50*, 4065-4072.
25. Zhang, J.; Xie, R.; Yang, W. A Simple Route for Highly Luminescent Quaternary Cu-Zn-In-S Nanocrystal Emitters. *Chem. Mater.* **2011**, *23*, 3357-3361.
26. Tan, Z.; Zhang, Y.; Xie, C.; Su, H.; Liu, J.; Zhang, C.; Dellas, N.; Mohney, S. E.; Wang, Y.; Wang, J.; Xu, J. Near-Band-Edge Electroluminescence from Heavy-Metal-Free Colloidal Quantum Dots. *Adv. Mater.* **2011**, *23*, 3553-3558.
27. Komarala, V. K.; Xie, C.; Wang, Y.; Xu, J.; Xiao, M. Time-Resolved Photoluminescence Properties of $CuInS_2$/ZnS Nanocrystals: Influence of Intrinsic Defects and External Impurities. *J. Appl. Phys.* **2012**, *111*, 124314.
28. Seo, J.; Raut, S.; Abdel-Fattah, M.; Rice, Q.; Tabibi, B.; Rich, R.; Fudala, R.; Gryczynski, I.; Gryczynski, Z.; Kim, W.-J.; Jung, S.; Hyun, R. Time-Resolved and Temperature-Dependent Photoluminescence of Ternary and Quaternary Nanocrystals of $CuInS_2$ with ZnS Capping and Cation Exchange. *J. Appl. Phys.* **2013**, *114*, 094310.
29. Xiang, W.-D.; Yang, H.-L.; Liang, X.-J.; Zhong, J.-S.; Wang, J.; Luo, L.; Xie, C.-P. Direct Synthesis of Highly Luminescent Cu–Zn–In–S Quaternary Nanocrystals with Tunable Photoluminescence Spectra and Decay Times. *J. Mater. Chem. C* **2013**, *1*, 2014-2020.
30. Zhang, W.; Lou, Q.; Ji, W.; Zhao, J.; Zhong, X. Color-Tunable Highly Bright Photoluminescence of Cadmium-Free Cu-Doped Zn−In−S Nanocrystals and Electroluminescence. *Chem. Mater.* **2014**, *26*, 1204-1212.
31. Liu, Z.; Tang, A.; Wang, M.; Yang, C.; Teng, F. Heating-Up Synthesis of Cadimum-Free and Color-Tunable Quaternary and Five-Component Cu–In–Zn–S-based Semiconductor Nanocrystals. *J. Mater. Chem. C* **2015**, *3*, 10114-10120.
32. Jiang, T.; Song, J.; Wang, H.; Ye, X.; Wang, H.; Zhang, W.; Yang, M.; Xia, R.; Zhu, L.; Xu, X. Aqueous Synthesis of Color Tunable Cu Doped Zn–In–S/ZnS Nanoparticles in the Whole Visible Region for Cellular Imaging. *J. Mater. Chem. B* **2015**, *3*, 2402-2410.
33. Zaiats, G.; Kinge, S.; Kamat, P. V. Origin of Dual Photoluminescence States in ZnS−$CuInS_2$ Alloy Nanostructures. *J. Phys. Chem. C* **2016**, *120*, 10641-10646.

34. Yuan, X.; Ma, R.; Hua, J.; Liu, Y.; Li, J.; Zhang, W.; Zhao, J.; Li, H. Thermal Stability of Photoluminescence in Cu-doped Zn–In–S Quantum Dots for Light-Emitting Diodes. *Phys. Chem. Chem. Phys.* **2016**, *18*, 10976-10982.

35. Park, J.; Kim, S.-W. $CuInS_2$/ZnS Core/Shell Quantum Dots by Cation Exchange and Their Blue-Shifted Photoluminescence. *J. Mater. Chem.* **2011**, *21*, 3745-3750.

36. De Trizio, L.; Prato, M.; Genovese, A.; Casu, A.; Povia, M.; Simonutti, R.; Alcocer, M. J. P.; D'Andrea, C.; Tassone, F.; Manna, L. Strongly Fluorescent Quaternary Cu−In−Zn−S Nanocrystals Prepared from $Cu_{1-x}InS_2$ Nanocrystals by Partial Cation Exchange. *Chem. Mater.* **2012**, *24*, 2400-2406.

37. Akkerman, Q. A.; Genovese, A.; George, C.; Prato, M.; Moreels, I.; Casu, A.; Marras, S.; Curcio, A.; Scarpellini, A.; Pellegrino, T.; Manna, L.; Lesnyak, V. From Binary Cu_2S toTernary Cu−In−S and Quaternary Cu−In−Zn−S Nanocrystals with Tunable Composition *via* Partial Cation Exchange. *ACS Nano* **2015**, *9*, 521-531.

38. Li, L.; Daou, T. J.; Texier, I.; Chi, T. T. K.; Liem, N. Q.; Reiss, P. Highly Luminescent $CuInS_2$/ZnS Core/Shell Nanocrystals: Cadmium-Free Quantum Dots for In Vivo Imaging. *Chem. Mater.* **2009**, *21*, 2422-2429.

39. Li, L.; Pandey, A.; Werder, D. J.; Khanal, B. P.; Pietryga, J. M.; Klimov, V. I. Efficient Synthesis of Highly Luminescent Copper Indium Sulfide-Based Core/Shell Nanocrystals with Surprisingly Long-Lived Emission. *J. Am. Chem. Soc.* **2011**, *133*, 1176-1179.

40. Kim, Y.-K.; Ahn, S.-H.; Chung, K.; Cho, Y.-S.; Choi, C.-J. The Photoluminescence of $CuInS_2$ Nanocrystals: Effect of Non-Stoichiometry and Surface Modification. *J. Mater. Chem.* **2012**, *22*, 1516-1520.

41. Berends, A. C.; van der Stam, W.; Hofmann, J. P.; Bladt, E.; Meeldijk, J. D.; Bals, S.; de Mello Donega, C. Interplay between Surface Chemistry, Precursor Reactivity, and Temperature Determines Outcome of ZnS Shelling Reactions on $CuInS_2$ Nanocrystals. *Chem. Mater.* **2018**, *30*, 2400-2413.

42. Dong, X.; Xu, J.; Zhang, X.; Shi, S.; Yang, H.; Mo, Z.; Li, L.; Yin, S. Investigating Photoluminescence Mechanism of Cu-doped Zn−In−Se Quantum Dots by Zn/In Ratio. *J. Phys. Chem. C* **2017**, *121*, 16978-16984.

43. Frisch, M. J.; Trucks, G. W.; Schlegel, H. B.; Scuseria, G. E.; Robb, M. A.; Cheeseman, J. R.; Scalmani, G.; Barone, V.; Mennucci, B.; Petersson, G. A.; Nakatsuji, H.; Caricato, M.; Li, X.; Hratchian, H. P.; Izmaylov, A. F.; Bloino, J.; Zheng, G.; Sonnenberg, J. L.; Hada, M.; Ehara, M.; Toyota, K.; Fukuda, R.; Hasegawa, J.; Ishida, M.; Nakajima, T.; Honda, Y.; Kitao, O.; Nakai, H.; Vreven, T.; Montgomery Jr., J. A.; Peralta, J. E.; Ogliaro, F.; Bearpark, M. J.; Heyd, J.; Brothers, E. N.; Kudin, K. N.; Staroverov, V. N.; Kobayashi, R.; Normand, J.; Raghavachari, K.; Rendell, A. P.; Burant, J. C.; Iyengar, S. S.; Tomasi, J.; Cossi, M.; Rega, N.; Millam, N. J.; Klene, M.; Knox, J. E.; Cross, J. B.; Bakken, V.; Adamo, C.; Jaramillo, J.; Gomperts, R.; Stratmann, R. E.; Yazyev, O.; Austin, A. J.; Cammi, R.; Pomelli, C.; Ochterski, J. W.; Martin, R. L.; Morokuma, K.; Zakrzewski, V. G.; Voth, G. A.; Salvador, P.; Dannenberg, J. J.; Dapprich, S.; Daniels, A. D.; Farkas, Ö.; Foresman, J. B.; Ortiz, J. V.; Cioslowski, J.; Fox, D. J. *Gaussian 09*, Gaussian, Inc.: Wallingford, CT, USA, 2009.

44. Perdew, J. P.; Burke, K.; Ernzerhof, M. Generalized Gradient Approximation Made Simple. *Phys. Rev. Lett.* **1996**, *77*, 3865-3868.

45. Adamo, C.; Barone, V. Toward Reliable Density Functional Methods without Adjustable Parameters: The PBE0 Model. *J. Chem. Phys.* **1999**, *110*, 6158-6170.

46. Hay, P. J.; Wadt, W. R. *Ab initio* Effective Core Potentials for Molecular Calculations. Potentials for K to Au Including the Outermost Core Orbitals. *J. Chem. Phys.* **1985**, *82*, 299-310.

47. Wadt, W. R.; Hay, P. J. *Ab initio* Effective Core Potentials for Molecular Calculations. Potentials for Main Group Elements Na to Bi. *J. Chem. Phys.* **1985**, *82*, 284-298.

48. Hay, P. J.; Wadt, W. R. *Ab initio* Effective Core Potentials for Molecular Calculations. Potentials for the Transition Metal Atoms Sc to Hg. *J. Chem. Phys.* **1985**, *82*, 270-283.

49. Nelson, H. D.; Li, X.; Gamelin, D. R. Computational Studies of the Electronic Structures of Copper-Doped CdSe Nanocrystals: Oxidation States, Jahn−Teller Distortions, Vibronic Bandshapes, and Singlet−Triplet Splittings. *J. Phys. Chem. C* **2016**, *120*, 5714-5723.

50. Beaulac, R.; Feng, Y.; May, J. W.; Badaeva, E.; Gamelin, D. R.; Li, X. Orbital Pathways for Mn^{2+}-carrier *s p-d* Exchange in Diluted Magnetic Semiconductor Quantum Dots. *Phys. Rev. B* **2011**, *84*, 195324.

51. Badaeva, E.; Feng, Y.; Gamelin, D. R.; Li, X. Investigation of Pure and Co^{2+}-Doped ZnO Quantum Dot Electronic Structures Using the Density Functional Theory: Choosing the Right Functional. *New J. Phys.* **2008**, *10*, 055013.

52. Goings, J. J.; Schimpf, A. M.; May, J. W.; Johns, R. W.; Gamelin, D. R.; Li., X. Theoretical Characterization of Conduction-Band Electrons in Photodoped and Aluminum-Doped Zinc Oxide (AZO) Quantum Dots. *J. Phys. Chem. C* **2014**, *118*, 26584−26590.

53. Badaeva, E.; Isborn, C. M.; Feng, Y.; Ochsenbein, S. T.; Gamelin, D. R.; Li, X. Theoretical Characterization of Electronic Transitions in Co^{2+}- and Mn^{2+}-Doped ZnO Nanocrystals. *J. Phys. Chem. C* **2009**, *113*, 8710-8717.

54. Huang, X.; Lindgren, E.; Chelikowsky, J. R. Surface Passivation Method for Semiconductor Nanostructures. *Phys. Rev. B* **2005**, *71*, 165328.

55. Wang, L.-W.; Li, J. First-Principles Thousand-Atom Quantum Dot Calculations. *Phys. Rev. B* **2004**, *69*, 153302.

56. Shay, J. L.; Tell, B.; Kasper, H. M.; Schiavone, L. M. *p-d* Hybridization of the Valence Bands of I-III-VI_2 Compounds. *Phys. Rev. B* **1972**, *5*, 5003-5005.

57. Braun, W.; Goldmann, A.; Cardona, M. Partial Density of Valence States of Amorphous and Crystalline $AgInTe_2$ and $CuInS_2$. *Phys. Rev. B* **1974**, *10*, 5069-5074.

58. Jaffe, J. E.; Zunger, A. Electronic Structure of the Ternary Chalcopyrite Semiconductors $CuAlS_2$, $CuGaS_2$, $CuInS_2$, $CuAlSe_2$, $CuGaSe_2$, and $CuInSe_2$. *Phys. Rev. B* **1983**, *28*, 5822-5847.

59. Jaffe, J. E.; Zunger, A. Theory of the Band-Gap Anomaly in ABC_2 Chalcopyrite Semiconductors. *Phys. Rev. B* **1984**, *29*, 1882-1906.

60. Yang, L.; Knowles, K. E.; Gopalan, A.; Hughes, K. E.; James, M. C.; Gamelin, D. R. One-Pot Synthesis of Monodisperse Colloidal Copper-Doped CdSe Nanocrystals Mediated by Ligand−Copper Interactions. *Chem. Mater.* **2016**, *28*, 7375–7384.

61. Xie, R.; Rutherford, M.; Peng, X. Formation of High-Quality I–III–VI Semiconductor Nanocrystals by Tuning Relative Reactivity of Cationic Precursors. *J. Am. Chem. Soc.* **2009**, *131*, 5691-5697.

Chapter 5. Strong Dependence of Quantum-Dot Delayed Luminescence on Excitation Pulse Width

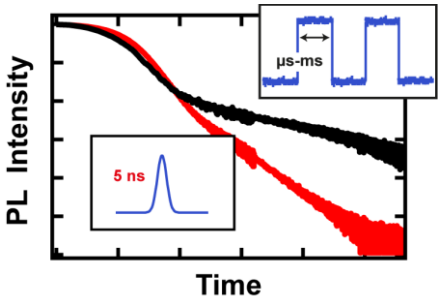

5.1 **Overview**

Delayed luminescence involving charge-carrier trapping and detrapping has recently been identified as a widespread and possibly universal phenomenon in colloidal quantum dots. Its near-power-law decay suggests a relationship with blinking. Here, using colloidal $CuInS_2$ and CdSe quantum dots as model systems, we show that short (nanosecond) excitation pulses yield less delayed luminescence intensity and faster delayed luminescence decay than observed with long (millisecond) square-wave excitation pulses. Increasing the excitation power also affects the delayed luminescence intensity, but the delayed luminescence decay kinetics appear much less sensitive to excitation power than to excitation pulse width. An idealized four-state kinetic model reproduces the major experimental trends and highlights the very slow approach to steady state during photoexcitation, stemming from extremely slow detrapping of the metastable charge-separated state responsible for delayed luminescence. The impacts of these findings on proposed relationships between delayed luminescence and blinking are discussed.

5.2 Introduction

Several groups have reported extremely slow photoluminescence decay in various colloidal semiconductor nanostructures, including CdSe[1-5] and copper-doped CdSe (Cu^+:CdSe)[3,5] quantum dots, CdSe nanoplatelets,[6] lead-halide perovskite nanocrystals,[7] and $CuInS_2$ quantum dots,[5,8] persisting for times that vastly exceed the natural excited-state lifetimes of these materials. In each case, the delayed luminescence shows broadly distributed decay kinetics with components ranging from submicrosecond to beyond seconds. This delayed luminescence is explained by invoking temporary charge-carrier trapping at a quantum dot surface, followed by spontaneous detrapping to reform the emissive core state. Detrapping occurs *via* tunneling.[5-6] This delayed luminescence has been related to the photoluminescence blinking of single quantum dots.[1,3-5,8-9] A better understanding of the carrier trapping and detrapping processes responsible for delayed luminescence would provide insight into the characteristics of surface traps to help guide optimization of the photophysical properties of colloidal semiconductor quantum dots.

We recently reported that the ratio of delayed to prompt luminescence intensities depends strongly on the quantum dot photoexcitation rate[8] because the delayed luminescence saturates at excitation rates that are orders of magnitude smaller than required to saturate the prompt luminescence of the same quantum dot. This explanation invokes efficient nonradiative recombination (*e.g.*, Auger, Shockley−Read−Hall) upon photoexcitation of a quantum dot that is already in a metastable charge-separated excited state, as also invoked to explain the low photoluminescence quantum yields of blinking "off" states.[10-12] Here, using two model nanocrystals ($CuInS_2$ and CdSe quantum dots, see Appendix D. for details), we report that even at fixed photoexcitation rates the ratio of delayed to prompt luminescence intensities changes as the excitation pulse width is increased from nanoseconds to milliseconds. This result is illustrated

using an idealized four-state kinetic model that accounts for trapping, detrapping, and recombination processes. Additionally, we find that even the *kinetics* of the delayed luminescence are influenced by the photoexcitation pulse width, with increasing pulse widths yielding slower delayed luminescence decay. These effects have not been previously observed.

5.3 **Results**

To illustrate the central new observation reported here, Figure 5.1 plots two photoluminescence decay curves measured for the same $d = 3.9$ nm $CuInS_2$ quantum dot sample using two different common photoexcitation conditions, both with the same excitation wavelength (405 nm). In one, a 5 ns excitation pulse was used, and in the other a 100 ms square pulse was used. Both curves show prompt decay on the microsecond time scale ($\tau_{prompt} = 2$ μs), followed by delayed luminescence extending to milliseconds and beyond. Strikingly, the two delayed luminescence decay curves have very different power-law slopes in this log–log plot (1.11 for the 5 ns pulse versus 0.48 for the 100 ms pulse, between 50 μs and 2 ms). The delayed luminescence generated using nanosecond pulses has decayed almost completely within ~50 ms, whereas that generated using 100 ms pulses is much longer-lived, being >100 times more intense than the former after 10 ms. The slopes of such log–log delayed luminescence plots have been related to blinking power-law exponents,[1,4,9] but the data in Figure 5.1 demonstrate that these slopes are dramatically influenced by the photoexcitation pulse profile itself, an observation that has not been noted previously. It is important to identify the source of the difference in decay dynamics shown in Figure 5.1.

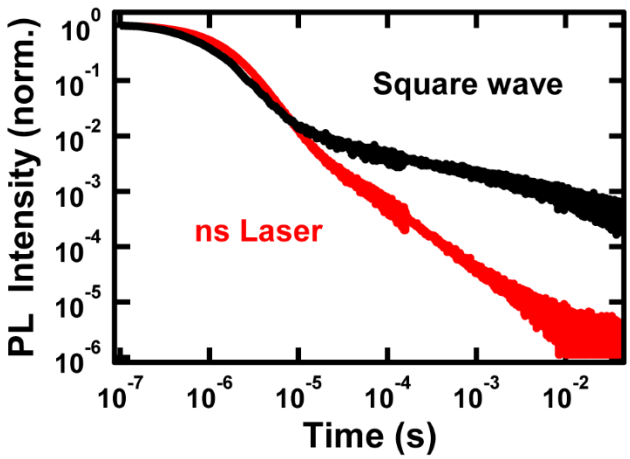

Figure 5.1. PL decay of $CuInS_2$ NCs under pulsed and square-wave excitation. Photoluminescence decay curves measured for the same d = 3.9 nm $CuInS_2$ quantum dots using the same photoexcitation wavelength (405 nm) but different types of common excitation pulses. Black: 100 ms square-wave excitation pulse, 8 mW/cm^2 pulse power, 5 Hz repetition rate. Red: 5 ns excitation pulse, 30 μJ/cm^2, 20 Hz repetition rate. These data show that delayed luminescence decay dynamics depend on photoexcitation conditions. Data are normalized using the peak prompt luminescence intensity for the 5 ns pulse data and the luminescence intensity during excitation for the 100 ms pulse data. For these and all other data in this manuscript, t = 0 coincides with the end of the square-wave pulse. All data were collected at 20 K.

We hypothesized that two major experimental parameters might contribute to the differences observed in Figure 5.1: the excitation power and its duration. To test the roles of these two parameters, variable pulse-width photoexcitation experiments were performed at different laser powers. Because the delayed luminescence decay dynamics are temperature-independent over a very broad range,[5-6] all data reported here were collected at 20 K to minimize thermally activated nonradiative decay[5] and irreversible photodegradation. Figure 5.2 summarizes the effects of photoexcitation pulse duration and power on the delayed luminescence decay dynamics of the same $CuInS_2$ quantum dots. Figure 5.2A plots the $CuInS_2$ quantum dot delayed luminescence decay dynamics (normalized to the prompt luminescence intensity, which is independent of pulse duration under these conditions) as a function of excitation pulse duration from 50 μs to 100 ms. Except for a small amount of irreversible photodegradation over these very long measurements

(*e.g.*, <10% over ~20 h of continuous measurement for the data in Figure 5.2A), the prompt luminescence intensity is linearly proportional to the photoexcitation power.[8] As the pulse width increases, the delayed luminescence intensity grows and the slopes of the delayed luminescence decay curves in the log−log plot decrease. We interpret this result as indicating that accumulation of population in the metastable charge-separated excited state is very slow, and hence very long excitation pulses are required to reach steady state.

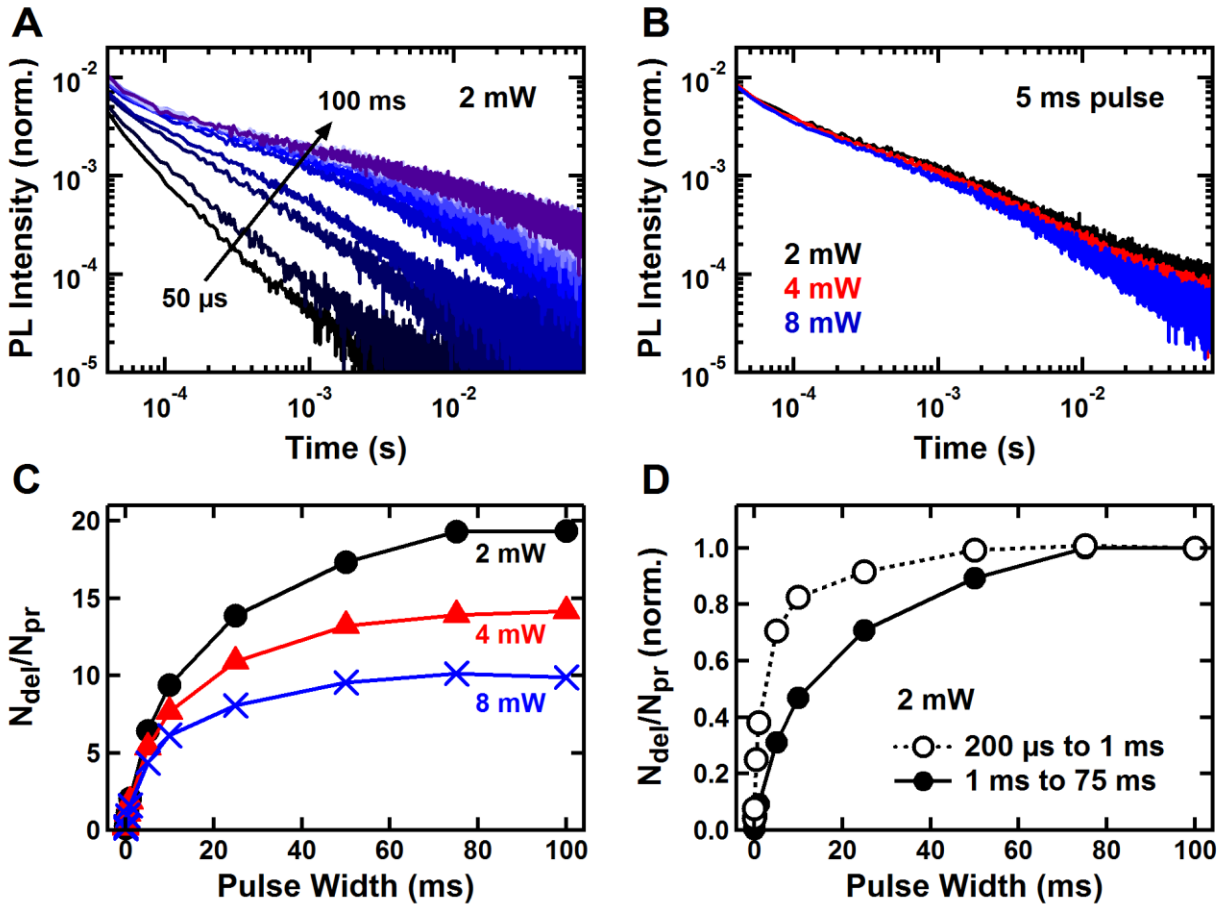

Figure 5.2. Dependence of delayed luminescence on pulse width and power for $CuInS_2$ NCs. Dynamics of delayed luminescence for increasing pulse width for d = 3.9 nm $CuInS_2$ quantum dots (50 µs (black) to 100 ms (purple) excitation pulse width). Traces are normalized to the prompt luminescence intensity. **(B)** Dynamics of delayed luminescence measured using 2 (black), 4 (red), and 8 mW (blue) excitation powers (power densities = 6.7, 13.3, and 26.7 mW/cm^2) for the same $CuInS_2$ quantum dots, with a 5 ms excitation pulse. Traces are normalized to the prompt luminescence intensity. Linear plots of the data in (A) and (B) are provided in Appendix D. . **(C)** N_{del}/N_{pr} calculated from decay curves such as those in (A) and

(B) for the same $CuInS_2$ quantum dots, plotted versus excitation pulse width and measured at three different excitation powers: 2 (black circles), 4 (red triangles), 8 mW (blue crosses). **(D)** N_{del}/N_{pr} for the same $CuInS_2$ quantum dots, collected at 2 mW, plotted versus excitation pulse width, and normalized to the value of N_{del}/N_{pr} at 100 ms pulse width. Two delayed luminescence integration windows are represented: a shorter window (open circles, t_1 = 200 μs, t_2 = 1 ms) and a longer window (filled circles, t_1 = 1 ms, t_2 = 75 ms). These specific integration windows were chosen to reflect the broadest overall timespan in which signal-to-noise was good, but the same trends are obtained using different integration windows. All data were collected at 20 K.

Figure 5.2B plots delayed luminescence decay curves measured for these same $CuInS_2$ quantum dots using fixed excitation pulse widths but excitation powers of 2, 4, and 8 mW (power densities = 6.7, 13.3, and 26.7 mW/cm^2), again normalized to the prompt luminescence intensities. The decay dynamics measured at these different excitation powers are almost indistinguishable when the pulse width is kept constant. Together, the data in Figure 5.2A,B demonstrate that quantum dot delayed luminescence decay *dynamics* are quite sensitive to the excitation pulse duration but are relatively insensitive to its peak power. The same conclusion holds when comparing data representing similar increases in the total number of photons per excitation pulse generated *via* an increased pulse width or excitation power. For example, the power-law slope at ~1 ms decreases from 1.15 to 0.68 upon increasing the pulse width from 100 to 500 μs at fixed 2 mW excitation power, but it remains nearly unchanged (1.23) upon increasing the excitation power from 2 to 8 mW for a fixed 100 μs pulse width (see Appendix D.).

To quantify the trends of Figure 5.2A,B, Figure 5.2C,D plots the number of delayed luminescence photons (N_{del}) normalized by the number of prompt luminescence photons (N_{pr}) for each experiment from Figure 5.2A,B. N_{del} is obtained by integrating delayed luminescence decay curves such as those in Figure 5.2A,B over a specified time range (t_1 to t_2, eq 5.1), while N_{pr} is obtained by integrating the prompt luminescence up to a specified cutoff time (t_f, eq 5.2).

$$N_{del} = \int_{t_1}^{t_2} I(t)dt \tag{5.1}$$

$$N_{pr} = \int_{0}^{t_f} I_0 e^{-k_{PL}t} dt \tag{5.2}$$

Here I(t) is the time-dependent luminescence intensity as seen in Figure 5.2A,B, I_0 is the steady-state luminescence intensity measured when the excitation pulse is on, and k_{PL} is the experimental prompt luminescence decay constant measured by single-photon counting. For the $CuInS_2$ quantum dots, $k_{PL} = 1/\tau_{prompt} = 5\times10^5\ s^{-1}$ from a single-exponential fit, t_1 and t_2 correspond to 200 μs and 75 ms, respectively, and t_f corresponds to 10 μs (= $5\,\tau_{prompt}$). Figure 5.2C shows that for fixed excitation power N_{del}/N_{pr} increases with increasing pulse width before eventually reaching a plateau value, while N_{pr} is independent of pulse width under these conditions. The ratio of delayed to prompt luminescence photons is thus pulse-width dependent, first growing with increasing excitation pulse width before plateauing at excitation pulse widths of almost 100 ms. The plateau of N_{del}/N_{pr} suggests that only with such extremely long excitation pulses does the population of the charge-separated state responsible for delayed luminescence reach steady state under photoexcitation.

For any given excitation pulse width, N_{del}/N_{pr} also decreases with increasing excitation power. This trend stems from the fact that N_{pr} increases linearly with excitation power in the investigated power range, whereas N_{del} shows a sublinear power dependence.[8] When normalized, it is evident that the curvatures of the data in Figure 5.2C are essentially independent of excitation power (see Appendix D.).

Figure 5.2D compares experimental N_{del}/N_{pr} values obtained by integrating over two different delayed luminescence time windows (*i.e.*, different t_1 and t_2 in eq 5.1) for these $CuInS_2$

quantum dots. For ease of comparison, each N_{del}/N_{pr} curve is normalized to the value obtained using a pulse width of 100 ms. From these data, the delayed luminescence probed at earlier times plateaus at shorter excitation pulse widths than that collected at later times. This observation reflects the impact of the excitation pulse width on the distribution of delayed luminescence decay dynamics, as illustrated in Figure 5.1. Faster delayed luminescence can be generated from shorter excitation pulses, while slower delayed luminescence requires longer excitation pulses.

To test the generality of the trends observed in Figure 5.2, analogous measurements were also performed on $d = 3.3$ nm CdSe quantum dots. Figure 5.3A plots delayed luminescence decay data for these quantum dots collected using 50 μs and 25 ms pulses. In this case, the change in decay dynamics is less pronounced in the range of pulse widths explored than observed in Figure 5.2A, but it is still significant. Figure 5.3B plots delayed luminescence decay curves measured at various excitation powers. As in Figure 5.2B, the decay dynamics change very little across this series. Figure 5.3C,D plots N_{del}/N_{pr} for each experiment from Figure 5.3A,B. k_{PL} is taken as 5×10^8 s^{-1} for the CdSe quantum dots; their decay is actually multiexponential with components of ~5×10^8 s^{-1} and ~6.3×10^7 s^{-1}, but this distinction does not qualitatively alter the results. t_1 and t_2 correspond to 200 ns and 500 μs, and t_f corresponds to 40 ns (= ~2.5−20 τ_{prompt}). Very similar trends are observed for the CdSe quantum dots (Figure 5.3C,D) as were observed with the $CuInS_2$ quantum dots, including the very slow (millisecond) approach to plateau values of N_{del}/N_{pr} with increasing pulse width (Figure 5.3C), the power dependence of the plateau values of N_{del}/N_{pr} but not of their curvature with increasing pulse width (Figure 5.3C, see also Appendix D.), and the dependence of the curvature on the luminescence monitoring window (Figure 5.3D). N_{del}/N_{pr} does plateau at much longer excitation pulse widths for the $CuInS_2$ quantum dots (~80 ms, Figure 5.2C) than for the CdSe quantum dots (~5 ms, Figure 5.3C), reflecting the slower prompt luminescence

of the $CuInS_2$ quantum dots and the competition between prompt luminescence and charge trapping[5] as well as differences in the trapping/detrapping rates and experimental measurement windows (*vide infra*). Overall, the general qualitative trends are very similar for the $CuInS_2$ and CdSe quantum dots.

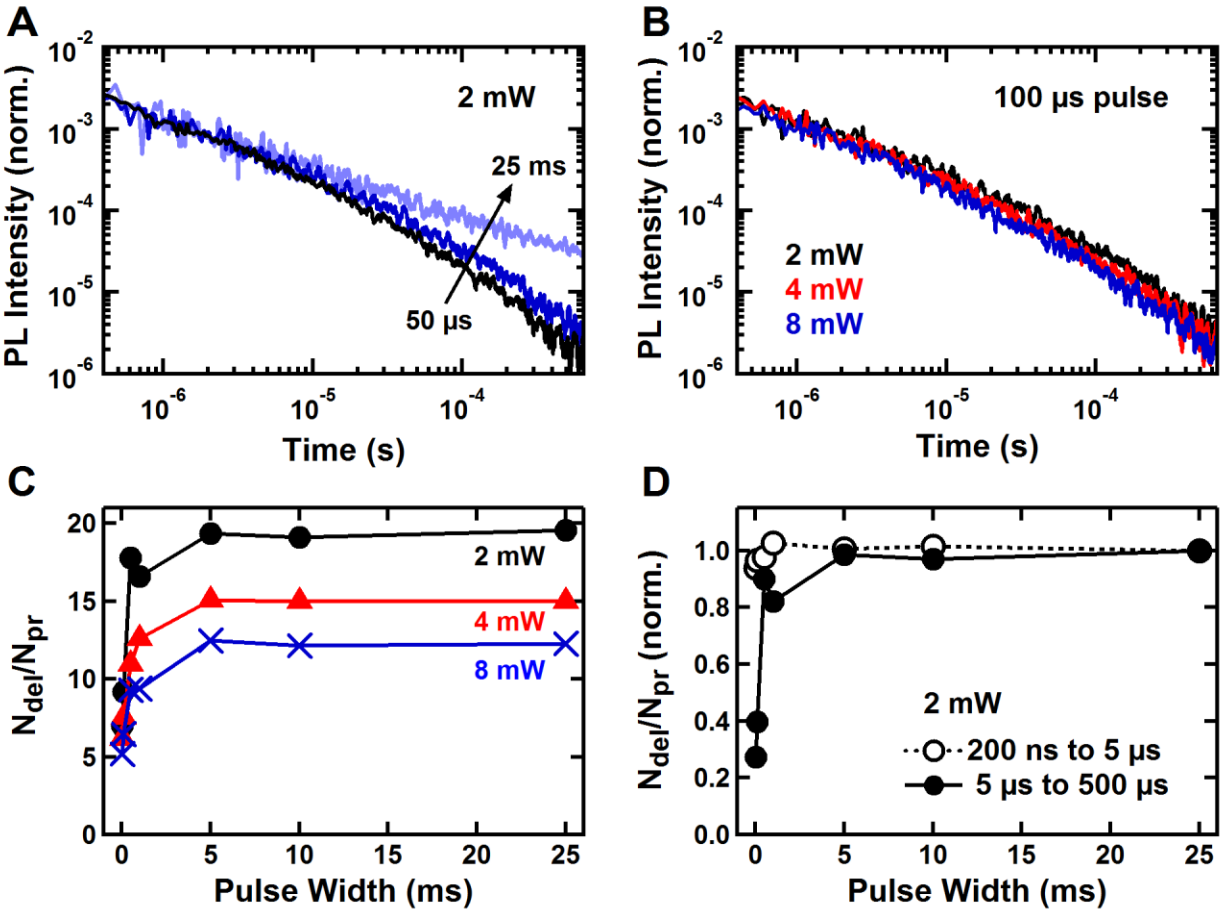

Figure 5.3. Dependence of delayed luminescence on pulse width and power for CdSe NCs. Dynamics of delayed luminescence for increasing pulse width for d = 3.3 nm CdSe quantum dots (50 µs, 100 µs, and 25 ms excitation pulse width). Traces are normalized to the prompt luminescence intensity. **(B)** Dynamics of delayed luminescence measured using 2 (black), 4 (red), and 8 mW (blue) excitation powers (power densities = 6.7, 13.3, and 26.7 mW/cm^2) for the same CdSe quantum dots, with a 100 µs excitation pulse. Traces are normalized to the prompt luminescence intensity. Linear plots of the data in (A) and (B) are provided in Appendix D. . **(C)** N_{del}/N_{pr} calculated from decay curves such as those in (A) and (B) for the same CdSe quantum dots, plotted versus excitation pulse width and measured at three different excitation powers: 2 (black circles), 4 (red triangles), 8 mW (blue crosses). **(D)** N_{del}/N_{pr} for the same CdSe quantum dots, collected at 2 mW, plotted versus excitation pulse width, and normalized to the value of N_{del}/N_{pr}

at 25 ms pulse width. Two delayed luminescence integration windows are represented: a shorter window (open circles, t_1 = 200 ns, t_2 = 5 μs) and a longer window (filled circles, t_1 = 5 μs, t_2 = 500 μs). These specific integration windows were chosen to reflect the broadest overall timespan in which signal-to-noise was good, but the same trends are obtained using different integration windows. All data were collected at 20 K.

5.4 **Model**

For interpretation of these experimental results, we use the four-state kinetic model summarized in Figure 5.4 to explore the effects of various microscopic parameters on the excitation pulse-width dependence of N_{del}/N_{pr}. State populations within this model are described by the coupled differential equations given in eq 5.3. For simplicity, we adhere to idealized homogeneous (nondistributed) rate constants for these illustrations, and we discuss the implications of this idealization below.

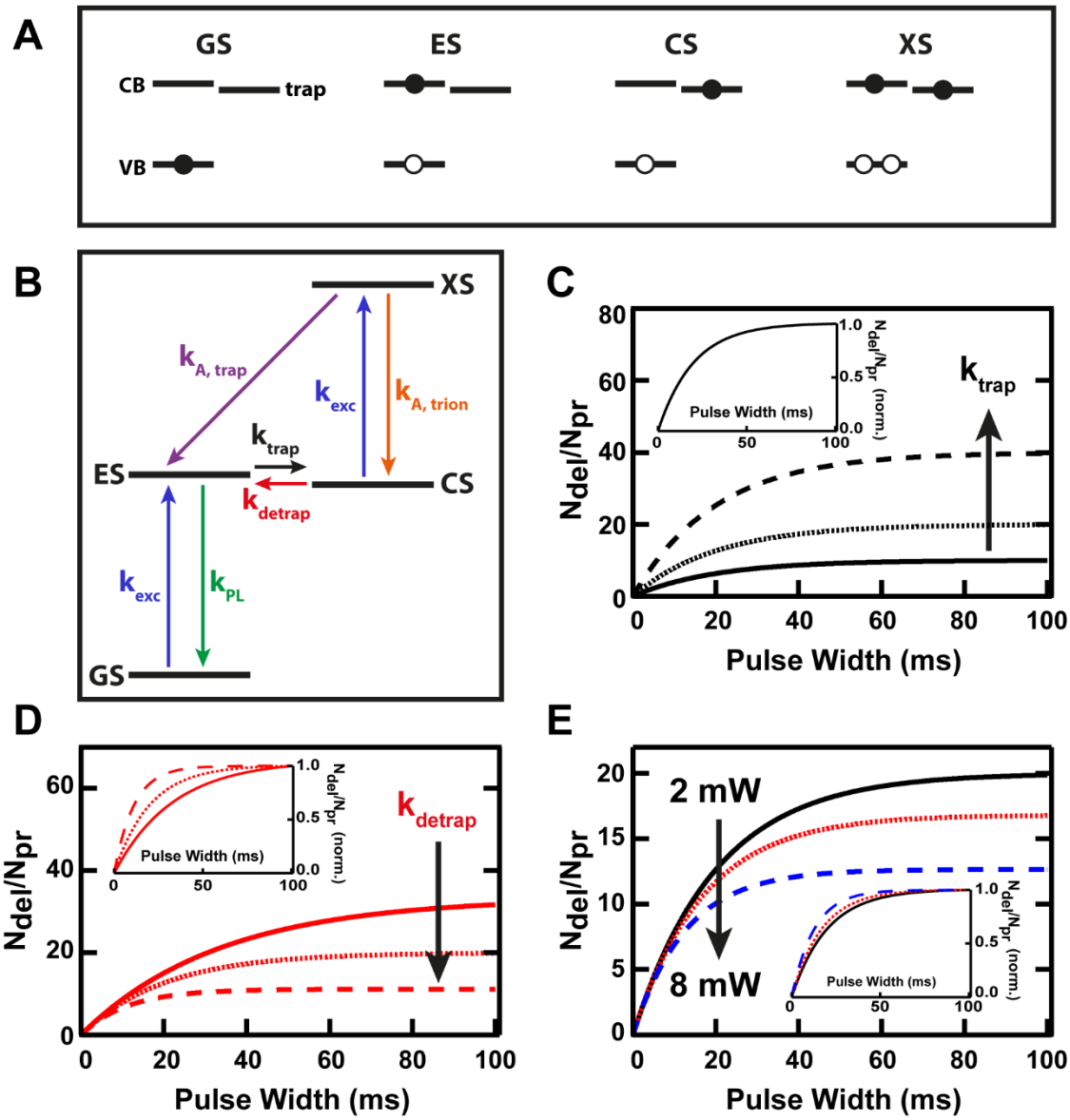

Figure 5.4. Delayed luminescence model and simulated results. (A) Electronic configurations of the four states used in the model. GS = ground state, ES = excited state, CS = charge-separated state, and XS = doubly excited state. For simplicity, electron trapping is illustrated here, but the model does not depend on which specific carrier is trapped. **(B)** Four-state model used to illustrate the experimental trends. k_{exc} represents the excitation rate constant (with power embedded), k_{PL} is the rate constant for prompt luminescence, k_{trap} is the rate constant for formation of the metastable charge-separated state, and k_{detrap} describes detrapping from this state to reform the emissive excited state. $k_{A,trap}$ and $k_{A,trion}$ represent nonradiative trap-assisted and trion Auger processes, respectively. **(C,D)** Simulated results from this model using parameters appropriate for the $CuInS_2$ quantum dots, plotting the ratio N_{del}/N_{pr} versus excitation pulse width. k_{trap} and k_{detrap} are varied systematically, while all the other parameters are held fixed ($k_{exc} = 20\ s^{-1}$, $k_{PL} = 5 \times 10^5\ s^{-1}$, $k_{A,trap} = k_{A,trion} = 10^{10}\ s^{-1}$). (C) $k_{trap} = 500\ s^{-1}$ (solid), $1000\ s^{-1}$ (dotted), and $2000\ s^{-1}$

(dashed), all with $k_{detrap} = 40\ s^{-1}$. (D) $k_{detrap} = 20\ s^{-1}$ (solid), $40\ s^{-1}$ (dotted), and $80\ s^{-1}$ (dashed), all with $k_{trap} = 1000\ s^{-1}$. The insets show the normalized curves for each plot. The arrows show the directions of increasing k_{trap} and k_{detrap}, respectively. **(E)** Simulated results for excitation powers of 2 ($k_{exc} = 20\ s^{-1}$, solid), 4 ($k_{exc} = 39\ s^{-1}$, dotted), and 8 mW ($k_{exc} = 78\ s^{-1}$, dashed), keeping all other parameters constant ($k_{PL} = 5 \times 10^5\ s^{-1}$, $k_{A,trap} = k_{A,trion} = 10^{10}\ s^{-1}$, $k_{trap} = 1000\ s^{-1}$, $k_{detrap} = 40\ s^{-1}$). The insets show the normalized curves.

$$\frac{d[GS]}{dt} = k_{PL}[ES] - k_{exc}[GS]$$

$$\frac{d[ES]}{dt} = k_{exc}[GS] + k_{detrap}[CS] + k_{A,trap}[XS] - k_{PL}[ES] - k_{trap}[ES]$$

$$\frac{d[CS]}{dt} = k_{trap}[ES] + k_{A,trion}[XS] - k_{detrap}[CS] - k_{exc}[CS]$$

$$\frac{d[XS]}{dt} = k_{exc}[CS] - k_{A,trap}[XS] - k_{A,trion}[XS] \quad (5.3)$$

Solving eq 5.3 yields the populations of the ground state (GS), the emissive excited state (ES), the metastable charge-separated excited state (CS), and the doubly excited state (XS) during and after excitation. Electronic configurations associated with each of these states are depicted in Figure 5.4A. For simplicity, we illustrate electron dynamics as rate-determining for delayed luminescence,[3] but it is likely that the hole is also localized in the metastable state for $CuInS_2$;[13] the kinetic model does not rely on these specifics. In eq 5.3 and Figure 5.4B, k_{trap} and k_{detrap} describe the formation and detrapping of the metastable state, and, along with k_{exc}, are the meaningful variables in these simulations. To account for the observed excitation power dependence of N_{del}/N_{pr}, the model also includes excitation from the charge-separated state to a doubly excited state, which can decay to the emissive excited state through a trap-assisted Auger process described by $k_{A,trap}$ or to the charge-separated state through a trion Auger process described by $k_{A,trion}$. These fast nonradiative processes are modeled with $k_{A,trap} = k_{A,trion} = 10^{10}\ s^{-1}$ for all simulations, consistent with experimentally measured rates for similar Auger processes in small NCs.[14-16]

To simulate the evolution of the state populations during the excitation pulse, eq 5.3 was solved with k_{exc} determined from the experimental excitation powers and extinction coefficients and initial conditions of $[GS]_0 = 100$ and $[ES]_0 = [CS]_0 = [XS]_0 = 0$. Evaluating this result at the end of the pulse gives the populations of the states when the excitation pulse is turned off. These populations can then be used as initial conditions for solving eq 5.3 again with $k_{exc} = 0$ to simulate their decay with time. Simulated luminescence decay curves illustrating the effects of changing the various model parameters are included in Appendix D. .

We note that in the model calculations, all trapping and detrapping processes are much slower than the prompt luminescence (*i.e.*, k_{trap} and $k_{detrap} \ll k_{PL}$), so effectively, after termination of the excitation pulse the entire [ES] decays as prompt luminescence and the entire initial [CS] decays as delayed luminescence. Consequently, to a very good approximation, the values of N_{del}/N_{pr} obtained from complete integration of the model decay curves (eqs 5.1 and 5.2) equal the values of [CS]/[ES] computed at the ends of the excitation pulses (see Appendix D.). The experimental systems are complicated by their distributed trapping/detrapping kinetics, because trapping/detrapping and prompt luminescence may now occur on overlapping time scales,[4] and moreover the [CS] can decay by other routes, such as *via* population of even deeper traps.[5-6] Additionally, while the model simulates only a single pulse and all excited-state populations are zero at the beginning of the pulse, ensuring complete depopulation of the charge-separated state before beginning any excitation pulse is more challenging in the laboratory because of the extremely broad distribution of detrapping kinetics and the need for signal averaging over multiple excitation pulses; delayed luminescence from these quantum dots persists even seconds after excitation,[5] albeit with very small rates.

For comparison with the experimental data in Figure 5.2, Figure 5.4C−E plots simulated values of N_{del}/N_{pr} (taken as [CS]/[ES] at the ends of the excitation pulses) as a function of excitation pulse width for various model conditions using parameters appropriate for the $CuInS_2$ quantum dots. The simulated data in Figure 5.4C show that increasing k_{trap} increases the plateau magnitude of N_{del}/N_{pr}, but the inset to Figure 5.4C shows that the curvature of the pulse-width dependence of N_{del}/N_{pr} is only modestly influenced by k_{trap}. On the other hand, Figure 5.4D and its inset show that k_{detrap} influences both the plateau magnitude of N_{del}/N_{pr} and the curvature of its pulse-width dependence. From these simulations, it is thus apparent that the pulse-width dependence of N_{del}/N_{pr} is mainly dictated by k_{detrap}. In other words, the time required to reach steady state under photoexcitation is determined mainly by the slower detrapping kinetics.

Figure 5.4E illustrates the effect of varying the excitation pulse power, with all other parameters fixed. N_{pr} increases linearly with excitation power, whereas N_{del} saturates because of nonradiative Auger processes in the doubly excited state, resulting in a reduction of N_{del}/N_{pr} with increased excitation power at any given pulse width, as observed experimentally (Figure 5.2C). Notably, reproducing the experimental dependence of N_{del}/N_{pr} on excitation power requires the presence of the trap-assisted Auger pathway, though the strength of this power dependence is influenced by the ratio of $k_{A,trap}$ to $k_{A,trion}$ (see Appendix D.). This result can be understood by recognizing that of these two processes, only the trap-assisted Auger process introduces a power-dependent pathway for depopulating the charge-separated state. Trap-assisted Auger processes have been largely overlooked in nanocrystal photophysics, and only relatively recently has their significance gained recognition.[16-18] The inset to Figure 5.4E shows the same curves normalized to their plateau magnitudes. Again, the curvature shows very little power dependence, consistent

with experiment. Overall, the model of Figure 5.4B and eq 5.3 thus successfully reproduces the major experimental trends summarized in Figure 5.2C for the $CuInS_2$ quantum dots.

5.5 Discussion

Although it captures the major trends, this idealized model cannot reproduce the experimental observations of Figure 5.2D. Specifically, this model does not capture the effect of changing the delayed luminescence integration window on the curvature of the pulse-width dependence (see Appendix D.). This discrepancy occurs because of the model's reliance on single rate constants for each microscopic process depicted in Figure 5.4B. The experimental observations thus allow the conclusion that the different excitation pulse-width dependence obtained when probing different delayed luminescence decay windows (Figure 5.2D and Figure 5.3D) reflects the *distributed* kinetics of these processes. Importantly, when the experimental curves in Figure 5.2D and Figure 5.3D are made by sampling earlier (or later) during delayed luminescence (different t_1 and t_2 in eq 5.1), they selectively report on faster (or slower) subsets of dynamical processes within the distribution. These data thus point to a weak correlation between k_{trap} and k_{detrap}, both of which are broadly distributed. This insight, together with the experimental luminescence decay data in Figure 5.1, Figure 5.2, and Figure 5.3, therefore highlights how both the experimental excitation pulse width *and* the experimental detection window can bias the observed delayed luminescence intensities and dynamics toward a specific subset of behaviors within a broadly distributed range. These observations have important implications for any quantitative analysis of delayed luminescence amplitudes or decay dynamics.

The data presented here are in some ways reminiscent of prior observations made for CdSe/CdS core/shell quantum dots in which multipulse excitation with an 80 MHz repetition rate was found to yield different excitonic photoluminescence decay dynamics for few versus many

concatenated excitation pulses.[19] This difference was analyzed in terms of an enhanced contribution from multiply excited quantum dots when multiple excitation pulses were delivered in short succession. The approach of using rapid sequential photoexcitation with a tunable number of short pulses is analogous to our use of variable square-wave pulse widths in the present study. Just like at high powers in ref. 19, simulation of our long-pulse decay data by the addition of multiple offset short-pulse decay curves fails to reproduce the experimental long-pulse data (see Appendix D.), pointing to multiexcitation effects and supporting the conclusion of trap-assisted Auger recombination deduced from the data in Figure 5.2C and Figure 5.3C. Of course, the microscopic processes described in ref. 19 occurred on much shorter time scales than those studied here. For example, steady state was reached within ~100 ns of quasi-continuous excitation in ref. 19, whereas Figure 5.2C shows that steady state is not reached until ~80 ms of continuous excitation for the $CuInS_2$ quantum dots (or ~5 ms for CdSe quantum dots, Figure 5.3C), that is, ~10^5 times slower.

The data here may also have ramifications for understanding the relationships between delayed luminescence and single-quantum-dot blinking proposed in several studies.[1,3-5,8] If it is correct to equate the metastable charge-separated state of delayed luminescence with a blinking "off" state, then the finding that the excitation pulse duration affects the detrapping kinetics should imply a dependence of blinking "off"-time statistics on similar excitation parameters. To our knowledge, there have been no single-quantum-dot blinking studies employing variable pulse-width excitation, however. An early study reported a change in the number of "on"/"off" cycles with different continuous-wave (cw) excitation powers between 0.4 and 7.8 kW/cm^2.[20] Another study varied the cw excitation power density from 0.1 to 2.0 kW/cm^2 and did not see any effect on the "off"-time statistics.[21] A recent study compared pulsed versus cw excitation at the

same average intensity and found that the main impact of pulsed excitation was to increase photobleaching.[22] These authors also reported that pulsed excitation lowers the probability of long "on" events, but they do not describe any significant change in "off"-time statistics.[22] As noted recently,[5] one complication in any direct comparison between blinking and delayed luminescence is the fact that only a subset of the traps that contribute to blinking will also generate delayed luminescence. Moreover, it is conceivable that some of the kinetic dispersion observed in the delayed luminescence arises from the quantum dot ensemble and would therefore not be observed from an individual quantum dot, although we note that even single-quantum-dot delayed luminescence shows broadly distributed decay dynamics.[1]

In summary, we report two main observations that have not been previously described: (*i*) quantum-dot delayed luminescence decay dynamics are strongly influenced by the experimental excitation conditions, and (*ii*) such dynamics are particularly sensitive to excitation pulse duration, a parameter that is rarely examined systematically or controlled for experimentally. For both CdSe and $CuInS_2$ quantum dots, decay of the delayed luminescence is strikingly slower when longer excitation pulses are used. Short (*e.g.*, nanosecond) excitation pulses generate markedly less delayed luminescence than long (*e.g.*, microsecond) excitation pulses, and very long (greater than millisecond) excitation pulses are required to reach a regime in which the delayed luminescence no longer depends on the excitation pulse width. Modeling shows that this behavior reflects the extremely long excitation times required for the population of the metastable charge-separated excited states responsible for delayed luminescence to reach steady state and that the main parameter affecting this approach to steady state is the detrapping rate constant. Although these simulations successfully reproduce the major experimental observations from our excitation pulse-width- and power-dependence measurements, our idealized model does not include distributed rate

constants and consequently does not reproduce the experimental dependence of N_{del}/N_{pr} on the delayed luminescence integration window or the change in average decay rate with changing excitation pulse width, emphasizing the importance of such distributed kinetics. Overall, these findings shed new light on the ubiquitous phenomenon of delayed luminescence in colloidal quantum dots and hence on the underlying charge-carrier trapping and detrapping processes that so strongly impact the physical properties of this class of materials.

5.6 Supporting Information

Appendix D. : Additional experimental details, absorption and ensemble photoluminescence data, linear plots of delayed luminescence dynamics, comparison of the change in dynamics for changing the excitation power and pulse width by similar factors, normalized plots of power-dependence data, simulated luminescence decay curves, simulated pulse-width dependence of N_{del}/N_{pr} for different integration windows and with different nonradiative processes, and comparison of experimental long-pulse decay curves with decay curves simulated by summing experimental short-pulse decay curves.

5.7 Acknowledgments

Financial support from the National Science Foundation (DMR-1505901 to D.R.G. and CHE-1404674 to P.J.R.) is gratefully acknowledged. A.M. acknowledges the support of an Early Postdoc Mobility Fellowship from the Swiss National Science Foundation. K.E.K. thanks the Department of Energy for support through an Energy Efficiency and Renewable Energy (EERE) postdoctoral research award. We thank Dr. Charles Barrows and Mr. Troy Kilburn for synthesis of the CdSe and $CuInS_2$ quantum dot samples used in these studies. Part of this work was conducted at the UW Molecular Analysis Facility, which is supported in part by funds from the

UW Molecular Engineering & Sciences Institute, the UW Clean Energy Institute, the National Science Foundation, and the National Institutes of Health.

5.8 References

1. Sher, P. H.; Smith, J. M.; Dalgarno, P. A.; Warburton, R. J.; Chen, X.; Dobson, P. J.; Daniels, S. M.; Pickett, N. L.; O'Brien, P. Power Law Carrier Dynamics in Semiconductor Nanocrystals at Nanosecond Timescales. *Appl. Phys. Lett.* **2008**, *92*, 101111.
2. Jones, M.; Lo, S. S.; Scholes, G. D. Quantitative Modeling of the Role of Surface Traps in CdSe/CdS/ZnS Nanocrystal Photoluminescence Decay Dynamics. *Proc. Nat. Acad. Sci. U. S. A.* **2009**, *106*, 3011-3016.
3. Whitham, P. J.; Knowles, K. E.; Reid, P. J.; Gamelin, D. R. Photoluminescence Blinking and Reversible Electron Trapping in Copper-Doped CdSe Nanocrystals. *Nano Lett.* **2015**, *15*, 4045-4051.
4. Rabouw, F. T.; Kamp, M.; van Dijk-Moes, R. J. A.; Gamelin, D. R.; Koenderink, A. F.; Meijerink, A.; Vanmaekelbergh, D. Delayed Exciton Emission and Its Relation to Blinking in CdSe Quantum Dots. *Nano Lett.* **2015**, *15*, 7718-7725.
5. Marchioro, A.; Whitham, P. J.; Knowles, K. E.; Kilburn, T. B.; Reid, P. J.; Gamelin, D. R. Tunneling in the Delayed Luminescence of Colloidal CdSe, Cu^{+}-Doped CdSe, and $CuInS_2$ Semiconductor Nanocrystals and Relationship to Blinking. *J. Phys. Chem. C* **2016**, *120*, 27040-27049.
6. Rabouw, F. T.; van der Bok, J. C.; Spinicelli, P.; Mahler, B.; Nasilowski, M.; Pedetti, S.; Dubertret, B.; Vanmaekelbergh, D. Temporary Charge Carrier Separation Dominates the Photoluminescence Decay Dynamics of Colloidal CdSe Nanoplatelets. *Nano Lett.* **2016**, *16*, 2047-2053.
7. Chirvony, V. S.; González-Carrero, S.; Suarez, I.; Galian, R. E.; Sessolo, M.; Bolink, H. J.; Martinez-Pastor, J. P.; Pérez-Prieto, J. Delayed Luminescence in Lead Halide Perovskite Nanocrystals. *J. Phys. Chem. C* **2017**, *121*, 13381-13390.
8. Whitham, P. J.; Marchioro, A.; Knowles, K. E.; Kilburn, T. B.; Reid, P. J.; Gamelin, D. R. Single-Particle Photoluminescence Spectra, Blinking, and Delayed Luminescence of Colloidal $CuInS_2$ Nanocrystals. *J. Phys. Chem. C* **2016**, *120*, 17136-17142.
9. Tachiya, M.; Seki, K. Unified Explanation of the Fluorescence Decay and Blinking Characteristics of Semiconductor Nanocrystals. *Appl. Phys. Lett.* **2009**, *94*, 081104.
10. Nirmal, M.; Dabbousi, B. O.; Bawendi, M. G.; Macklin, J. J.; Trautman, J. K.; Harris, T. D.; Brus, L. E. Fluorescence Intermittency in Single Cadmium Selenide Nanocrystals. *Nature* **1996**, *383*, 802-804.
11. Efros, A. L.; Nesbitt, D. J. Origin and Control of Blinking in Quantum Dots. *Nat. Nanotechnol.* **2016**, *11*, 661-671.

12. Cordones, A. A.; Leone, S. R. Mechanisms for Charge Trapping in Single Semiconductor Nanocrystals Probed by Fluorescence Blinking. *Chem. Soc. Rev.* **2013**, *42*, 3209-3221.

13. van Schooten, K. J.; Huang, J.; Talapin, D. V.; Boehme, C.; Lupton, J. M. Spin-Dependent Electronic Processes and Long-Lived Spin Coherence of Deep-Level Trap Sites in CdS Nanocrystals. *Phys. Rev. B* **2013**, *87*, 125412.

14. Jha, P. P.; Guyot-Sionnest, P. Trion Decay in Colloidal Quantum Dots. *ACS Nano* **2009**, *3*, 1011-1015.

15. Cohn, A. W.; Rinehart, J. D.; Schimpf, A. M.; Weaver, A. L.; Gamelin, D. R. Size Dependence of Negative Trion Auger Recombination in Photodoped CdSe Nanocrystals. *Nano Lett.* **2014**, *14*, 353-358.

16. Cohn, A. W.; Schimpf, A. M.; Gunthardt, C. E.; Gamelin, D. R. Size-Dependent Trap-Assisted Auger Recombination in Semiconductor Nanocrystals. *Nano Lett.* **2013**, *13*, 1810-1815.

17. Allan, G.; Delerue, C. Fast Relaxation of Hot Carriers by Impact Ionization in Semiconductor Nanocrystals: Role of Defects. *Phys. Rev. B* **2009**, *79*, 195324.

18. Sun, J.; Ikezawa, M.; Wang, X.; Jing, P.; Li, H.; Zhao, J.; Masumoto, Y. Photocarrier Recombination Dynamics in Ternary Chalcogenide $CuInS_2$ Quantum Dots. *Phys. Chem. Chem. Phys.* **2015**, *17*, 11981-11989.

19. Singh, G.; Guericke, M. A.; Song, Q.; Jones, M. A Multipulse Time-Resolved Fluorescence Method for Probing Second-Order Recombination Dynamics in Colloidal Quantum Dots. *J. Phys. Chem. C* **2014**, *118*, 14692-14702.

20. Banin, U.; Bruchez, M.; Alivisatos, A. P.; Ha, T.; Weiss, S.; Chemla, D. S. Evidence for a Thermal Contribution to Emission Intermittency in Single CdSe/CdS Core/Shell Nanocrystals. *J. Chem. Phys.* **1999**, *110*, 1195-1201.

21. Shimizu, K. T.; Neuhauser, R. G.; Leatherdale, C. A.; Empedocles, S. A.; Woo, W. K.; Bawendi, M. G. Blinking Statistics in Single Semiconductor Nanocrystal Quantum Dots. *Phys. Rev. B* **2001**, *63*, 205316.

22. Smyder, J. A.; Amori, A. R.; Odoi, M. Y.; Stern, H. A.; Peterson, J. J.; Krauss, T. D. The Influence of Continuous vs. Pulsed Laser Excitation on Single Quantum Dot Photophysics. *Phys. Chem. Chem. Phys.* **2014**, *16*, 25723-25728.

Chapter 6. Picosecond Dynamics of Excitonic Magnetic Polarons in Colloidal Diffusion-Doped $Cd_{1-x}Mn_xSe$ Quantum Dots

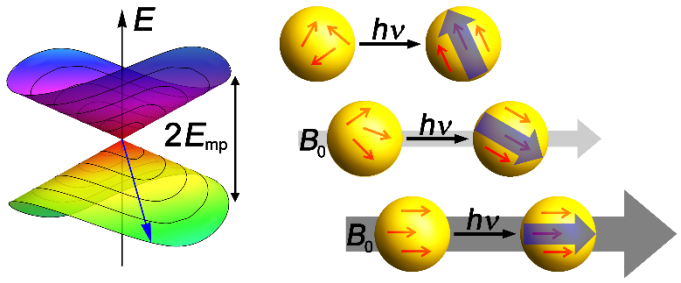

Reproduced with permission from Nelson, H. D.; Bradshaw, L. R.; Barrows, C. J.; Vlaskin, V. A.; Gamelin, D. R. *ACS Nano* **2015**, *9*, 11177-11191. Copyright 2015 American Chemical Society.

6.1 Overview

Spontaneous magnetization is observed at zero magnetic field in photoexcited colloidal $Cd_{1-x}Mn_xSe$ (x = 0.13) quantum dots (QDs) prepared by diffusion doping, reflecting strong Mn^{2+}–exciton exchange coupling. The picosecond dynamics of this phenomenon, known as an excitonic magnetic polaron (EMP), are examined using a combination of time-resolved photoluminescence, magneto-photoluminescence, and Faraday rotation (TRFR) spectroscopies, in conjunction with continuous-wave absorption, magnetic circular dichroism (MCD), and magnetic circularly polarized photoluminescence (MCPL) spectroscopies. The data indicate that EMPs form with random magnetization orientations at zero external field, but their formation can be directed by an external magnetic field. After formation, however, external magnetic fields are unable to reorient the EMPs within the luminescence lifetime, implicating anisotropy in the EMP potential-energy surfaces. TRFR measurements in a transverse magnetic field reveal rapid (<5 ps) spin transfer from excitons to Mn^{2+} followed by coherent EMP precession at the Mn^{2+} Larmor

frequency for over a nanosecond. A dynamical TRFR phase inversion is observed during EMP formation attributed to the large shifts in excitonic absorption energies during spontaneous magnetization. Partial optical orientation of the EMPs by resonant circularly polarized photoexcitation is also demonstrated. Collectively, these results highlight the extraordinary physical properties of colloidal diffusion-doped $Cd_{1-x}Mn_xSe$ QDs that result from their unique combination of strong quantum confinement, large Mn^{2+} concentrations, and relatively narrow size distributions. The new insights gained from these measurements advance our understanding of spin dynamics and magnetic exchange in colloidal doped semiconductor nanostructures, with potential ramifications for future spin-based information technologies.

6.2 Introduction

Diluted magnetic semiconductors (DMSs)[1-4] are envisioned as key functional components of future spintronics and spin-photonics technologies. Formed by incorporation of magnetic impurities into nonmagnetic semiconductors, DMSs display physical properties defined by magnetic exchange interactions between localized impurity spins and delocalized semiconductor charge-carrier spins, the so-called *sp*−*d* exchange interactions. An intriguing feature of *sp*−*d* exchange is that the large electronic delocalization lengths in semiconductors allow simultaneous coupling of a single carrier with a multitude of magnetic dopants occupying the same volume as the carrier. The individual pairwise carrier−dopant exchange interactions contribute additively to generate "giant" Zeeman splittings of the semiconductor band structure, introducing the possibility of long-range cooperative magnetic effects. Extraordinary physical properties resulting from such giant Zeeman splittings have been demonstrated, both in the ground states (*e.g.*, magneto-transport) and in electronic excited states (*e.g.*, photo- or electro-excitation) of DMSs, including giant Faraday rotations,[5-6] carrier-induced magnetic ordering,[7-10] electrical spin polarization,[11-14]

and magnetically tunable lasing,[15] offering glimpses into the diverse possibilities for using spins to control the functionalities of semiconductor devices.

By localizing the carriers somewhat within confinement potentials provided by defects (in bulk) or interfaces (in nanostructures), *sp*−*d* exchange effects can be enhanced relative to bulk, and both self-assembled[16-17] and colloidal[18-19] DMS quantum dots (QDs) have therefore attracted intense interest in recent years. In the low-doping extreme, single and small-number dopant−carrier exchange splittings have been observed in the excitonic states of self-assembled QDs that may prove useful for coherent optical spin manipulations in information processing technologies.[20-23] In the other extreme, very large excitonic Zeeman splittings and charge-controlled magnetism have been observed in colloidal QDs with substantial (x = 0.01−0.20) magnetic ion contents.[24-25] Among the most dramatic manifestations of strong *sp*−*d* exchange in DMSs is the so-called excitonic magnetic polaron (EMP), in which photoexcitation leads to spontaneous magnetization of the dopant spin sublattice,[26-37] aided by enhanced effective exchange fields within spatially confined volumes.

EMP formation in a DMS QD is illustrated schematically in the single-magnetic-coordinate diagram of Figure 6.1.[35] At zero external magnetic field ($B_0 = 0$), the QD ground state shows no net magnetization (represented by the spin expectation value, $\langle S_\phi \rangle = 0$), but the ensemble of dopant spins is subject to statistical magnetic fluctuations.[38] Photoexcitation generates an exciton that is exchange-coupled with this entire ensemble of dopant spins, introducing a force that lowers the excited-state energy by magnetizing the QD, *i.e.*, $dE/d\langle S_\phi \rangle \neq 0$. In other words, the initial excited state formed at the intersection of excitonic Zeeman sublevels is unstable with respect to spontaneous displacement along some magnetization coordinate, ϕ. EMP formation is thus a magnetic analog of the more common Jahn−Teller effect, with a displacement coordinate that is

magnetic rather than geometric. Magnetization of the dopant sublattice lowers the excited-state energy until the displacement force is counterbalanced by kT (quasi-thermal equilibrium), magnetization reaches completion (saturation), or the electron and hole recombine. A photon released from the QD during or after this relaxation will have less energy than the absorbed photon. Typically, EMP formation occurs on the ~200 ps time scale, much faster than the Mn^{2+} spin–lattice relaxation in the absence of the exciton ($\tau_{mp} \ll \tau_{SLR}$). This process is likely so fast because of efficient mediation *via* Mn^{2+}–Mn^{2+} spin–spin interactions at these high Mn^{2+} concentrations,[39] and it may also reflect the large acceleration of Mn^{2+} spin–lattice relaxation in the presence of charge carriers.[40-42]

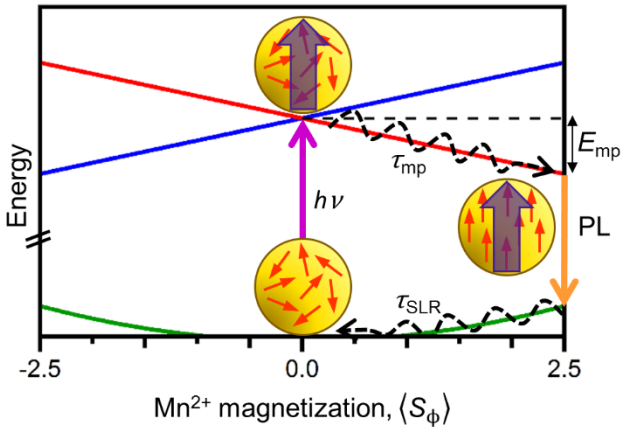

Figure 6.1. Single-magnetic-coordinate diagram describing EMP formation in a DMS QD. Here, EMP formation occurs along direction ϕ at zero applied magnetic field ($B_0 = 0$). Prior to photoexcitation, dopant spins are uncorrelated and randomly oriented, *i.e.*, $\langle S_\phi \rangle = 0$. Upon photoexcitation ($h\nu$), the dopant spins experience an exchange field (B_{eff}) due to the overlapping exciton, which introduces a displacement force ($dE/d\langle S_\phi \rangle \neq 0$) that splits the excitonic state into Zeeman components (red and blue lines) and thereby lowers the total energy of the QD excited state by $E_{mp} = (1/2)|\Delta E_{Zeeman}|$. The magnetization time scale is characterized by τ_{mp}. A photon emitted during or after this relaxation is redshifted relative to the absorbed photon. After recombination, the dopant spins in the ground-state QD relax back to $\langle S_\phi \rangle = 0$ on the time scale defined by Mn^{2+} τ_{SLR}. To describe real QDs, this diagram must be expanded to include all possible magnetization coordinates in three-dimensional space.

Colloidal QDs offer even stronger carrier confinement than epitaxial quantum wells or self-assembled QDs. In recent years, colloidal $Cd_{1-x}Mn_xSe$ QDs prepared by cluster thermolysis[43] have served as a workhorse model system for detailing the unique physical properties of colloidal DMS QDs,[18] displaying "giant" excitonic Zeeman splittings (ΔE_{Zeeman}) by MCD and magneto-absorption spectroscopies,[44-45] strong spin-polarized excitonic luminescence,[45] and robust EMPs in the absence of an external magnetic field.[35] Whereas EMPs in most self-assembled DMS QDs typically show exchange fields of a few Tesla (B_{eff} < ~3.5 T) that are insufficient to achieve facile magnetic saturation, those of the colloidal $Cd_{1-x}Mn_xSe$ QDs reach approximately an order of magnitude larger values when estimated at short times (B_{eff} > ~40 T, 1 ns), with additional slow-relaxation contributions hypothesized to arise from anisotropic forces raising them to >100 T in some instances.[35] Such large exchange fields, combined with the longer excited-state lifetimes of the colloidal QDs, have yielded extremely robust EMPs that show spontaneous magnetic saturation of the Mn^{2+} spins up to ~50 K at $B_0 = 0$.[35] To date, no other colloidal EMPs have been reported beyond those described above, and several important aspects of colloidal EMPs remain wholly unexplored.

Recently, we reported a new method for synthesizing high-quality colloidal $Cd_{1-x}Mn_xSe$ (and related) QDs involving Mn^{2+} diffusion into preformed undoped CdSe QDs.[25] This synthesis provides unprecedented control over the QD composition, reaching Mn^{2+} contents of $x > 0.20$ while maintaining the narrow size distributions of the undoped QD seeds. The high Mn^{2+} concentrations accessible by diffusion doping yield enormous magneto-optical effects characterized by effective excitonic g values ($g_{eff} = \Delta E_{Zeeman}/\mu_B B_0$) as large as $|g_{eff}| > 900$ at 1.8 K,[25,46] and at the same time their narrow size distributions allow direct detection of first-excitonic Zeeman splittings by magneto-absorption spectroscopy[46] as well as analysis of the Zeeman

splittings of many upper excitonic states.[47] These properties make diffusion-doped colloidal $Cd_{1-x}Mn_xSe$ QDs attractive for time-resolved investigations of dopant−carrier exchange effects.

Here, we report on the dynamical properties of EMPs formed in colloidal diffusion-doped $Cd_{1-x}Mn_xSe$ QDs. Using a combination of continuous-wave (CW) and time-resolved (TR) magneto-optical techniques, we describe the picosecond evolution of EMPs in these QDs as a function of applied magnetic field. Analysis of CW MCD and magneto-absorption data reveals extremely large excitonic Zeeman splittings characterized by $|g_{eff}| \sim 1180$ at 1.8 K with saturation values reaching $|\Delta E_{Zeeman}| \sim 78$ meV. Whereas random EMP orientation at $B_0 = 0$ leads to zero net magnetization within the QD ensemble, application of B_0 in the Faraday geometry directs EMP formation along the field axis, leading to net alignment of EMPs and the emergence of circularly polarized luminescence during EMP formation. At large B_0 and low T, where Mn^{2+} spins are prealigned prior to photoexcitation, the resulting EMPs are mostly aligned and large luminescence circular polarizations are obtained. Intrinsic barriers to EMP reorientation by B_0 result in much weaker magnetic-field dependence of the MCPL polarization ratios than expected from the magnitudes of ΔE_{Zeeman} observed by magneto-absorption and MCD spectroscopies. Picosecond time-resolved Faraday rotation (TRFR) spectroscopy reveals rapid (<5 ps) spin transfer from excitons to Mn^{2+} ions followed by long-lived coherent Mn^{2+} spin precession with $T_2^* \sim 370$ ps. A dynamical TRFR phase inversion is observed, coming from the large exciton energy shifts during EMP formation, confirming precession of the EMPs themselves. These results provide a wealth of new information about the physical properties of these unique colloidal EMPs, particularly in the time domain and under applied magnetic fields. Relationships between these colloidal EMPs and the more common self-assembled EMPs are discussed.

6.3 Results and Analysis

6.3.1 Continuous-Wave Spectroscopies

Figure 6.2a plots electronic absorption and PL spectra of $d \sim 4.5$ nm colloidal $Cd_{0.87}Mn_{0.13}Se$ QDs measured at several temperatures. The absorption spectrum narrows and shifts to higher energy with decreasing temperature, following the well-known Varshni temperature dependence. The PL shows a more complex temperature dependence. Figure 6.2b plots the PL peak energies. With decreasing temperature, the PL energy increases, reaches a maximum at ~60 K, and then decreases by ~20 meV below ~60 K. These data suggest a Stokes shift that grows as temperature is lowered, and are consistent with EMP formation. Figure 6.2c plots the temperature-dependent component of the Stokes shift vs $1/T$. A temperature-independent shift of ~35 meV, which is typical in colloidal QDs and not associated with EMP formation, has been subtracted from these data (see Appendix E.). The temperature-dependent contribution to the Stokes shift represents the EMP stabilization energy, E_{mp} (Figure 6.1). The data in Figure 6.2 are thus interpreted as reflecting EMP formation with E_{mp} increasing to a maximum of ~44 meV at 10 K and below.

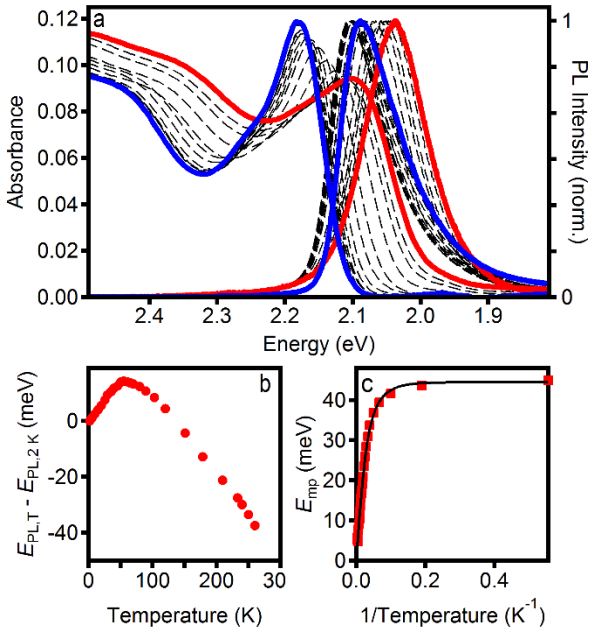

Figure 6.2. Temperature-dependent CW absorption and PL. (a) Variable-temperature absorption and CW-PL spectra of colloidal $Cd_{0.87}Mn_{0.13}Se$ QDs (d ~ 4.5 nm) recorded between 5 K (blue) and 280 K (red) at zero magnetic field. The absorption maximum blueshifts with decreasing temperature following Varshni-like behavior. The PL peak blueshifts with decreasing temperature down to ~60 K and then redshifts at lower temperatures. This temperature-dependent redshift is characteristic of EMP formation. **(b)** Temperature dependence of the PL peak energy, plotted relative to the PL energy at T = 2 K. **(c)** Temperature dependence of the EMP energy obtained from the absorption and PL energies. The linear increase in the EMP energy at high temperatures reflects Curie paramagnetism. The plateau at low temperature reflects saturation of the nanocrystal magnetization. The solid line is a fit to the Brillouin function of eq 6.1 using S = 5/2 and g_{Mn} = 2.00, which yields B_{eff} = 17 T for the exchange field acting on the Mn^{2+} spins in the QDs.

Following previous analyses,[31-32,35,48] the Stokes shift data in Figure 6.2c are fit using the isotropic S = 5/2 Brillouin function given in eq 6.1, which allows the effective exchange field (B = B_{eff}) experienced by the paramagnetic Mn^{2+} within the QDs to be estimated. The exchange field B_{eff} aligns the Mn^{2+} spins along the EMP direction ϕ. Here, μ_B is the Bohr magneton, k is the Boltzmann constant, g_{Mn} = 2.00, and C_1 is a scaling constant related to the number of Mn^{2+} per QD and their location. Note that B_{eff} is determined by the curvature of the data set, not its height.

$$E_{\mathrm{mp}} = \frac{1}{2} C_1 \langle S_\phi \rangle = \frac{1}{2} C_1 \left[\frac{(2S+1)}{2} \coth\left((2S+1)\left(\frac{g_{\mathrm{Mn}} \mu_{\mathrm{B}} B}{2kT} \right) \right) - \frac{1}{2} \coth\left(\frac{g_{\mathrm{Mn}} \mu_{\mathrm{B}} B}{2kT} \right) \right] \quad (6.1)$$

The data are reproduced well using $B_{\mathrm{eff}} = 17$ T (solid line in Figure 6.2c). Although similar analyses of PL energies have been commonly used to estimate B_{eff} in the EMPs of self-assembled QDs,[31,48] we note that there is some uncertainty in this approach related to accounting for other possible contributions to the Stokes shift, such as dark−bright exciton splittings. This approximation does appear reasonable, however, because (*i*) E_{mp} (~44 meV) is much greater than the dark−bright exciton splitting energies for CdSe QDs of this diameter (~2.5 meV[49]), and (*ii*) the value of E_{mp} obtained from this analysis is close to half the value of $\Delta E_{\mathrm{Zeeman}}$ measured by MCD spectroscopy on the same sample (*vide infra*), as expected. Although smaller than the maximum values of B_{eff} achieved in colloidal DMS QDs[35] and type-II self-assembled DMS QDs,[50] 17 T is large compared to typical B_{eff} values measured from the EMPs of type-I self-assembled DMS QDs (*e.g.*, $B_{\mathrm{eff}} \sim 3.5$ T[31]). From these data, EMP formation is evident already at >100 K and reaches saturation by ~10 K. Below, we describe the EMP dynamics measured at $T \leq 10$ K, where the EMPs have reached magnetic saturation.

We note that the PL peak is quite asymmetric at low temperature. The entire PL band displays a similar magnetic-field dependence in MCPL measurements (*vide infra*), strongly arguing against attribution of this asymmetry to trap emission or other spurious effects. Instead, we interpret this asymmetry as resulting from the slow time-dependent PL redshift after EMP formation, as discussed below.

Figure 6.3 summarizes absorption, magnetic circular dichroism (MCD), and magnetic circularly polarized luminescence (MCPL) data collected for the $d \sim 4.5$ nm $Cd_{0.87}Mn_{0.13}Se$ QDs. Generally, the giant excitonic Zeeman splittings of colloidal DMS QDs have been assessed by

analysis of their MCD intensities.[19] As described recently, the first-excitonic Zeeman splittings in these diffusion-doped $Cd_{1-x}Mn_xSe$ QDs can be observed directly in their magneto-absorption spectra.[46] The absorption and MCD spectra of Figure 6.3a show a clear Zeeman splitting of the first excitonic absorption peak and a large derivative-shaped *A*-term MCD response when the magnetic field is increased from 0 to 5 T at 1.8 K. The excitonic Zeeman splitting energies (ΔE_{Zeeman}) quantified from these data are plotted in Figure 6.3b with fits to the Brillouin function in eq 6.2, where $\langle S_z \rangle$ describes the magnetization along the observation axis *z*. The $\langle S_z \rangle$ term has the same form as the $\langle S_\phi \rangle$ term from eq 6.1, but is defined as negative and with $B = B_0$ because the magnetization is induced by the external field (B_0). At 1.8 K and small B_0, this splitting is characterized by $g_{eff} \sim -1180$. At saturation (largest B_0 and lowest *T*), $\Delta E_{Zeeman} = -78$ meV, which is similar in magnitude to $2 \times E_{mp} = 88$ meV from Figure 6.2c, as anticipated from Figure 6.1. For the scaling constant in eqs 6.1 and 6.2, $C_1 = x_{eff}\gamma N_0(\alpha - \beta)$, where x_{eff} is the effective Mn^{2+} concentration accounting for antiferromagnetic coupling in Mn^{2+} dimers and clusters, γ represents the overlap between the exciton and the ensemble of Mn^{2+} ions ($\gamma = 1$ in the uniform doping limit), and $N_0(\alpha - \beta)$ represents the *sp*−*d* exchange energies. On the basis of this relationship, ΔE_{Zeeman} is approximately half as large as would be expected from $\gamma = 1$, the empirical dependence of x_{eff} on *x*,[51] and the bulk *sp*−*d* mean-field exchange energies ($N_0(\alpha - \beta) \approx 1.5$ eV[52-53]). Because the bulk value of $N_0(\alpha - \beta)$ has been shown to be valid for QDs,[54] this this discrepancy is related to the product $x_{eff}\gamma$ and could possibly reflect a small Mn^{2+} concentration gradient within these diffusion-doped $Cd_{1-x}Mn_xSe$ QDs.

$$\Delta E_{Zeeman} = C_1 \langle S_z \rangle \tag{6.2}$$

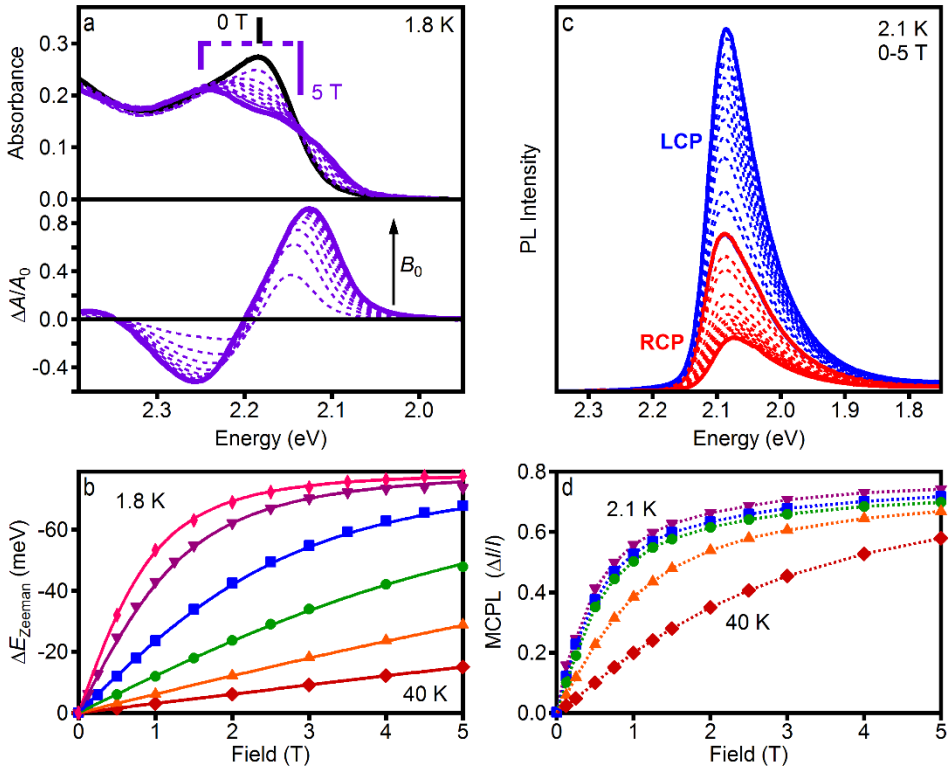

Figure 6.3. Temperature- and field-dependent absorption, MCD and MCPL. **(a)** Variable-field absorption and MCD spectra of colloidal $Cd_{0.87}Mn_{0.13}Se$ QDs (d ~ 4.5 nm) at 1.8 K. As B_0 increases along z, the Mn^{2+} spin sublattice is magnetized and the excitonic Zeeman splitting (ΔE_{Zeeman}) increases in magnitude. This splitting is visible directly in the absorption spectrum at high fields, and gives rise to the large MCD intensities and the positive sign of the MCD leading-edge intensity. **(b)** Field and temperature dependence of ΔE_{Zeeman}, from analysis of the MCD and magnetoabsorption data (T = 1.8, 2.5, 5, 10, 20, 40 K). **(c)** Variable-field left circularly polarized (LCP) and right circularly polarized (RCP) photoluminescence spectra (MCPL) of the same colloidal $Cd_{0.87}Mn_{0.13}Se$ QDs measured at 2.1 K. **(d)** Field and temperature dependence of the MCPL polarization ratio, $\Delta I/I$ (T = 2.1, 5, 10, 20, 40 K). The dotted lines in (d) are guides to the eye.

The 2.1 K MCPL spectra presented in Figure 6.3c show the emergence of strong circular polarization upon application of B_0, reaching a maximum of $\Delta I/I$ ~ 0.75 at the highest fields. Interestingly, these MCPL spectra do not show an energy shift with magnetic field comparable to that observed by absorption spectroscopy in Figure 6.3a. Instead, a PL redshift of only ~3.5 meV is observed upon increasing B_0 from 0 to 5 T at 2.1 K and above (see Appendix E.). This small shift is attributed to the magnetic-field stabilization of excitons at very short times ($t < \tau_{mp}$).

Although the PL lifetime is much longer than τ_{mp} and the CW-PL spectrum is dominated by emission from fully formed EMPs, a small portion of photons is emitted by excitons that recombine before EMP formation is complete. The alignment of Mn^{2+} spins by the external field stabilizes these excitons at $t < \tau_{mp}$. A weak field dependence of the CW-PL energy was also observed in self-assembled type-II DMS QDs, where the PL lifetime is also much longer than τ_{mp}.[50]

Figure 6.3d plots the MCPL polarization ratio $\Delta I/I$ vs B_0 for a series of temperatures. Each isotherm shows saturation magnetization, but the curvature is different from that measured by MCD (Figure 6.3b). Specifically, for a given temperature, saturation is reached at slightly lower magnetic fields in the MCPL experiment. Notably, the MCPL magnetic field dependence does not reflect the giant excitonic Zeeman splittings of these QDs. With $g_{eff} \sim -1180$, magnetic saturation should be achieved at extremely small B_0 at the lowest temperatures.

6.3.2 **Time-Resolved Magneto-Luminescence**

Figure 6.4 describes the time-resolved PL of these $Cd_{0.87}Mn_{0.13}Se$ QDs. Figure 6.4a plots the $B_0 = 0$ PL spectrum vs time over the first 0.8 ns following the excitation pulse. The solid line traces the PL maximum in time. Starting at 2.14 eV, the PL shifts to 2.11 eV over the first ~600 ps following the excitation pulse. This dynamical redshift is characteristic of EMP formation and reflects the QD magnetization dynamics under the exchange field of the exciton.[55] This redshift occurs significantly faster than the PL decay, which is multiexponential but is fit well to a biexponential with $\tau_1 = 4.2$ ns and $\tau_2 = 16.7$ ns (see Appendix E.). The PL continues to redshift at longer times (see Appendix E.), suggesting an additional very slow component to EMP equilibration. This very slow component is the source of the previously discussed asymmetry in the CW-PL line shape.

Similar biphasic energy shifts have been observed in other EMPs and their slow components attributed to EMP reorientation after formation.[35,56]

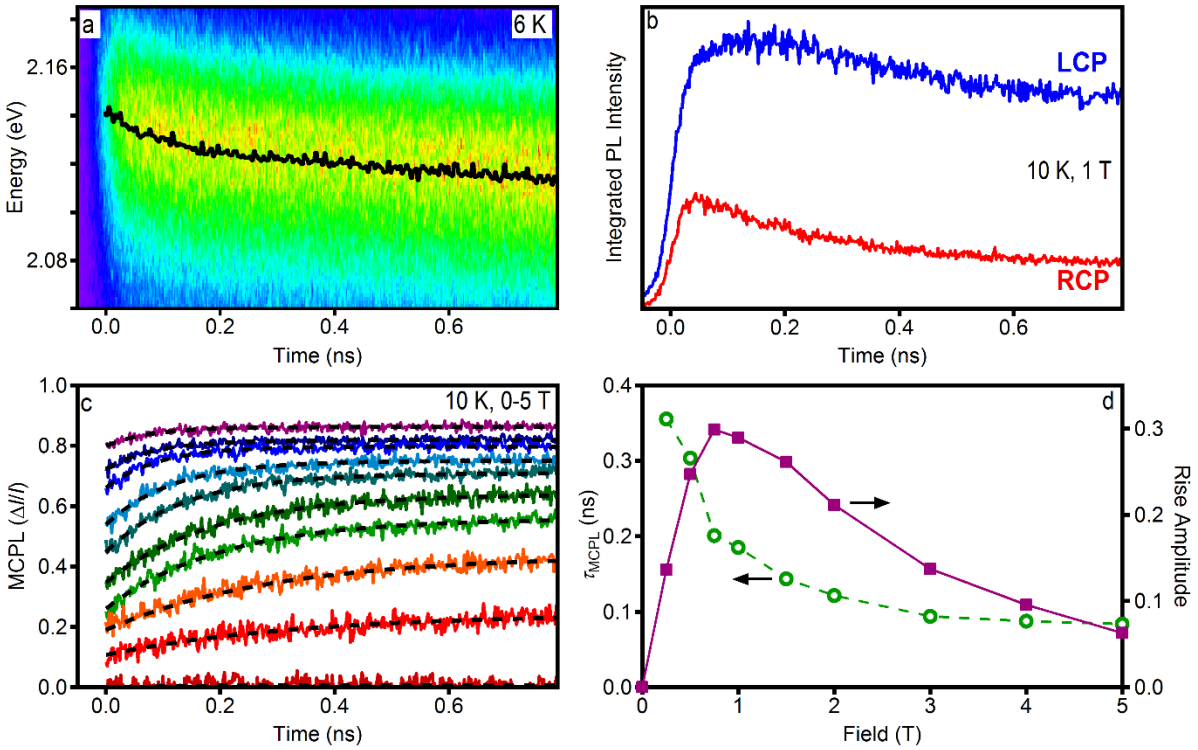

Figure 6.4. Time-resolved MCPL. (a) Streak-camera image of PL from $Cd_{0.87}Mn_{0.13}Se$ QDs ($d \sim 4.5$ nm) at $T = 6$ K. The solid line traces the peak emission energy, which redshifts due to EMP formation. **(b)** Spectrally integrated intensities of RCP and LCP emission as a function of time for the same QDs at $T = 10$ K and $B_0 = 1$ T along z. **(c)** MCPL polarization ratio ($\Delta I/I$) as a function of time for the same QDs at $T = 10$ K, $B_0 = 0-5$ T. The black dashed lines are single-exponential fits to the data. $\Delta I/I$ increases with similar dynamics to EMP formation. **(d)** Field dependence of the MCPL rise time (τ_{MCPL}, green circles; from the fits in panel c) and rise amplitude (purple squares; defined as MCPL(0.8 ns) − MCPL(0 ns)).

Figure 6.4b shows the time evolution of the RCP and LCP emission intensities for the same QDs at $B_0 = 1$ T and $T = 10$ K. Comparison with Figure 6.4a shows that the LCP intensity increases and the RCP intensity decreases as the EMP forms. From these data, TR-MCPL polarization ratios ($\Delta I/I$) can be obtained. Figure 6.4c plots TR-MCPL data over the same 0.8 ns window for several field strengths. At $B_0 = 0$ T, there is no net circular polarization of the luminescence. With $B_0 > 0$

along z, the circular polarization emerges (Figure 6.3c,d). Fitting each TR-MCPL curve of Figure 6.4c to a single exponential yields a rise time (τ_{MCPL}, related to the process of EMP formation and orientation) and a relaxation amplitude for each value of B_0. Figure 6.4d plots these fitted values vs B_0. τ_{MCPL} decreases smoothly with increasing B_0, but the relaxation amplitude first increases with increasing B_0 up to ~0.75 T and then decreases again at higher fields. These data reflect the dual role of the applied field: At low fields, the small Mn^{2+} magnetization before photoexcitation biases EMP formation toward the observation axis. At larger fields, more of the Mn^{2+} spins are aligned prior to photoexcitation and fewer Mn^{2+} spins remain to be aligned by the exciton. The small redshift in the CW-PL energy with increasing B_0 (see Appendix E.) is also consistent with this interpretation. Overall, the data in Figure 6.4 provide unambiguous confirmation that the magnitudes and dynamics of the Stokes shifts in these $Cd_{0.87}Mn_{0.13}Se$ QDs shown in Figure 6.2 and Figure 6.4a are indeed magnetic in origin, *i.e.*, reflect EMP formation.

Figure 6.5 replots the data from Figure 6.4c as the MCPL polarization ratio vs magnetic field, focusing on initial ($t = 0$) and relaxed ($t = 0.8$ ns) TR-MCPL polarization ratios. Both $\Delta I/I(0)$ and $\Delta I/I(0.8\text{ ns})$ increase with increasing magnetic field, but to different extents. Specifically, $\Delta I/I(0.8\text{ ns})$ approaches saturation more quickly than $\Delta I/I(0)$. For comparison, Figure 6.5 also plots the relevant MCD and MCPL data measured under approximately the same conditions, taken from Figure 6.3. The $\Delta I/I(0)$ TR-MCPL data are similar to the saturation magnetization observed by MCD, and the $\Delta I/I(0.8\text{ ns})$ TR-MCPL data are superimposable upon the CW-MCPL data. This comparison illustrates that the TR-MCPL measurement traces the evolution of the EMP from its initial state, which is dictated by the magnetization of the Mn^{2+} spins by B_0, to its final state, which is dominated by the exchange field, B_{eff}. The small difference between the $\Delta I/I(0)$ TR-MCPL and

MCD data in Figure 6.5 is consistent with some degree of EMP relaxation within the TR-MCPL instrument response time (26 ps).

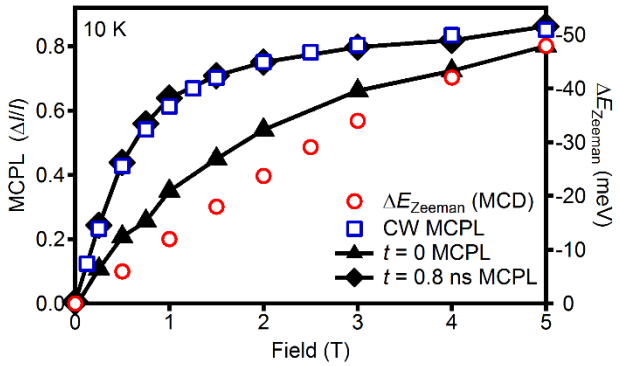

Figure 6.5. Comparison of CW and time-dependent magnetization. Field dependence of ΔE_{Zeeman} from MCD (Figure 6.3b), CW-MCPL ratio (Figure 6.3d, scaled by 1.2 due to differences in the sample film quality and experimental alignment), MCPL ratio at $t = 0$, and MCPL ratio at $t = 0.8$ ns (Figure 6.4c), all measured at $T = 10$ K. The field dependence of the MCPL ratio at $t = 0$, before EMP formation, resembles the field dependence of ΔE_{Zeeman} from MCD. The field dependence of the MCPL ratio at $t = 0.8$ ns, after EMP formation, resembles the field dependence of the CW-MCPL. The change in the TR-MCPL ratio from $t = 0$ to $t = 0.8$ ns reflects the change in Mn^{2+} magnetization during EMP formation.

6.3.3 Magnetic Fluctuations and the CW-MCPL

Whereas the absorption and MCD experiments probe the initially prepared excitonic state, the CW-MCPL measurement primarily probes the same excited state after the EMP magnetic relaxation illustrated in Figure 6.1. The absorption spectrum (Figure 6.3a) shows stabilization of the first excited state upon application of a magnetic field, but the PL peak energy does not redshift significantly with magnetic field (see Appendix E.), indicating that emission comes from an excited state that is already fully magnetized at $B_0 = 0$ and $T \approx 2$ K, *i.e.*, the saturated EMP. The magnetic field does increase $\Delta I/I$, however, from which it follows that the primary effect of B_0 is to align EMP magnetization along the experimental viewing axis. This observation holds the key to understanding the slow approach to saturation with increasing B_0 measured by CW-MCPL

(Figure 6.3d), which implicates internal forces that cause EMP misalignment and impede EMP reorientation by B_0 during the PL lifetime.

To clarify these points, Figure 6.6 replots the data from Figure 6.3d as $\Delta I/I$ vs $1/T$ for each external field, B_0. In this representation, these data closely resemble the EMP stabilization energies (E_{mp}) plotted in Figure 6.2c. Both measurements show similar saturation at $1/T > \sim 0.1$ K^{-1}, attributable to complete Mn^{2+} magnetization under the exciton's exchange field, B_{eff}. Figure 6.6 further illustrates that this saturation occurs at the same temperature for each applied field, but with different values of $\Delta I/I$. This result indicates that B_0 affects only the net alignment of these EMPs and not their thermal stability. The latter is dominated by B_{eff}.

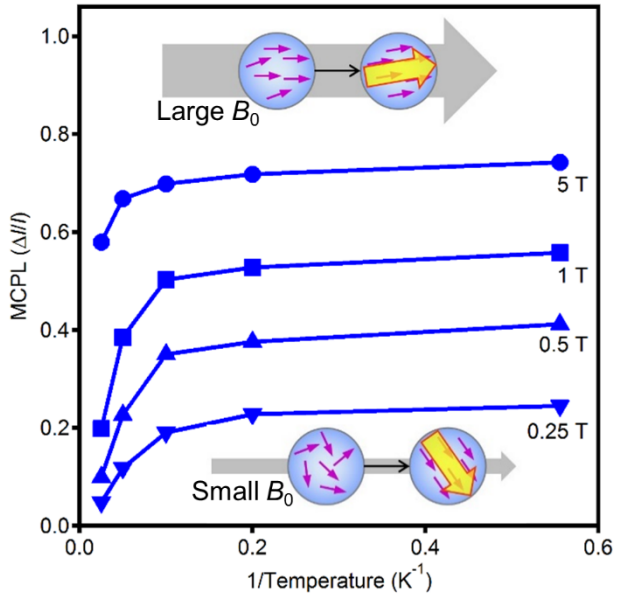

Figure 6.6. Saturation of the MCPL polarization ratio at low temperatures. Temperature dependence of the MCPL polarization ratio at $B_0 = 0.25$, 0.5, 1, and 5 T along z, taken from Figure 6.3d. At all fields, the MCPL ratio saturates in the same temperature range as the EMP energy in Figure 6.2c. The insets illustrate the effect of B_0 on EMP orientation. In a weak external field, the Mn^{2+} spins show small net alignment along the field axis, but the average EMP is oriented along an off-axis direction, resulting in small MCPL ratios. In a strong external field, the Mn^{2+} spins are closer to alignment prior to photoexcitation. The resulting EMPs are then oriented along the field axis, leading to large MCPL ratios.

Figure 6.7 compares the experimental MCPL intensities from Figure 6.3d with predicted MCPL intensities from two models. The first model, based simply on Boltzmann distributions within the giant Zeeman splittings measured by MCD (Figure 6.3b), predicts that the CW-MCPL intensity should saturate at much smaller magnetic fields than observed (Figure 6.7b), even with no additional magnetization due to B_{eff}. For example, at 10 K the CW-MCPL should saturate by ~0.5 T, but experimentally it reaches only ~1/2 of its saturation value at this field. Such rapid saturation is indeed observed in self-assembled $Cd_{1-x}Mn_xSe$ QDs that do not display EMPs.[57] This comparison highlights the weak B_0 dependence of the experimental MCPL intensities observed here. An unexpectedly weak magnetic-field dependence of EMP MCPL has also been observed in $Cd_{1-x}Mn_xTe$ epitaxial layers and QWs,[56,58] where it was interpreted in terms of Mn^{2+} magnetization fluctuations. EMPs are believed to form along the direction of the net Mn^{2+} magnetic moment at the instant of photoexcitation, a direction determined by the combination of B_0 and random thermal magnetic fluctuations within the ensemble of Mn^{2+} ions in the QD. Once formed, these EMPs are not reoriented by B_0 on the PL time scale. A similar interpretation appears to apply here. We note that the PL lifetime in these epitaxial $Cd_{1-x}Mn_xTe$ QWs is only ~350 ps at 1.6 K, but in our $Cd_{0.87}Mn_{0.13}Se$ QDs, it is ~10 ns at 10 K (see Appendix E.).

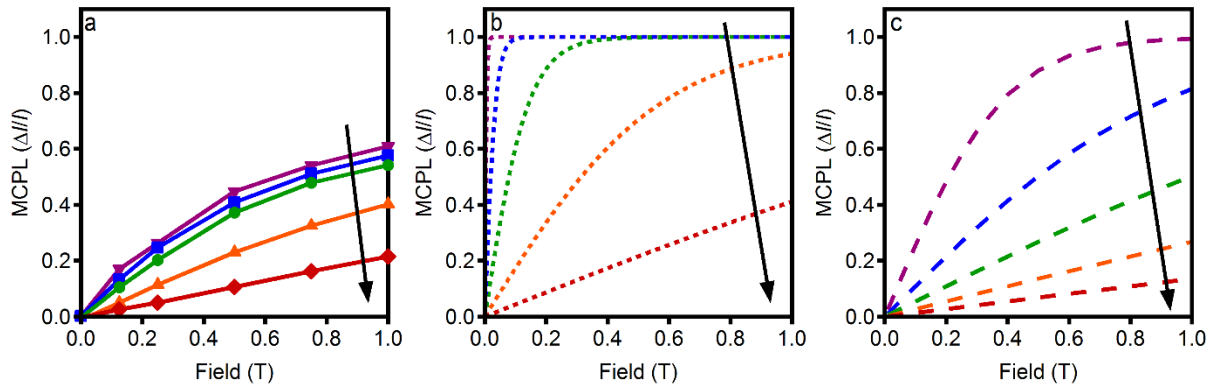

Figure 6.7. Comparison of experimental and simulated MCPL temperature and field dependence. Experimental and calculated MCPL polarization ratios in the low-field regime at $T = 2.1$, 5, 10, 20, and 40 K. The arrows indicate increasing

temperature. **(a)** Experimental MCPL polarization ratios (from Figure 6.3d). **(b)** Calculated MCPL polarization ratios based on Boltzmann populations of the experimental excitonic Zeeman splittings. This model overestimates the polarization ratio at all temperatures and predicts saturation at much lower fields than observed experimentally. **(c)** Calculated MCPL polarization ratios based on the fluctuation model of ref. 56. This model predicts the observed MCPL field and temperature dependence at high temperatures reasonably well, but deviates from the data at low temperatures (≤10 K) and high magnetic fields, where EMP saturation is observed experimentally.

To test this interpretation, the impact of magnetic fluctuations on the MCPL field dependence can be modeled as detailed in ref. 56. The average Mn^{2+} magnetization M induced by B_0 is expressed in terms of the $S = 5/2$ Brillouin function, as in eqs 6.1 and 6.2, with $B = B_0$ and with a different scaling constant (eq 6.3, $C_2 = x_{\text{eff}} N_0 V g_{\text{Mn}} \mu_{\text{B}}$, where N_0 is the cation density and V is the QD volume).

$$M = C_2 \langle S_z \rangle \tag{6.3}$$

The fluctuation-dissipation theorem enables the variance of the Mn^{2+} magnetization fluctuations ($\langle M^2 \rangle$) to be expressed in terms of M (eq 6.4).[38,56]

$$\langle M^2 \rangle = kT \frac{dM}{dB_0} \tag{6.4}$$

Equation 6.5 represents a Gaussian distribution of Mn^{2+} magnetic moments.[55-56,58] Here, M_x, M_y, and M_z are the directional components of the magnetization. The distribution is centered at $M_x = M_y = 0$ and $M_z = M(B_0)$.

$$\Phi(M_x, M_y, M_z, B_0) = \frac{1}{\left(2\pi \langle M^2 \rangle\right)^{3/2}} \exp\left[- \frac{M_x^2 + M_y^2 + \left(M_z - M(B_0)\right)^2}{2\langle M^2 \rangle} \right] \tag{6.5}$$

For an EMP oriented at an angle ϕ with respect to z, the intensities of LCP and RCP emission are given by eqs 6.6a and 6.6b, where $I_L(\phi) + I_R(\phi) = I(\phi)$. The relative intensities of LCP and RCP emission should also depend on the Boltzmann populations of the EMP Zeeman

sublevels, but this contribution to the MCPL polarization ratio is not significant because $E_{mp} \gg kT$ under our conditions.

$$I_L(\phi) = (1 + \cos(\phi))^2 \tag{6.6a}$$

$$I_R(\phi) = (1 - \cos(\phi))^2 \tag{6.6b}$$

With these intensities and the distribution of EMP alignments given by eq 6.5, the MCPL polarization ratio can be calculated using eq 6.7.

$$\frac{\Delta I}{I} = \frac{\iiint dM_x dM_y dM_z [I_L(\phi) - I_R(\phi)] \Phi(M_x, M_y, M_z, B_0)}{\iiint dM_x dM_y dM_z [I_L(\phi) + I_R(\phi)] \Phi(M_x, M_y, M_z, B_0)} \tag{6.7}$$

Figure 6.7c shows $\Delta I/I$ values calculated using this model for different temperatures and B_0 within the linear (low-field) region of dM/dB_0. The calculated $\Delta I/I$ values agree reasonably well with the experimental data at the three highest temperatures (40, 20, 10 K). Both appear approximately linearly dependent on B_0 and both increase by similar amounts with decreasing temperature. These trends are understood as follows: Decreasing the temperature increases the initial magnetization for a given B_0, simultaneously decreasing the magnetic fluctuations. These changes lead to a narrower distribution of EMP orientations around the z axis and consequently an increased $\Delta I/I$.

Although it represents a significant improvement over the predicted MCPL in Figure 6.7b, the fluctuation model fails to reproduce the data at T < ~10 K. Specifically, the model presented above predicts $\Delta I/I$ to continue increasing with decreasing temperature, but the data show saturation at T < ~10 K. The model also fails when saturation is approached using large B_0. We note that this model does not account for the effect of anisotropy on EMP orientation, as discussed below. Thermally activated EMP reorientation has been reported previously for acceptor-bound

magnetic polarons in bulk $Cd_{0.95}Mn_{0.05}Se$,[59] and the presence of an energy barrier to reorientation could contribute to the observed temperature dependence. It is also probable that some EMP reorientation by B_0 occurs even during EMP formation, as well as on time scales exceeding τ_{mp}. Nonetheless, the fluctuation model as applied here successfully explains the origin of the weak MCPL field dependence observed experimentally by accounting for spontaneous off-axis alignment of EMPs. Further theoretical work is required to describe the full temperature- and field-dependent behavior displayed by these colloidal EMPs within this model.

6.3.4 **Time-Resolved Faraday Rotation**

In addition to PL, picosecond spin dynamics in these QDs were probed by TRFR spectroscopy. Figure 6.8a plots low-temperature TRFR traces for CdSe QDs and two $Cd_{1-x}Mn_xSe$ QD samples (x = 0.005 and 0.13) collected in a transverse field of B_{tr} = 0.84 T. Figure 6.8b plots the Fourier transforms of these three traces with the x axis represented as $g = \hbar\omega_L/\mu_B B_{tr}$, where ω_L is the frequency at which the spins precess around the transverse field (Larmor frequency). The undoped CdSe QDs display two precession frequencies characterized by g_1 = 1.3 and g_2 = 1.7, very similar to data published for undoped CdSe QDs elsewhere.[60-61] In contrast, both sets of $Cd_{1-x}Mn_xSe$ QDs display only a single precession frequency characterized by g = 2.0. These traces are similar to those reported for self-assembled $Cd_{1-x}Mn_xSe/Zn_{1-x}Mn_xSe$ QDs[16] and for MnSe quantum wells within CdSe films,[62] in which rapid spin transfer from the host semiconductor to Mn^{2+} within the first few picoseconds is followed by long-lived coherent Mn^{2+} spin precession. The g = 2.0 signals in our $Cd_{1-x}Mn_xSe$ QDs are thus also attributed to Mn^{2+} spin precession.[62] Only in large, extremely lightly doped $Cd_{1-x}Mn_xSe$ (x < 0.005) do we observe rapid precession of the exchange-coupled exciton, which shows an apparent g value of ~35 (see Appendix E.). Even in this limit of low doping, spin transfer to Mn^{2+} is complete within ~5 ps. Spin transfer to Mn^{2+} is thus extremely

rapid in the $Cd_{1-x}Mn_xSe$ QDs that show EMPs. Analysis of the $g = 2.0$ oscillation decay in Figure 6.8a yields ensemble spin-dephasing times of $T_2^* \sim 250$ and 370 ps for $x = 0.005$ and 0.13, respectively,[63] comparable to those observed in self-assembled $Cd_{1-x}Mn_xSe/Zn_{1-x}Mn_xSe$ QDs ($T_2^* \sim 500$ ps).[16]

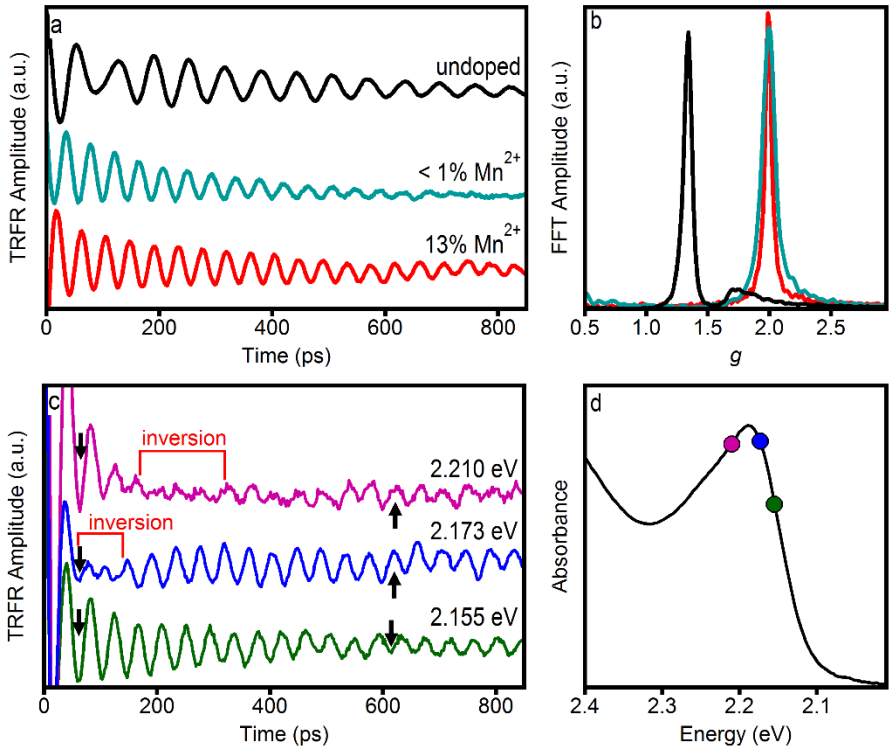

Figure 6.8. TRFR for varying Mn^{2+} concentrations and pump/probe energies. **(a)** Time-resolved Faraday rotation traces for $d \sim 3.6$ nm CdSe QDs ($T = 5$ K, $E_{pump/probe} = 2.222$ eV), $d \sim 3.8$ nm $Cd_{0.995}Mn_{0.005}Se$ QDs ($T = 10$ K, $E_{pump/probe} = 2.216$ eV), and $d \sim 4.5$ nm $Cd_{0.87}Mn_{0.13}Se$ QDs ($T = 8$ K, $E_{pump/probe} = 2.114$ eV), measured at $B_{tr} = 0.84$ T. **(b)** Fourier transforms of the TRFR traces in panel a, plotted on an x axis represented by $g = \hbar\omega_L/\mu_B B_{tr}$. **(c)** Time-resolved Faraday rotation traces for the $Cd_{0.87}Mn_{0.13}Se$ QDs, measured at $T = 8$ K and $B_{tr} = 0.84$ T with different pump/probe energies. **(d)** Absorption spectrum of the $Cd_{0.87}Mn_{0.13}Se$ QDs at $T = 10$ K with the pump/probe energies from panel c indicated.

Figure 6.8c plots TRFR traces for the same colloidal EMP QDs measured at three different pump/probe energies, illustrated in Figure 6.8d relative to the absorption maximum. The two traces with pump/probe energies closest to the excitonic maximum, 2.210 and 2.173 eV, initially display

the same phase as that measured at 2.155 eV, but their oscillation amplitudes decrease and subsequently return with the opposite phase within the first ~250 ps, after which they are stable. Such phase inversion is not observed in the $Cd_{0.995}Mn_{0.005}Se$ QDs at any pump/probe energy. In contrast with the undoped CdSe QDs, this TRFR anomaly in the $Cd_{0.87}Mn_{0.13}Se$ QDs is not explainable in terms of a superposition of two precession frequencies. Instead, Fourier transforms of these TRFR data show only very broad peaks (see Appendix E.). To our knowledge, this kind of dynamical TRFR phase inversion has not been reported previously.

To understand the origin of this anomalous energy-dependent phase inversion, we consider first the origin of the Faraday rotation signal and its dependence on the photon energy near an electronic transition. Faraday rotation occurs when plane-polarized light passes through a magnetized medium. Magnetization along the propagation direction and occupancy of spin-polarized excited states cause the refractive index of the medium to be different for RCP and LCP light, shifting the relative phases of the RCP and LCP components of linearly polarized light and thus rotating the plane of polarization. The rotation angle (θ) is described by eq 6.8, in which E is the photon energy, c is the speed of light, $\hbar$ is the reduced Planck constant, n_R and n_L are the RCP and LCP refractive indices in the medium, and L is the optical path length through the sample.[64]

$$\theta = \frac{E}{2\hbar c}(n_R - n_L)L \tag{6.8}$$

The energy dependence of the Faraday rotation phase comes from $E(n_R - n_L)$. The difference between n_R and n_L is caused by magnetization along the optical propagation direction (z). In the traditional Faraday rotation measurement, a static magnetic field is applied along z (Faraday geometry). In the TRFR experiment performed here,[64] a static transverse magnetic field is applied. Spins that precess coherently around the transverse field constitute an oscillating magnetization in the z direction. The TRFR phase is thus related to the CW Faraday rotation sign.[64]

During EMP formation, the electronic transition with energy E_0 splits into two transitions with energies $E_0 \pm E_{mp}$. In the TRFR experiment, the combination of a transverse applied field and circularly polarized excitation causes the Mn^{2+} spins to align off-axis with respect to the observation direction, and these two transitions are coupled to different *elliptical* polarizations of light. In contrast, the MCD experiment (*e.g.*, Figure 6.3) involves magnetization solely along the *z* axis, which results in selection rules coupling the transitions to *circularly* polarized light. Nonetheless, coupling to elliptically polarized light still provides a difference in refractive index for RCP and LCP light that can be measured by the Faraday rotation experiment. The ellipticity, which depends on the angle of magnetization, thus affects the magnitude of the Faraday rotation signal but not its energy or time dependence.

Figure 6.9 illustrates the proposed origin of the dynamical TRFR phase inversion schematically. For reference, Figure 6.9a plots the $Cd_{0.87}Mn_{0.13}Se$ QD absorption spectrum measured at 0 T from Figure 6.2a. Figure 6.9b(top) illustrates schematically the absorption at the first exciton at $t = 0$ under the experimental TRFR conditions, for simplicity simulated using Lorentzians for the two Zeeman components. Even at the small transverse fields used here, the Mn^{2+} magnetization is sufficient to cause an excitonic Zeeman splitting of $|\Delta E_{Zeeman}| \sim 10$ meV at 10 K. Photoexcitation of a given QD by the pump pulse bleaches the absorption of its lowest-energy Zeeman component completely because of occupancy of this state (dashed line). Consequently, the TRFR response detected by the probe pulse (which only probes QDs that have been excited by the pump pulse) is determined solely by the upper Zeeman branch. Photoexcitation with circularly polarized light also introduces a small net magnetization component along the *z* axis, but the total magnetization remains primarily orthogonal to *z*. The resulting off-axis QD magnetization means that absorption by this upper branch is elliptically polarized, and the RCP

and LCP absorption components that make up the elliptical absorption by this branch are also illustrated in Figure 6.9b(middle), with arbitrary ellipticity. Finally, Figure 6.9b(bottom) plots the corresponding $t = 0$ Faraday rotation response, $E(n_R - n_L)$, anticipated from this absorption spectrum. This shape of this signal closely resembles that which is expected in the limit of magnetization only along z, as in the MCD experiment, because the Faraday rotation is only sensitive to the z component of the magnetization.

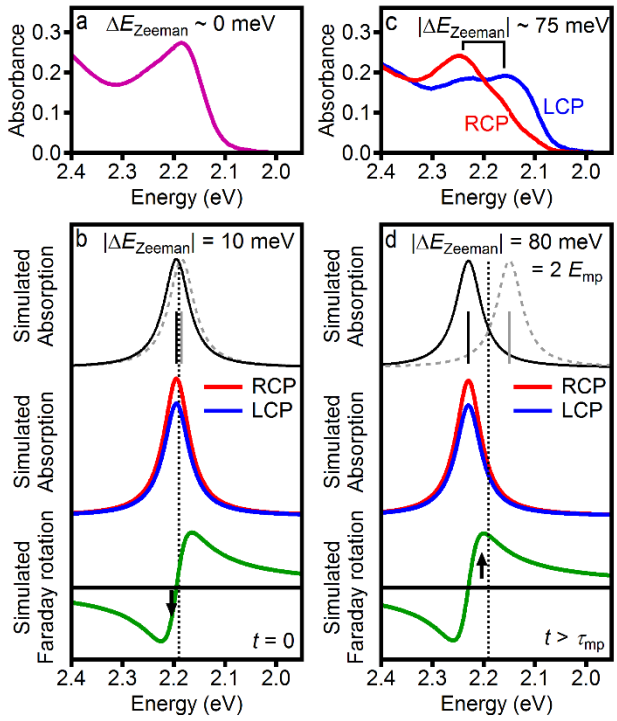

Figure 6.9. Simulated pump/probe energy dependence of the TRFR phase. (a) Experimental absorption spectrum of $Cd_{0.87}Mn_{0.13}Se$ QDs at 10 K. **(b)** Simulated absorption spectra showing the two transitions, RCP and LCP absorption spectra, and Faraday rotation, $E(n_R - n_L)$, spectra for an excitonic transition near $t = 0$, with $|\Delta E_{Zeeman}| = 10$ meV due to the magnetization from B_{tr}. The dotted vertical line indicates the average energy (E_0) of the electronic transition. The solid black line is the absorption spectrum of the upper Zeeman component, while the dashed gray line represents the lower Zeeman component, which is bleached. The arrow indicates a probe energy where phase inversion during EMP formation would be observed. **(c)** Experimental RCP and LCP absorption spectra of $Cd_{0.87}Mn_{0.13}Se$ QDs measured at 3 K and $B_0 = 3$ T, near magnetic saturation conditions where $|\Delta E_{Zeeman}| \sim 75$ meV. **(d)** Simulated absorption spectra showing the two transitions, RCP and LCP absorption spectra, and Faraday rotation, $E(n_R - n_L)$, spectra for the same excitonic transition with $|\Delta E_{Zeeman}| = 2\ E_{mp} = 80$ meV.

A few hundred picoseconds after photoexcitation ($t > \tau_{mp}$), the EMP has formed and the QD is fully magnetized. At this point, $|\Delta E_{Zeeman}| = 2E_{mp} \sim 80$ meV. For reference, Figure 6.9c plots RCP and LCP absorption spectra of the $Cd_{0.87}Mn_{0.13}Se$ QDs measured at $T = 3$ K and $B_0 = 3$ T ($|\Delta E_{Zeeman}| \sim 75$ meV), obtained by deconvolution of the data in Figure 6.3a as detailed in ref. 46. In the TRFR experiment, the first excitonic transition splits with a similar magnitude, although the two transitions are instead coupled to elliptically polarized light due to the off-axis magnetization. Paralleling Figure 6.9b, Figure 6.9d plots simulated excited-state energies, RCP and LCP absorption spectra, and Faraday rotation response anticipated after EMP formation. Absorption by the lower excitonic Zeeman branch (dashed) is still bleached because EMP formation is much faster than excited-state decay in these QDs, and transitions to the upper branch are again elliptically polarized. Importantly, EMP formation causes the upper Zeeman component to shift to higher energies, leading the Faraday rotation to change sign at some energies near E_0. The arrows in Figure 6.9b,d illustrate one such energy at which the Faraday rotation sign is inverted after EMP formation relative to $t = 0$.

Clearly, the Faraday rotation response must evolve continuously as the EMP forms, resulting in a dynamical phase inversion on the ps time scale precisely as observed experimentally (Figure 6.8). The inversion dynamics depend on the exact probe energy. For example, the 2.173 eV TRFR phase inverts at shorter times (~100 ps) than the 2.210 eV TRFR phase (~200 ps), presumably because the former is closer to the sign crossover energy. Inversion at 2.173 eV also occurs over a shorter time window (two oscillations vs several) because of the greater rate of EMP energy change at shorter times after the excitation pulse. Although contributions from overlapping absorption features lead to a complicated relationship between the precise energies and TRFR phase inversion dynamics, the schematic in Figure 6.9 captures the essence of the effect. The

observation of a dynamical TRFR phase inversion during EMP formation is an important verification of spin precession associated with the EMPs themselves. Once formed, the EMPs precess at the Mn^{2+} Larmor frequency with long coherence times under the influence of B_{tr}.

6.4 Discussion

6.4.1 Anisotropy and EMP Orientation

Figure 6.1 represents EMP formation for only one single magnetization coordinate, ϕ. In spherically symmetric QDs, this diagram must be expanded to include all possible magnetization coordinates in three-dimensional space, where it would appear as a conical intersection with cylindrical symmetry. At $B_0 = 0$, EMPs typically form rapidly along the direction of net Mn^{2+} magnetic moment at the instant of photoexcitation (or of carrier localization in extended DMSs), determined by random thermal magnetization fluctuations. B_0 can align the EMPs, but saturation of the MCPL $\Delta I/I$ occurs at much larger B_0 than expected based on Boltzmann population distributions within the excitonic spin states and the giant excitonic Zeeman splittings measured by MCD spectroscopy. The anomalously small values of $\Delta I/I$, particularly at low fields, are explained by invoking off-axis EMP formation induced by thermal magnetization fluctuations and slow (relative to PL) EMP reorientation by the external field.[56,58] Even in the isotropic (spherical) limit, EMP reorientation by B_0 is expected to be slower than τ_{mp} by a factor of $(E_{mp}/2kT)^{1/2}$.[56]

The discrepancy between the experimental data and the fluctuation model predictions at low temperatures (Figure 6.7c) indicates that EMP orientation is not entirely dictated by Mn^{2+} magnetization at the time of photoexcitation. The difference is attributed to exciton anisotropies, which are not represented in the fluctuation model. Hole effective-mass anisotropies are evident from the anisotropic EMP stabilization energies in 2D DMS quantum wells[65] and BMP

stabilization energies in bulk hexagonal $Cd_{1-x}Mn_xSe$,[59] and they are likely exacerbated by additional shape anisotropies in strongly confined nanocrystals.[66-67] Such anisotropy gives the exciton a preferred orientation that contributes to the EMP energy gradient $dE/d\langle S_\Phi \rangle$, thus introducing an additional force that directs EMP orientation.[68] Spin-diffusion bottlenecks[69] and phase transitions to spin-glass states[70] have also been discussed in relation to similar anomalous temperature dependence of the MCPL polarization ratio in epitaxial EMPs.

Figure 6.10a depicts upper and lower excitonic Zeeman surfaces for the simplest deviation from the isotropic limit, namely an axially anisotropic EMP, illustrating the appearance of an energy barrier to magnetization rotation. More complex warping of this energy landscape can be anticipated in the colloidal DMS QDs examined here, arising from their wurtzite lattice structures, local surface dipoles, or low-symmetry shapes and faceting. In the ensemble, these colloidal DMS QDs show a powder distribution of their individual anisotropies.

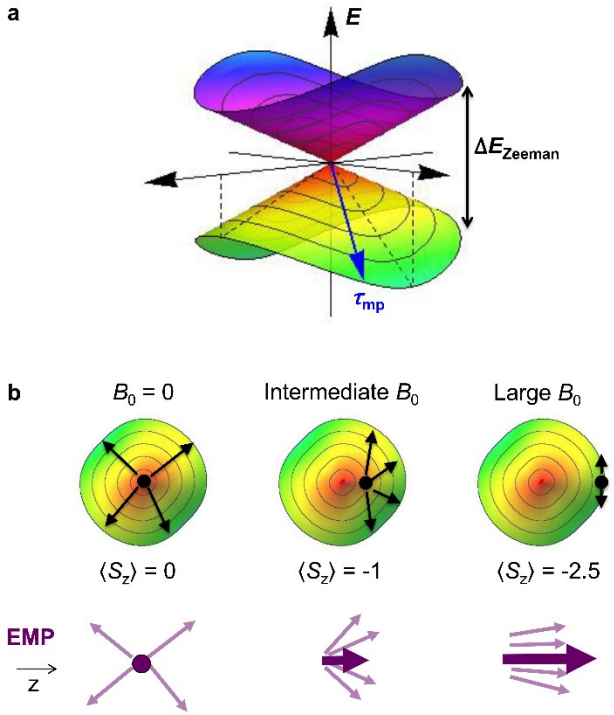

Figure 6.10. Multidimensional magnetic coordinate diagram. (a) Multidimensional magnetic-coordinate diagram describing the excitonic Zeeman

splitting of a low-symmetry (axial) $Cd_{1-x}Mn_xSe$ QD. The potential energy surface is warped by anisotropic effects, which introduce barriers to EMP rotation in an external magnetic field. Concentric contour lines represent increments of $\langle S_\phi \rangle = 1/2$. **(b)** Illustration of the effect of increasing B_0 (left to right) on EMP formation on the lower Zeeman potential energy surface. The black circles indicate the initial Mn^{2+} magnetization ($M(B_0)$), the thin arrows indicate various EMP formation trajectories, and the thick arrows indicate the net EMP projection onto the laboratory z axis, which parallels B_0.

Figure 6.10b summarizes the effect of B_0 on EMP evolution in a QD with axial anisotropy oriented randomly relative to the laboratory z axis. For a fully formed EMP, $\langle S_\phi \rangle = 5/2$ in all cases, but $\langle S_z \rangle$ varies due to the distribution of EMP directions ϕ relative to the observation axis z. When $B_0 = 0$, $\langle S_z \rangle = 0$ at $t = 0$, and random magnetic fluctuations ensure that EMPs form in random directions in the ensemble of QDs. This scenario yields no net EMP alignment along the experimental z axis, as required by the simultaneous observation of magnetic saturation (Figure 6.2c) and $\Delta I/I = 0$ (Figure 6.3d). When $B_0 \neq 0$, a nonzero $\langle S_z \rangle$ at $t = 0$ displaces the initial photoexcitation away from the center of the potential energy surface, yielding ensemble EMP formation with a net projection along z, and hence $\Delta I/I \neq 0$ (Figure 6.3d). Magnetic fluctuations still cause EMPs to form misaligned with z. These off-axis EMPs emit light that is elliptically polarized along z, making $\Delta I/I < 1.0$. The small values of $\Delta I/I$ at intermediate fields thus indicate that EMP reorientation occurs on a longer time scale than emission, so that off-axis EMPs are effectively "stuck" in misalignment. B_0 prealigns the Mn^{2+} spins before photoexcitation, accelerating EMP formation and increasing $\Delta I/I$, with only a small decrease in the CW-PL energy. At large B_0 and low temperature, $\langle S_z \rangle = -5/2$ prior to photoexcitation, and the ensemble of EMPs reaches its maximal alignment along z with its minimal formation time (Figure 6.4d). In this limit, some EMPs are still not fully aligned with B_0, leading to $(\Delta I/I)_{max} \sim 0.8$ instead of 1.0. The dependence of $\Delta I/I$ on B_0 in Figure 6.3d thus arises primarily from orientation of the initial EMP

formation along the observation axis, z, not from subsequent reorientation of the EMPs after formation. Overall, we conclude that EMP orientation in these colloidal DMS QDs is influenced by (*i*) B_0, (*ii*) magnetic fluctuations, and (*iii*) an intrinsic factor most likely stemming from anisotropy.

6.4.2 **Dynamical TRFR Phase Inversion**

In addition to EMP orientation by B_0, the observation of TRFR signals from the same $Cd_{0.87}Mn_{0.13}Se$ QDs indicates that these EMPs can be at least partially oriented by resonant circularly polarized excitation, because optical magnetization along the observation axis is required for detection of a TRFR signal. The high Mn^{2+} concentrations and exciton confinement result in rapid spin transfer to Mn^{2+}. A particularly striking observation is the dynamical phase inversion in the TRFR responses of these QDs, which is associated with the spontaneous shifting of the excitonic absorption during EMP formation. This inversion indicates that exciton and Mn^{2+} spins in the EMP are precessing together with $g = 2$. Instead of precessing with $|g_{eff}| \sim 1180$, the exciton spin remains aligned with the Mn^{2+} spins as they precess more slowly, because the two are very strongly coupled to one another and the Mn^{2+} precession is rate-limiting.

6.5 **Summary**

Strong excitonic magnetic polarons are observed in colloidal $Cd_{1-x}Mn_xSe$ QDs prepared by nanocrystal diffusion doping. The picosecond formation and precession dynamics of EMPs in colloidal $Cd_{0.87}Mn_{0.13}Se$ QDs have been measured using a combination of TR-PL, TR-MCPL, and TRFR spectroscopies. The results have been analyzed in conjunction with the corresponding CW-absorption, CW-MCD, and CW-MCPL data. The analysis shows that EMPs form on the picosecond time scale following photoexcitation, with magnetization along directions determined

primarily by random Mn^{2+} magnetization fluctuations prior to photoexcitation. These fluctuations can be mostly suppressed by an external magnetic field, which then yields EMPs that are predominantly oriented along our laboratory viewing axis. The external magnetic field is not effective at reorienting the EMPs once they have formed in other directions, however, implicating rotational barriers in the EMP potential energy surface. TRFR measurements reveal very rapid (<5 ps) spin transfer from excitons to Mn^{2+} ions, followed by long-lived Mn^{2+} spin precession. A dynamical TRFR phase inversion is observed when excitonic absorption shifts relative to the pump/probe energy during EMP formation, confirming the origin of these TRFR signals in the EMPs themselves. The observation of TRFR signals from EMPs indicates both partial optical EMP orientation by resonant circularly polarized photoexcitation as well as coherent EMP precession in the transverse magnetic field. Overall, these observations highlight the extraordinary physical properties embodied by colloidal diffusion-doped $Cd_{1-x}Mn_xSe$ QDs. These results enhance the fundamental understanding of EMP formation and spin manipulation in colloidal DMS nanostructures and could further the development of spintronic devices and technologies based on these unique materials.

6.6 Methods

6.6.1 Synthesis and Characterization

Colloidal wurtzite $Cd_{1-x}Mn_xSe$ quantum dots were prepared by nanocrystal diffusion doping.[25] Briefly, in a typical synthesis, CdSe nanocrystals (~0.13 mmol in terms of CdSe units) were dried and added to 0.17 g (2.2 mmol) of selenium powder, 1 mL of 1-octadecene (ODE), and 1 mL of tributylphosphine in a septum-capped 5 mL round-bottom flask in a nitrogen-atmosphere glovebox. Separately, 12 g of ODE, 0.5 g of stearic acid, and 1.0 g of hexadecylamine were added to a 100 mL three-neck round-bottom flask. Following heating of the latter solution for 60 min at

100 °C under vacuum, 0.03 g (0.10 mmol) of $Mn(OAc)_2 \cdot 4H_2O$ was added against a nitrogen overpressure. The flask was then placed under vacuum to remove acetic acid and water and then heated under nitrogen to 300 °C, at which point the CdSe/selenide solution was injected rapidly. This reaction mixture was held at 300 °C for 4−24 h. As the solution was cooled to room temperature, 3 mL of toluene was added at ~110 °C. The nanocrystals were then precipitated from solution by addition of ethanol and washed by repeated suspensions in toluene and flocculation with ethanol. In select samples, a < 1 monolayer ZnSe shell was added using literature methods.[71] Relative atomic concentrations were obtained by analysis of dried nanocrystals digested in ultrapure nitric acid (EMD Chemicals) using inductively coupled plasma atomic emission spectrometry (ICP-AES; PerkinElmer). X-ray diffraction (XRD) data were collected from evaporated nanocrystal films on glass slides using a Bruker D8 Discover spectrometer at the University of Washington NanoTech User Facility.

6.6.2 **Physical Measurements**

All variable-temperature experiments were performed on films of NCs in poly(lauryl methacrylate-*co*-ethylene glycol dimethacrylate) prepared according to literature methods[72] and sandwiched between c-plane sapphire plates (for TRFR) or quartz disks (all other measurements).

Temperature-dependent absorption spectra were collected using a Cary 500 spectrophotometer (Varian) and closed-cycle helium cryostat. For CW-PL experiments, the nanocrystals were excited by a 405 nm laser diode. Photoluminescence data were collected using a 0.5 m monochromator (150 g/mm grating blazed at 500 nm) and a liquid-nitrogen-cooled CCD. For time-resolved PL experiments, the nanocrystals were excited by the frequency-doubled output of a mode-locked Ti:sapphire laser (400 nm, ~150 fs pulse width). The 76 MHz output of the Ti:sapphire laser was reduced to 10 kHz using a pulse picker. Photoluminescence was collected

using a streak camera (instrument response ~26 ps) mounted on a 0.5 m monochromator (50 g/mm grating blazed at 600 nm).

For MCD and MCPL measurements, samples were mounted in a superconducting magneto-optical cryostat with a variable-temperature sample compartment (Cryo-Industries SMC-1659 OVT or Oxford SM-2) oriented in the Faraday geometry. Before measurement, samples were checked for depolarization using the circular dichroism signal of a chiral molecule placed before and after the sample. All samples reported here showed depolarization of less than 10% at liquid helium temperatures. MCD and magneto-absorption spectra were collected using an Aviv 40DS spectropolarimeter. MCD intensities are reported as differential absorbance: $\Delta A = A_L - A_R$, where A_L and A_R refer to the absorption of LCP and RCP photons according to the sign convention outlined in Piepho and Schatz.[73] Excitonic Zeeman splittings (ΔE_{Zeeman}) were calculated from these data following literature methods.[19,46]

For all MCPL experiments, photoluminescence was collected along the magnetic-field axis and passed through a liquid-crystal variable retardation plate set to $\lambda/4$ at the emission maximum and subsequently a linear polarizer to separate left (LCP) and right (RCP) circularly polarized components. For CW-MCPL experiments, the excitation and collection were the same as described above for zero-field CW-PL, except that PL was collected through a multimode fiber coupled to the monochromator. For time-resolved MCPL experiments, the excitation and collection were otherwise the same as described above for zero-field TR-PL. MCPL polarization ratios are reported as $\Delta I/I = (I_L - I_R)/(I_L + I_R)$, where I_L and I_R refer to the intensity of LCP and RCP emission according to the sign convention outlined in Piepho and Schatz.[73]

For time-resolved Faraday rotation (TRFR) spectroscopy, the pump and probe pulses were generated from the same Ti:sapphire laser (76 MHz, ~150 fs pulse width) and the excitation energy

was tuned using an optical parametric oscillator with intracavity second-harmonic generation. The pump and probe beams were separated with a beam splitter and the probe was delayed with a mechanical translation stage. The pump polarization was modulated between LCP and RCP by a PEM operating at 50 kHz. Both spot sizes were ~100 μm and the average pump and probe powers were always < 30 mW. The polarization of the probe beam after passing through the sample was measured using a Wollaston prism and matched silicon photodiode bridge. The sample was mounted in an optical cryostat and a transverse magnetic field of 0.84 T was applied using permanent magnets.

6.7 Acknowledgments

This research was funded by the U.S. National Science Foundation (DMR-1206221 and DMR-1505901 to D.R.G., and Graduate Research Fellowship DGE-1256082 to H.D.N.) and the UW Clean Energy Institute (Graduate Fellowship to C.J.B.).

6.8 Supporting Information

Appendix E. : X-ray diffraction data, temperature dependence of the absorption energy, field dependence of the CW-PL energy, additional PL decay curves, time-resolved PL images, and TRFR traces. Fourier transforms of the TRFR traces showing the dynamical phase inversion, and energy dependence of the TRFR phase inversion.

6.9 References

1. *Diluted Magnetic Semiconductors*, ed.; Furdyna, J. K.; Kossut, J., Eds.; Semiconductors and Semimetals Vol. 25; Academic: New York, 1988.
2. Furdyna, J. K. Diluted Magnetic Semiconductors. *J. Appl. Phys.* **1988**, *64*, R29-R64.
3. *Introduction to the Physics of Diluted Magnetic Semiconductors*, ed.; Kossut, J.; Gaj, J. A., Eds.; Springer Series in Materials Science 144; Springer–Verlag: Berlin, 2010.

4. Dietl, T. Dilute Magnetic Semiconductors: Functional Ferromagnets. *Nat. Mater.* **2003**, *2*, 646–648.

5. Bartholomew, D. U.; Furdyna, J. K.; Ramdas, A. K. Interband Faraday Rotation in Diluted Magnetic Semiconductors: $Zn_{1-x}Mn_xTe$ and $Cd_{1-x}Mn_xTe$. *Phys. Rev. B* **1986**, *34*, 6943–6950.

6. Yasuhira, T.; Uchida, K.; Matsuda, Y. H.; Miura, N.; Twardowski, A. Giant Faraday Rotation Spectra of $Zn_{1-x}Mn_xSe$ Observed in High Magnetic Fields up to 150 T. *Phys. Rev. B* **2000**, *61*, 4685–4688.

7. Koshihara, S.; Oiwa, A.; Hirasawa, M.; Katsumoto, S.; Iye, Y.; Urano, C.; Takagi, H.; Munekata., H. Ferromagnetic Order Induced by Photogenerated Carriers in Magnetic III-V Semiconductor Heterostructures of (In,Mn)As/GaSb. *Phys. Rev. Lett.* **1997**, *78*, 4617–4620.

8. Boukari, H.; Kossacki, P.; Bertolini, M.; Ferrand, D.; Cibert, J.; Tatarenko, S.; Wasiela, A.; Gaj, J. A.; Dietl, T. Light and Electric Field Control of Ferromagnetism in Magnetic Quantum Structures. *Phys. Rev. Lett.* **2002**, *88*, 207204.

9. Chiba, D.; Yamanouchi, M.; Matsukura, F.; Ohno, H. Electrical Manipulation of Magnetization Reversal in a Ferromagnetic Semiconductor. *Science* **2003**, *301*, 943–945.

10. Yamanouchi, M.; Chiba, A.; Matsukura, F.; Dietl, T.; Ohno, H. Velocity of Domain-Wall Motion Induced by Electrical Current in the Ferromagnetic Semiconductor (Ga,Mn)As. *Phys. Rev. Lett.* **2006**, *96*, 096601.

11. Ohno, Y.; Young, D. K.; Beschoten, B.; Matsukura, F.; Ohno, H.; Awschalom, D. D. Electrical Spin Injection in a Ferromagnetic Semiconductor Heterostructure. *Nature* **1999**, *402*, 790–792.

12. Fiederling, R.; Keim, M.; Reuscher, G.; Ossau, W.; Schmidt, G.; Waag, A.; Molenkamp, L. W. Injection and Detection of a Spin-Polarized Current in a Light-Emitting Diode. *Nature* **1999**, *402*, 787–790.

13. Jonker, B. T.; Park, Y. D.; Bennett, B. R.; Cheong, H. D.; Kioseoglou, G.; Petrou, A. Robust Electrical Spin Injection into a Semiconductor Heterostructure. *Phys. Rev. B* **2000**, *62*, 8180–8183.

14. Rüster, C.; Borzenko, T.; Gould, C.; Schmidt, G.; Molenkamp, L. W.; Liu, X.; Wojtowicz, T. J.; Furdyna, J. K.; Yu, Z. G.; Flatté, M. E. Very Large Magnetoresistance in Lateral Ferromagnetic (Ga,Mn)As Wires with Nanoconstrictions. *Phys. Rev. Lett.* **2003**, *91*, 216602.

15. Isaacs, E. D.; Heiman, D.; Zayhowski, J. J.; Bicknell, R. N.; Schetzina, J. F. Magnetically Tunable Diluted Magnetic Semiconductor (Cd,Mn)Te Quantum Well Laser. *Appl. Phys. Lett.* **1986**, *48*, 275–277.

16. Bacher, G.; Schömig, H.; Scheibner, M.; Forchel, A.; Maksimov, A. A.; Chernenko, A. V.; Dorozhkin, P. S.; Kulakovskii, V. D.; Kennedy, T.; Reinecke, T. L. Spin–Spin Interaction in Magnetic Semiconductor Quantum Dots. *Physica E* **2005**, *26*, 37–44.

17. Henneberger, F.; Puls, J. Diluted Magnetic Quantum Dots. In *Introduction to the Physics of Diluted Magnetic Semiconductors*; Kossut, J., Gaj, J. A., Eds.; Springer Series in Materials Science 144; Springer–Verlag: Berlin, 2010; pp 161–190.

18. Beaulac, R.; Archer, P. I.; Ochsenbein, S. T.; Gamelin, D. R. Mn^{2+}-Doped CdSe Quantum Dots: New Inorganic Materials for Spin-Electronics and Spin-Photonics. *Adv. Funct. Mater.* **2008**, *18*, 3873–3891.

19. Beaulac, R.; Ochsenbein, S. T.; Gamelin, D. R. Colloidal Transition-Metal-Doped Quantum Dots. In *Nanocrystal Quantum Dots,* 2nd ed.; Klimov, V. I., Ed.; CRC Press: Boca Raton, FL, 2010; pp 397–453.

20. Besombes, L.; Léger, Y.; Maingault, L.; Ferrand, D.; Mariette, H.; Cibert, J. Probing the Spin State of a Single Magnetic Ion in an Individual Quantum Dot. *Phys. Rev. Lett.* **2004**, *93*, 207403.

21. Léger, Y.; Besombes, L.; Maingault, L.; Ferrand, D.; Mariette, H. Geometrical Effects on the Optical Properties of Quantum Dots Doped with a Single Magnetic Atom. *Phys. Rev. Lett.* **2005**, *95*, 047403.

22. Krebs, O.; Lemaître, A. Optically Induced Coupling of Two Magnetic Dopant Spins by a Photoexcited Hole in a Mn-Doped InAs/GaAs Quantum Dot. *Phys. Rev. Lett.* **2013**, *111*, 187401.

23. Kobak, J.; Smoleński, T.; Goryca, M.; Papaj, M.; Gietka, K.; Bogucki, A.; Koperski, M.; Rousset, J.-G.; Suffczyński, J.; Janik, E.; Nawrocki, M.; Golnik, A.; Kossacki, P.; Pacuski, W. Designing Quantum Dots for Solotronics. *Nat. Commun.* **2014**, *5*, 3191.

24. Ochsenbein, S. T.; Feng, Y.; Whitaker, K. M.; Badaeva, E.; Liu, W. K.; Li, X.; Gamelin, D. R. Charge-Controlled Magnetism in Colloidal Doped Semiconductor Nanocrystals. *Nat. Nanotechnol.* **2009**, *4*, 681–687.

25. Vlaskin, V. A.; Barrows, C. J.; Erickson, C. S.; Gamelin, D. R. Nanocrystal Diffusion Doping. *J. Am. Chem. Soc.* **2013**, *135*, 14380–14389.

26. Harris, J. H.; Nurmikko, A. V. Formation of the Bound Magnetic Polaron in (Cd,Mn)Se. *Phys. Rev. Lett.* **1983**, *51*, 1472–1475.

27. Awschalom, D. D.; Warnock, J.; von Molnár, S. Low-Temperature Magnetic Spectroscopy of a Dilute Magnetic Semiconductor. *Phys. Rev. Lett.* **1987**, *58*, 812–815.

28. Mackh, G.; Ossau, W.; Yakovlev, D. R.; Waag, A.; Landwehr, G.; Hellmann, R.; Göbel, E. O. Localized Exciton Magnetic Polarons in $Cd_{1-x}Mn_xTe$. *Phys. Rev. B* **1994**, *49*, 10248–10258.

29. Oka, Y.; Shen, J.; Takabayashi, K.; Takahashi, N.; Mitsu, H.; Souma, I.; Pittini, R. Dynamics of Excitonic Magnetic Polarons in Nanostructure Diluted Magnetic Semiconductors. *J. Lumin.* **1999**, *83-84*, 83–89.

30. Kavokin, K. V.; Merkulov, I. A.; Yakovlev, D. R.; Ossau, W.; Landwehr, G. Exciton Localization in Semimagnetic Semiconductors Probed by Magnetic Polarons. *Phys. Rev. B* **1999**, *60*, 16499–16505.

31. Maksimov, A. A.; Bacher, G.; McDonald, A.; Kulakovskii, V. D.; Forchel, A.; Becker, C. R.; Landwehr, G.; Molenkamp, L. W. Magnetic Polarons in a Single Diluted Magnetic Semiconductor Quantum Dot. *Phys. Rev. B* **2000**, *62*, R7767–R7770.

32. Seufert, J.; Bacher, G.; Scheibner, M.; Forchel, A.; Lee, S.; Dobrowolska, M.; Furdyna, J. K. Dynamical Spin Response in Semimagnetic Quantum Dots. *Phys. Rev. Lett.* **2001**, *88*, 027402.

33. Dorozhkin, P. S.; Chernenko, A. V.; Kulakovskii, V. D.; Brichkin, A. S.; Maksimov, A. A.; Schoemig, H.; Bacher, G.; Forchel, A.; Lee, S.; Dobrowolska, M.; Furdyna, J. K. Longitudinal and Transverse Fluctuations of Magnetization of the Excitonic Magnetic Polaron in a Semimagnetic Single Quantum Dot. *Phys. Rev. B* **2003**, *68*, 195313.

34. Zaitsev, S. V.; Schömig, H.; Forchel, A.; Bacher, G. Magnetooptics and Dynamics of a Magnetic Polaron in Semimagnetic CdSe/ZnMnSe Quantum Dots. *JETP Lett.* **2007**, *85*, 323–327.

35. Beaulac, R.; Schneider, L.; Archer, P. I.; Bacher, G.; Gamelin, D. R. Light-Induced Spontaneous Magnetization in Doped Colloidal Quantum Dots. *Science* **2009**, *325*, 973–976.

36. Sellers, I. R.; Oszwałdowski, R.; Whiteside, V. R.; Eginligil, M.; Petrou, A.; Zutic, I.; Chou, W.-C.; Fan, W. C.; Petukhov, A. G.; Kim, S. J.; Cartwright, A. N.; McCombe, B. D. Robust Magnetic Polarons in Type-II (Zn,Mn)Te/ZnSe Magnetic Quantum Dots. *Phys. Rev. B* **2010**, *82*, 195320.

37. Kłopotowski, Ł.; Cywiński, Ł.; Wojnar, P.; Voliotis, V.; Fronc, K.; Kazimierczuk, T.; Golnik, A.; Ravaro, M.; Grousson, R.; Karczewski, G.; Wojtowicz, T. Magnetic Polaron Formation and Exciton Spin Relaxation in Single $Cd_{1-x}Mn_xTe$ Quantum Dots. *Phys. Rev. B* **2011**, *83*, 081306.

38. Bacher, G.; Maksimov, A. A.; Schömig, H.; Kulakovskii, V. D.; Welsch, M. K.; Forchel, A.; Dorozhkin, P. S.; Chernenko, A. V.; Lee, S.; Dobrowolska, M.; Furdyna, J. K. Monitoring Statistical Magnetic Fluctuations on the Nanometer Scale. *Phys. Rev. Lett.* **2002**, *89*, 127201.

39. Dietl, T.; Peyla, P.; Grieshaber, W.; Merle d'Aubigné, Y. Dynamics of Spin Organization in Diluted Magnetic Semiconductors. *Phys. Rev. Lett.* **1995**, *74*, 474-477.

40. Scherbakov, A. V.; Yakovlev, D. R.; Akimov, A. V.; Merkulov, I. A.; König, B.; Ossau, W.; Molenkamp, L. W.; Wojtowicz, T.; Karczewski, G.; Cywinski, G.; Kossut, J. Acceleration of the Spin-Lattice Relaxation in Diluted Magnetic Quantum Wells in the Presence of a Two-Dimensional Electron Gas. *Phys. Rev. B* **2001**, *64*, 155205.

41. Kneip, M. K.; Yakovlev, D. R.; Bayer, M.; Maksimov, A. A.; Tartakovskii, I. I.; Keller, D.; Ossau, W.; Molenkamp, L. W.; Waag, A. Spin-Lattice Relaxation of Mn Ions in ZnMnSe/ZnBeSe Quantum Wells Measured under Pulsed Photoexcitation. *Phys. Rev. B* **2006**, *73*, 045305.

42. Schimpf, A. M.; Rinehart, J. D.; Ochsenbein, S. T.; Gamelin, D. R. Charge-State Control of Mn^{2+} Spin Relaxation Dynamics in Colloidal *n*-Type $Zn_{1-x}Mn_xO$ Nanocrystals. *J. Phys. Chem. Lett.* **2015**, *6*, 1748-1753.

43. Archer, P. I.; Santangelo, S. A.; Gamelin, D. R. Inorganic Cluster Syntheses of TM^{2+}-Doped Quantum Dots (CdSe, CdS, CdSe/CdS): Physical Property Dependence on Dopant Locale. *J. Am. Chem. Soc.* **2007**, *129*, 9808–9818.

44. Archer, P. I.; Santangelo, S. A.; Gamelin, D. R. Direct Observation of sp–d Exchange Interactions in Colloidal Mn^{2+}- and Co^{2+}-Doped CdSe Quantum Dots. *Nano Lett.* **2007**, *7*, 1037–1043.

45. Beaulac, R.; Archer, P. I.; Liu, X.; Lee, S.; Salley, G. M.; Dobrowolska, M.; Furdyna, J. K.; Gamelin, D. R. Spin-Polarizable Excitonic Luminescence in Colloidal Mn^{2+}-Doped CdSe Quantum Dots. *Nano Lett.* **2008**, *8*, 1197–1201.

46. Barrows, C. J.; Vlaskin, V. A.; Gamelin, D. R. Absorption and Magnetic Circular Dichroism Analyses of Giant Zeeman Splittings in Diffusion-Doped Colloidal $Cd_{1-x}Mn_xSe$ Quantum Dots. *J. Phys. Chem. Lett.* **2015**, *6*, 3076–3081.

47. Fainblat, R.; Muckel, F.; Barrows, C. J.; Vlaskin, V. A.; Gamelin, D. R.; Bacher, G. Valence-Band Mixing Effects in the Upper-Excited-State Magneto-Optical Responses of Colloidal Mn^{2+}-Doped CdSe Quantum Dots. *ACS Nano* **2014**, *8*, 12669−12675.

48. Bacher, G.; Schömig, H.; Welsch, M. K.; Zaitsev, S.; Kulakovskii, V. D.; Forchel, A.; Lee, S.; Dobrowolska, M.; Furdyna, J. K.; König, B.; Ossau, W. Optical Spectroscopy on Individual CdSe/ZnMnSe Quantum Dots. *Appl. Phys. Lett.* **2001**, *79*, 524–526.

49. Efros, A. L.; Rosen, M.; Kuno, M.; Nirmal, M.; Norris, D. J.; Bawendi, M. Band-Edge Exciton in Quantum Dots of Semiconductors with a Degenerate Valence Band: Dark and Bright Exciton States. *Phys. Rev. B* **1996**, *54*, 4843-4856.

50. Barman, B.; Oszwałdowski, R.; Schweidenback, L.; Russ, A. H.; Pientka, J. M.; Tsai, Y.; Chou, W.-C.; Fan, W. C.; Murphy, J. R.; Cartwright, A. N.; Sellers, I. R.; Petukhov, A. G.; Zutic, I.; McCombe, B. D.; Petrou, A. Time-Resolved Magnetophotoluminescence Studies of Magnetic Polaron Dynamics in Type-II Quantum Dots. *Phys. Rev. B* **2015**, *92*, 035430.

51. Shapira, Y.; Foner, S.; Ridgley, D. H.; Dwight, K.; Wold, A. Technical Saturation and Magnetization Steps in Diluted Magnetic Semiconductors: Predictions and Observations. *Phys. Rev. B.* **1984**, *30*, 4021–4023.

52. Arciszewska, M.; Nawrocki, M. Determination of the Band Structure Parameters of $Cd_{0.95}Mn_{0.05}Se$ from Magnetoabsorption Measurements. *J. Phys. Chem. Solids* **1986**, *47*, 309–314.

53. Beaulac, R.; Gamelin, D. R. Two-Center Formulation of Mn^{2+}-Electron *s–d* Exchange Coupling in Bulk and Quantum-Confined Diluted Magnetic Semiconductors. *Phys. Rev. B* **2010**, *82*, 224401.

54. Beaulac, R.; Feng, Y.; May, J. W.; Badaeva, E.; Gamelin, D. R.; Li, X. Orbital Pathways for Mn^{2+}-Carrier *sp–d* Exchange in Diluted Magnetic Semiconductor Quantum Dots. *Phys. Rev. B* **2011**, *84*, 195324.

55. Yakovlev, D. R.; Ossau, W. Magnetic Polarons. In *Introduction to the Physics of Diluted Magnetic Semiconductors*; Kossut, J., Gaj, J. A., Eds.; Springer Series in Materials Science 144; Springer–Verlag: Berlin, 2010; pp 221–262.

56. Merkulov, I. A.; Yakovlev, D. R.; Kavokin, K. V.; Mackh, G.; Ossau, W.; Waag, A.; Landwehr, G. Hierarchy of Relaxation Times in the Formation of an Excitonic Magnetic Polaron in (CdMn)Te. *JETP Lett.* **1995**, *62*, 335–339.

57. Hundt, A.; Puls, J.; Henneberger, F. Spin Properties of Self-Organized Diluted Magnetic $Cd_{1-x}Mn_xSe$ Quantum Dots. *Phys. Rev. B* **2004**, *69*, 121309(R).

58. Merkulov, I. A.; Pozina, G. R.; Coquillat, D.; Paganotto, N.; Siviniant, J.; Lascaray, J. P.; Cibert, J. Parameters of the Magnetic Polaron State in Diluted Magnetic Semiconductors Cd-Mn-Te with Low Manganese Concentration. *Phys. Rev. B* **1996**, *54*, 5727–5731.

59. Scalbert, D.; Cernogora, J.; Benoit à la Guillaume, C.; Nawrocki, M. Bistability of Magnetic Polarons Bound to Acceptors in a Wurtzite Semimagnetic Semiconductor. *Phys. Rev. B* **1988**, *38*, 13246–13256.

60. Gupta, J. A.; Awschalom, D. D.; Peng, X.; Alivisatos, A. P. Spin Coherence in Semiconductor Quantum Dots. *Phys. Rev. B* **1999**, *59*, R10421–R10424.

61. Gupta, J. A.; Awschalom, D. D.; Efros, A. L.; Rodina, A. V. Spin Dynamics in Semiconductor Nanocrystals. *Phys. Rev. B* **2002**, *66*, 125307.

62. Crooker, S. A.; Awschalom, D. D.; Baumberg, J. J.; Flack, F.; Samarth, N. Optical Spin Resonance and Transverse Spin Relaxation in Magnetic Semiconductor Quantum Wells. *Phys. Rev. B* **1997**, *56*, 7574–7588.

63. Jana, S.; Manna, G.; Srivastava, B. B.; Pradhan, N. Tuning the Emission Colors of Semiconductor Nanocrystals Beyond their Bandgap Tunability: All in the Dope. *Small* **2013**, *9*, 3753-3758.

64. Crooker, S. A. Coherent Spin Dynamics of Carriers and Magnetic Ions in Diluted Magnetic Semiconductors. In *Introduction to the Physics of Diluted Magnetic Semiconductors*; Kossut, J., Gaj, J. A., Eds.; Springer Series in Materials Science 144; Springer–Verlag: Berlin, 2010; pp 305–334.

65. Fiederling, R.; Yakovlev, D. R.; Ossau, W.; Landwehr, G.; Merkulov, I. A.; Kavokin, K. V.; Wojtowicz, T.; Kutrowski, M.; Grasza, K.; Karczewski, G.; Kossut, J. Exciton Magnetic Polarons in (100)- and (120)-Oriented Semimagnetic Digital Alloys (Cd,Mn)Te. *Phys. Rev. B.* **1998**, *58*, 4785–4792.

66. Výborný, K.; Han, J. E.; Oszwałdowski, R.; Žutić, I.; Petukhov, A. G. Magnetic Anisotropies of Quantum Dots Doped with Magnetic Ions. *Phys. Rev. B* **2012**, *85*, 155312.

67. Peng, B.; May, J. W.; Gamelin, D. R.; Li, X. Effects of Crystallographic and Shape Anisotropies on Dopant-Carrier Exchange Interactions in Magnetic Semiconductor Quantum Dots. *J. Phys. Chem. C* **2014**, *118*, 7630−7636.

68. Merkulov, I. A.; Kavokin, K. V.; Mackh, G.; Kuhn-Heinrich, B.; Ossau, W.; Waag, A.; Landwehr, G.; Yakovlev, D. R. Luminescence Polarization and Spontaneous Lowering of Symmetry Caused by Magnetic-Polaron Formation in Semimagnetic-Semiconductor Quantum Wells. *Phys. Solid State* **1997**, *39*, 1859–1863.

69. Heiman, D.; Warnock, J.; Wolff, P. A.; Kershaw, R.; Ridgley, D.; Dwight, K.; Wold, A. Polarized Photoluminescence from Bound Magnetic Polarons in (Cd,Mn)Se. *Solid State Commun.* **1984**, *52*, 909–912.

70. Kudinov, A. V.; Kusraev, Y. G.; Yakimovich, V. N. Polarized Luminescence of CdMnTe in an External Magnetic Field. *Phys. Solid State* **1995**, *37*, 359–362.

71. Reiss, P.; Protière, M.; Li, L. Core/Shell Semiconductor Nanocrystals. *Small* **2009**, *5*, 154–168.

72. Lee, J.; Sundar, V. C.; Heine, J. R.; Bawendi, M. G.; Jensen, K. F. Full Color Emission from II-VI Semiconductor Quantum Dot–Polymer Composites. *Adv. Mater.* **2000**, *12*, 1102-1105.

73. Piepho, S. B.; Schatz, P. N. *Group Theory in Spectroscopy with Applications to Magnetic Circular Dichroism*; Wiley: New York, 1983.

Appendix A. Supporting Information for Chapter 2

Table A.1. Convergence of optimization calculations. Calculated forces and displacements for the ground-state geometry optimization of the Cu^{+}:$Cd_{33}Se_{34}$ structure, using the default threshold set by Gaussian and a higher threshold (keyword opt=tight).

	Default threshold			**Higher threshold (opt=tight)**		
	Threshold	Value (est. 2nd deriv.)	Value (calc. 2nd deriv.)	Threshold	Value (est. 2nd deriv.)	Value (calc. 2nd deriv.)
Max. force	0.000450	0.000073	0.000212	0.000015	0.000009	0.000212
RMS force	0.000300	0.000008	0.000033	0.000010	0.000001	0.000035
Max. displacement	0.001800	0.001453	0.049797	0.000060	0.000021	0.049841
RMS displacement	0.001200	0.000165	0.006584	0.000040	0.000003	0.006552

The optimization calculation uses estimated second derivatives and indicates that the structure has converged, but calculating the second derivative indicates that a true stationary point has not been reached. Changing the thresholds used in the optimization calculation appears to improve the obtained values, but the geometry does not change significantly and the second derivative calculation shows that a stationary point still has not been reached. Because changing the optimization thresholds does not significantly change the resulting energy or geometry, and because the forces are small in all cases, we conclude that the potential energy surface is very flat in this region and the calculated energy and geometry are very close to the true minimum. These results could potentially be improved by calculating the second derivatives at every step of the optimization (using keyword opt=CalcFC in Gaussian), but this approach is too computationally expensive to be practical, especially for the larger NC structures and the excited-state optimization calculations. Therefore, the results reported here are for structures that are converged according to the default threshold with estimated second derivatives.

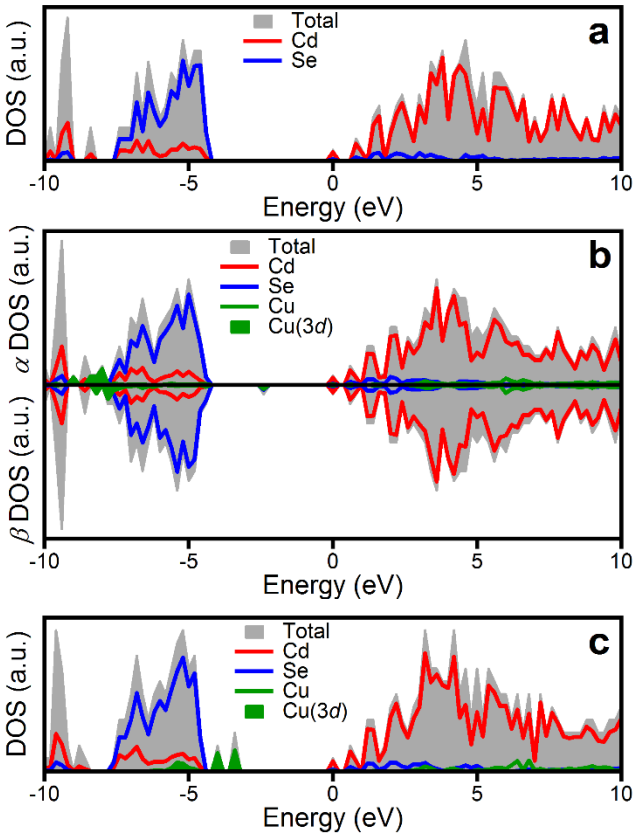

Figure A.1. Binned density-of-states plots. Calculated densities of states (DOS) for **(a)** $Cd_{34}Se_{34}$, **(b)** Cu^{2+}:$Cd_{33}Se_{34}$, and **(c)** Cu^{+}:$Cd_{33}Se_{34}$ NCs. The total DOS is shown in solid gray, while the partial DOS is shown as red lines for Cd (4*d*, 5*s*, 5*p*), blue lines for Se (4*s*, 4*p*), and green lines for Cu (3*d*, 4*s*, 4*p*). The Cu(3*d*) character in the doped NCs is further highlighted in solid green. For the Cu^{2+}-doped NC, which has an open-shell configuration, the α and β DOS are represented by positive and negative values, respectively. These densities of states provide an alternative representation of the molecular-orbital energies shown in Figure 2.1.

Table A.2. Compositions of selected mid-gap molecular orbitals. Calculated atomic orbital contributions (as percentages) to selected copper-based molecular orbitals in Cu^{2+}:$Cd_{33}Se_{34}$, Cu^{+}:$Cd_{33}Se_{34}$, and Cu^{+}:$Cd_{76}Se_{77}$ NCs.

Atomic orbital	Cu^{2+}:$Cd_{33}Se_{34}$ LUMO	Cu^{+}:$Cd_{33}Se_{34}$ HOMO	Cu^{+}:$Cd_{76}Se_{77}$ HOMO
Cu(3*d*)	38.4	50.2	45.6
Cu(4*s*)	0.0	0.0	0.0
Cu(4*p*)	3.4	2.7	2.8
Cd(4*d*)	0.9	0.9	1.0
Cd(5*s*)	2.9	2.1	2.1
Cd(5*p*)	4.3	4.2	4.3
Se(4*s*)	1.1	0.9	0.9
Se(4*p*)	47.6	38.4	42.8
H(1*s*)	1.6	0.8	0.4
Total Cu	41.8	52.8	48.4
Total Cd	8.1	7.2	7.5
Total Se	48.6	39.2	43.7

All of these molecular orbitals have primarily Cu(3*d*) and Se(4*p*) character. The LUMO of the Cu^{2+}-doped NC is similar to the HOMO of the Cu^{+}-doped NC (as shown in Figure 2.1 and discussed in Chapter 2). The Se(4*p*) contribution to the HOMO of the Cu^{+}-doped NCs increases with increasing NC size, consistent with the trend in binding energy discussed in Chapter 2.

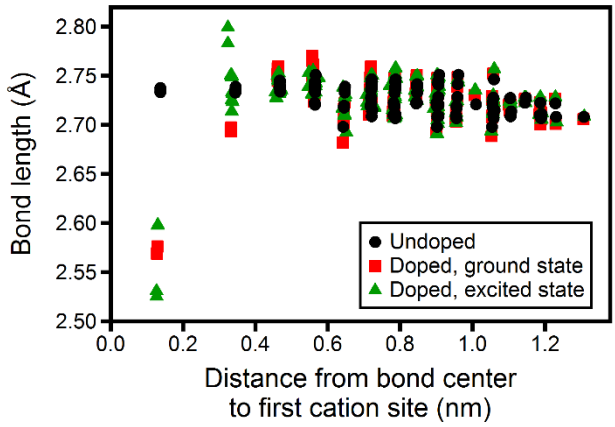

Figure A.2. Comparison of ground- and excited-state bond lengths. Calculated bond lengths for all Cu−Se and Cd−Se bonds in the ground state of an undoped $Cd_{77}Se_{77}$ NC (black circles) and the ground state (red squares) and the lowest-energy $^1ML_{CB}CT$ excited state (green triangles) of a Cu^+:$Cd_{76}Se_{77}$ NC.

In the undoped NC and the ground state of the Cu^+-doped NC, the symmetry around the first cation site (the site occupied by the Cu^+ dopant) is very close to tetrahedral, while the symmetry is clearly broken in the excited state due to the Jahn−Teller distortion. Replacing Cd^{2+} with Cu^+ causes a large contraction of the lattice around the dopant; these bond length changes are larger than the bond length changes between the ground state and the excited state. The distortion associated with Cu^+ doping and the distortion associated with the $ML_{CB}CT$ excited state are both centered around the dopant and cause minimal changes in Cd−Se bond lengths elsewhere in the lattice.

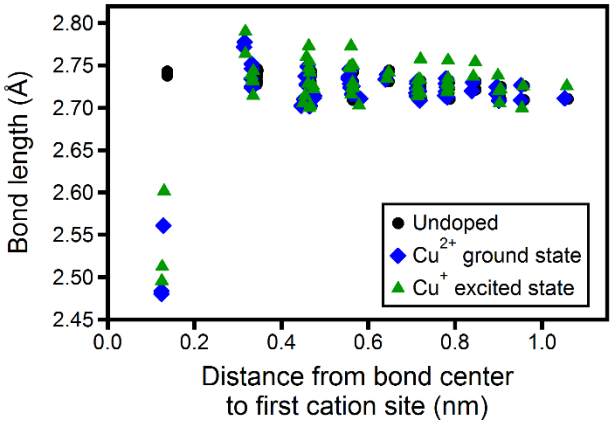

Figure A.3. Comparison of bond lengths for a ground-state Cu^{2+}-doped NC and an excited-state Cu^{+}-doped NC. Calculated bond lengths for all Cu−Se and Cd−Se bonds in the ground state of an undoped $Cd_{34}Se_{34}$ NC (black circles), the ground state of a Cu^{2+}:$Cd_{33}Se_{34}$ NC (blue diamonds), and the lowest-energy $^1ML_{CB}CT$ excited state of a Cu^{+}:$Cd_{33}Se_{34}$ NC (green triangles).

In both the ground state of the Cu^{2+}-doped NC (Table A.3) and the excited state of the Cu^{+}-doped NC (Table A.4), the Cu^{2+} character of the dopant results in a net contraction and asymmetric Jahn−Teller distortion around the dopant site. The other Cd−Se bond lengths in these distorted states are also similar.

Table A.3. Local geometry around the dopant site. Calculated ground-state geometry (Cd−Se or Cu−Se bond lengths, Se−Cd−Se or Se−Cu−Se bond angles, and dihedral angles) around the first cation site (the site occupied by the Cu dopant in the doped NCs) for $Cd_{34}Se_{34}$, Cu^{2+}:$Cd_{33}Se_{34}$, and Cu^{+}:$Cd_{33}Se_{34}$ NCs. Atom 1 is the cation (Cd^{2+}, Cu^{2+}, or Cu^{+}) and atoms 2−5 are the adjacent Se^{2-} anions.

	Undoped	Cu^{2+}-doped	Cu^{+}-doped
r_{12} (Å)	2.738	2.561	2.579
r_{13} (Å)	2.738	2.561	2.579
r_{14} (Å)	2.743	2.480	2.580
r_{15} (Å)	2.742	2.484	2.579
θ_{213}	109.8	111.2	109.8
θ_{214}	109.4	110.9	109.3
θ_{215}	109.6	112.0	109.7
θ_{314}	109.4	110.9	109.3
θ_{315}	109.6	112.0	109.7
θ_{415}	109.6	99.3	109.1
D_{5423}	70.6	72.8	70.6
D_{5234}	70.4	63.5	70.4
D_{5342}	70.6	72.8	70.6

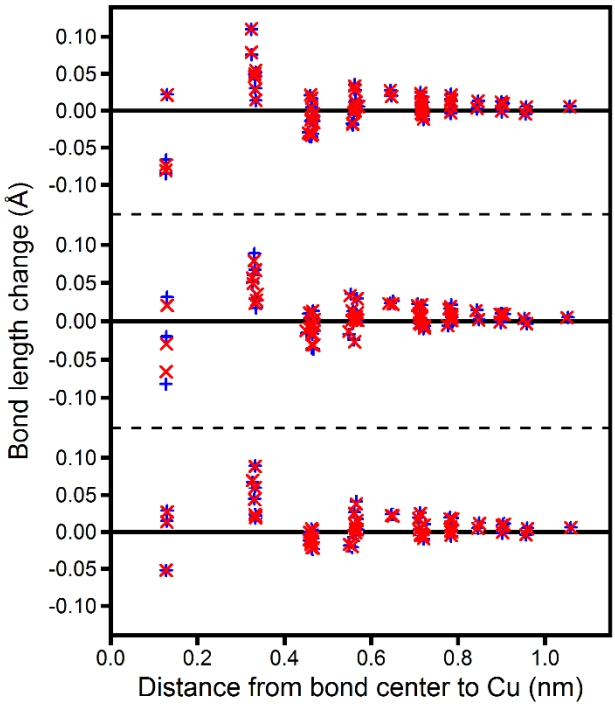

Figure A.4. Excited-state distortions for a 34-cation NC. Excited-state bond length changes for all Cu–Se and Cd–Se bonds in the Cu^+:$Cd_{33}Se_{34}$ NC, for the first three $^1ML_{CB}CT$ (blue + symbols) and first three $^3ML_{CB}CT$ (red × symbols) excited states. Each singlet–triplet pair is shown on a different *y*-axis.

These results are similar to those shown in Figure 2.5 for the Cu^+:$Cd_{76}Se_{77}$ NC, with the distortion centered around the Cu^+ dopant and the Cu–Se bond changes reflecting a totally symmetric contraction and asymmetric Jahn–Teller distortion.

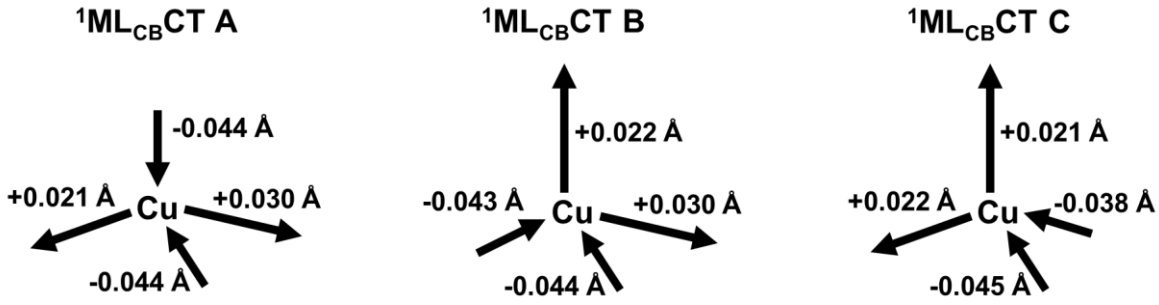

Figure A.5. Excited-state bond length changes at Cu. Calculated changes in Cu–Se bond lengths for the first three $^1ML_{CB}CT$ excited states of a Cu^+:$Cd_{76}Se_{77}$ NC. All three excited states involve a totally symmetric contraction and a Jahn–Teller distortion with T_2 symmetry, but each state has a different Jahn–Teller axis.

Table A.4. Excited-state distortion for the 34-cation NC. Calculated ground-state geometry and complete list of excited-state distortions around Cu^+ (Cu−Se bond lengths, Se−Cu−Se bond angles, and dihedral angles) for the first six excited states of a Cu^+:$Cd_{33}Se_{34}$ NC with the Cu^+ located at the center of the NC.

	Ground state	$^1ML_{CB}CT$ A	$^3ML_{CB}CT$ A	$^1ML_{CB}CT$ B	$^3ML_{CB}CT$ B	$^1ML_{CB}CT$ C	$^3ML_{CB}CT$ C
r_{12} (Å)	2.579	-0.052	-0.051	-0.030	-0.020	0.021	0.022
r_{13} (Å)	2.579	-0.052	-0.051	-0.030	-0.020	0.021	0.022
r_{14} (Å)	2.580	0.014	0.015	-0.066	-0.082	-0.081	-0.085
r_{15} (Å)	2.579	0.027	0.029	0.021	0.032	-0.074	-0.066
θ_{213}	109.8	-5.5	-5.2	10.6	7.7	1.1	1.2
θ_{214}	109.3	2.0	2.1	-5.0	-4.5	1.9	1.5
θ_{215}	109.7	1.6	1.5	-2.0	1.0	1.6	2.0
θ_{314}	109.3	2.0	2.1	-5.0	-4.5	1.9	1.5
θ_{315}	109.7	1.6	1.5	-2.0	1.0	1.6	2.0
θ_{415}	109.1	-1.6	-1.9	3.5	-1.3	-8.6	-8.5
D_{5423}	70.6	1.7	1.7	0.0	-2.8	2.0	1.8
D_{5234}	70.4	-2.1	-2.1	1.7	6.3	-6.2	-6.3
D_{5342}	70.6	1.7	1.7	0.0	-2.8	2.0	1.8

Table A.5. Excited-state distortion for the 77-cation NC. Calculated ground-state geometry and complete list of excited-state distortions around Cu^+ (Cu−Se bond lengths, Se−Cu−Se bond angles, and dihedral angles) for the first six excited states of a Cu^+:$Cd_{76}Se_{77}$ NC with the Cu^+ located at the center of the NC. The bond length changes for the $^1ML_{CB}CT$ excited states are illustrated in Figure A.5.

	Ground state	$^1ML_{CB}CT$ A	$^3ML_{CB}CT$ A	$^1ML_{CB}CT$ B	$^3ML_{CB}CT$ B	$^1ML_{CB}CT$ C	$^3ML_{CB}CT$ C
r_{12} (Å)	2.576	-0.044	-0.018	0.022	0.020	0.021	0.021
r_{13} (Å)	2.576	0.021	-0.016	-0.043	-0.044	0.022	0.021
r_{14} (Å)	2.570	-0.044	-0.012	-0.044	0.000	-0.045	-0.042
r_{15} (Å)	2.569	0.030	-0.009	0.030	0.005	-0.038	-0.043
θ_{213}	109.3	2.9	6.4	2.5	-0.1	0.2	0.2
θ_{214}	109.4	-5.2	-2.8	0.9	1.4	0.9	1.7
θ_{215}	109.4	2.0	-2.8	-0.4	1.2	1.9	1.1
θ_{314}	109.4	0.5	-2.7	-5.2	-2.5	1.9	1.7
θ_{315}	109.4	-0.4	-2.7	2.2	-2.4	0.9	1.0
θ_{415}	109.8	0.2	5.0	0.0	2.2	-5.9	-5.8
D_{5423}	70.5	-1.2	-3.0	1.8	-1.5	0.9	1.2
D_{5234}	70.6	1.1	5.7	0.8	1.7	-4.5	-4.4
D_{5342}	70.5	1.5	-3.0	-1.2	0.4	1.9	1.3

Table A.6. Excited-state energies for the 34-cation NC. Calculated excited-state energies, measured relative to the ground state energy, before and after excited-state geometry relaxation, for the first six excited states of a Cu^+:$Cd_{33}Se_{34}$ NC with the Cu^+ located at the center of the NC. The nuclear reorganization energy is also shown. These energies are illustrated in Figure 2.3b.

	Energy with frozen geometry (eV)	Energy with relaxed geometry (eV)	Reorganization energy (eV)
$^1ML_{CB}CT$ A	2.699	2.463	0.236
$^1ML_{CB}CT$ B	2.728	2.426	0.302
$^1ML_{CB}CT$ C	2.748	2.409	0.339
$^3ML_{CB}CT$ A	2.649	2.427	0.222
$^3ML_{CB}CT$ B	2.675	2.389	0.286
$^3ML_{CB}CT$ C	2.703	2.386	0.317

Table A.7. Excited-state energies for the 77-cation NC. Calculated excited-state energies, measured relative to the ground state energy, before and after excited-state geometry relaxation, for the first six excited states of a Cu^+:$Cd_{76}Se_{77}$ NC with the Cu^+ located at the center of the NC. The nuclear reorganization energy is also shown. These energies are illustrated in Figure 2.3c.

	Energy with frozen geometry (eV)	Energy with relaxed geometry (eV)	Reorganization energy (eV)
$^1ML_{CB}CT$ A	2.414	2.221	0.193
$^1ML_{CB}CT$ B	2.416	2.227	0.189
$^1ML_{CB}CT$ C	2.423	2.216	0.207
$^3ML_{CB}CT$ A	2.380	2.188	0.192
$^3ML_{CB}CT$ B	2.381	2.205	0.176
$^3ML_{CB}CT$ C	2.391	2.200	0.191

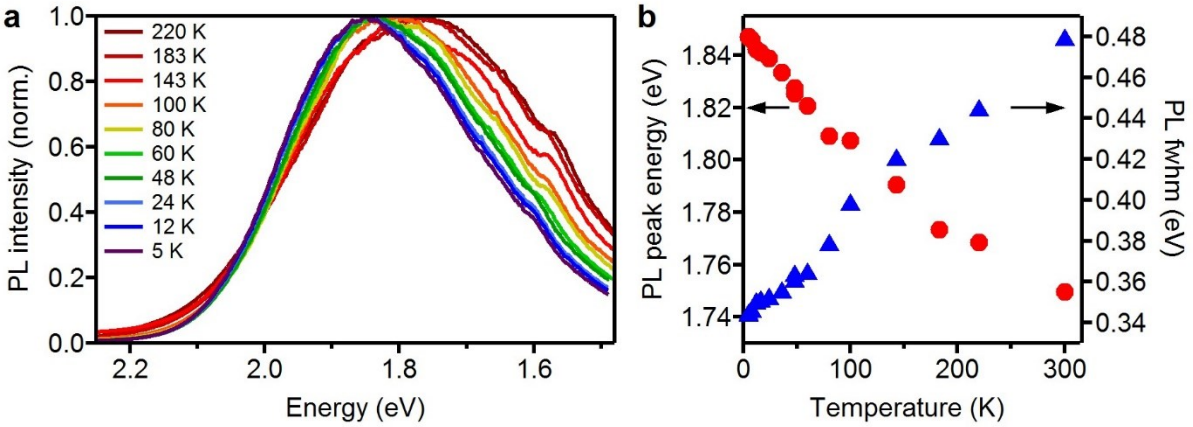

Figure B.1. Variable-temperature PL spectra of Ag^+:CdSe NCs. (a) Variable-temperature photoluminescence (PL) spectra of the d = 3.5 nm Ag^+:CdSe nanocrystals (NCs) shown in Figure 3.1. **(b)** Temperature dependence of the PL peak energy (red circles) and full-width at half-maximum (fwhm; blue triangles) of the same Ag^+:CdSe NCs. With decreasing temperature, the PL shifts to higher energy, similar to the temperature dependence observed in Cu^+:CdSe NCs. With decreasing temperature, the PL also narrows, consistent with a vibronic contribution to the band shape.

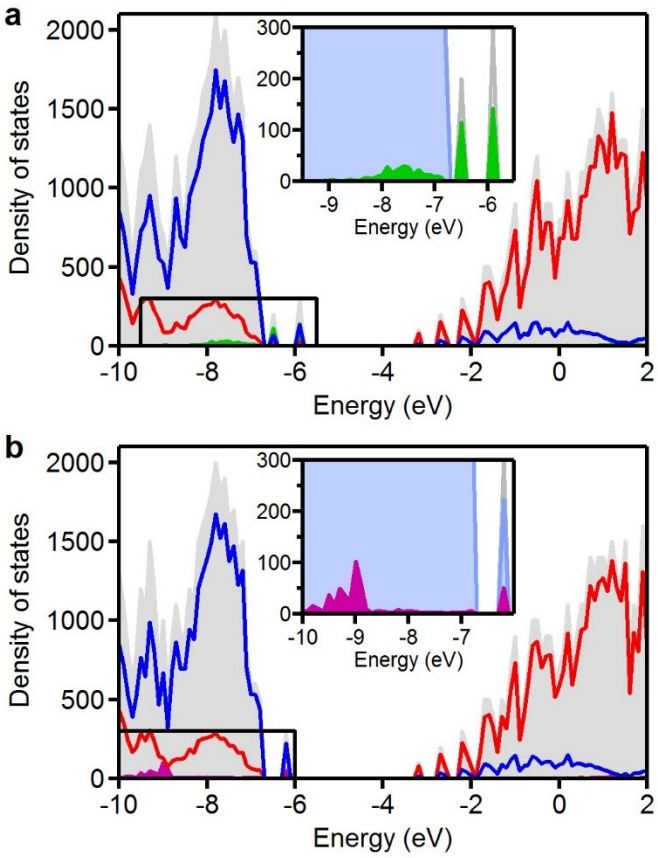

Figure B.2. Binned density-of-states plots for Cu^+:CdSe and Ag^+:CdSe NCs. Calculated densities of states (DOS) for **(a)** Cu^+:$Cd_{133}Se_{134}$ and **(b)** Ag^+:$Cd_{133}Se_{134}$ NCs. The total DOS is shown in gray, while the partial DOS is shown as red lines for Cd^{2+}, blue lines for Se^{2-}, solid green for Cu^+, and solid purple for Ag^+. Inset: close-up of the mid-gap and VB DOS, indicated by the boxed region of the main figure, with the Se^{2-} partial DOS shown as solid blue. These densities of states provide an alternative representation of the same molecular-orbital energies shown in Figure 3.3.

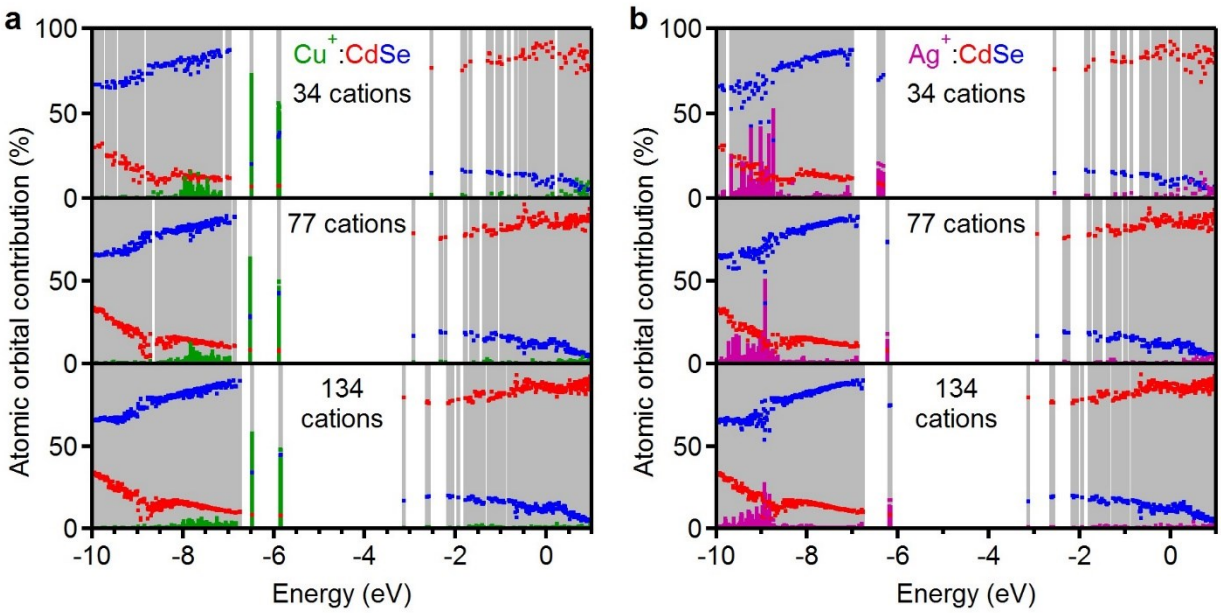

Figure B.3. Molecular-orbital energies for different sizes of Cu^+:CdSe and Ag^+:CdSe NCs. Calculated molecular-orbital (MO) energies for **(a)** Cu^+:CdSe and **(b)** Ag^+:CdSe NCs of different sizes. Fractional atomic-orbital contributions are shown as red dots for Cd^{2+}, blue dots for Se^{2-}, green (Cu^+) or purple (Ag^+) dots for the total dopant orbital contribution, and green (Cu^+) or purple (Ag^+) lines for the dopant *d* orbital contributions. MO energies for 34-cation (d = 1.6 nm), 77-cation (d = 2.1 nm), and 134-cation (d = 3.0 nm, also included in Figure 3.3) NCs are shown.

Table B.1. NC Size Dependence of Calculated Mid-Gap Molecular Orbital Properties.

	Average absolute energy of t_2 mid-gap MOs (eV)		Average energy difference between t_2 mid-gap MOs and VB edge (eV)		Average metal *d* orbital contribution to t_2 mid-gap MOs (%)	
# cations	Cu^+:CdSe	Ag^+:CdSe	Cu^+:CdSe	Ag^+:CdSe	Cu^+:CdSe	Ag^+:CdSe
34	-5.88	-6.37	1.09	0.64	52.2	16.4
77	-5.88	-6.23	0.97	0.64	47.0	14.8
134	-5.85	-6.17	0.89	0.59	45.1	14.1

From Figure B.3 and Table B.1, changing the NC size (and the energy of the VB edge) can affect the metal *d* orbital contributions to the mid-gap MOs, their absolute energies, and their energies relative to the valence-band (VB) edge (acceptor depth).

Table B.2. NC Size Dependence of Calculated Excited-State Energies.

	Energy of the lowest singlet excited state, frozen geometry (eV)		Energy of the lowest singlet excited state, relaxed geometry (eV)		Reorganization energy (eV)	
# cations	Cu^+:CdSe	Ag^+:CdSe	Cu^+:CdSe	Ag^+:CdSe	Cu^+:CdSe	Ag^+:CdSe
34	2.71	3.12	2.48	2.83	0.24	0.29
77	2.41	2.76	2.23	2.53	0.18	0.22

The energy of the luminescent excited state in Cu^+:CdSe NCs is consistently lower than the energy of the luminescent excited state in Ag^+:CdSe NCs, for both 34-cation and 77-cation NCs and in both the frozen ground-state and relaxed excited-state geometries.

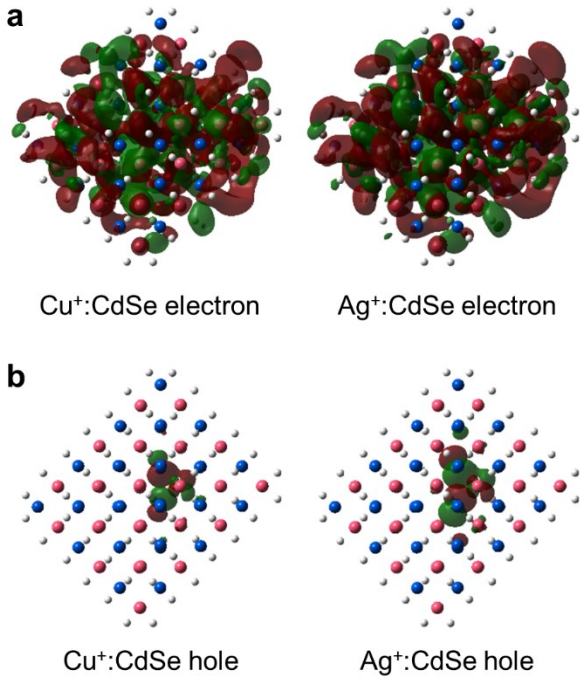

Figure B.4. Natural transition orbitals for 34-cation NCs. (a) Electron and **(b)** hole natural transition orbitals for the lowest-energy singlet transitions of Cu^+:$Cd_{33}Se_{34}$ and Ag^+:$Cd_{33}Se_{34}$ NCs, showing the electron and hole wavefunctions in the excited state. Isosurface values were chosen to enclose 70% of the total electron or hole wavefunction density. These wavefunctions are qualitatively similar to those shown in Figure 3.6 for the larger Cu^+:$Cd_{76}Se_{77}$ and Ag^+:$Cd_{76}Se_{77}$ NCs.

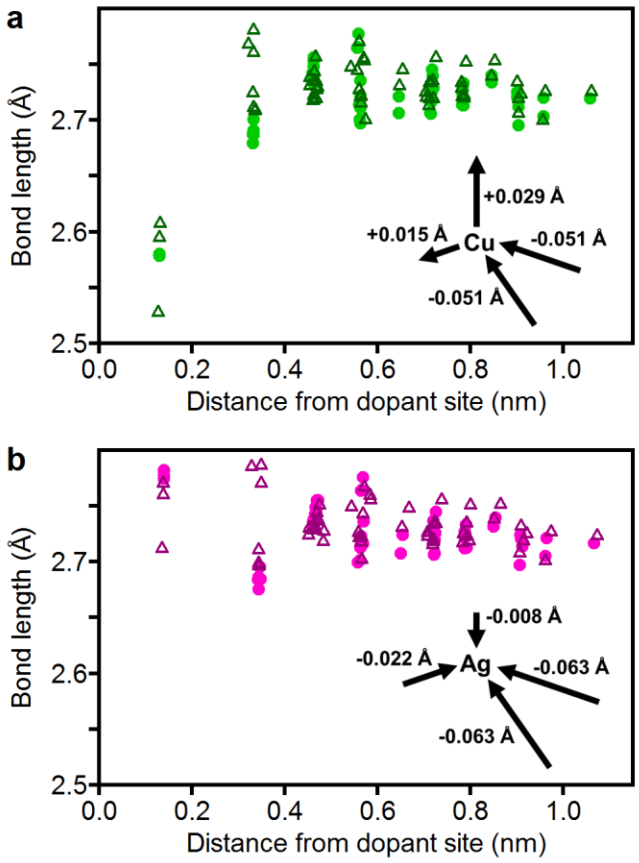

Figure B.5. Ground- and excited-state bond lengths for 34-cation NCs. Comparison of computed M−Se bond lengths for the ground states (closed circles) and lowest-energy singlet excited states (open triangles) of **(a)** Cu^{+}:$Cd_{33}Se_{34}$ and **(b)** Ag^{+}:$Cd_{33}Se_{34}$ NCs, plotted vs distance from the dopant. Insets: first-coordination-sphere bond-length changes at the dopants for the same NCs upon excitation to the same lowest-energy singlet excited states. These ground- and excited-state geometries are qualitatively similar to those shown in Figure 3.7 for the larger Cu^{+}:$Cd_{76}Se_{77}$ and Ag^{+}:$Cd_{76}Se_{77}$ NCs.

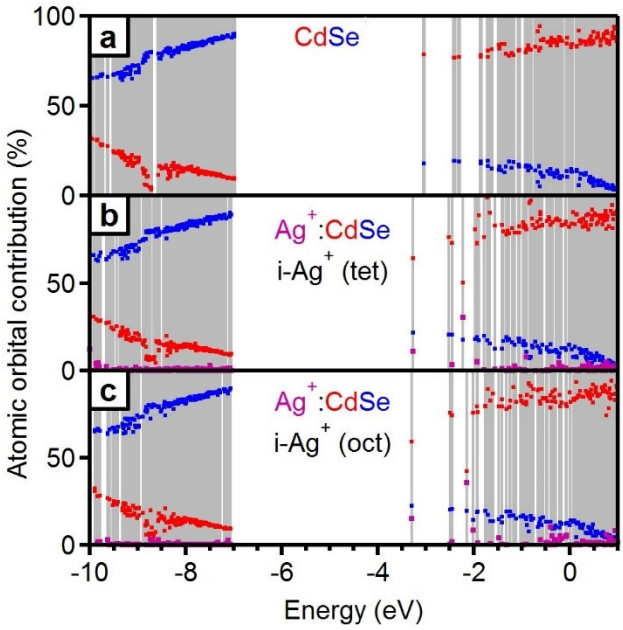

Figure B.6. Molecular orbitals of interstitially doped NCs. Calculated MO energies for **(a)** undoped $Cd_{77}Se_{77}$ and **(b-c)** interstitially doped Ag^{+}:$Cd_{77}Se_{77}$ NCs. The atomic-orbital contributions are shown as red dots for Cd^{2+}, blue dots for Se^{2-}, purple dots for the total Ag^{+} orbital contribution, and purple lines for the Ag^{+} *d*-orbital contributions. MO energies are shown for NCs with Ag^{+} in both tetrahedral and octahedral interstitial sites of the zinc-blende CdSe lattice. For both interstitially doped NCs, the CB edge shifts to slightly lower energy, with a 10-15% contribution from the Ag(5*s*) atomic orbitals. Interstitial Ag^{+} doping does not result in mid-gap acceptor states and is therefore not expected to activate mid-gap luminescence in *i*-Ag^{+}-doped NCs.

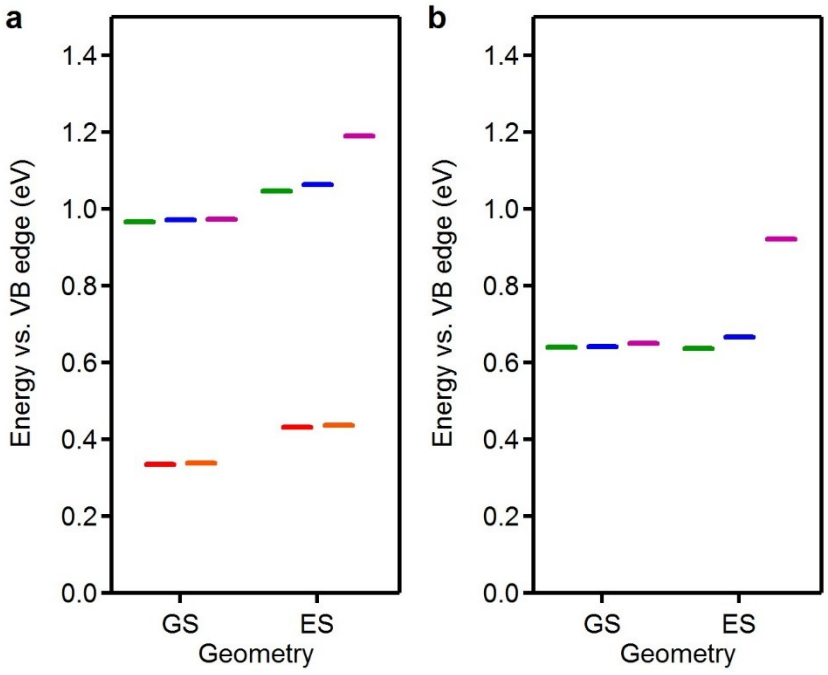

Figure B.7. Mid-gap MO energies in ground-state and excited-state geometry. Energies of the dopant-induced mid-gap MOs of **(a)** Cu^+:$Cd_{76}Se_{77}$ and **(b)** Ag^+:$Cd_{76}Se_{77}$ NCs relative to the VB edge, in the approximately tetrahedral ground-state and broken-symmetry relaxed excited-state geometries (as shown in Figure 3.7). In the ground-state geometry, the three mid-gap MOs are very nearly degenerate, as expected for t_2 orbitals of the tetrahedral cation site. In the excited state, a Jahn-Teller distortion breaks this degeneracy, preferentially stabilizing one t_2 MO relative to the other two. Similar excited-state splittings are observed for both Cu^+- and Ag^+-doped CdSe NCs.

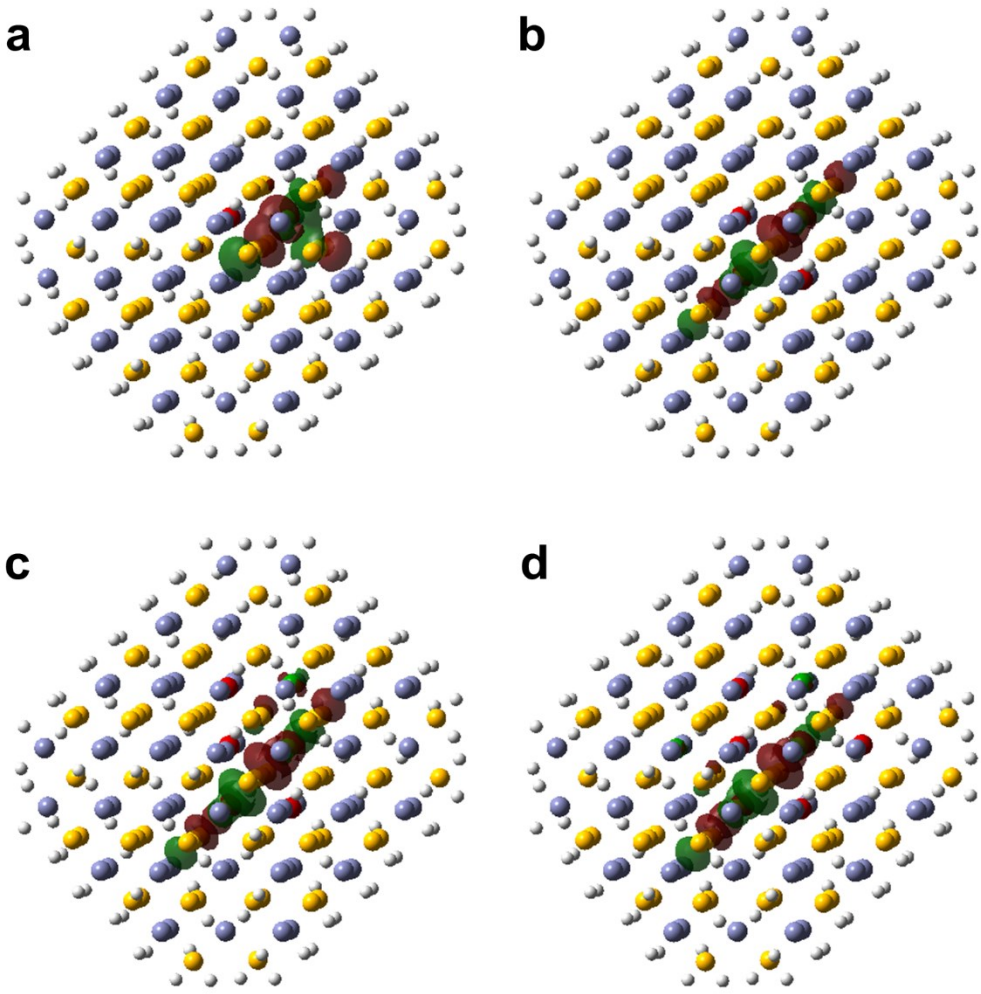

Figure C.1. HOMOs of Cu^{+},In^{3+}:ZnS NCs with increasing Cu^{+} and In^{3+} concentrations. Highest occupied molecular orbital (HOMO) wavefunction surfaces for 77-cation ZnS NCs with **(a)** 1 Cu^{+} and 1 In^{3+}; **(b)** 2 Cu^{+} and 2 In^{3+}; **(c)** 3 Cu^{+} and 3 In^{3+}; and **(d)** 4 Cu^{+} and 4 In^{3+} dopants. Cu^{+} atoms are shown in green, In^{3+} in red, Zn^{2+} in gray, and S^{2-} in yellow. All surfaces are visualized at 80% density (*i.e.*, 80% probability that an electron occupying this orbital is inside the pictured surface).

This figure shows the complete structures of the NCs whose HOMOs are shown in Figure 4.3.

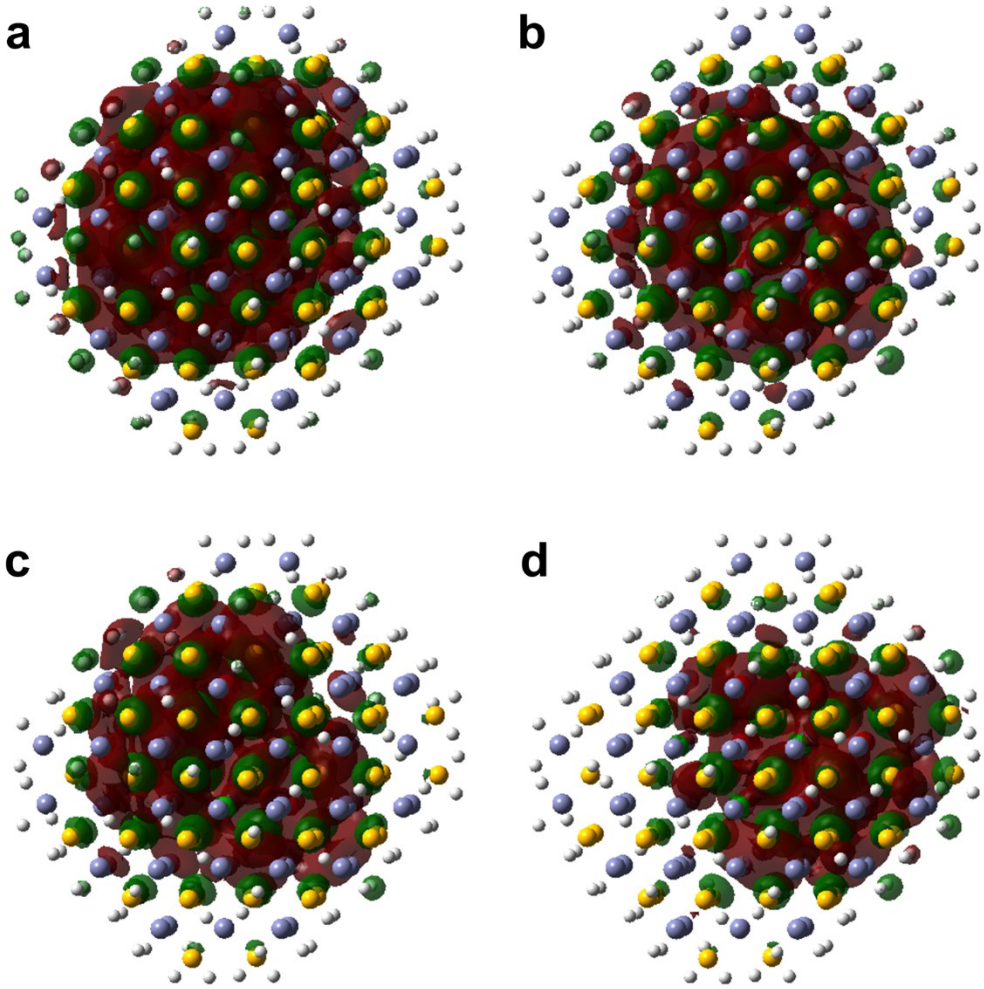

Figure C.2. LUMOs of Cu^+,In^{3+}:ZnS NCs with increasing Cu^+ and In^{3+} concentrations. Lowest unoccupied molecular orbital (LUMO) wavefunction surfaces for 77-cation ZnS NCs with **(a)** 1 Cu^+ and 1 In^{3+}; **(b)** 2 Cu^+ and 2 In^{3+}; **(c)** 3 Cu^+ and 3 In^{3+}; and **(d)** 4 Cu^+ and 4 In^{3+} dopants. Cu^+ atoms are shown in green, In^{3+} in red, Zn^{2+} in gray, and S^{2-} in yellow. All surfaces are visualized at 80% wavefunction density.

This figure shows the complete structures of the NCs whose HOMOs are shown in Figure C.1 and Figure 4.3. With increasing In^{3+} concentration, the LUMO becomes contracted around the In^{3+} dopants, but it is still much more delocalized than the HOMO. The LUMO of $CuInS_2$ NCs also appears fully delocalized (Figure 4.2f).

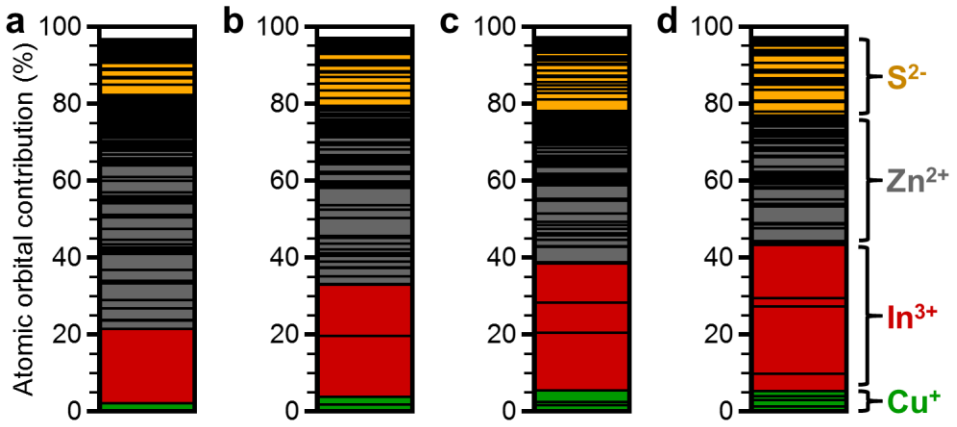

Figure C.3. LUMOs of Cu^{+},In^{3+}:ZnS NCs with increasing Cu^{+} and In^{3+} concentrations. Atomic-orbital contributions to the LUMO for 77-cation ZnS NCs with **(a)** 1 Cu^{+} and 1 In^{3+}; **(b)** 2 Cu^{+} and 2 In^{3+}; **(c)** 3 Cu^{+} and 3 In^{3+}; and **(d)** 4 Cu^{+} and 4 In^{3+} dopants. Contributions from each individual atom are shown separately (S^{2-}: yellow, Zn^{2+}: gray, In^{3+}:red, Cu^{+}: green).

These LUMOs are illustrated in Figure C.2, and the HOMOs of the same NCs are depicted in Figure 4.3 and Figure C.1. Although the different In^{3+} dopants contribute unequally to the LUMO, each NC's LUMO includes significant contributions from many more atoms, and is much more delocalized, than its corresponding HOMO in Figure 4.3.

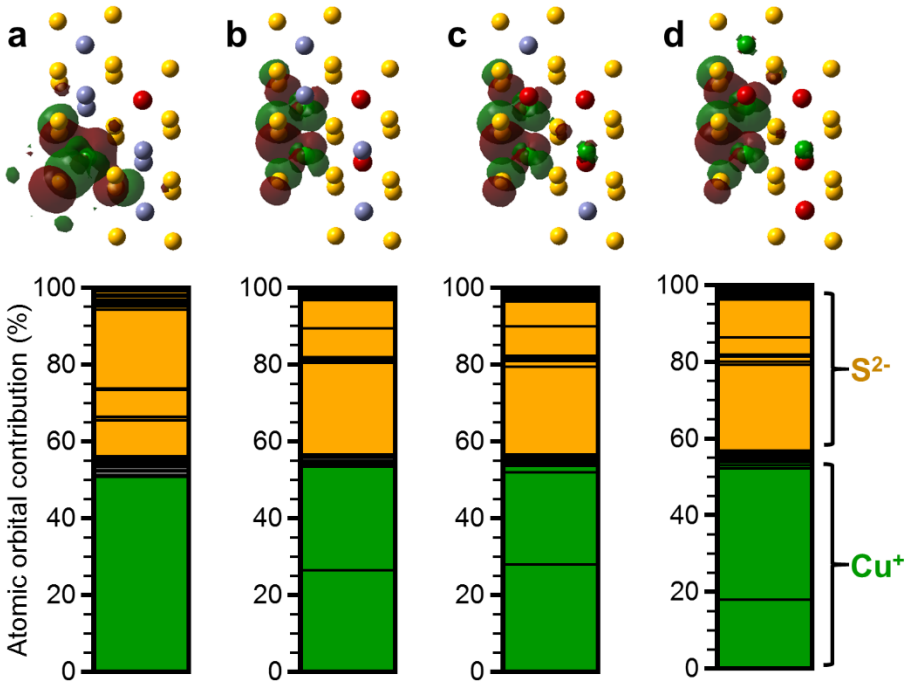

Figure C.4. LUMOs of oxidized Cu^+:ZnS NCs with increasing Cu^+ concentration. LUMO surfaces and atomic-orbital contributions for oxidized 77-cation ZnS NCs with **(a)** 1 Cu^+ and 1 In^{3+}; **(b)** 2 Cu^+ and 2 In^{3+}; **(c)** 3 Cu^+ and 3 In^{3+}; and **(d)** 4 Cu^+ and 4 In^{3+} dopants. Top: LUMO surfaces visualized at 80% density, showing only the 8 cation sites doped with Cu^+ or In^{3+} and their adjacent S^{2-} anions. Cu^+ are shown in green, In^{3+} in red, Zn^{2+} in gray, and S^{2-} in yellow. Bottom: Atomic-orbital contributions (%) to the same LUMOs. Contributions from each individual atom are shown separately (Cu^+: green, S^{2-}: yellow, In^{3+} and Zn^{2+} contributions to these orbitals are negligible).

To determine whether the HOMOs shown in Chapter 4 are a good representation for the wavefunction of a hole added to the NC, electronic-structure calculations were performed on oxidized NCs (+1 charge) in their relaxed ground-state. For each NC, this oxidation represents the removal of an electron from the HOMO shown in Figure 4.3, followed by nuclear reorganization. Figure C.4 illustrates the LUMOs of the oxidized NCs, representing the wavefunction of the hole added upon oxidation. These wavefunctions are very similar to those shown in Figure 4.3. The primary difference is that this MO has slightly more S^{2-} character (less Cu^+ character) than the HOMOs in Figure 4.3. Addition of the hole does not result in any change in localization or breaking of symmetry within the Cu^+ cluster where the HOMO is already localized.

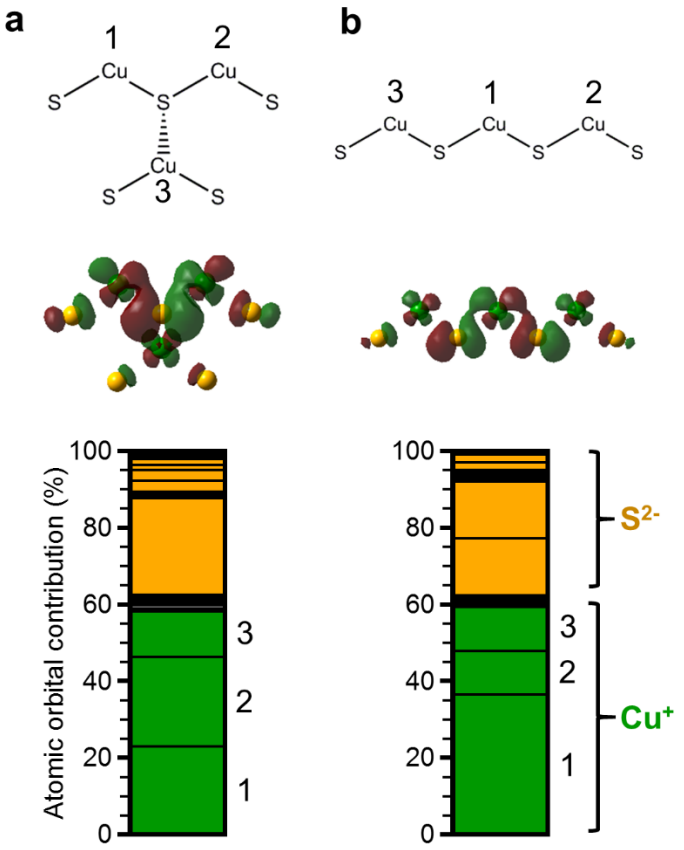

Figure C.5. HOMOs of 77-cation ZnS NCs containing Cu^+ trimers. HOMO surfaces and atomic-orbital contributions for 77-cation ZnS NCs containing Cu^+ trimers. **(a)** and **(b)** represent NCs with different trimer configurations. Top: schematic illustrations of the Cu^+ trimer configurations. Middle: HOMO surfaces visualized at 80% density, showing the same atoms as above. Bottom: Breakdowns of atomic-orbital contributions (%) for the same HOMOs. Contributions from each individual atom are shown separately (Cu^+: green, S^{2-}: yellow, Zn^{2+} contributions to these orbitals are negligible). The numbers next to these plots correspond to the numbered Cu^+ ions in the trimer configurations above.

This figure is an extension of Figure 4.4, showing two more trimer configurations. Neither of these configurations occur in the chalcopyrite lattice (except when a Cu_{In} antisite defect is present). The trimer in Figure C.5a has the same symmetry as the trimer in Figure 4.4c, but all three Cu^+ share the same S^{2-} anion. The trimer in Figure C.5b has an open configuration, but all three Cu^+ are in the same plane. These results further support the conclusion that higher-symmetry Cu^+ clusters

and greater connectivity between Cu^+ facilitate delocalization of the HOMO, while the Cu^+ configurations that occur in the defect-free chalcopyrite lattice are not conducive to delocalization..

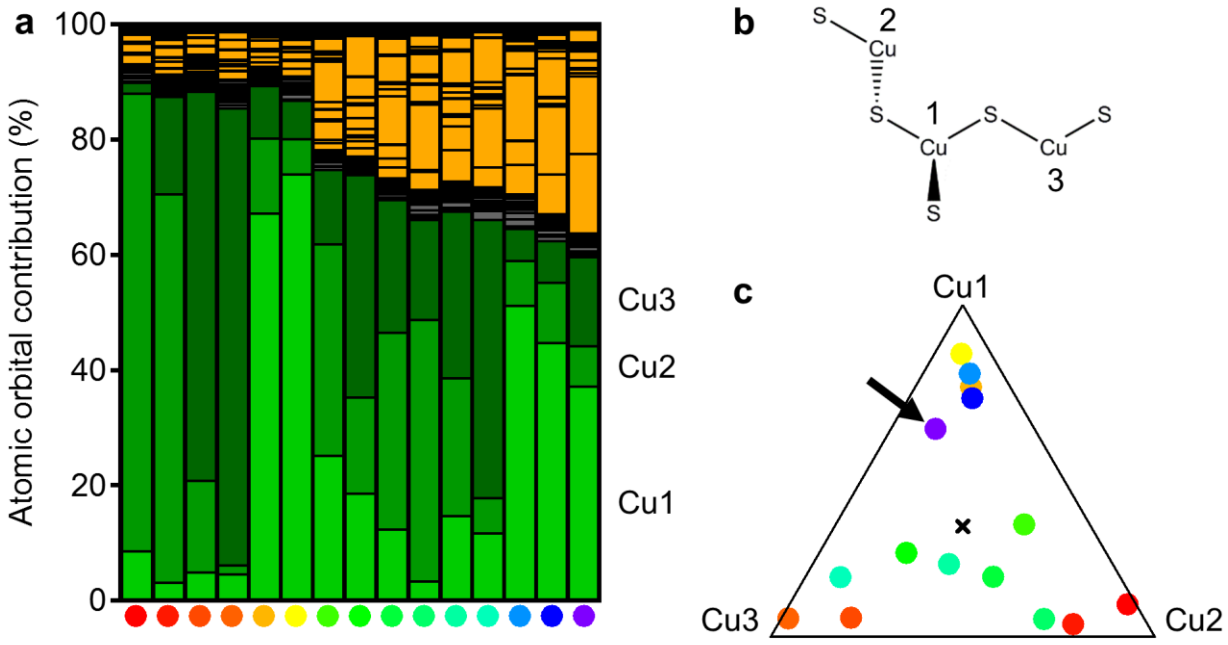

Figure C.6. Mid-gap Cu-based MOs of the same $Cu_3Zn_{74}S_{77}$ NC as in Figure 4.4a. (a) Atomic-orbital contributions to all fifteen Cu(3*d*)-based MOs, showing contributions from each individual atom in the NC. Contributions from Cu^+ are shown in green, Zn^{2+} in gray, and S^{2-} in yellow. The three different shades of green represent the three different Cu^+ atoms. MOs are arranged by increasing energy from left to right; the HOMO is on the far right. **(b)** Schematic illustration of the relative positions of the three Cu^+ cations. **(c)** Ternary plot showing the relative contributions of each Cu^+ to the fifteen Cu(3*d*)-based MOs. Each point represents one of the fifteen MOs shown in (a). The color of each point represents the energy of that MO and is also shown in (a). Points located near the vertices of the triangle represent MOs which are highly localized on a single Cu^+, while points near the center represent MOs with even contributions from all three Cu^+. The X represents the center of the triangle, and the arrow indicates the HOMO.

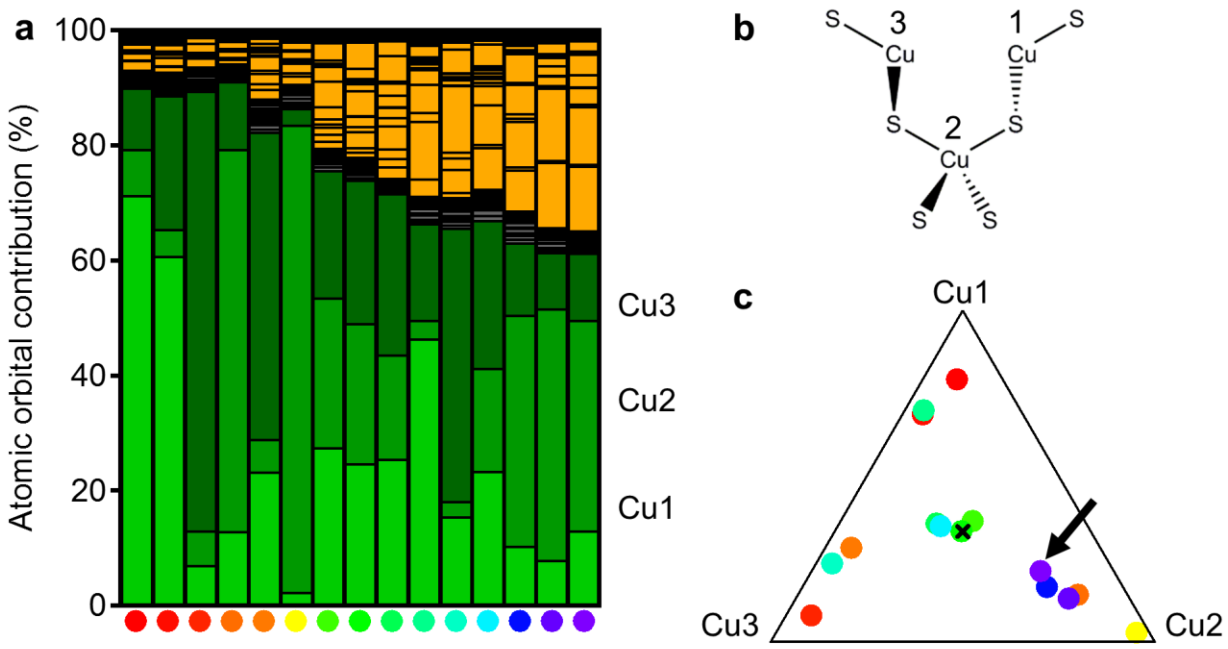

Figure C.7. Mid-gap Cu-based MOs of the same $Cu_3Zn_{74}S_{77}$ NC as in Figure 4.4b. (a) Atomic-orbital contributions to all fifteen Cu(3*d*)-based MOs, showing contributions from each individual atom in the NC. Contributions from Cu^+ are shown in green, Zn^{2+} in gray, and S^{2-} in yellow. The three different shades of green represent the three different Cu^+ atoms. MOs are arranged by increasing energy from left to right; the HOMO is on the far right. **(b)** Schematic illustration of the relative positions of the three Cu^+ cations. **(c)** Ternary plot showing the relative contributions of each Cu^+ to the fifteen Cu(3*d*)-based MOs. Each point represents one of the fifteen MOs shown in (a). The color of each point represents the energy of that MO and is also shown in (a). Points located near the vertices of the triangle represent MOs which are highly localized on a single Cu^+, while points near the center represent MOs with even contributions from all three Cu^+. The X represents the center of the triangle, and the arrow indicates the HOMO.

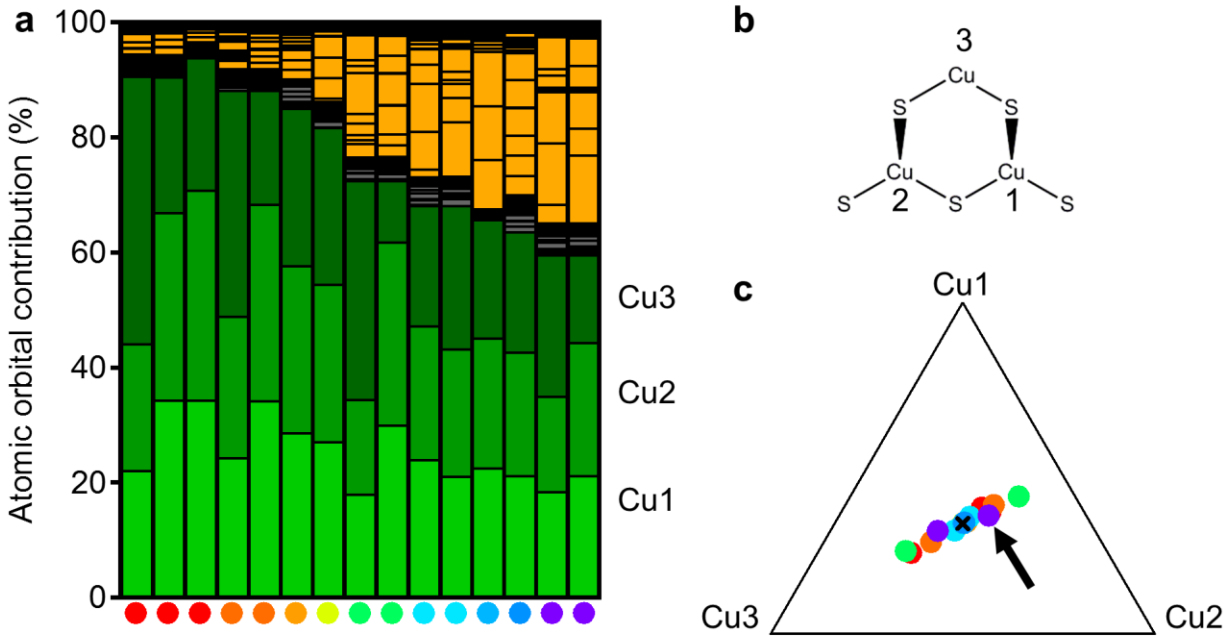

Figure C.8. Mid-gap Cu-based MOs of the same $Cu_3Zn_{74}S_{77}$ NC as in Figure 4.4c. (a) Atomic-orbital contributions to all fifteen Cu(3*d*)-based MOs, showing contributions from each individual atom in the NC. Contributions from Cu^+ are shown in green, Zn^{2+} in gray, and S^{2-} in yellow. The three different shades of green represent the three different Cu^+ atoms. MOs are arranged by increasing energy from left to right; the HOMO is on the far right. **(b)** Schematic illustration of the relative positions of the three Cu^+ cations. **(c)** Ternary plot showing the relative contributions of each Cu^+ to the fifteen Cu(3*d*)-based MOs. Each point represents one of the fifteen MOs shown in (a). The color of each point represents the energy of that MO and is also shown in (a). Points located near the vertices of the triangle represent MOs which are highly localized on a single Cu^+, while points near the center represent MOs with even contributions from all three Cu^+. The X represents the center of the triangle, and the arrow indicates the HOMO.

Together, Figure C.6, Figure C.7, and Figure C.8 show that even when the Cu(3*d*)-based HOMO is clearly localized, some of the other Cu(3*d*)-based MOs are more delocalized. In Figure C.6 and Figure C.7, the six lowest-energy Cu(3*d*)-based MOs involve the *e* subset of the Cu(3*d*) atomic orbitals, which have weaker interactions with the tetrahedrally coordinated S^{2-} anions (also evident in the smaller contributions of S^{2-} to these MOs). The nine highest-energy MOs, involving the t_2 subset of the Cu(3*d*) atomic orbitals, have stronger antibonding interactions with the S^{2-} anions and are pushed higher in energy. The lowest-energy t_2-based MOs are the most delocalized.

Although delocalized Cu(3*d*)-based states can exist, even in lower-symmetry Cu^+ trimer configurations, the HOMOs are consistently more localized. Due to the weak electronic coupling between Cu(3*d*) orbitals, symmetry-breaking can have a significant impact on the energy of localized MOs.

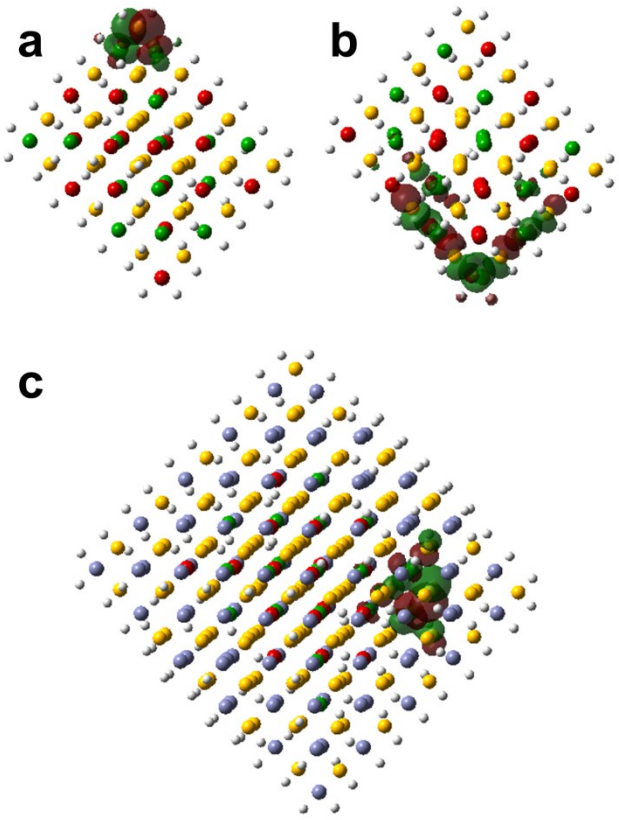

Figure C.9. HOMOs of $CuInS_2$ and $CuInS_2$/ZnS core/shell NCs. HOMO surfaces for **(a-b)** two different 34-cation $CuInS_2$ NCs and **(c)** a $CuInS_2$/ZnS core/shell NC with 134 total cations (18 Cu^+, 17 In^{3+}, 99 Zn^{2+}, corresponding to 1 monolayer of ZnS). Surfaces are visualized at 80% density. The NC in (b) is the same structure as in Figure 4.2f and Figure 4.6, shown from a different angle.

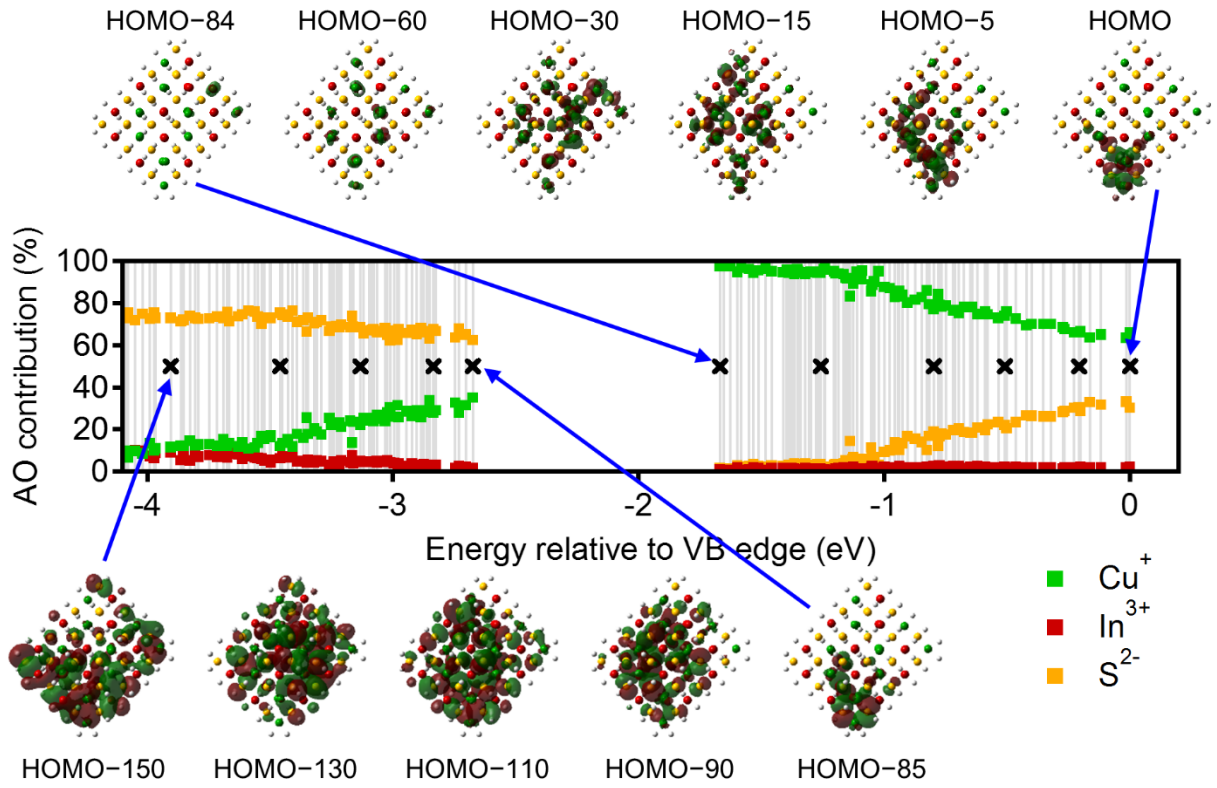

Figure C.10. Valence-band MO energies and selected MO surfaces for a 34-cation $CuInS_2$ NC. In this plot, each vertical line represents one calculated molecular orbital. The atomic-orbital contributions from different types of atoms are shown as percentages in green for Cu^+, red for In^{3+}, and yellow for S^{2-}. The X symbols indicate the energies of the MOs whose surfaces are shown. All MO surfaces are visualized at 80% density. In this calculation, the valence band has distinct Cu^+-based and S^{2-}-based bands, separated by a ~1 eV gap, as also seen in Figure 4.1.

Although the HOMO is clearly localized, some of the deeper VB MOs (HOMO−5, HOMO−15, HOMO−30) are more delocalized. This result is consistent with the calculations presented above for Cu^+ trimers in Cu^+-doped NCs (Figure C.6, Figure C.7, and Figure C.8), in which the HOMO is localized while some of the deeper Cu(3*d*)-based MOs are more delocalized. The deepest orbitals in the Cu^+-based part of the valence band, however, are very localized (HOMO−60, HOMO−84). These orbitals are made up of the *e* subset of the Cu(3*d*) atomic orbitals, which do not have the correct symmetry to interact with the tetrahedrally coordinated S^{2-} anions. The highest-energy MOs in the Cu(3*d*)-based band are pushed up in energy by their stronger

antibonding interactions with the S^{2-} anions.[1] Finally, the MOs in the S(3*p*)-based part of the valence band tend to be more delocalized, indicating that the S(3*p*) atomic orbitals facilitate delocalization more effectively than the Cu(3*d*) atomic orbitals. The S(3*p*)-based band is analogous to the valence band of a II−VI semiconductor (see also Figure 4.1).

1. Jaffe, J. E.; Zunger, A. Theory of the band-gap anomaly in ABC_2 chalcopyrite semiconductors. *Phys. Rev. B* **1984**, *29*, 1882-1906.

Appendix D. Supporting Information for Chapter 5

D.1 Experimental Methods

D.1.1 Synthesis of $CuInS_2$ quantum dots.

$CuInS_2$ quantum dots were synthesized by a previously reported method[1] adapted from the literature.[2] A mixture of indium acetate (0.292 g, 1 mmol), copper iodide (0.190 g, 1 mmol), and dodecanethiol (5 mL) was degassed using nitrogen at room temperature. The reaction mixture was heated to 110 °C under nitrogen and held for 10 min before heating to 230 °C. The reaction was held for 10 min at this temperature, then cooled rapidly to <60 °C. Quantum dots were purified with several cycles of precipitation with ethanol and centrifugation followed by resuspension in toluene. Powder X-ray diffraction shows that these $CuInS_2$ quantum dots have the chalcopyrite crystal phase.[1]

D.1.2 Synthesis of CdSe quantum dots.

CdSe quantum dots were prepared as detailed previously[3] by a method adapted from the literature.[4] Briefly, 0.19 g of selenium powder and 4 mL of trioctylphosphine were mixed in a nitrogen-atmosphere glovebox. Separately, 0.152 g of CdO, 1.01 g of oleic acid, and 16 g of ODE were degassed under vacuum at 100 °C. The solution was then heated to 270 °C under nitrogen until it turned from red to clear and colorless. The solution was cooled to 100 °C, whereupon 2.01 g of hexadecylamine and 2.02 g of trioctylphosphine oxide were added against nitrogen overpressure. The solution was degassed under vacuum at 100 °C for 30 minutes and then heated to 300 °C under nitrogen atmosphere. After reaching 300 °C, the solution containing selenium was rapidly injected with vigorous stirring. The resulting quantum dots were allowed to grow for 10 minutes.

The solution was then rapidly cooled to <60 °C. Quantum dots were purified with several cycles of precipitation with ethanol and centrifugation followed by resuspension in toluene.

D.1.3 **General characterization.**

Samples were characterized by UV-Vis absorption spectroscopy and ensemble photoluminescence (see Figure D.1). Absorption spectra of quantum dots suspended in toluene at room temperature were measured using an Agilent Cary 5000 spectrometer. Photoluminescence spectra were collected using continuous-wave 405 nm photoexcitation. The photoluminescence was passed through a 420 nm long-pass filter, focused into a monochromator (0.5 m, 150 g/mm grating blazed at 500 nm), and collected on a liquid-N_2-cooled charge-coupled device (CCD). $CuInS_2$ quantum dot sizes were determined by transmission electron microscopy, and CdSe quantum dot sizes were determined from absorption spectra following a previously reported method.[5] All photoluminescence measurements were performed on drop-coated films of quantum dots sandwiched between quartz disks and mounted in a closed-cycle helium cryostat held at a temperature of 20 K.

D.1.4 **Short-pulse vs square-wave photoexcitation.**

Square-wave excitation pulses were generated by a 405 nm diode laser modulated using a square pulse waveform output from a function generator at a 5 Hz repetition rate. The fluence at the sample was 8 mW/cm^2 during the pulse. Short-pulse excitation was provided by a N_2-pumped dye laser tuned to 405 nm using α-NPO dye, with 5 ns pulse duration. The fluence at the sample was 30 μJ/cm^2. Photoluminescence decay traces were measured near the peak emission maximum for each sample, integrating over a spectral bandwidth of < 3 nm. In both experiments, the photoluminescence was passed through a 420 nm long-pass filter and focused into a

monochromator (0.5 m, 150 g/mm grating blazed at 500 nm) equipped with a PMT. The signal was processed using a multichannel scaler and recorded using a custom LabView program.

D.1.5 **Excitation pulse-width dependence.**

The same samples described above were excited using a 405 nm diode laser modulated with a square pulse waveform output from a function generator. Excitation pulse durations (ON) were varied between 50 μs and 100 ms and inter-pulse (OFF) durations were kept constant (100 ms). The excitation area was 0.3 cm^2 for all measurements. Excitation power (measured during the ON phase) was varied between 2, 4, and 8 mW, corresponding to fluences of 6.7, 13.3, and 26.7 mW/cm^2, respectively. Photoluminescence decay traces were measured near the peak emission maximum for each sample, integrating over a spectral bandwidth of < 3 nm. The detection scheme was identical to the one described above. The total measurement time, including all excitation powers and pulse widths, was ~2 days of continuous illumination for the $CuInS_2$ sample and ~3 days for the CdSe sample.

D.2 **Supplemental Data**

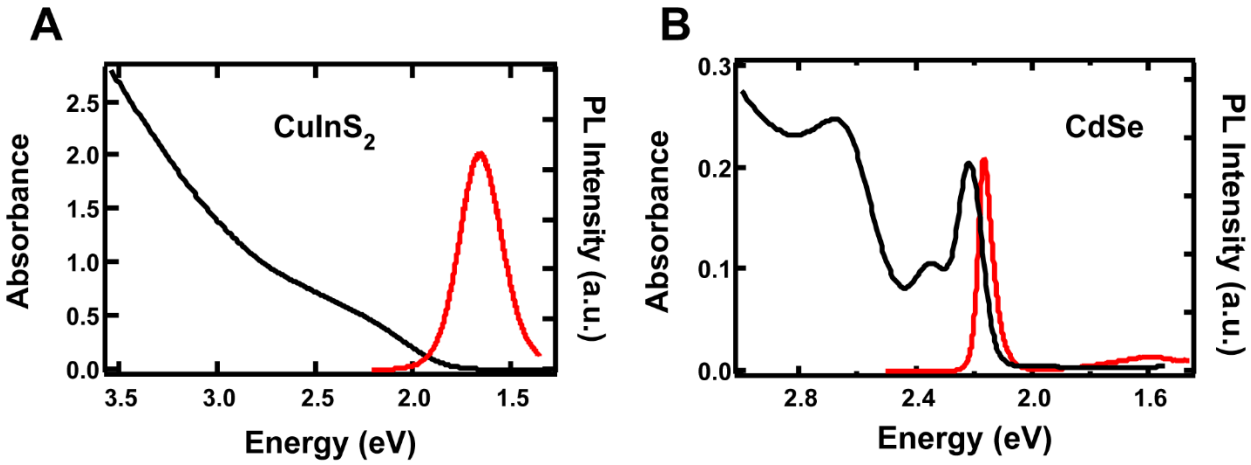

Figure D.1. Absorption and PL spectra of $CuInS_2$ and CdSe NCs. Room-temperature electronic absorption and 20 K photoluminescence spectra of **(A)** d = 3.9 nm $CuInS_2$ quantum dots and **(B)** d = 3.3 nm CdSe quantum dots. Luminescence spectra are corrected for instrument response.

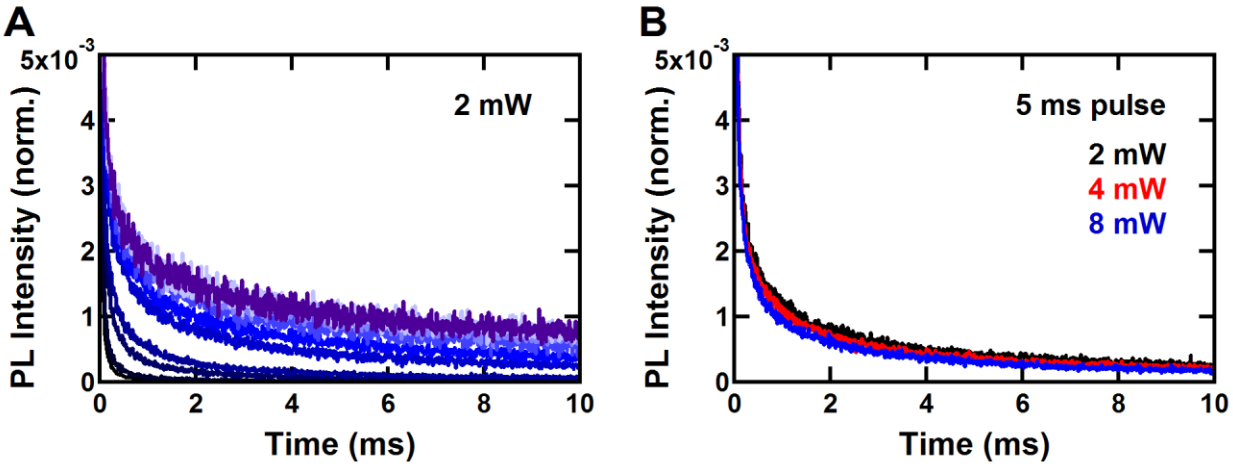

Figure D.2. Delayed luminescence decay curves for $CuInS_2$ NCs. (A) Delayed luminescence decay dynamics measured with different excitation pulse widths for d = 3.9 nm $CuInS_2$ quantum dots (50 μs (black) to 100 ms (purple) excitation pulses). Traces are normalized to their prompt luminescence intensities. **(B)** Dynamics of delayed luminescence measured using 2 (black), 4 (red), and 8 mW (blue) excitation powers for the same $CuInS_2$ quantum dots with a 5 ms excitation pulse. Traces are normalized to the prompt luminescence intensity. All data collected at 20 K. The same data are shown on logarithmic axes in Figure 5.2.

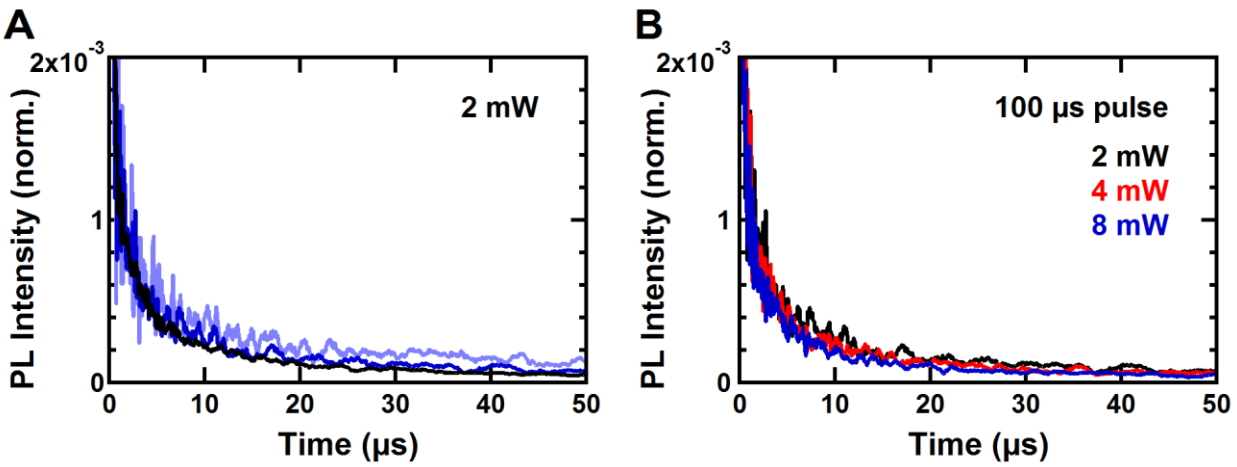

Figure D.3. Delayed luminescence decay curves for CdSe NCs. (A) Delayed luminescence decay dynamics measured with different excitation pulse widths for $d = 3.3$ nm CdSe quantum dots (50 μs (black), 100 μs (dark blue), and 25 ms (light blue) excitation pulses). Traces are normalized to their prompt luminescence intensities. **(B)** Dynamics of delayed luminescence measured using 2 (black), 4 (red), and 8 mW (blue) excitation powers for the same CdSe quantum dots with a 100 μs excitation pulse. Traces are normalized to the prompt luminescence intensity. All data collected at 20 K. The same data are shown on logarithmic axes in Figure 5.3.

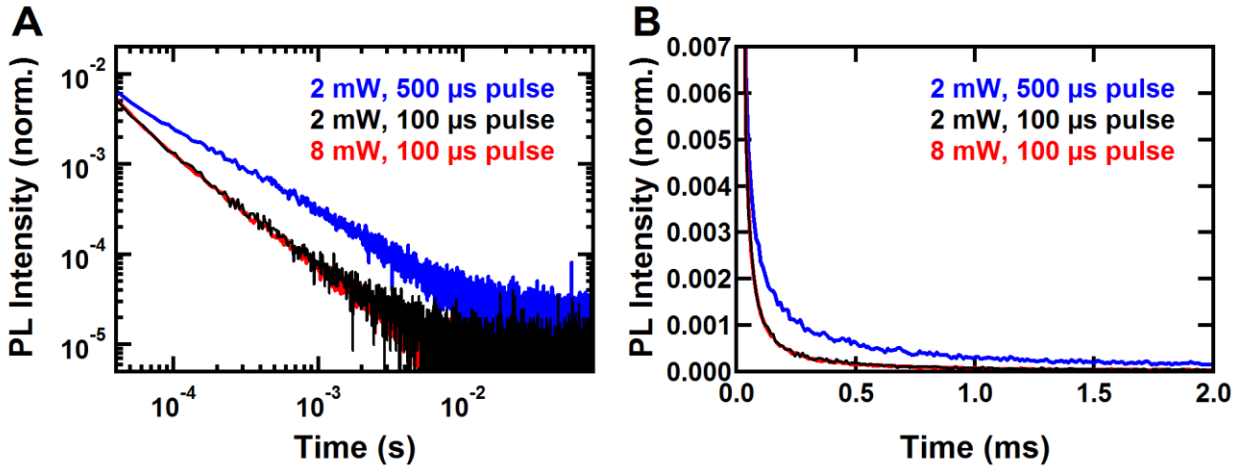

Figure D.4. Delayed luminescence decay dynamics for 4x increase in power and 5x increase in pulse width. Dynamics of delayed luminescence for (black) excitation pulse width = 100 μs, excitation power = 2 mW, (blue) excitation pulse width = 500 μs, excitation power = 2 mW, and (red) excitation pulse width = 100 μs, excitation power = 8 mW. Traces are normalized to the prompt luminescence intensity and are shown on both logarithmic (A) and linear (B) axes. The power-law slopes measured from 100 μs to 1 ms are: (black) 1.15, (blue) 0.68, (red) 1.23. The power-law slope drops by nearly one half when increasing the pulse width 5x but is almost unchanged when increasing the pulse power 4x. These data

demonstrate that the delayed luminescence decay dynamics are much more sensitive to excitation pulse width than to excitation pulse power for a similar total number of photons per pulse.

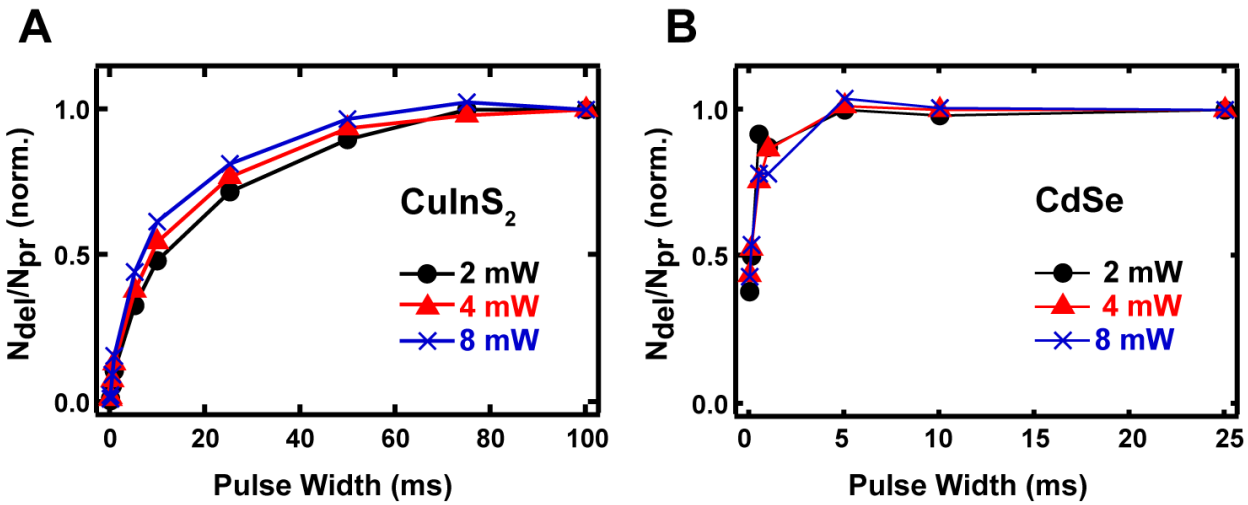

Figure D.5. Pulse width dependence normalized at the longest pulse width. (A, B) N_{del}/N_{pr} plotted as a function of the excitation pulse width for **(A)** $CuInS_2$ quantum dots and **(B)** CdSe quantum dots. These curves represent the same data as presented in Figure 5.2C and Figure 5.3C, normalized by their value at the longest pulse width. Three different excitation powers are shown for each sample: 2 mW (black circles), 4 mW (red triangles), 8 mW (blue crosses). All data collected at 20 K.

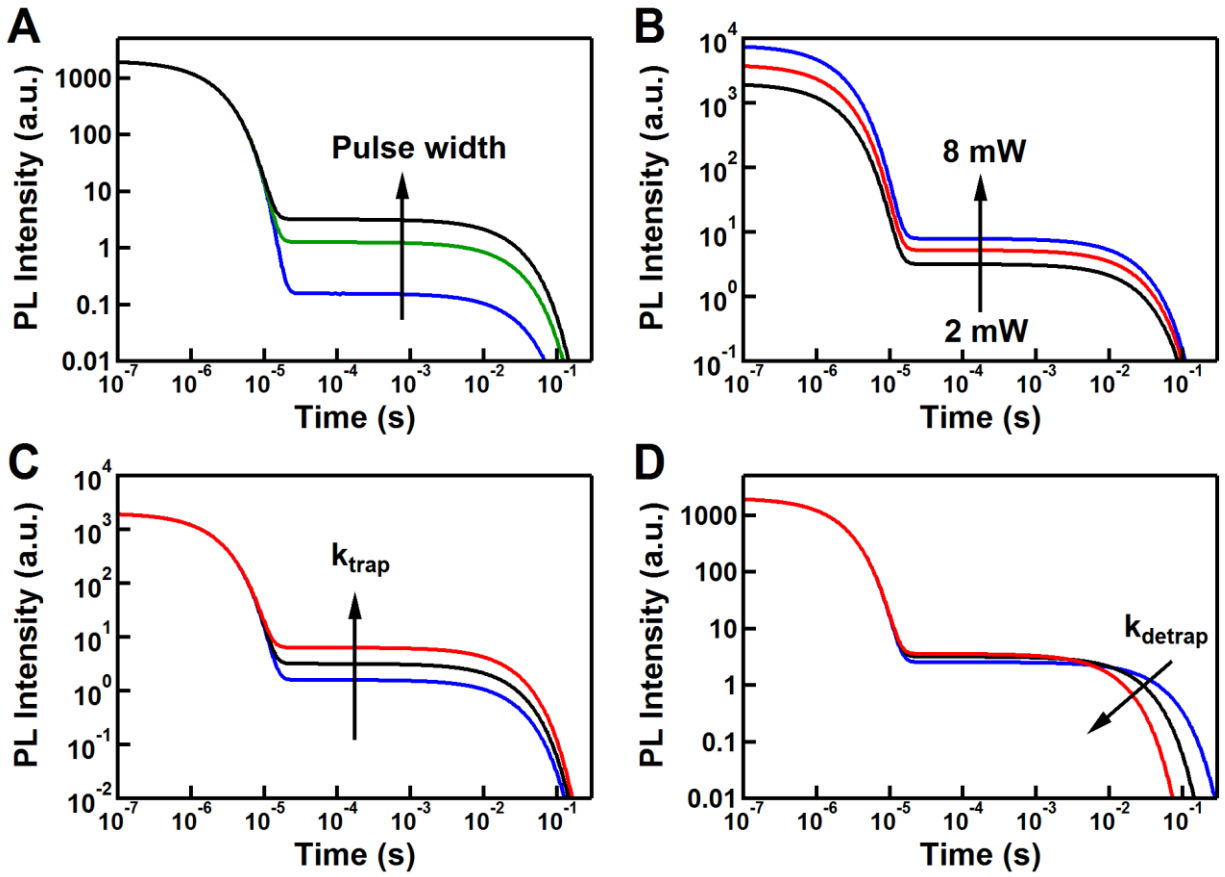

Figure D.6. Simulated photoluminescence decay curves. All simulated decay curves shown here are presented with the following parameters, except where indicated: $k_{exc} = 20\ s^{-1}$, $k_{trap} = 1000\ s^{-1}$, $k_{detrap} = 40\ s^{-1}$, $k_{PL} = 5 \cdot 10^5\ s^{-1}$, $k_{A,trap} = k_{A,trion} = 10^{10}\ s^{-1}$, pulse width = 100 ms. Black curves in all panels are simulated with this unchanged set of parameters. Arrows indicate the direction of increasing parameter values. **(A)** Decay curves simulated with varying pulse width (1 ms, 10 ms, 100 ms). **(B)** Decay curves simulated with varying excitation power (2, 4, 8 mW) by varying k_{exc} (20, 39, 78 s^{-1}). **(C)** Decay curves simulated with varying k_{trap} (500, 1000, 2000 s^{-1}). **(D)** Decay curves simulated with varying k_{detrap} (20, 40, 80 s^{-1}).

These curves display two distinct time regimes for prompt and delayed luminescence, unlike the experimental decay curves in Figure 5.1, Figure 5.2A, and Figure 5.3A. This difference is due to the model's reliance on single rate constants for the trapping and detrapping processes, which does not capture the distributed kinetics that characterize the experiment. Overall, however, these simulations reproduce the pulse-width dependence of the magnitude of delayed luminescence and further illustrate the effect of changing other conditions and parameters.

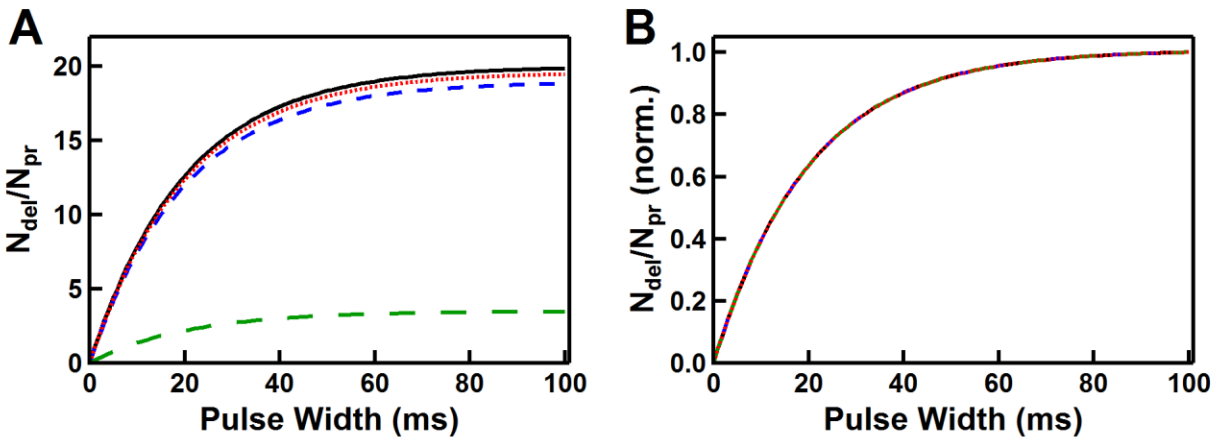

Figure D.7. Simulated pulse-width dependence determined from integration of PL and from excited state populations. Simulated pulse-width dependence of N_{del}/N_{pr}, comparing the determination of N_{del}/N_{pr} from integration of luminescence decay curves (eq 5.1 and 5.2) and directly from the charge-separated state and emissive excited state populations at the end of the excitation pulse, [CS]/[ES]. The following parameters were used for all simulations: $k_{exc} = 20\ s^{-1}$, $k_{trap} = 1000\ s^{-1}$, $k_{detrap} = 40\ s^{-1}$, $k_{PL} = 5 \cdot 10^5\ s^{-1}$, $k_{A,trap} = k_{A,trion} = 10^{10}\ s^{-1}$. **(A)** Simulated N_{del}/N_{pr} determined from [CS]/[ES] at the end of the excitation pulse (black solid line), and using eq 5.1 and 5.2 with simulated luminescence decay curves, with $t_1 = 200\ \mu s$ and varying t_2 (red dotted line: $t_2 = 100$ ms; blue dashed line: $t_2 = 75$ ms; green dashed line: $t_2 = 5$ ms). **(B)** Curves from panel A, normalized to the value of N_{del}/N_{pr} at 100 ms. All four curves lie on top of one another.

Increasing the integration window causes the simulated N_{del}/N_{pr} to approach [CS]/[ES], but changing the integration window has no effect on the *curvature* of the pulse-width dependence of the simulated N_{del}/N_{pr}, in contrast with the experimental results shown in Figure 5.2D and Figure 5.3D. Both of these findings originate from the model's use of single rather than distributed rate constants for k_{trap} and k_{detrap}.

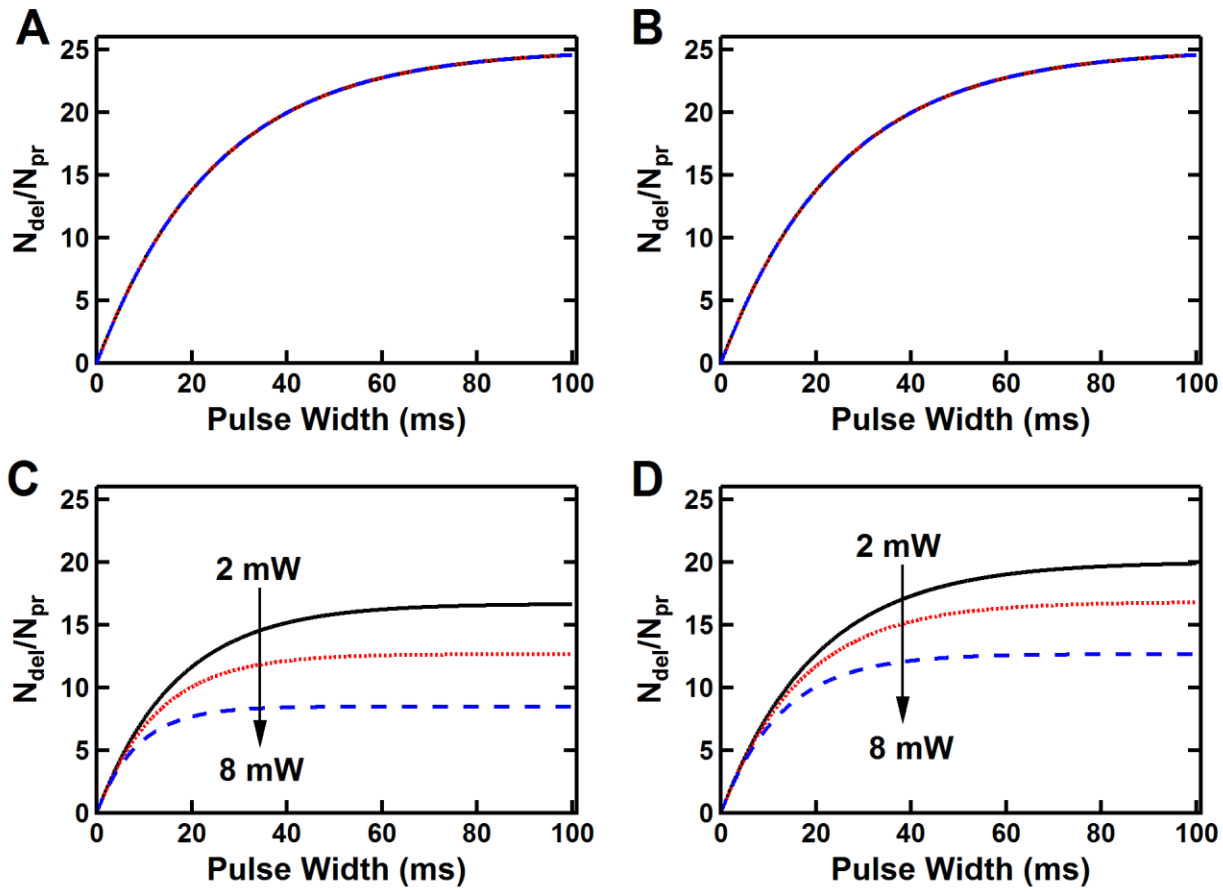

Figure D.8. Comparison of model with different Auger processes included. Simulated pulse-width dependence of N_{del}/N_{pr}, illustrating the effect of different nonradiative processes on the power dependence of N_{del}/N_{pr}. All parameters are fixed except $k_{A,trap}$ and $k_{A,trion}$, with $k_{trap} = 1000$ s^{-1}, $k_{detrap} = 40$ s^{-1}, $k_{PL} = 5 \cdot 10^5$ s^{-1}. Excitation powers are 2 mW ($k_{exc} = 20$ s^{-1}, black solid line), 4 mW ($k_{exc} = 39$ s^{-1}, red dotted line), and 8 mW ($k_{exc} = 78$ s^{-1}, blue dashed line). **(A)** Result from a three-state model, related to the model described in Chapter 5 but without the doubly excited state and its associated processes (excitation from the charge-separated state, trion Auger, and trap-assisted Auger). **(B)** Result from the four-state model described in Chapter 5 with the trion Auger process only: $k_{A,trap} = 0$ and $k_{A,trion} = 10^{10}$ s^{-1}. **(C)** Result from the four-state model described in Chapter 5 with the trap-assisted Auger process only: $k_{A,trap} = 10^{10}$ s^{-1} and $k_{A,trion} = 0$. **(D)** Result from the four-state model described in Chapter 5 with both trap-assisted and trion Auger processes: $k_{A,trap} = 10^{10}$ s^{-1} and $k_{A,trion} = 10^{10}$ s^{-1}, as in Figure 5.4E.

The three-state model cannot account for the observed power dependence of N_{del}/N_{pr} in this excitation power regime, and the trion Auger process alone also does not yield an observable power dependence of N_{del}/N_{pr}. Instead, the trap-assisted Auger process is necessary for this power

dependence, effectively providing an additional power-dependent pathway for detrapping from the charge-separated state to the emissive excited state. The trion Auger process influences the overall efficiency of this mechanism by providing an alternative pathway for decay of the doubly excited state, but inclusion of the trap-assisted Auger process in the model is necessary to reproduce the experimentally observed power dependence of N_{del}/N_{pr}.

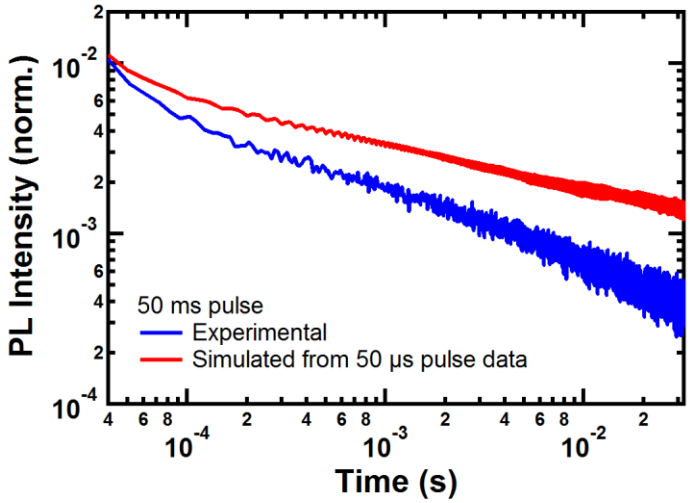

Figure D.9. Comparison of experimental long-pulse decay curve with sum of offset short-pulse decay curves. Following ref. 6, the luminescence decay data measured after a 50 ms pulse (2 mW, blue) are compared with those simulated by summing 1000 decay curves measured from a 50 µs pulse (also 2 mW, red), each shifted by 50 µs. The experimental decay curve is clearly different from the simulated curve. This difference is attributed to quantum dot multi-excitation. Specifically, the data point to Auger processes that require both (*i*) extremely slow accumulation of metastable populations (N_{del}), which is accounted for in both the experimental and the simulated data, *and* (*ii*) a second photoexcitation of a quantum dot that is already in its metastable charge-separated excited state. The latter occurs with long excitation pulses but does not occur with short excitation pulses, so simulating the decay resulting from a long excitation pulse by adding staggered decay curves from many short excitation pulses cannot reproduce this aspect of the data.

D.3 **References**

1. Marchioro, A.; Whitham, P. J.; Knowles, K. E.; Kilburn, T. B.; Reid, P. J.; Gamelin, D. R. Tunneling in the Delayed Luminescence of Colloidal CdSe, Cu^{+}-Doped CdSe, and $CuInS_2$ Semiconductor Nanocrystals and Relationship to Blinking. *J. Phys. Chem. C* **2016**, *120*, 27040-27049.
2. Li, L.; Pandey, A.; Werder, D. J.; Khanal, B. P.; Pietryga, J. M.; Klimov, V. I. Efficient Synthesis of Highly Luminescent Copper Indium Sulfide-Based Core/Shell Nanocrystals with Surprisingly Long-Lived Emission. *J. Am. Chem. Soc.* **2011**, *133*, 1176-1179.
3. Vlaskin, V. A.; Barrows, C. J.; Erickson, C. S.; Gamelin, D. R. Nanocrystal Diffusion Doping. *J. Am. Chem. Soc.* **2013**, *135*, 14380-14389.
4. Qu, L.; Peng, X. Control of Photoluminescence Properties of CdSe Nanocrystals in Growth. *J. Am. Chem. Soc.* **2002**, *124*, 2049-2055.
5. Yu, W. W.; Qu, L.; Guo, W.; Peng, X. Experimental Determination of the Extinction Coefficient of CdTe, CdSe, and CdS Nanocrystals. *Chem. Mater.* **2003**, *15*, 2854-2860.
6. Singh, G.; Guericke, M. A.; Song, Q.; Jones, M. A Multipulse Time-Resolved Fluorescence Method for Probing Second-Order Recombination Dynamics in Colloidal Quantum Dots. *J. Phys. Chem. C* **2014**, *118*, 14692−14702.

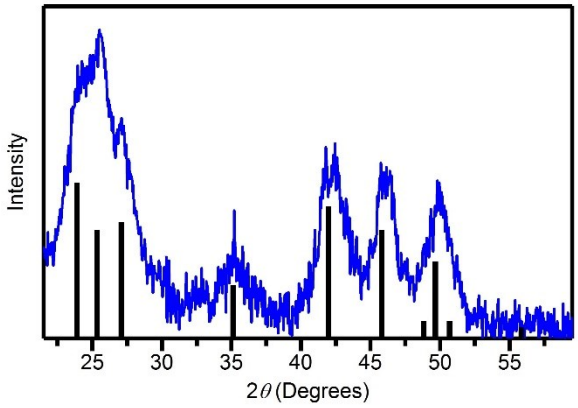

Figure E.1. XRD of $Cd_{0.87}Mn_{0.13}Se$ QDs. X-ray diffraction (XRD) data for colloidal $Cd_{0.87}Mn_{0.13}Se$ QDs (d ~ 4.5 nm). The diffraction pattern matches the reference wurtzite pattern (black lines) well.

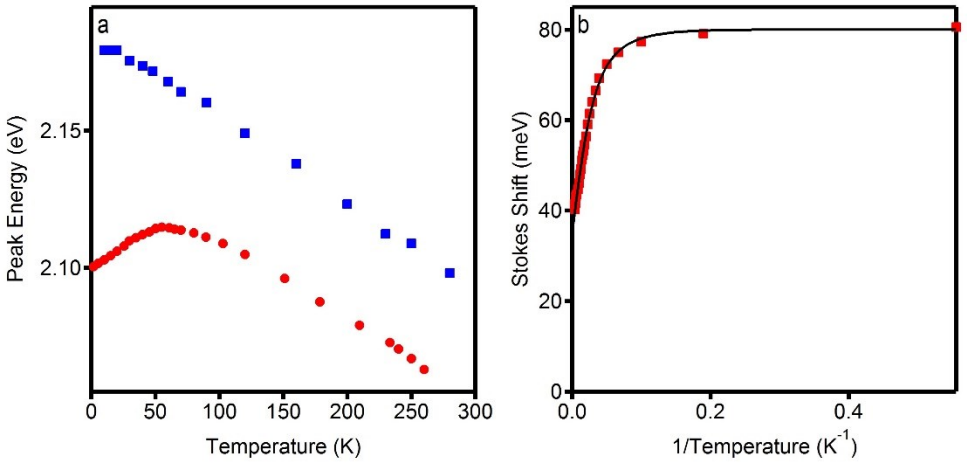

Figure E.2. Temperature dependence of absorption and PL energies. (a) Temperature dependence of the CW-absorption and CW-PL peak energies for the spectra in Figure 6.2a. The absorption maximum blueshifts with decreasing temperature following Varshni behavior. The PL maximum follows the same behavior but then redshifts below ~60 K. **(b)** Temperature dependence of the Stokes shift. The solid line is a fit to the Brillouin function of eq E.1 using $g = 2.0$ and $S = 5/2$, which gives $B_{eff} = 17$ T and $E_{offset} = 36$ meV. This energy offset was subtracted to give the EMP energies plotted in Figure 6.2c.

Equation E.1. The data in Figure E.2b were fit to a modified Brillouin function (Eq 6.1 with a constant offset energy, E_{offset}) to obtain the EMP energy from the Stokes shift data.

$$\Delta E_{\text{Stokes}} = \frac{1}{2} C_1 \langle S_\phi \rangle + E_{\text{offset}} = \frac{1}{2} C_1 \left[\frac{(2S+1)}{2S} \coth\left((2S+1) \left(\frac{g_{Mn} \mu_B B_{eff}}{2kT} \right) \right) - \frac{1}{2S} \coth\left(\frac{g_{Mn} \mu_B B_{eff}}{2kT} \right) \right] + E_{\text{offset}} \tag{E.1}$$

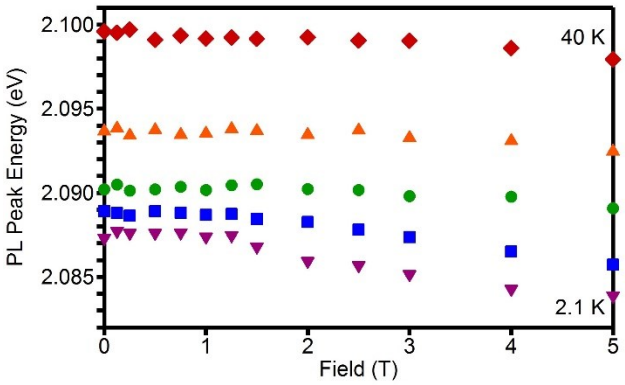

Figure E.3. Field dependence of CW PL peak energy. Field dependence of the CW-PL peak energy at $T = 2.1$, 5, 10, 20, and 40 K. With increasing field B_0, the PL peak energy shifts by $<\sim 3.5$ meV. This result indicates that most of the CW PL emission comes from a state that is fully magnetized, with the Mn^{2+} spins aligned by the EMP.

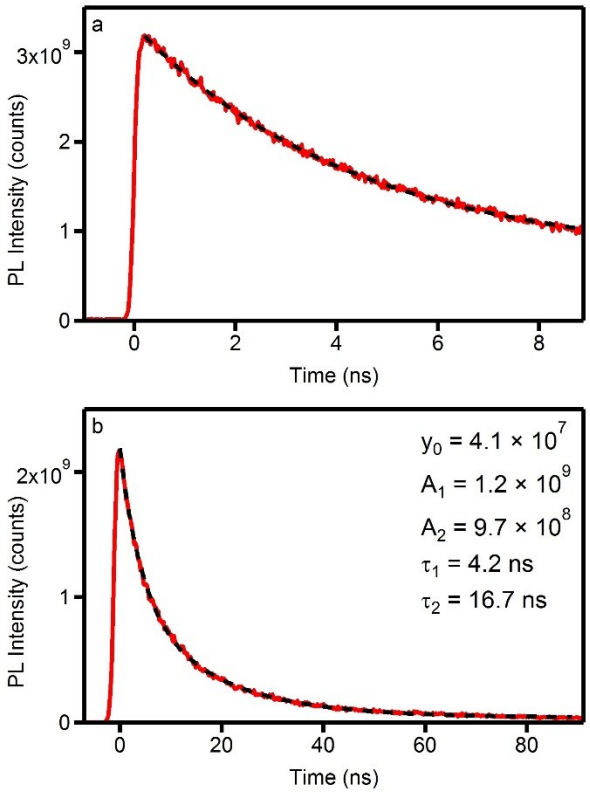

Figure E.4. PL decay curves. PL decay curves (solid red lines) for $d \sim 4.5$ nm $Cd_{0.87}Mn_{0.13}Se$ QDs at $T = 10$ K. The PL lifetime is multiexponential and is fit here to a biexponential decay (dashed black lines) with components characterized by $\tau_1 = 4.2$ ns and $\tau_2 = 16.7$ ns.

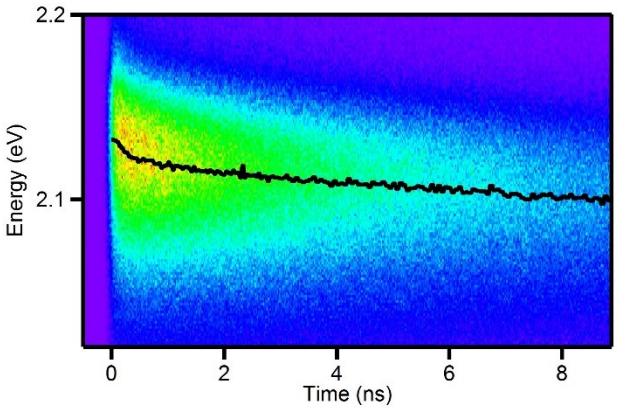

Figure E.5. Streak-camera PL image. Streak-camera image of the PL from $d \sim 4.5$ nm $Cd_{0.87}Mn_{0.13}Se$ QDs over a 10 ns window at $T = 10$ K. The black line traces the PL peak energy. The time-dependent redshift has a fast component (~300 ps) attributed to EMP formation, and a slow component attributed to EMP reorientation.

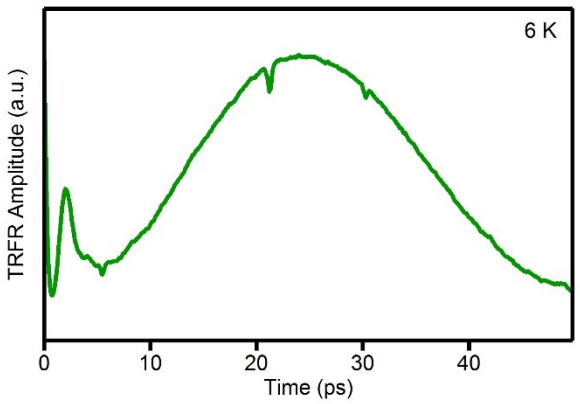

Figure E.6. TRFR trace showing fast oscillation. Time-resolved Faraday rotation trace for $d \sim 5.8$ nm $Cd_{0.995}Mn_{0.005}Se$ QDs at $T = 6$ K. The oscillation at $t = 0$ to 4 ps is attributed to the precession of an exchange-coupled exciton with $|g| \sim 35$.

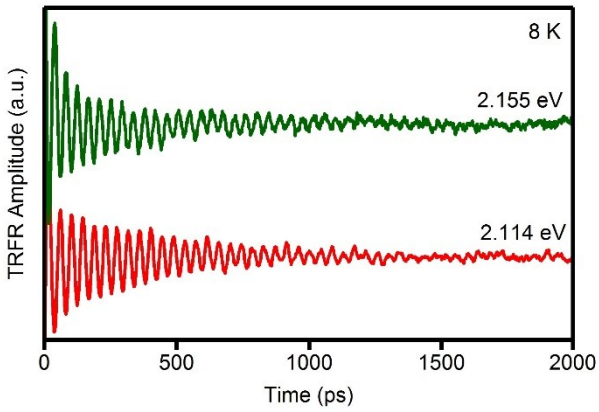

Figure E.7. TRFR trace showing Mn^{2+} precession beyond 1 ns. Time-resolved Faraday rotation traces for $Cd_{0.87}Mn_{0.13}Se$ QDs ($d \sim 4.5$ nm) from Figure 6.8c, plotted out to $t = 2$ ns. The coherent Mn^{2+} precession persists for well over 1 ns.

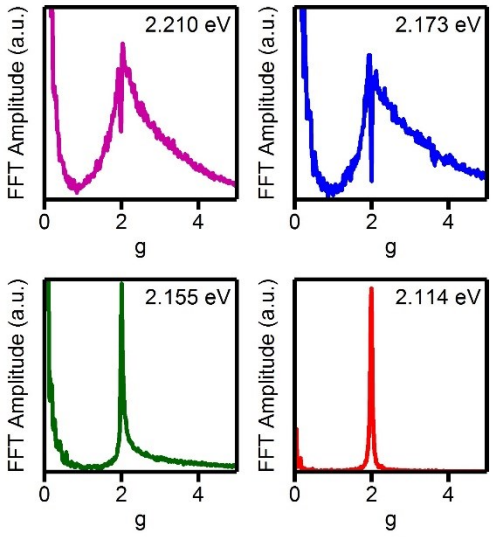

Figure E.8. Fourier transforms of TRFR traces showing dynamic phase inversion. Fourier transform plots of the TRFR traces in Figure 6.8c, plotted on an x axis represented by $g = \hbar\omega_L/\mu_B B_{tr}$. At all pump energies, the Mn^{2+} precession occurs at $g = 2.0$ and no other distinct precessions are observed. Fourier transforms of TRFR traces showing dynamic phase inversion appear very broad, whereas those of TRFR traces without dynamic phase inversion appear sharp.

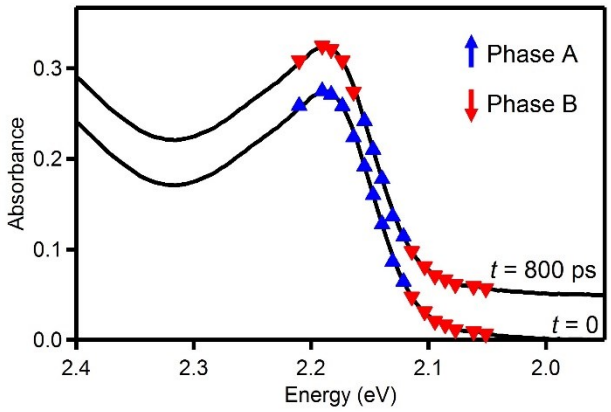

Figure E.9. Absorption spectra showing pump/probe energy dependence of TRFR phases. Absorption spectra with pump/probe energy dependence of the TRFR phase at $t = 0$ and $t = 800$ ps for $Cd_{0.87}Mn_{0.13}Se$ QDs ($d \sim 4.5$ nm). The spectrum representing the $t = 800$ ps TRFR phases is vertically offset for clarity. The red circles and blue triangles indicate the two different phases of the oscillating TRFR signal. For several pump/probe energies near the absorption peak ($E > 2.164$ eV), the phase inverts dynamically between $t = 0$ and $t = 800$ ps. At lower pump/probe energies, no dynamical phase inversion is observed. At very low pump/probe energies ($E < 2.114$ eV), the opposite phase is observed, again with no dynamical phase inversion. The different phase in this low-energy region is tentatively attributed to the effects of off-resonant measurement.

Equation S2. The scaling constant C_2 in eq 6.3 can be expressed in terms of experimentally measured quantities related to the EMP, although eq 6.3 describes the magnetization by the external field, not by the EMP. For the data in Chapter 6, $E_{mp} = 44$ meV at saturation and $B_{eff} = 17$ T in eq E.2, determined by the fitting shown in Figure 6.2c.

$$C_2 = x_{eff} N_0 V g_{Mn} \mu_B = \frac{\left(\frac{1}{2} x_{eff} N_0 (\alpha - \beta) S\right)}{\left(\frac{N_0(\alpha - \beta)}{2\mu_B g_{Mn}} \frac{1}{N_0 V}\right)} \frac{1}{S} = \frac{E_{mp}}{B_{eff}} \frac{1}{S} \tag{E.2}$$